This is to certify that the
dissertation entitled

THERMALLY ACTIVATED ESCAPE FROM A PERIODICALLY MODULATED OPTICAL TRAP

presented by

James Ryan Kruse

has been accepted towards fulfillment
of the requirements for the

Ph.D. degree in Physics

Major Professor's Signature

May 5, 2004

Date

THERMALLY ACTIVATED ESCAPE FROM A PERIODICALLY MODULATED OPTICAL TRAP

By

James Ryan Kruse

A DISSERTATION

Submitted to
Michigan State University
in partial fulfillment of the requirements
for the degree of

DOCTOR OF PHILOSOPHY

Department of Physics and Astronomy

2004

ABSTRACT

THERMALLY ACTIVATED ESCAPE FROM A PERIODICALLY MODULATED OPTICAL TRAP

By

James Ryan Kruse

Thermally activated escape is a ubiquitous process that underlies a wide variety of physical, chemical, and biological phenomena, such as diffusion in crystals, chemical reactions, and protein folding. More than 60 years ago, Kramers developed a quantitative theory of thermal activation based on a model of a Brownian particle in a metastable potential well coupled to a thermal reservoir. Fluctuations of the heat bath lead to a finite probability for the particle to escape. Since the escape rate is exponentially sensitive to an external force, modulation of the potential may be used as means to control the escape rate. At large modulation amplitude the rate is enhanced as the barrier is reduced, approaching a bifurcation point where it disappears. Recent theoretical work has predicted a power-law scaling of the mean escape rate W with the amplitude of periodic modulation A, $\ln(W) \propto (A_c - A)^{\mu}$, where A_c is the bifurcation amplitude. The critical exponent μ depends on modulation frequency, and is expected to be $\mu = 3/2$ for a quasi-stationary system. As frequency increases, the exponent changes to $\mu = 2$ when a nonadiabatic regime is entered. This thesis reports the first observation of a nonadiabatic critical exponent and explores the frequency dependence of the bifurcation amplitude.

The physical system consists of an overdamped Brownian particle in a three dimensional bistable optical potential under periodic modulation. Two visible laser

beams are focused through a high-power microscope objective into an aqueous solution containing a 0.6 μm silica sphere. Interaction of the optical fields and sphere creates two stable potential minima, a fraction of a μm apart, with an intervening energy barrier. The surrounding medium causes positional fluctuations of the particle in the vicinity of one of the stable points, until a particularly large fluctuation drives the sphere over the barrier where it is captured by the other stable point. The potential is tilted periodically by modulating the laser power at rates from 0.2 Hz to 2 kHz. A camera records the image of the sphere at 5 ms intervals. Real-time digital image processing is used to obtain the sphere position $\vec{r}(t)$ as a function of time and the time evolution of the particle is analyzed to calculate the full three dimensional potential. Knowledge of the potential enables the components of the relaxation time of the particle in the potential to be calculated. Over-barrier transition rate statistics in the static and modulated potentials are evaluated.

An adiabatic regime is identified at modulation frequencies below 0.5 Hz. The loss of adiabaticity is seen at higher frequencies, consistent with the onset of internal relaxation times that cause the particle to fall out of equilibrium at these driving rates. In the weakly nonadiabatic regime it is found that $\ln(W) \propto \left(A_c^{sl} - A\right)^{2.3\pm0.3}$. The critical amplitude A_c^{sl} is seen to vary linearly with frequency, as predicted by theoretical considerations. These results are the first experimental observations of nonadiabatic Brownian dynamics as a bifurcation point is approached.

To my parents

ACKNOWLEDGEMENTS

I would like to thank my advisor, Brage Golding, for the opportunity to work on this project from its inception, and his boundless optimism that I could complete it.

I would also like to thank Lowell McCann for his work on this project. The basis for many of the techniques described in this thesis were developed during his initial experiments, and his visits in the subsequent years gave me much needed boosts of enthusiasm.

Ann Kirchmeier, Darla Conley, and Debbie Simmons made the bureaucratic aspects of university research totally transparent. With every new building there are problems, and the Biomedical and Physical Sciences building had it share. I would like to thank Sandy Teague and Marc Conlin for finding solutions when they existed, and simply letting me complain when they did not.

Tom Palazzolo, Jim Muns, Tom Hudson, and the rest of the Physics and Astronomy machine shop staff patiently answered my questions and gave me the confidence to make those small parts that every experiment needs. They also allowed me to develop a new hobby, a relaxing diversion from the lab. Special thanks go to Tom Palazzolo for not banning me from the student shop after I filled it with sawdust.

I would like to thank my labmates: Connie Meinke, Zhongning Dai, An-Ping Li, Mahdokht Behravan, and Murari Regmi for their outside perspectives and the lessons on growth of heteroepitaxial diamond films. I also thank Reza Loloee and Baokang Bi for their assistance and encouragement.

Finally I would like to thank my family, my parents Jim and Suzeahn Kruse, my sister Michelle, and Eric, Jayme, and Libby. They were always there for me.

TABLE OF CONTENTS

LIST OF TABLES

LIST OF FIGURES

Images in this dissertation are presented in color.

Chapter 1 Introduction

Thermally activated escape over an energy barrier provides the basis for many physical phenomena, including chemical reactions, nucleation in phase transitions, and diffusion of atoms in crystals. For example, an atom on the surface of a crystal resides in an extended periodic potential. Thermal fluctuations cause the atom to move over the barrier separating two stable points; the atom diffuses along the surface. Eventually it reaches a step (where the potential is much deeper) and stops diffusing, becoming part of the next crystal layer.

The probability of escape from a metastable state is exponentially sensitive to an external force. A periodic field, weak compared to the barrier height, could thus be used to control the rate and direction of diffusion in an extended system. Strong modulation distorts the potential, eliminating the metastable point and ultimately leading to a reduction of the stochastic aspects of the dynamics. Approaching this critical modulation amplitude the escape rate dependence on the amplitude displays singular behavior.

The present experiments investigate the effect of periodic modulation on an overdamped Brownian particle in a bistable potential. A sub-micron diameter sphere is trapped by two laser beams, creating two stable points in the trapping potential. Suspended in water, Brownian motion causes the sphere to fluctuate around a stable point until a large thermal fluctuation drives it over the intervening potential barrier. Modulation of the laser power tilts the potential, changing the barrier height.

The particle position is obtained by analyzing particle images recorded by a CCD camera. Each image is transferred to a computer and the three coordinates of the particle's center determined using pattern matching analysis. The image is analyzed in

real time at 200 frames per second, storing the position $\vec{r}(t)$. Since there is no need to save the image, this reduces memory usage, allowing the particle to be tracked for more than 12 hours. The full three dimensional potential energy is calculated from $\vec{r}(t)$ assuming a Boltzmann distribution. The time series is analyzed to determine the transition statistics and the time scales of the particle motions.

The beam power in a single well is modulated electro-optically with varying amplitude and frequency, tilting the potential. The amplitude is varied from zero (static potential) to above the bifurcation amplitude, the amplitude at which the barrier disappears.

The most probable trajectory for a transition is calculated for a static potential. The particle moves in both x (the direction connecting stable points) and z (the direction of beam propagation). The z restoring force is much weaker, with a relaxation time larger than the other directions. This affects the crossover from adiabatic to nonadiabatic modulation.

The effect of modulation is investigated as a function of modulation amplitude and frequency by measuring the interwell transition rate. Multiple regions in phase space are identified, including the adiabatic and weakly nonadiabatic regimes.

To ensure that the static potential does not change during modulation experiments the stability of the optical system was improved using passive and active control methods. The laser beam power fluctuations were reduced through stabilization.

This thesis is organized into six sections. Chapter 2 provides the theoretical description of a Brownian particle in a driven system. Chapter 3 introduces the experimental techniques of optical trapping and particle tracking, and discusses prior

optical experiments. Chapter 4 describes the experimental apparatus used to create and drive the bistable potential, to determine particle position, and to establish long-term system stability. Chapter 5 describes the data analysis and results, including measurement of the most probable transition path and the power law dependence of the activation energy in the adiabatic and nonadiabatic frequency regimes. Chapter 6 summarizes these results and makes suggestions for further work. Since there is substantial reliance on computer control, acquisition, and analysis, detailed descriptions of the software algorithms and interfaces are provided in the body of the dissertation.

Chapter 2 Driven systems with a fluctuating force

The present experiment measures the dynamics of a Brownian particle undergoing thermally activated transitions in a bistable potential. This chapter provides a theoretical description of the dynamics. In a static potential the particle behaves like a damped harmonic oscillator. The addition of a random force (Brownian motion) causes the particle position to fluctuate, exploring the potential. The position probability in the potential is given by Boltzmann statistics.

In a metastable or bistable potential the particle makes thermally activated transitions over the potential energy barrier ΔU. The rate of transitions is proportional to the Arrhenius factor, $\exp(-\Delta U/k_B T)$. In the Kramers theory, the constant of proportionality is a function of the potential curvatures near the stable point and the barrier top [1]. For large barriers ($\Delta U >> k_B T$), the fluctuation responsible for a transition is rare and the distribution of paths the particle follows over the barrier is sharply peaked around an optimal path [2].

Periodic modulation of the barrier height breaks the temporal symmetry; the particle is more likely to escape when the barrier is low. In some systems, a small input signal in a noisy system results in a large output, a phenomenon called stochastic resonance. When the spatial symmetry of the potential or the temporal symmetry of the modulation is broken the transition rates in opposite directions can be independently adjusted, leading to a net current in extended systems.

Calculation of the activation energy under periodic modulation shows three regions of universal dependence of transition rate on modulation amplitude. For large amplitudes

the stable and unstable points approach as the potential tilts. In this regime there is a power law dependence of the change in activation energy δR on the distance from this critical amplitude A_c, $\delta R \propto |A_c - A|^{\mu}$. The power law exponent μ depends on the modulation frequency regime. In the adiabatic regime the modulation frequency Ω is much less than the relaxation rate t_r^{-1}, the particle follows the potential, and μ = 3/2. When $\Omega \geq t_r^{-1}$ the activation energy changes too quickly for the particle to respond and $\mu = 2$. For modulation amplitudes approaching the bifurcation amplitude (for which the stable and unstable points merge), $t_r^{-1} \to 0$. Therefore every system becomes nonadiabatic at some modulation amplitude.

2.1. Fluctuations of a Classical Particle

An overdamped particle in a stable potential $U(\vec{r})$ is approximated as a damped harmonic oscillator for small displacements from the stable point. In this experiment the particle is confined in three dimensions. In each direction the damping rate Γ is much larger than the eigenfrequency of the potential ω; the motion is overdamped. A random driving force is added and the amplitude of random fluctuations determined using the power spectrum. For a general potential the equation of motion is written as a Langevin equation, explicitly including the random force. The stationary position distribution is found from the Fokker-Planck equation, resulting in the Boltzmann distribution.

2.1.1. Damped Harmonic Oscillator

To second order in displacement a stable potential (where $U'' > 0$) is harmonic for small displacements from the stable point. In one dimension the equation of motion is

$$m\ddot{x} + \gamma\dot{x} + kx = 0,$$

where m is the mass, γ is the damping constant and k is the spring constant [3]. The steady state solution is $x(t) = A\exp(-\Gamma_+ t) + B\exp(-\Gamma_- t)$, where $\Gamma_\pm = \Gamma/2 \pm \sqrt{(\Gamma/2)^2 - \omega^2}$ and $\omega = \sqrt{k/m}$.

For an overdamped particle, $\Gamma >> \omega$, and the damping rates $\Gamma_\pm$ are approximated:

$$\Gamma_\pm = \Gamma/2 \pm \Gamma/2\sqrt{1 - (\omega/2\Gamma)^2} \approx \Gamma/2 \pm \Gamma/2 \pm \omega^2/\Gamma.$$

The motion of a particle displaced from the stable point becomes $x(t) = A\exp(-\Gamma t) + B\exp(-\omega^2/\Gamma t)$, with a fast decaying rate Γ and a slower relaxation rate ω^2/Γ. For a 0.6 μm diameter silica sphere ($m = 2.3\times10^{-16}$ kg) in water (viscosity η = 0.001 kg/m s) the damping rate $\Gamma = 6\pi\eta a/m = 2.5\times10^7$ s^{-1}. For the potential in the present experiment the curvature in the y direction is $\omega_y = 2\times10^5$ s^{-1}, so that $\omega_y^2/\Gamma = 1.6\times10^3$ s^{-1} (Section 5.2). The $\Gamma >> \omega$ approximation is equivalent to removing the inertial term from the equation of motion,

$$\Gamma\dot{x} + \omega^2 x = 0$$

with solution $x(t) = A\exp(-\omega^2/\Gamma t)$ for $t >> 1/\Gamma$.

Driven by an external force, the equation of motion becomes

$$\ddot{x} + \Gamma\dot{x} + \omega^2 x = F/m\cos(\Omega t),$$

with steady state solution

$$x(t) = \frac{F/m}{\sqrt{(\omega^2 - \Omega^2)^2 + \Gamma^2\Omega^2}}\sin(\Omega t + \beta),$$

where $\beta = \tan^{-1}\left(\frac{\omega^2 - \Omega^2}{\Gamma\Omega}\right)$.

The amplitude due to the driving force depends on the driving frequency Ω, the natural frequency ω, and the damping rate Γ. Calculating the power spectrum of the position $S_x(\Omega) = |x(\Omega)|^2$, the mean amplitude for an arbitrary force $\xi(t)$ is calculated from the power spectrum $S_\xi(\Omega) = |\xi(\Gamma)|^2$ [4].

$$S_x(\Omega) = \frac{1}{\omega^4 + \Omega^2\Gamma^2} S_\xi(\Omega)$$

in the overdamped system. For white noise the power spectrum is a constant (for small frequency), $S_\xi(\Omega) = 4m\Gamma k_B T$. The position spectrum is a Lorentzian

$$S_x(\Omega) = \frac{4m\Gamma k_B T}{\omega^4 + \Omega^2\Gamma^2},$$

with a corner frequency at $\Omega = \omega^2/\Gamma$, the relaxation rate.

2.1.2. Randomly Fluctuating Particles in a General Potential

The harmonic approximation is limited to a quadratic potential or small fluctuations about the stable point of a more general potential. For larger displacements the equation of motion is rewritten as the Langevin equation for an overdamped particle in potential $U(x)$ with random force $\xi(t)$ [5-7], $\gamma\dot{x}(t) = -\nabla U(x) + \xi(t)$.

There is a time scale τ_c such that the random force on the particle at time t is independent of the force at time $t + \tau_c$. Averaging over times larger than τ_c the force is delta correlated $\langle \xi(t)\xi(t') \rangle = 2D\delta(t - t')$ with noise amplitude D.

The spectral density of this noise, $S_\xi(\Omega)$, is independent of frequency (up to $\Omega = 2\pi/\tau_c$).

$$S_\xi(\Omega) = 2\int_0^\infty e^{i\Omega t}\langle\xi(t)\xi(0)\rangle dt = 4D$$

Fluctuations that satisfy this condition produce *white noise*. (Noise with $S_\xi(\Omega)$ having dependence on Ω is called colored noise.) The fluctuating force has a Gaussian amplitude distribution with zero mean [5].

The probability distribution for a particle in potential $U(x)$ is found with the Fokker-Planck equation. $P(x,t \mid x_0,t_0)$ is the conditional probability that the particle will be at position x at time t if it was initially at x_0 at time t_0. The Fokker-Planck equation relates this probability to the Langevin equation of motion [6]

$$\frac{\partial P}{\partial t} = \frac{\partial(-\nabla U(x)P)}{\partial x} + k_B T\frac{\partial^2 P}{\partial x^2}.$$

The stationary solution $\partial P/\partial t = 0$ for the probability is

$$(2.1)\quad P_S(x) = P_0\exp\left(\frac{-U(x)}{k_B T}\right),$$

the Boltzmann distribution.

Figure 2.1 shows a schematic drawing of the bistable potential used in this experiment (solid line). The probability distribution (dashed) is peaked at the stable points. The probability of the particle being found at the top of the barrier is proportional to the Arrhenius factor $\exp(-\Delta U/k_B T)$, where the barrier height ΔU is the difference between the potential at the local minima and the barrier maximum.

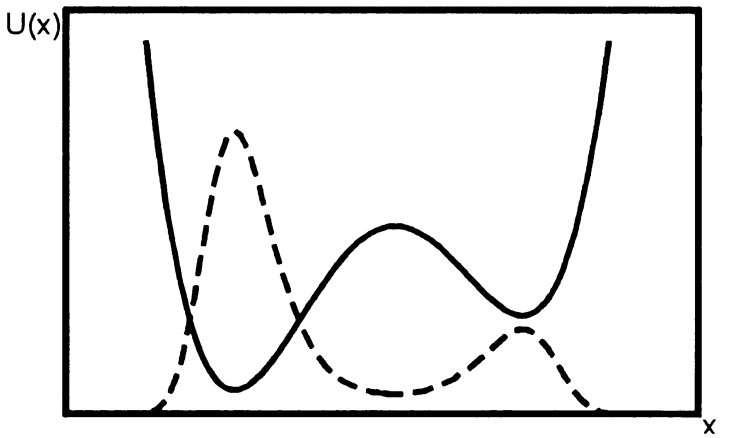

Figure 2.1 Probability distribution of an arbitrary potential. The dashed line is the probability distribution, the solution to equation (2.1) for the bistable potential (solid line).

If the random fluctuations place the particle at the barrier top, it has an equal probability to roll down in either direction. The transition rate is expected to also be proportional to $\exp(-\Delta U/k_B T)$. The next section examines the transition rate and the particle motions as it makes a transition.

2.2. Thermally Activated Transitions

The particle fluctuates in the regions around a in Figure 2.2. Eventually a large fluctuation pushes the particle up the barrier to the point b and across to c. The rate depends on the exponential of the activation energy, $W = C\exp(-R/k_B T)$. In a static potential $R = \Delta U$. The prefactor C depends on the shape of the potential at the stable point and the barrier.

For large barriers ($\Delta U/k_B T >> 1$) escapes are rare. The probability of a fluctuation large enough to cause a transition is sharply peaked around an optimal (most probable) fluctuation. The corresponding path, called the optimal path, depends on the shape of the potential.

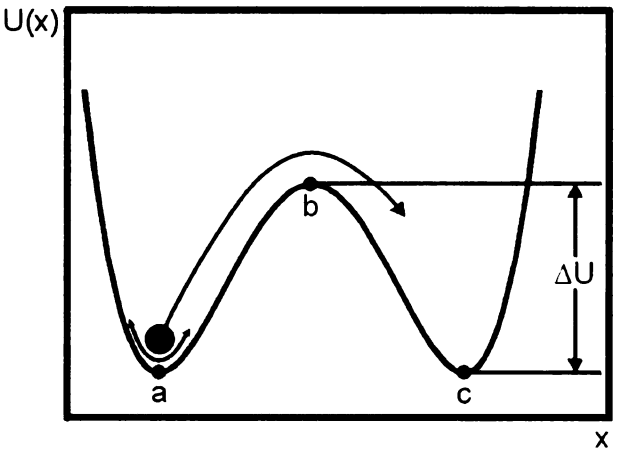

Figure 2.2 Escape over a potential barrier. The particle moves randomly in the area around the stable point a until a large fluctuation pushes it over the barrier of height ΔU at b to the stable point c.

2.2.1. Mean Rate of Transitions

The Arrhenius factor demonstrates the temperature dependence of the transition rate, but it does not give the exact rate for an arbitrary potential. In 1940 Kramers [1] solved the Fokker-Planck equation to find the prefactor for an overdamped particle. The transition rates are

$$W = \frac{\omega_a \omega_b}{2\pi\Gamma} \exp\left(\frac{-\Delta U}{k_B T}\right).$$

Given a known potential with curvatures ω_a at the stable point and ω_b at the barrier, this gives the exact transition rate. For a bistable potential the curvatures in Figure 2.3 are calculated using the Taylor series approximations

$$\begin{aligned} U_a(x) &\approx U(a) + \frac{1}{2}\omega_a^2 (x-a)^2 \\ U_b(x) &\approx U(b) - \frac{1}{2}\omega_b^2 (x-b)^2 \end{aligned} \tag{2.2}$$

at the stable point a and barrier b [6].

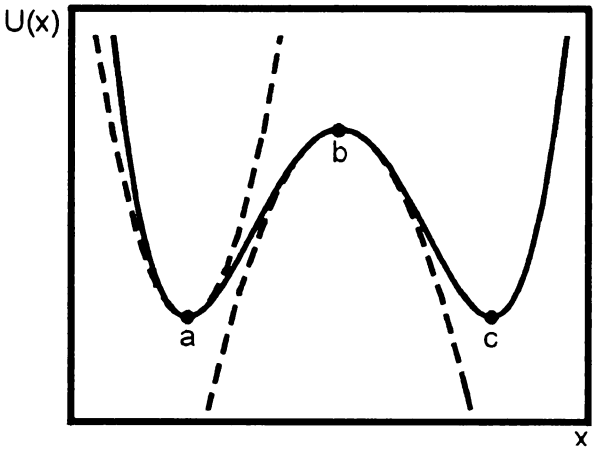

Figure 2.3 Quadratic approximations to the extrema of a bistable potential. The dashed lines represent the quadratic approximations in equation (2.2), centered at x = a and x = b with curvatures ω_a and ω_b, respectively.

In the present experiment the Brownian particle moves in three dimensions. For a potential that is metastable only in the x dimension and stable in the y and z dimensions, the rate equation for an overdamped particle becomes [8]

$$(2.3) \quad W = \frac{\omega_a^x \omega_b^x}{2\pi\Gamma} \frac{\omega_a^y}{\omega_b^y} \frac{\omega_a^z}{\omega_b^z} \exp\left(\frac{-\Delta U}{k_B T}\right).$$

Here ω_a^i and ω_b^i are the curvatures of the potential in the i^{th} direction at a and b.

The Kramers theory has been investigated since its first formulation [9,10]. Corrections have been made for non-white noise [11] and finite barrier heights [12]. The crossover from low damping to high damping adds an additional term to the prefactor, peaked around $\Gamma/\omega = 10$ [12,13]. The transient solutions have also been studied [14-17].

There have been few tests of Kramer's theory. A quantitative test requires complete knowledge of the potential energy. Thus the tests only occur in metastable potentials that can be calculated exactly [18] or that can be measured precisely.

In the overdamped regime, the Kramers theory has been verified by McCann et al [8]. A 0.6 μm diameter dielectric sphere was optically trapped in a bistable potential and driven by Brownian motion. The potential was formed by electric field gradient forces on a dielectric sphere created by two focused laser beams. The static particle position distribution is given by equation (2.1). The potential energy was calculated for three dimensions and the potential curvatures were calculated by quadratic fits to the well and barrier (Figure 2.3). The Stokes damping rate was calculated from the fluid viscosity and particle radius.

The transition rate was modified in a controlled way by changing beam power and spacing. The transition rate was measured (W^{meas}) over four orders of magnitude and compared to the value calculated from equation (2.3) (Figure 2.4). Prefactors calculated for left-to-right (squares) and right-to-left (triangles) transitions agreed with the measurements over the entire range (solid line in Figure 2.4)

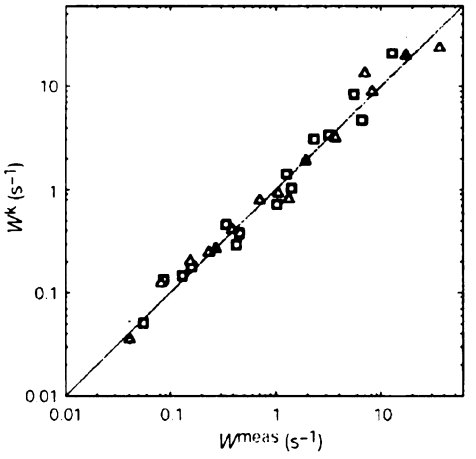

Figure 2.4 Comparison of Kramers theory to measured transition rates [8]. The points each represent a data set where the prefactor and barrier height were calculated from the potential and damping rate (W^k) and the transition rate measured (W^{meas}). The boxes represent left-to-right transitions and the triangles right-to-left transitions. The line with unity slope represents exact correspondence between W^k and W^{meas}.

2.2.2. Optimal Path

The particle fluctuates around a stable point until a large, rare fluctuation drives it over the barrier. The most probable path for the particle to follow is the result of the most probable fluctuation that causes a transition [11]. These are called the optimal path $q_{opt}(t)$ and optimal fluctuation $\xi_{opt}(t)$, respectively.

For the overdamped particle in an arbitrary potential the Langevin equation of motion for the coordinate $q(t)$ is $\dot{q}(t) = K(q) + \xi(t)$, where $K(q)$ contains the deterministic forces ($K(q) = -\nabla U(q)$) and ξ(t) is the random force. The spectrum of the noise $\phi(\Omega)$ is the Fourier transform of the correlation function $\phi(t) = \langle \xi(t)\xi(0) \rangle$.

The particle makes a transition when there is a sufficiently large $\xi(t)$. Following the derivation in [19], the probability of this force is given by the functional

$$P[\xi(t)] = \exp\left[-\frac{1}{2k_B T} \int_{-\infty}^{\infty} dt dt' \xi(t) F(t-t') \xi(t') \right]$$

with noise amplitude $k_B T$. F(t) is the reciprocal of $\phi(t)$, satisfying $\int dt' F(t-t')\phi(t'-t_1) = k_B T \delta(t-t_1)$. For white noise $F(t) = \delta(t)/2$. For small noise intensity the probability is exponentially small to have a force $\xi(t)$ that causes a transition. Also, the probabilities of different transition inducing forces are exponentially different. There is an optimal fluctuation $\xi_{opt}(t)$ around which the probability distribution is peaked. The path the particle follows under this fluctuation is the optimal path $q_{opt}(t)$.

The optimal path and optimal fluctuation maximize the probability functional and minimize the activation energy,

$$R[q(t),\xi(t)]=\frac{1}{2}\int_{-\infty}^{\infty}dtdt'\xi(t)F(t-t')\xi(t)+\int_{-\infty}^{\infty}dt\,\lambda(t)[\dot{q}-K(q)-\xi(t)],$$

with the Lagrange multiplier $\lambda(t)$. (The Lagrange multiplier relates $\xi_{\text{opt}}(t)$ and $q_{\text{opt}}(t)$, finding the probability maximum provided that the equation of motion is satisfied.) The particle starts near the stable point q_a for $t \to -\infty$ and approaches the unstable point q_b as $t \to \infty$.

The transition rate depends exponentially on the minimum activation energy functional that takes the particle from q_a to q_b, $W = C\exp[-R_{\min}/k_BT]$. Assuming white noise (averaging over time much larger than the noise correlation time τ_c) the probability functional is constant and $R_{\min}$ is the minimum of the action,

$$R[q(t)]=\frac{1}{4}\int_{-\infty}^{\infty}dt[\dot{q}-K(q)]^2 .$$

The path that minimizes the activation energy is the solution to $\dot{q}_{\text{opt}}(t)=K(q_{\text{opt}}(t))$. This is the time reversed path of a particle sliding from the unstable point to the stable point in the absence of random noise. The process takes on the order of one relaxation time t_r.

Applying these results to this experiment, the bistable potential is approximated as a one dimensional quartic,

$$U(q)=-\frac{B}{2}q^2+\frac{C}{4}q^4 . \tag{2.4}$$

The optimal path is

$$q_{\text{opt}}(t)=\pm\sqrt{\frac{B}{C+\exp[2B(t+t_c)]}}$$

with constant t_c. The transition is degenerate in time; it can occur for any t_c.

For a real system there is a distribution of paths that lead to a transition, grouped around the optimal path. Stepping backwards in time, the paths that arrive at position q_f at time t_f are described by the prehistory probability density, described in [2]. The distribution $p_h(q,t;q_f,t_f)$ is defined as the probability of a path $q(t)$ that ends at point q_f at time t_f having passed through point q at time t. Equivalently it is the probability of the fluctuation $\xi(t)$ that brings the system to q_f from the stable point q_a through q at time t. $p_h(q,t;q_f,t_f) \equiv p_h(q,t-t_f;q_f,0) = C\exp[-\rho(q,t-t_f;q_f)/k_BT]$, where ρ, analogous to an activation energy, is defined as $\rho(q,t;q_f) = \tilde{\rho}(q,t;q_f) - \tilde{\rho}(q,0;q_f)$, where $\tilde{\rho}(q,t;q_f) = \min R[q(t),\xi(t)]$.

$\tilde{\rho}(q,0;q_f)$ is determined by the optimal path, which minimizes the activation energy function. Therefore $\tilde{\rho}(q,t;q_f) \geq \tilde{\rho}(q,0;q_f)$ and $\rho(q,t;q_f) \geq 0$. When q coincides with $q_{opt}(t)$, $\rho(q_{opt}(t),t;q_f) = 0$. The peak of the prehistory probability density is $p_h(q_{opt}(t),t;q_f,0)$, following the optimal path.

In the next section a periodic driving term is added to the force $K(q;t)$. The activation energy gains a time dependent term, changing the transition rate. Transitions are exponentially more likely to occur when the barrier is a minimum, synchronizing the transitions with the field. This lifts the time degeneracy of the optimal path and leads to control of the stochastic system [20].

2.3. *Transitions in a Periodically Driven System*

The introduction of a time-dependent external field causes a strong, nonlinear response in the dynamics of the system. When the amplitude of the external field is much less than the barrier height ($A << \Delta U$) the system is weakly modulated. The amplitude A can still be larger than $k_B T$, and therefore affect the transition rate exponentially strongly. The transitions become partially synchronized with the field. At higher amplitudes (strong modulation), the potential becomes deformed until eventually a bifurcation point is reached. The stable point and barrier merge and the barrier disappears.

At modulation frequencies Ω much smaller than the relaxation rate ($\Omega t_r << 1$), the particle has time to respond to the changes in the potential. The particle's dynamics depend on the instantaneous value of the potential and the system is adiabatic. At higher modulation frequencies ($\Omega t_r \geq 1$) the system is nonadiabatic. The particle can no longer equilibrate to changes in the potential.

2.3.1. Stochastic Resonance

A system with a weak periodic input and a strong noisy input is expected to have a noisy output with a small periodic component. In some nonlinear systems the noise enhances the signal, producing a large periodic output with small fluctuations. Similarly, the output signal increases with increasing noise, experiencing a peak in the signal to noise ratio at an optimal noise amplitude. This phenomenon is called stochastic resonance [21-25].

Stochastic resonance appears for an overdamped Brownian particle in a bistable potential with a periodic tilt modulation [26]. Figure 2.5 shows how a tilt in the potential lowers the barrier for the left stable point (dashed line). The particle, driven by thermal fluctuations, has an exponentially larger probability to make a transition than in the static case. After the modulation phase changes by π (dotted line), the barrier increases and the transition probability is reduced. The barrier height modulation for the two wells is π out of phase.

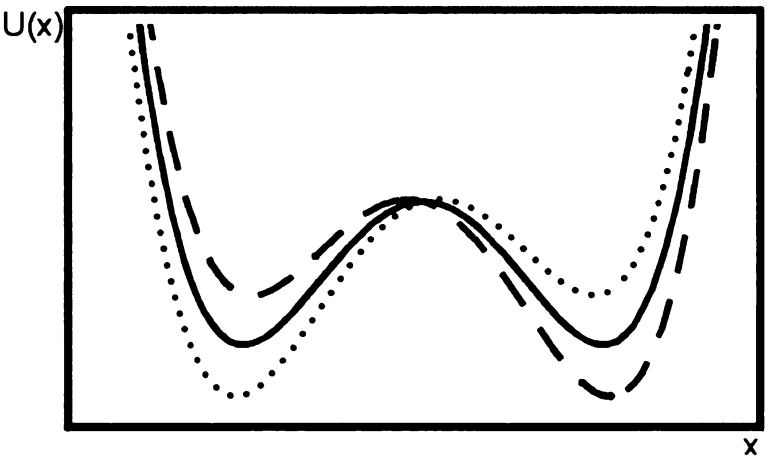

Figure 2.5 Quartic potential with a tilt modulation. The potential undergoes a linear tilt, represented in equation (2.5). The curves represent zero modulation (solid line), 0 phase (dotted line), and π phase (dashed line).

A Brownian particle in a symmetric bistable potential $U(x)$ with periodic driving of amplitude A and frequency Ω has an equation of motion

$$\dot{q} = -\frac{\partial U}{\partial q} + A\cos(\Omega t) + \xi(t). \tag{2.5}$$

The potential has stable points at $q_{1,2}$ and a barrier at $q_b = 0$.

The dynamics of the system are described using linear response theory [24]. (The derivation up to equation (2.13) follows [26].) The input $A\cos(\Omega t)$ causes the

coordinate $q(t)$ to oscillate at the same frequency (and its harmonics). Averaging over many modulation periods,

$$\langle q(t)\rangle = \sum_{n\geq 0} a(n)\cos[n\Omega t + \phi(n)], \tag{2.6}$$

where $a(n)$ and $\phi(n)$ are the amplitude and phase shift for each harmonic component.

For small modulation amplitude A, the amplitudes $a(n) \propto A^n$. The amplitude $a(1)$ can be written $a(1) = A|\chi(\Omega)|$, where $\chi(\Omega)$ is the susceptibility, relating the driving force $A\cos(\Omega t)$ to the response $\langle q(t)\rangle$. The phase shift is

$$\phi(1) = -\arctan\left(\frac{\mathrm{Im}\,\chi(\Omega)}{\mathrm{Re}\,\chi(\Omega)}\right).$$

The spectral density of the position fluctuations is the square of the Fourier transform

$$Q(\omega) = \lim_{\tau\to\infty}\frac{1}{4\pi\tau}\left|\int_{-\tau}^{\tau} dt\, q(t)\exp(i\omega t)\right|^2.$$

The response in equation (2.6) gives rise to δ-peaks at the frequencies $n\Omega$ with area $\frac{1}{4}a(n)^2$. The signal to noise ratio (SNR) is defined as the area under the peak at frequency Ω divided by the spectral density in the absence of modulation $Q^{(0)}(\Omega)$. For small modulation amplitude, $SNR = (1/4)A^2|\chi(\Omega)|/Q^{(0)}(\Omega)$.

The dependence of this signal to noise ratio on noise intensity D has a peak, the defining trait of stochastic resonance. To determine if a system displays this phenomenon, one need only measure the susceptibility $\chi(\Omega)$ and spectral density

$Q^{(0)}(\Omega)$. However, these quantities are related through the fluctuation dissipation theorem [27,28]

$$(2.7)\quad \mathrm{Re}\,\chi(\omega)=\frac{2}{D}\mathrm{P}\int_0^\infty d\omega_1 Q^{(0)}(\omega_1)\frac{\omega_1^2}{\omega_1^2-\omega^2},$$

$$(2.8)\quad \mathrm{Im}\,\chi(\omega)=\frac{\pi\omega}{D}Q^{(0)}(\omega),$$

where P implies the Cauchy principal part of the integral.

For the symmetric bistable system defined above, the susceptibility, spectral density, and SNR can be calculated for small noise intensities ($D << \Delta U$, with barrier height ΔU). The particle spends most of its time at the stable points q_1 and q_2 with intrawell fluctuations with decay rate $\Omega_{1,2} = U''(q_{1,2})$ and infrequent interwell transitions. The spectral density is approximated as the sum of contributions from these fluctuations

$$(2.9)\quad Q^{(0)}(\omega)=w_1Q_1^{(0)}(\omega)+w_2Q_2^{(0)}(\omega)+Q_{tr}^{(0)}(\omega),$$

where w_n (n = 1,2) is the population of the nth stable state. The susceptibility is also approximated as three components, calculated from the spectral density in equations (2.2) and (2.8).

In the symmetric bistable system the populations w_n and curvatures Ω_n for the stable states are equal. Therefore those spectral density and susceptibility components are also equal ($Q_1^{(0)}(\omega)=Q_2^{(0)}(\omega)$, $\chi_1(\omega)=\chi_2(\omega)$). Assuming the potential is quadratic at the stable points, its Taylor series expansion is truncated after the fourth order in q. The spectral density is approximated in terms of the spectral density of a driven, overdamped harmonic oscillator, $L_n(\omega)=(1/\pi)D/(U_n''^2+\omega^2)$.

Allowing for perturbations by the higher order corrections, the spectral density of intrawell fluctuations becomes

$$(2.10)\quad Q_n^{(0)}(\omega) \approx L_n(\omega) - \pi L_n^2(\omega)\left[U_n^{(\mathrm{IV})} - \frac{9U_n'''^2 U_n''}{4U_n''^2 + \omega^2}\right],$$

where the primed variables represent spatial derivatives evaluated at q_n.

The contribution to equation (2.9) from noise induced transitions is

$$(2.11)\quad Q_{tr}^{(0)}(\omega) = \frac{1}{\pi} w_1 w_2 \frac{\left(\langle q\rangle_1^{(0)} - \langle q\rangle_2^{(0)}\right)^2 W^{(0)}}{W^{(0)^2} + \omega^2},$$

where $W^{(0)}$ is the sum of the Kramers rates for transitions out of each well in the absence of modulation, $W^{(0)} = W_{12}^{(0)} + W_{21}^{(0)} = 2W_{12}^{(0)}$ where $W_{12}^{(0)} \propto \exp[-\Delta U/D]$. $\langle q\rangle_n^{(0)}$ is the average value of the coordinate q in each well (neglecting interwell transitions). For small noise amplitudes q remains near the harmonic region of the potential and

$$\langle q\rangle_n^{(0)} = q_n - \frac{1}{2}\frac{DU_n'''}{U_n''^2}.$$

So far the derivation has assumed $D << \Delta U$ and $W^{(0)} << \Omega_r$, where Ω_r the relaxation rate. Transitions occur infrequently due to low noise amplitude, with a rate much smaller than the relaxation rate. Keeping only terms to first order in $D/\Delta U$ and zeroth order in Ω/Ω_r (low modulation frequency), but without constraint on $W^{(0)}/\Omega$, the signal to noise ratio and phase shift become

$$(2.12)\quad SNR = \frac{\pi A^2}{4D^2}\frac{\Omega_r^2 W^{(0)^2} + \Omega^2 D^2}{\Omega_r^2 W^{(0)} + \Omega^2 D} \quad \text{and}$$

$$(2.13)\quad \varphi = -\arctan\left[\frac{\Omega}{\Omega_r}\frac{\Omega_r^2 W^{(0)} + \Omega^2 D}{\Omega_r W^{(0)^2} + \Omega^2 D}\right].$$

At low noise amplitude, $R \sim 1/D$; as D increases, R decreases. For larger D the $W^{(0)^2}$ term grows, causing R to increase with D up to $D \sim \Delta U/2$, where the assumption of small noise amplitude fails. At large D the barrier effectively disappears. The particle diffuses across the entire potential, causing the δ-peak at $Q(\Omega)$ to spread out and decreasing R.

Figure 2.6 is a plot of R/A^2 vs. D in equation (2.12) for the quartic potential with $B = 1$ and $C = 1$ in equation (2.4). The relaxation rate $\Omega_r = 2$ and the barrier height $\Delta U = ¼$. The modulation frequency is set to $\Omega = 0.01$ and amplitude $A = 0.1$. With increasing D the signal to noise ratio falls until it reaches a minimum. It then rises to a peak at $D \sim \Delta U/2$, where the approximations break down. Extrapolating up to $D = \Delta U$ shows R falling as the barrier disappears. This has been observed in a bidirectional ring laser [29] and other systems (see references in [22,24,25]).

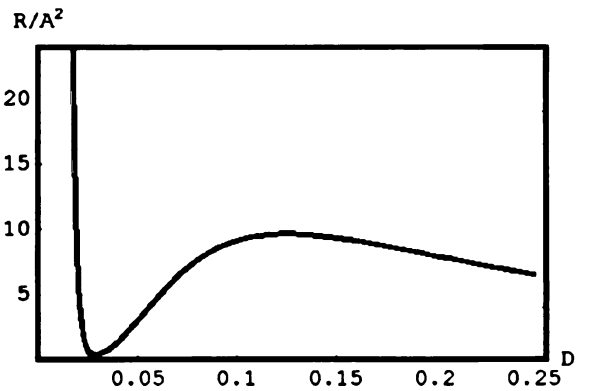

Figure 2.6 Signal to noise ratio for stochastic resonance. The normalized signal to noise ratio (SNR), calculated from linear response theory in the low noise limit, is plotted vs. noise intensity D up to $D = \Delta U$. The peak near $D = 0.125$ indicates that the SNR is enhanced with increasing D up to a maximum. Additional noise then reduces the SNR as the barrier is reduced.

For a thermally activated transition, the nonzero signal to noise is counterintuitive. If there is no noise the rate is zero as there are no transitions. This is the case in discrete two state systems (such as thermal switching of magnetic spins). However, the stable points of a continuous system move under modulation, introducing components to $\chi(\Omega)$ through $Q_n^{(0)}(\Omega)$ in equation (2.9).

In this experimental system it is easier to change the modulation frequency Ω than to change the noise amplitude D. For a one-dimensional bistable system the particle has varying degrees of synchronization, depending on the modulation frequency. At low frequency $\Omega << W^{(0)}$ the modulation is adiabatic. The particle sees a static potential with barrier height $\Delta U = \Delta U^{(0)} + \delta U(t)$, where $dU(t) \approx \Lambda \cos(\Omega t)$ with amplitude $\Lambda \propto A$ for small A. The transition probability is highest when the barrier is lowest, but the particle still has enough time to escape when the barrier is large.

At high frequency $\Omega >> \Omega_r$ the particle does not have time to respond to the instantaneous potential. Instead it sees a potential averaged over the relaxation time $t_r = \Gamma/\omega^2$, with modulation amplitude smaller than the adiabatic amplitude. The rate approaches the unmodulated rate $W^{(0)}$ for increasing modulation frequency.

At intermediate frequencies, the probability increases for making a transition while the barrier is low. If the particle does not make a transition, it tends to wait for a whole period until the barrier is low again. The distribution of dwell times (the amount of time the particle spends in each well before making a transition) has a decaying series of peaks at the odd half-integer multiples of the modulation period. When $\Omega = W^{(0)}$ the synchronization reaches a maximum. This effect was experimentally observed for a

Brownian particle in a bistable optical potential by Simon and Libchaber [30] (see Section 3.3.6).

Directed Diffusion

The dynamics of a symmetric bistable system under symmetric modulation is the same for both stable points. By breaking the spatial or temporal symmetry, the average escape rate for each well can be modified independently. For an extended periodic potential this leads to a net probability current, the direction of which is determined by the potential and modulation parameters.

This effect is illustrated by the probability distribution in a saw tooth potential, periodically turned on and off (Figure 2.7). The slope of the potential is greater on the left, but the barrier heights are the equal. The transition rates are equal and there is no net current. The particle resides in the minimum of the potential with a probability distribution given by equation (2.1). The potential is turned off and the particle diffuses freely. When the potential is turned on again, the probability that the particle has diffused past the left barrier is greater than the probability that it diffused past the right barrier, resulting in a net probability current. Spatially asymmetric potentials are called Brownian ratchets [31,32].

This effect was first considered by Magnasco in his investigation of motor proteins [33]. In a living cell, chemicals are transported in vesicles on a microtubule highway by motor proteins. The protein's attachment to the microtubule is highly asymmetric. The protein turns single molecules of adenosine triphosphate (ATP) into adenosine diphosphate (ADP), corresponding to an on-off modulation of the potential,

resulting in a net motion. The simple model ignored most of the complexities involved in biological systems, but yielded a similar qualitative effect.

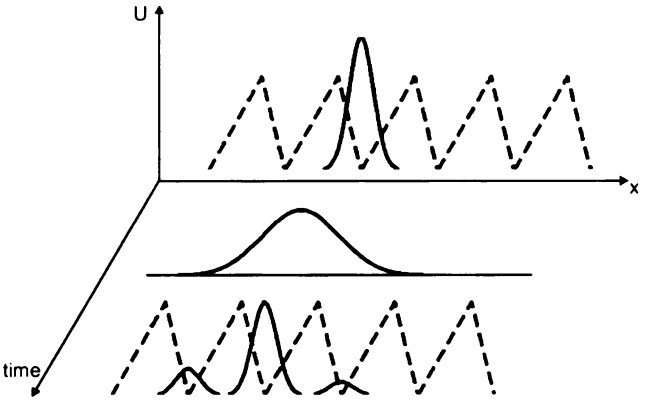

Figure 2.7 Net probability current in a periodically modulated saw tooth potential. The particle begins localized in one stable point with probability distribution represented by the solid curve (top). When the potential (dashed line) is turned off, the position probability distribution spreads out. When the potential is turned on again there is a greater probability that the particle moved to the left than the right. Averaged over multiple modulation periods this produces a net current to the left.

The biased diffusion of a 1.5 μm diameter sphere in an optical ratchet potential has been measured [34]. A single optical trap was scanned in a circle at 100 Hz with synchronized modulation of laser power. The potential was alternated between the ratchet potential and a circular potential around which the particle diffused freely. At the maximum asymmetry the probability of moving in the clockwise direction was 15% higher than moving in the counterclockwise direction.

Directed diffusion has also been observed in symmetric potentials with a zero-mean asymmetric tilt modulation [35-37]. The symmetry is broken, in the case of an asymmetric sawtooth potential, when the rate of change of the instantaneous barrier height is different for the two wells. Stochastic resonance theory says that the maximum synchronization occurs when modulation frequency is half of the escape rate. The

maximum synchronization frequency is different for the two directions resulting in a non-zero current.

The symmetry is also broken if the minimum barrier height is different for the two wells, as with a biharmonic modulation with non-zero phase. In this case the escape rate increases for the well with the lowest barrier, as has been observed in a bistable optical potential [19]. A 0.6 μm diameter sphere driven by Brownian motion was trapped in a potential created by two laser beams. The power in a single beam was modulated with the biharmonic function

$$\Delta P = \delta P[\sin(\Omega t) + (1/2)\sin(2\Omega t + \phi_{12})], \tag{2.14}$$

where δP is the change in beam power corresponding to 1/3 the barrier height, Ω is the modulation frequency ($\Omega/2\pi$ = 1 Hz), and ϕ_{12} is the phase shift (Figure 2.8 inset). For maximum asymmetry ($\phi_{12} = \pi/2$) the instantaneous escape probability varied with the phase of the modulation, with maxima corresponding to the minima in barrier heights (Figure 2.8). The populations differed by 20%. An additional π phase shift interchanged the populations.

These phenomena are described quantitatively using the susceptibility $\chi(\Omega)$ defined using linear response theory. In a symmetric system, the susceptibility for transitions to the left $|\chi^{-}(\Omega)|$ and to the right $|\chi^{+}(\Omega)|$ are equal. Breaking either the spatial or temporal symmetry of the system, the susceptibilities are not equal for certain modulation frequencies. Since the transition rate depends exponentially strongly on $\chi(\Omega)$ it is called the *logarithmic susceptibility* [19,38-41]. Calculation of the logarithmic susceptibility for certain modulation regimes shows power-law dependence on amplitude.

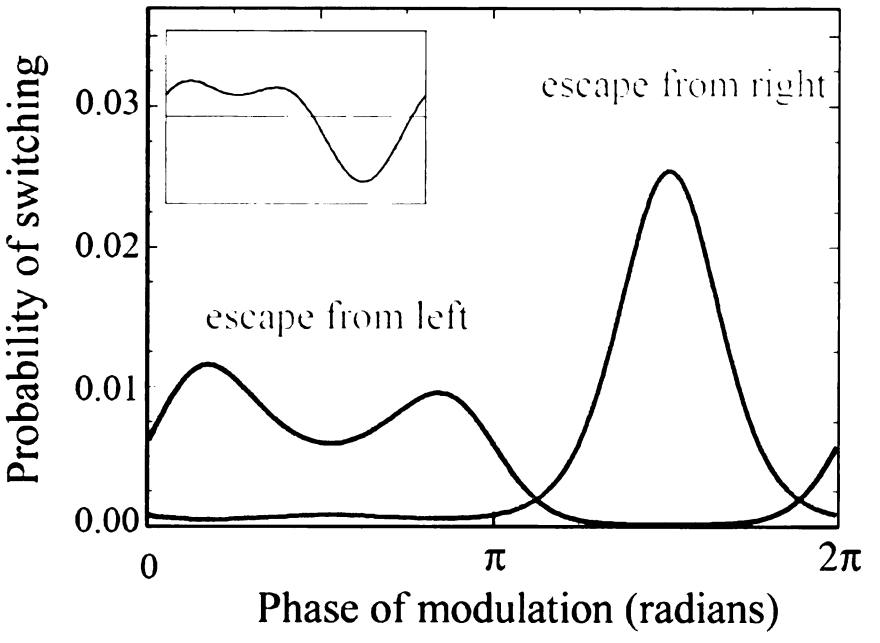

Figure 2.8 Directed diffusion of a Brownian particle in a bistable potential. The curves represent the least squares fit to the instantaneous escape rate as a function of phase for the right-to-left and left-to-right transitions under biharmonic modulation (equation (2.14)) at maximum asymmetry ($\phi_{12} = \pi/2$). The peak in the right-to-left rate shows a bias towards motion to the left. Inset: the waveform of the right beam power modulation. [8]

2.3.2. Logarithmic Susceptibility

At modulation frequencies greater than the intrawell relaxation rate t_r the particle no longer has time to respond to changes in the potential; the modulation is non-adiabatic. For small modulation amplitudes ($A \approx D$) the rapid modulation becomes an additional fluctuation, increasing the effective temperature of the system. The logarithm of the time averaged escape rate $\ln(\overline{W}) \propto A^2$ [13,18,42]. At higher amplitudes (but small compared to the barrier height, $A << \Delta U$) the solution of the escape problem shows $\ln(\overline{W}) \propto A$ [43]. As the modulation amplitude grows large compared to the barrier, the potential becomes tilted and the stable and unstable states approach each other. In this

regime the system shows a power-law dependence of $\overline{W}$ on A, with an exponent that changes with modulation frequency regime.

Following the derivation in [19] to equation (2.16), the escape of an overdamped particle in a potential $U(x)$ with periodic external modulation $F(t)$ and fluctuating force $\xi(t)$ is described by the Langevin equation $\dot{q} = K(q;t) + \xi(t)$, with $K(q;t) = -\nabla U(q) + F(t)$,

where q is the coordinate. The modulation is periodic $F(t) = F(t + \tau_F)$. In the case of white noise, $\xi(t)$ is δ correlated, $\langle \xi(0)\xi(t) \rangle = 2D\delta(t)$.

The potential with modulation has a periodic attractor $q_a(t) = q_a(t + \tau_F)$ (solid line in Figure 2.9). In the absence of driving, q_a is the stable point of the potential. There is an unstable state $q_b(t) = q_b(t + \tau_F)$ representing the potential barrier. An escape occurs (dashed line) when the particle crosses $q_b(t)$. The particle begins in the stable state at $t \to -\infty$ and reaches $q_b(t)$ at $t \to \infty$.

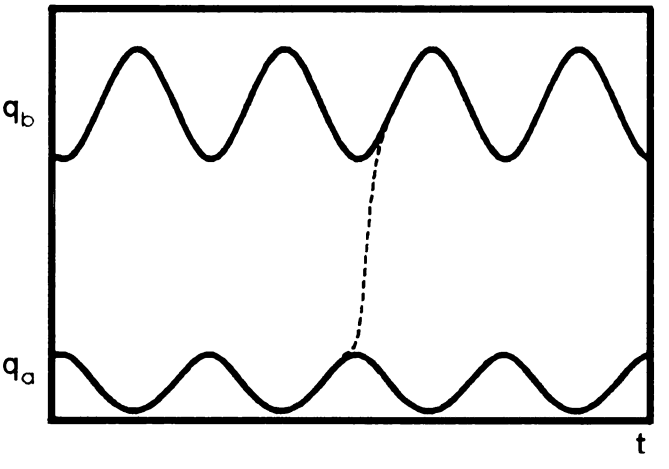

Figure 2.9 Periodic stable and unstable states at small driving amplitude. The stable state q_a and unstable state q_b approach as the potential in equation (2.4) is tilted. The dotted line is the optimal path for escape over the barrier, occurring when the states are closest.

In the regime where $F(t)$ is nonzero but does not distort the system, the modulation can still affect the escape probability exponentially strongly. The change in the activation energy due to the modulation is δR, and the change in the time averaged escape rate is $\overline{W}/W_0 = \exp(-\delta R/D)$. W_0 is the escape rate in the absence of driving, given by the Kramers expression (equation (2.3)).

The optimal path $q_{opt}(t)$ minimizes the time-dependent activation energy functional

$$(2.15)\quad R[q(t)] = \frac{1}{4}\int_{-\infty}^{\infty}[\dot{q} + U'(q) - F(t)]^2\,dt\,.$$

In the static system the escape can occur at any time t_c (Section 2.2.2). With periodic modulation the time degeneracy of the optimal path is broken. The most probable escape path occurs once per modulation period and the transitions become synchronized with the field (Figure 2.9).

To first order in F, the correction δR is calculated from equation (2.15) along the most probable escape path $q_{opt}(t)$. The escape path is an instanton with width on the order of the intrawell relaxation time (dotted line in Figure 2.9). The correction to the activation energy is

$$\delta R = \min_{t_c} \delta R(t_c)$$

$$(2.16)\quad \delta R(t_c) = \int_{-\infty}^{\infty}\chi(t - t_c)F(t)dt \equiv \sum_n \chi(n\Omega)F_n \exp(in\Omega t_c)$$

$\chi(\Omega)$ is the Fourier Transform of $\chi(t)$ and F_n is the n^{th} Fourier component of $F(t)$ [39]. For sinusoidal driving $F(t) = A\cos(\Omega t)$, $\delta R = -|\chi(\Omega)|A$.

The term $\chi(\Omega)$ is the linear response of δR to changes in $F(t)$, and thus the response of the logarithm of $\overline{W}$. $\chi(\Omega)$ is called the logarithmic susceptibility (LS). For white noise driven systems, the LS takes the form $\chi(t) = -\dot{q}_{\text{opt}}^{(0)}(t)$.

Using the LS, it is possible to derive both the exponent and the prefactor in the escape rate. For a white noise driven system [43]

$$\frac{\overline{W}}{W_0} = \frac{1}{2\pi}\int_{-\infty}^{\infty}\exp(-\delta R(\phi/\Omega)/D)d\phi$$

where $\delta R(t_c)$ comes from equation (2.16). In the limit of large modulation amplitude ($A/D >> 1$ but $A/\Delta U << 1$) the activation energy δR, and thus the logarithm of the escape rate, is linear with amplitude.

2.3.3. Strong Modulation

The third region of universality of the escape rate dependence on modulation amplitude occurs when the amplitude is large enough that the distance between stable and unstable states becomes small [44-46]. At frequencies small compared to t_r, there is a critical amplitude A_c^{ad} at which these states merge (Figure 2.10). The potential becomes flat and the restoring force disappears; the particle is free to diffuse. The relaxation rate slows down until eventually $\Omega >> t_r^{-1}$ for all modulation frequencies, leading to the universal behavior. (The derivation in this Section follows [45].)

The motion of an overdamped Brownian particle is described by the Langevin equation $\dot{q} = K(q;A,t) + \xi(t)$, where $K(q;A,t) = K(q;A,t+\tau_F)$ contains the periodic driving with amplitude A and period τ_F. (The modulation frequency $\omega_F = \Omega$ in previous

sections.) The barrier is assumed to be much larger than the noise intensity D (k_BT in this experiment), and the mean interwell transition rate $W << \omega_F,\ t_r^{-1}$.

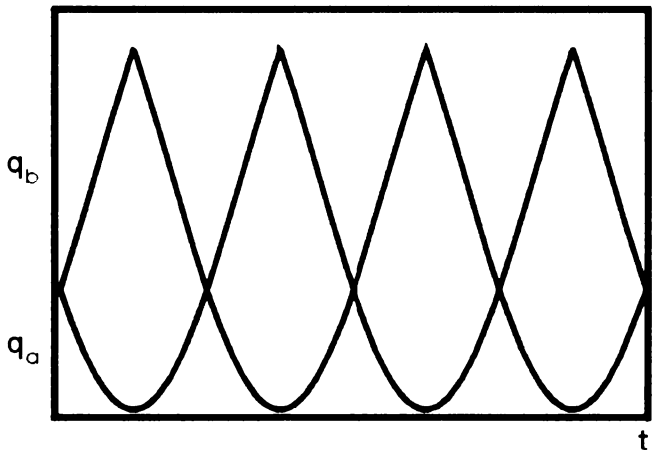

Figure 2.10 Periodic stable and unstable states under large amplitude adiabatic driving. The stable state q_a and unstable state q_b merge as the quartic potential (Figure 2.5) is tilted at the critical amplitude A_c^{ad}. Half of a period later q_b merges with the other stable state (not shown).

The motion of the particle is adiabatic when $\tau_f >> t_r$, the intrawell relaxation time. The adiabatic stable and unstable states $q_{a,b}^{\mathrm{ad}}(t)$ are the solutions to $K\left(q_{a,b}^{\mathrm{ad}}; A, t\right) = 0$ (Figures 2.9 and 2.10). The states merge when $A = A_c^{\mathrm{ad}}$, the adiabatic critical amplitude (Figure 2.10). Without loss of generality the coordinates are offset so $q_a^{\mathrm{ad}}(0) = q_b^{\mathrm{ad}}(0) = 0$ and $A = A_c^{\mathrm{ad}}$ at $t = n\tau_F$ ($n = 0, \pm 1, \ldots$).

As q_a^{ad} and q_b^{ad} approach the potential curvature decreases, changing the restoring force. Near the critical amplitude $\partial K/\partial q \to 0$, the instantaneous relaxation time $t_r = -\left(\partial K/\partial q\right)$ diverges, and the adiabatic approximation is violated.

The transition rate is affected exponentially strongly by the change in barrier height. Assuming $\Delta U >> D$ (or $W << \omega_F$), a transition is most probable for the small

interval about $t = n\tau_F$. Expanding $K(q;A,t)$ around t = 0 and $A = A_c^{ad}$ and keeping the lowest order terms,

(2.17) $K \approx \alpha q^2 + \beta \delta A^{ad} - \alpha\gamma^2(\omega_F t)^2$.

where $\delta A^{ad} = A - A^{ad}$, $\alpha = \frac{1}{2}\frac{\partial^2 K}{\partial q^2}$, $\beta = \frac{\partial K}{\partial A}$, and $\gamma^2 = \frac{-1}{2\alpha\omega_F^2}\frac{\partial^2 K}{\partial t^2}$, are evaluated at $A = A_c^{ad}$, t = 0, and $q = q_a^{ad}(0)$.

The adiabatic relaxation time becomes

(2.18) $t_r^{ad} = \frac{1}{2}\left[(\alpha\gamma\omega_F t)^2 - \alpha\beta\delta A^{ad}\right]^{-1/2}$

around the stable and unstable points $q_{a,b}^{ad} = \mp 1/(2\alpha t_r^{ad})$. For $t = 0$ and $\delta A^{ad} = 0$, t_r^{ad} diverges. Using equation (2.18) the condition for adiabaticity is $\omega_F t_r^{ad} << 1$. A second, stronger condition limits the maximum rate of change of the relaxation time, $|\partial t_r^{ad}/\partial t| << 1$. This condition is also expressed as $t_r^{ad} << t_l$ for $t_l = (\alpha\gamma\omega_F)^{-1/2}$, or $\omega_F << |\beta\delta A^{ad}|/\gamma$. The time scale t_l limits the adiabatic approximation.

As the stable and unstable points approach they become distorted (Figure 2.11). Solving equation (2.17) for K = 0 in as $\delta A^{ad} \to 0$, the extrema merge along the line $q_{a,b}(t) = \gamma\omega_F t$. The critical amplitude becomes frequency dependent, $A_c^{sl} = A_c^{ad} + \gamma\omega_F/\beta$, where A_c^{sl} is the critical amplitude in the nonadiabatic slow driving regime. The condition $\omega_F t_r^{ad} << 1$ remains valid.

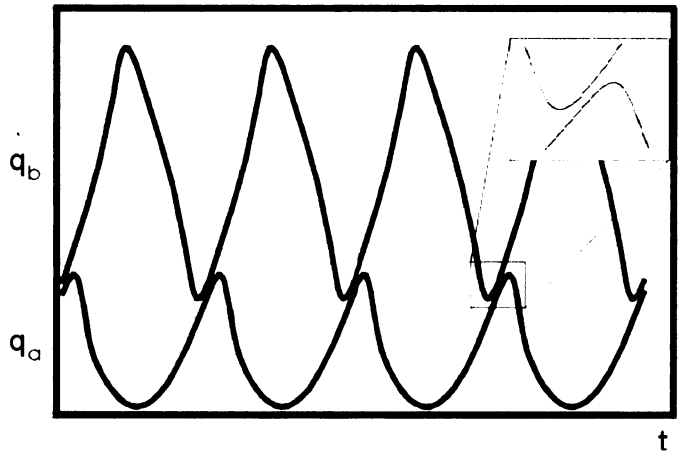

Figure 2.11 Periodic stable and unstable states at large driving amplitude and high frequency. The quartic potential is tilted with $A > A_c^{ad}$. The stable state q_a and unstable state q_b distort, finally merging at the bifurcation amplitude A_c^{sl} along the line $q = \gamma\omega_F t$.

Concerning units: The subsequent derivations use a set of reduced variables. Before explaining the derivation of the power law behavior, the length, time, and energy scales will be connected to those in the current experiment. The one dimensional equation of motion is $m\Gamma\dot{x}(t) = -\nabla U(x;A,t) + \xi(t)$, where the potential energy U has units of k_BT, position x has units of microns (μm), mass m is in kg, and Stokes damping rate Γ is s^{-1}. Therefore $K = -\nabla U/m\Gamma$.

Assuming the quartic potential (with modulation term) in equations (2.4) and (2.5), $\alpha = \frac{3Cx_a}{m\Gamma}$, $\beta = \frac{1}{m\Gamma}$, and $\gamma^2 = \frac{m\Gamma}{6Cx_s\omega_F^2}\frac{A_c^{ad}\omega_F^2}{m\Gamma} = \frac{A_c^{ad}}{6Cx_s}$, where the stable point $x_s = \sqrt{B/3C}$ at the critical amplitude $A_c^{ad} = 2B^{3/2}/3\sqrt{3C}$.

Transforming into dimensionless coordinates for position $Q = \alpha t_l q$, amplitude $\eta = \beta\left(A_c^{sl} - A\right)/\gamma\omega_F$, and time variable, $\tau = t/t_l$ and transforming the derivative $\dot{Q} = dQ/d\tau$, the equation of motion becomes

$\dot{Q} = G(Q,\eta,\tau) + \tilde{f}(\tau)$, where $G(Q,\eta,\tau) = Q^2 - \tau^2 + 1 - \eta$.

Since the system slows when the particle is most likely to escape, any correlation time in the noise is smaller than the relaxation time. The noise is approximated as δ-correlated, $\langle \tilde{f}(0)\tilde{f}(\tau)\rangle = 2\tilde{D}\delta(\tau)$ where $\tilde{D} = |\alpha/4|^{1/2}(\gamma\omega_F)^{-3/2}\int dt\langle \xi(t)\xi(0)\rangle$.

The activation energy $\tilde{R} = \tilde{D}/DR$ is given by the minimum of the energy functional

(2.19) $$\tilde{R} = \frac{1}{4}\int_{-\infty}^{\infty}\left(\dot{Q} - Q^2 + \tau^2 - 1 + \eta\right)^2 d\tau$$

where again the boundary conditions are $Q \to Q_a(\tau)$ as $\tau \to -\infty$ and $Q \to Q_b(\tau)$ as $\tau \to \infty$.

In the adiabatic regime ($\eta >> 1$) corresponding to slow modulation, escape is most likely when $\tau = 0$ and thus the τ^2 term is neglected. The optimal path that minimizes $\tilde{R}$ is the instanton $Q_{opt}(\tau) = (\eta-1)^{1/2}\tanh\left((\eta-1)^{1/2}(\tau-\tau_0)\right)$, where τ_0 is arbitrary. The escapes are distributed in time around $\tau = 0$. The activation energy

$$\tilde{R} = \frac{4}{3}(\eta-1)^{3/2} \propto \left(A_c^{\text{ad}} - A\right)^{3/2}.$$

In the nonadiabatic regime the τ^2 term must be included. This lifts the time degeneracy and synchronizes the escape, leading to a nonadiabatic correction in $\tilde{R}$. The minimum of the activation energy occurs for $\tau_0 = 0$. To first order,

$$\tilde{R} \approx \frac{4}{3}(\eta-1)^{3/2} + \frac{\pi^2}{6}(\eta-1)^{-1/2}.$$

Numerical simulations (also performed in [45]) show 7% agreement for $\eta > 3$.

Close to the bifurcation point A_c^{sl} ($\eta << 1$) the escape occurs when the stable and unstable states $Q_a(\tau)$ and $Q_b(\tau)$ are close to each other. $Q_a(\tau) = Q_b(\tau) \approx \tau$ in this regime, allowing the integrand of equation (2.19) to be linearized. The solution is

$$S = \sqrt{\frac{\pi}{8}}\eta^2, \ \eta << 1.$$

The activation energy is quadratic in the distance from the bifurcation point $\left(A_c^{sl} - A\right)^2$ in the slow driving regime.

The width of this interval is proportional to ω_F for $\omega_F t_r << 1$. The adiabatic exponent μ = 3/2 crosses over to the nonadiabatic exponent $\mu = 2$ at large modulation amplitudes ($A_c^{ad} < A < A_c^{sl}$) or large driving frequencies.

As $A \to A_c^{sl}$ the relaxation time t_r becomes long enough to invalidate the expansion of the driving force in equation (2.17). For long relaxation times the duration of the most probable escape path exceeds the modulation period; the particle requires many cycles to escape. In this case the activation energy shows the $R \propto \left(A_c^{sl} - A\right)^{3/2}$ dependence on modulation amplitude.

2.4. Summary

An overdamped particle confined to a potential and driven by a random force is analogous to a damped, driven harmonic oscillator. There is a relaxation time, the time it takes a displaced particle to return to the stable point, which is a function of the potential curvature and the damping rate. The random force causes the particle to explore the potential resulting in a position distribution given by the Boltzmann distribution.

In the bistable potential the thermal fluctuations drive the particle over the barrier with a rate proportional to $\exp(-\Delta U/k_b T)$ with a prefactor that depends on the shape of the potential. The trajectories the particle follows are distributed around the optimal path, caused by the most probable energy fluctuation that results in a transition. This path can be directly measured from the prehistory distribution, the distribution of all paths that result in a transition.

The optimal path minimizes the activation energy. With the addition of periodic modulation this minimum occurs once per period and the transitions become synchronized. The modulation frequency can be adjusted to maximize the transition rate, leading to directed diffusion in a spatially or temporally asymmetric system.

Calculations of the activation energy for large amplitude modulation reveal power law dependence on the distance to the critical amplitude, $\delta R \propto \left(A_c^{\mathrm{sl}} - A\right)^{\mu}$. For adiabatically slow modulation (compared to the relaxation rate) the critical exponent is $\mu = 3/2$ and $A_c^{\mathrm{sl}} \rightarrow A_c^{\mathrm{ad}}$. In the nonadiabatic regime, $\mu = 2$ and A_c^{sl} is linear in frequency. As the modulation amplitude increases the stable and unstable points approach and the relaxation rate, which depends on the curvature of the potential, approaches zero. The system becomes nonadiabatic for all modulation frequencies and there is a crossover of the power law from $\mu = 3/2$ to $\mu = 2$.

This theory has been developed recently, and only verified through numerical simulations [44-46]. The experiments presented in this thesis are the first to identify the adiabatic and weakly nonadiabatic frequency regimes and confirm the critical exponent $\mu = 2$ and linear frequency dependence of the critical amplitude A_c^{sl}.

Chapter 3 Optical Trapping

Prior experiments, beginning with the first radial optical trap [47] and the single beam three dimensional trap [48], have developed methods to create the traps, measure the potential created by the trapped particle in the beam, and to measure the position of a trapped particle. This chapter describes these methods and their relationship to the present work. Chapter 4 contains a detailed description of the experimental apparatus.

Optically transparent particles refract an incident laser beam, causing a momentum transfer that pushes the particle to the region of highest electromagnetic field gradient. These forces were used to trap particles in two and ultimately three dimensions.

The position of a trapped particle has been measured with a camera [8], a photodiode [49], and a position sensitive quadrant photodiode [50]. The camera recorded images of the particle under an external illumination source. These images were analyzed to determine the particle center. The photodiode devices measured the trapping beam scattered from the trapped particle. A calibration related the photodiode signal to absolute position.

The particle driven by Brownian motion explores the potential. The position fluctuations contain information about the potential that is extracted from either the fluctuation spectrum [49] or the position distribution [8]. The potential was also measured from the particle position under an external force [51].

Multiple laser beams are used to create multiple, independent traps. Two trapped particles have been used to measure the position dependence of hydrodynamic forces between the particles. A single particle in two beams, spaced a small distance apart so the traps overlap, makes thermally activated transitions between the stable points.

Additionally, the trapping forces of the independent traps have been modulated with beam power, synchronizing the transitions with the modulation.

3.1. Experimental Realizations of Optical Trapping

3.1.1. Radial Trap

In 1970 Ashkin discovered that micron-sized transparent particles in water were drawn into the axis of a laser beam and accelerated in the direction of propagation [47]. He focused a 6.2 μm diameter TEM_{00} Argon ion laser beam horizontally into a glass cell filled with water and a mixture of transparent latex spheres (polydisperse solution, 1 μm mean diameter). A single "trapped" sphere moved in the beam's direction of propagation until hitting the wall of the cell, where it remained in the beam center. When the beam was blocked the particle diffused freely.

The explanation invoked a force generated by momentum transfer due to reflection and refraction of the laser beam. A latex particle (with index of refraction n_L = 1.58) in water (index n_w = 1.33) deflects incident rays (Figure 3.1). With each deflection a ray transfers momentum to the sphere, represented by the gray arrows, creating a force pointing towards the ray and along the direction of propagation. If there are multiple rays with different intensities there is a net force towards the more intense rays. The TEM_{00} laser beam has a Gaussian radial intensity profile, with greatest intensity at the center of the beam. Therefore the spheres were drawn towards the center of the beam as they were pushed through the solution.

Ashkin and Dziedzic expanded on this work, levitating transparent particles and oil drops in air and vacuum [52-54]. A single lens focused the laser beam upward into an

air-filled cell. The particles, either 1 to 40 μm diameter silicone oil drops or 20 μm diameter fused glass spheres, were drawn into the center of the beam and accelerated upwards away from the beam waist. The particle came to rest when the axial radiation pressure and gravity balanced. For the oil drops [53] the equilibrium position varied with drop diameter; the smaller drops came to rest higher in the beam.

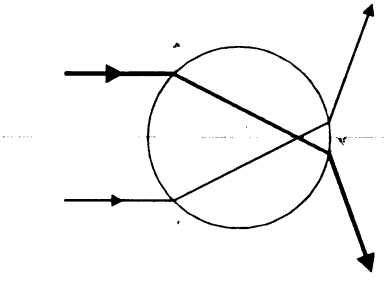

Figure 3.1 Radial optical trap. A ray incident on a transparent sphere is refracted, exchanging momentum with the sphere. If two parallel rays of different powers enter the sphere, this force pushes the sphere along the direction of propagation and towards the higher power ray.

3.1.2. Three Dimensional Trap

To create a stable, three dimensional trap the radiation pressure in the direction of beam propagation must be opposed by an additional axial force. Using the slightly diverging beams from the radial trapping experiment, a three dimensional trap was created with two counter-propagating laser beams [47]. The latex particles were radially trapped at the beam centers and axially trapped by opposed radiation pressure forces. In 1986, Ashkin et al. [48] three dimensionally trapped latex and silica spheres in a single laser beam focused with a large convergence angle. The resulting axial gradient produced a force towards the focal point large enough to overcome the scattering force. They successfully trapped particles ranging from 25 nm to 10 μm with input laser powers of 100 mW to 1.4 W.

Shown schematically in Figure 3.2, the focused beam was deflected by the sphere (due to its higher index of refraction than the surrounding water). The momentum exchanged with the particle when it moved axially or radially produced a force towards the focal point.

Expressions were derived for the trapping and scattering forces in the Rayleigh regime [48], where the particle diameter $2a$ is much smaller than the trapping beam wavelength λ. Under this approximation the intensity variation across the sphere due to time varying electromagnetic fields is assumed to be small. The electric field was treated as static.

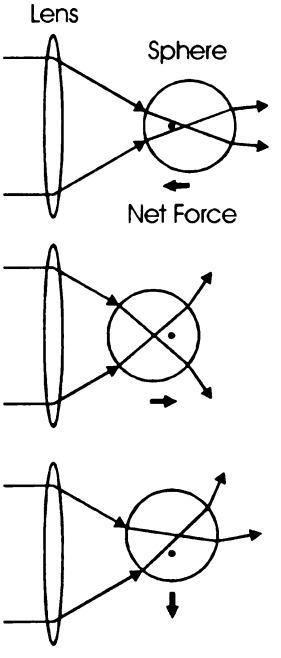

Figure 3.2 Three dimensional optical trap. The lens focuses the beam (represented by two rays) to the focal point (black dot). The beam is refracted, exchanging momentum with the sphere and creating a net force in the direction of the bold arrow. For axial and radial displacements of the particle the net force is towards the focal point.

The force created by light scattering off the sphere is

$$(3.1) \quad F_{\text{scat}} = \frac{I_0 n_b}{c} \frac{128\pi^5 a^6}{3\lambda^4} \left(\frac{m^2 - 1}{m^2 + 2} \right)^2,$$

where I_0 is the beam intensity, m was the effective index n_p/n_b, with particle index n_p and index of the surrounding medium n_b [48]. The force is in the direction of propagation.

In general, for a neutral, dielectric particle in a static electric field **E** there is an induced dipole moment $\mathbf{d} = \alpha \mathbf{E}$, where α is the polarizability of the particle. The electrostatic energy of this dipole is $U = -\mathbf{d} \cdot \mathbf{E} = -\alpha |\mathbf{E}|^2$. In a uniform electric field there is no force on the particle. If the field is nonuniform, the force is proportional to the spatial gradient of the energy, $\mathbf{F} = -\nabla U = \alpha \nabla |\mathbf{E}|^2$.

Substituting for the polarizability of a spherical Rayleigh particle [55] the gradient force in the axial direction is

$$(3.2) \quad F_{\text{grad}} = -\frac{n_b^3 a^3}{2} \left(\frac{m^2 - 1}{m^2 + 2} \right) \nabla |\mathbf{E}|^2,$$

with a negative sign showing that it opposes the scattering force. The maximum value of the gradient force occurs when the particle is at an axial displacement $z = \pi w_0^2 / \sqrt{3}\lambda$, where w_0 is the beam waist radius at the focal point. If, at that point F_{grad} is larger than F_{scat}, the particle is stably trapped. This sets a constraint on sphere size, wavelength, and beam waist radius through the ratio of forces R [48],

$$R = \frac{F_{\text{grad}}}{F_{\text{scat}}} = \frac{3\sqrt{3}}{64\pi^5} \frac{n_b^2}{\left(\frac{m^2 - 1}{m^2 + 2} \right)} \frac{\lambda^5}{a^3 w_0^2} \geq 1.$$

For the system in [48] (λ = 514 nm, $2w_0 = 1.5\lambda$, latex spheres with m = 1.24), setting $R = 3$ (the maximum gradient force was three times the scattering force) the maximum sphere diameter was 95 nm, for which the Rayleigh approximation ($\lambda >> a$) is no longer valid. The conclusion was that this did not imply a lack of stability for larger particles, where ray optics representations like Figures 3.1 and 3.2 became more valid. Trapping of 1 μm and 10 μm diameter spheres showed that this was the case.

The condition $R \geq 1$ is independent of beam power. To insure that the sphere did not diffuse out of the trap, they required the power be sufficiently large so the Boltzmann factor $\exp(-U/k_B T) << 1$, where

$$U = \frac{n_b^3 r^3}{2}\left(\frac{m^2 - 1}{m^2 + 2}\right)|\mathbf{E}|^2.$$

Requiring $U/k_b T \approx 10$, the minimum silica sphere diameter trapped by a 1.5 W input beam is predicted to be 19 nm. The smallest sphere actually trapped was 26 nm diameter silica, trapped with 1.4 W.

3.1.3. Trapping Optics

Ashkin et al. [48] used a laser emitting at λ = 514 nm focused by a 100x 1.25 NA microscope objective lens to create a three dimensional trap. Typical trapping systems, shown in Figure 3.3, contain a high numerical aperture (NA) lens (usually a microscope objective), a laser with an output of at least 10 mW, and beam steering mirrors, plus additional optics to modify beam size, power, stability, and polarization. A detailed description of our experimental apparatus is in Section 4.1.

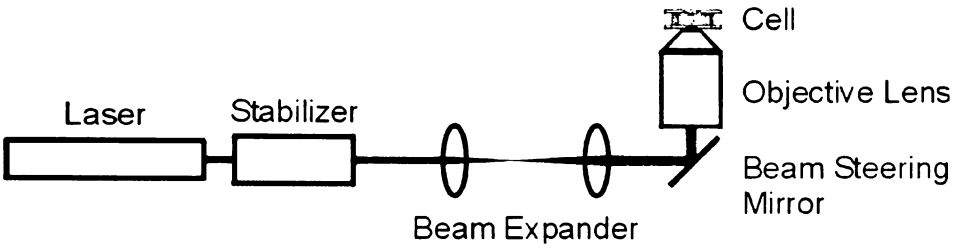

Figure 3.3 Basic trapping system. The beam emitted by the laser is stabilized and power controlled with the stabilizer. The beam diameter is expanded by two lenses. A beam steering mirror changes the angle at which the beam enters the objective lens. The objective focuses the beam to a diffraction limited spot in the water filled cell.

Objective Lens

To maximize the axial forces the trapping lenses are chosen to have a large numerical aperture, where the numerical aperture is defined as $\mathrm{NA} = n_b \sin\phi$ with index of refraction of the surrounding medium n_b and full beam convergence angle 2ϕ. In the Rayleigh regime the axial force depends on the NA to the fourth power (see Appendix B). Therefore a 60x microscope objective lens with NA 0.8 will have 50% of the maximum axial force from a 100x lens with NA 0.95, or 33 % of the maximum axial force from a 100x oil immersion lens with NA 1.4.

The largest available numerical apertures are found in microscope objectives. An objective is a system of lenses designed to magnify nearby objects with high angular magnification. Microscope objectives are corrected for spherical aberrations and dispersion, and an objective with 100x magnification focuses the beam to a diffraction limited diameter (under certain conditions, see Section 4.1). When the objective is part of a microscope, the position of the focal point in the cell is controlled in three dimensions with the sample stage and microscope focus controls. If the beam entering the objective is collimated (i.e., parallel), the beam waist will be in the focal plane of the

objective. A particle trapped at the beam waist will be visible when viewed through the microscope eyepieces and auxiliary viewports. In Section 3.2.1 the particle image is projected onto a camera by the trapping objective.

When a microscope is used, the laser beam is directed to the objective lens without disturbing the viewing path. The beam is brought in through the rear fluorescence port or a side port. A dichroic mirror reflects the laser wavelength into the objective, but transmits the returning microscope illumination for subsequent viewing (Figure 3.4).

Trapping Laser

The trapping laser is chosen for the wavelength, power, and stability necessary for the application. The minimum trapping power reported by Ashkin et al. [48] was less than 1 mW. Typical trapping systems use at least 10 mW, although some applications require more than 1 W (e.g., trapping very small particles). Trapping laser wavelengths vary from blue to near infrared. Biological trapping systems use near IR where the absorption by biological materials is lower than at the visible wavelengths. Experiments with inorganic materials tend to use visible wavelengths for simplicity.

Standing waves in a laser's resonance cavity create transverse electromagnetic modes (TEM), variations in the intensity and phase perpendicular to the direction of propagation. Lasers typically emit in the lowest order mode in both transverse directions, TEM_{00}, which has a cylindrically symmetric Gaussian intensity profile. Higher order modes have regions of zero intensity, for example the TEM_{01} mode has two bright regions separated by a node along the x axis. The intensity gradient (and the force for $m > 1$ in equation (3.2)) points away from the beam center. Typical trapping systems use

TEM_{00} emitting lasers, but a highly focused beam with cylindrically symmetric TEM_{01}^{*} (donut) mode has also stably trapped a particle in three dimensions [56].

Beam power is controlled to change the trapping force or to prevent damage to trapped objects [48]. This occurs through either a mechanical device, such as a polarizer, or an electro-optic device like a Pockels cell. Some experiments varied the beam power periodically to modulate the shape of the potential [8,30]. If constant power is required, changes in beam power due to laser power fluctuations are filtered using electro-optic stabilizers.

3.1.4. Other Trapping Geometries

The system described in Section 3.1.3 represents only one way to create a stable three dimensional trap. Traps have been created using lasers delivered through fiber optics [57-60], aligned to create the counter-propagating beam trap first developed by Ashkin [47]. For low numerical aperture focusing lenses the axial trapping force has been increased using standing wave traps [61,62]. The laser beam entering the cell was reflected by a mirror, interfering and creating a steep axial intensity gradient between the nodes and antinodes.

Other experiments have changed the trapping laser. Stable three dimensional traps have been created using diode lasers [63], corrected for the characteristic divergence angle difference parallel and perpendicular to the junction. Multiple stable traps have been constructed with vertical cavity surface emitting lasers (VSCEL) arrays, creating an 8 x 8 array of individually controllable traps [64].

Using conventional gas or solid state lasers, multiple traps have been created by scanning a single beam across the objective's focal plane with simultaneous modulation

of the power [65-68]. This makes multiple regions of high field gradient at the cost of overall trapping power and possible high frequency modulation effects. Arrays of traps have been created through static diffractive elements [69] and dynamic computer generated holograms [70-72].

3.2. Trapped Particle Position Tracking

There are three devices other groups [8,49,50,73] have used to track the particle position: a CCD camera, a single photodiode, and a quadrant photodiode. The CCD camera records images of the particle, illuminated by a light source, which are computer analyzed to find the particle position. The photodiode systems measure the intensity pattern of the trapping laser scattering off of the particle. The forward scattered component, combined with the unscattered portion of the trapping beam, changes intensity as the particle changes position. The CCD camera tracking system is advantageous for recording large particle displacements, as is the case for a particle in the two well trap used in the present experiment.

3.2.1. Camera Particle Tracking

McCann et al. [8] used a CCD camera to record the image of the particle in the focal plane. This allowed them to track the particle when it made large excursions from the trap center, necessary for their dual beam trapping experiment.

The particle was trapped by the laser, focused through the trapping objective lens (Figure 3.4). A lamp emitted white light, focused into the cell by a condenser lens, aligned to create a uniformly bright background. The particle was imaged onto the camera by the trapping objective and an eyepiece. A laser rejection filter prevented beam

reflections from reaching the camera. The image was then transferred via a framegrabber to a computer and a pattern matching algorithm used to find the center of the particle with ±10 nm resolution in x and y. The z position was measured by the method described in Section 4.2, with ±40 nm resolution.

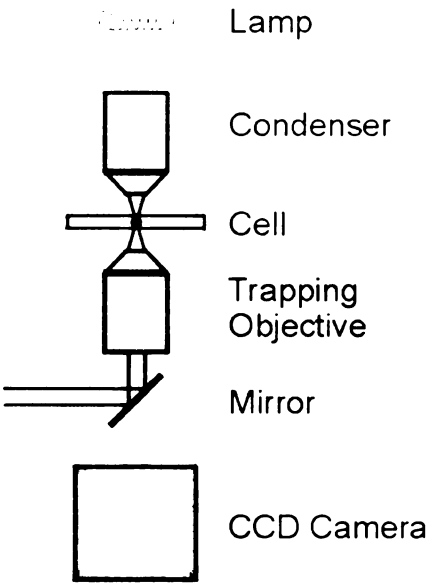

Figure 3.4 Camera tracking system. The optical trap is formed by the laser, reflected up by the mirror and focused through the trapping objective lens into the cell. The particle is trapped in the trapping objective's focal plane. The lamp is focused onto the cell by the condenser lens. The particle is imaged by the trapping objective. The image is sent to a CCD camera, where it is recorded or analyzed by a computer. [8]

3.2.2. Single Photodiode Particle Tracking

Ghislain et al. [49] used a single photodiode to measure the position fluctuation spectrum of a trapped sphere (Section 3.3.1). They trapped a particle in the focal plane of the trapping objective (Figure 3.5). The light forward scattered from the particle (along with any unscattered trapping beam) was collected by the imaging objective lens and directed to the photodiode. The imaging objective and photodiode were positioned so the

beam diameter at the photodiode was equal to the radius of the detector. The photodiode was positioned a distance Z_0 from the conjugate plane.

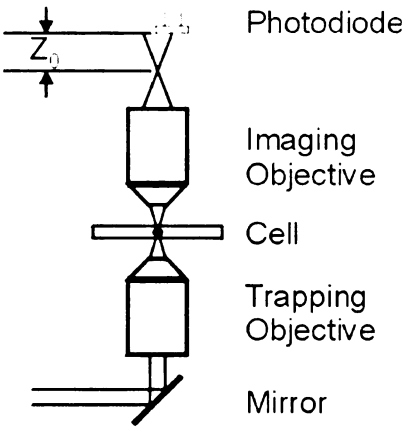

Figure 3.5 Photodiode tracking system. A particle is trapped in the focal plane of the trapping objective. The photodiode intercepts the forward scattered laser beam, expanded by an imaging objective lens over a distance Z_0. [49]

The particle was assumed to be a spherical lens, and the change in intensity due to an axial or radial displacement was calculated in the ray-optics limit. The change in signal power ΔP_z for a small axial displacement Δz is

$$\Delta P_z = \left(\frac{dP_{\text{ave}}}{dz}\right)\Delta z \approx 2P_{\text{ave}}\left(m_{\text{obj}}m_p\right)^2\frac{\Delta z}{Z_0}$$

where P_{ave} is the average power intercepted by the photodiode and m_{obj} and m_p are the magnifications of the imaging objective lens and the particle, respectively. Z_0 is the axial separation between the image plane of the second objective and the photodiode. The maximum signal occurred when the photodiode intercepted ½ of the total optical power.

The intensity profile at the photodiode was cylindrically symmetric. If the intensity profile were centered on the photodiode, position changes in the transverse direction would be measured in distance from the trap center $r = \sqrt{x^2 + y^2}$, with no

discrimination between x and y. To measure the position changes in the x direction the photodiode was positioned off center. The change in signal power ΔP_x is

$$\Delta P_x = \left(\frac{dP_{\text{ave}}}{dx}\right)\Delta x \approx \frac{2}{\pi} P_{\text{ave}}\left(m_{\text{obj}} m_p\right)\frac{\Delta x}{R_{\text{det}}},$$

where R_{det} is the radius of the detector. The maximum signal occurred when the detector was offset by R_{det}. A photodiode centered in the beam with half of its active area masked could also be used record x fluctuations, at the cost of halving the intercepted power P_{ave}.

Ghislain et al, [49] used this technique to measure the force constants of a single particle in an optical trap (Section 3.3.1). The position resolution was 1 nm in the radial direction and 10 nm in the axial direction. Their system was designed to measure the deflection in a single dimension, a projection along x and z. The three dimensional motion could not be measured.

3.2.3. Quadrant Photodiode Particle Tracking

Gittes and Schmidt [50] used a quadrant photodiode system (Figure 3.6) to track a trapped particle in three dimensions simultaneously. The quadrant detector consisted of four active elements in a 2 x 2 array, labeled A, B, C, and D. The imaging objective lens collected the forward scattered light, which was collimated by a second lens. The lens focused the image from the back focal plane onto the quadrant photodiode. This arrangement allowed Gittes and Schmidt to position the beam anywhere in the objective's field of view without affecting the intensity pattern. Changes in the particle's radial position deflected the bright spot in the intensity, changing the differential voltage between elements. Motions in the axial (z) direction changed the overall brightness.

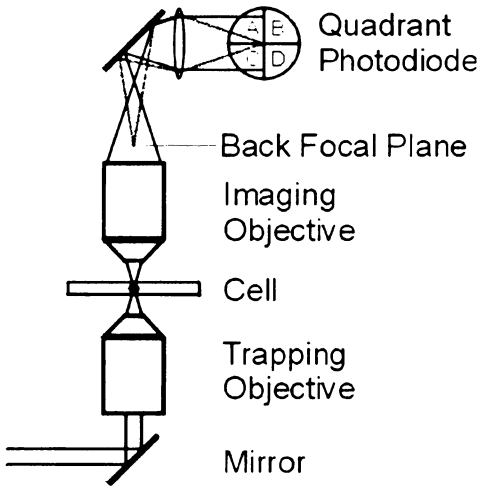

Figure 3.6 Quadrant photodiode tracking system. The quadrant photodiode is placed in a plane conjugate to the back focal plane of the imaging objective. The dotted line represents the imaging of the back focal plane. The quadrant photodiode, split into four regions labeled A, B, C, and D measures the position of the peak in the forward scattered intensity pattern. [50]

When the particle was centered in the trap the differential voltages $V_x = (B+D)-(A+C)$ and $V_y = (A+B)-(C+D)$ were zero. A change in the x position caused a change in V_x while V_y remained zero and vice versa; the x and y signals were decoupled. A change in the z position resulted in an overall intensity change, $V_z = A+B+C+D$. For small particle displacements from the trap center, these signals were linear.

For a static displacement in x, changes in the intensity (due to z motions) appeared as motions in the x direction as well. When the intensity in all four elements doubled, V_x also doubled. To compensate, the displacements were calculated by

$$\Delta x \propto \frac{V_x}{V_z} = \frac{(B+D)-(A+C)}{A+B+C+D}$$

$$\Delta y \propto \frac{V_x}{V_z} = \frac{(A+B)-(C+D)}{A+B+C+D}$$

$$\Delta z \propto V_z = A + B + C + D$$

The differential signal increased the sensitivity ($\leq$ 1 nm) but required an analog electronic circuit and introduced extra noise. As with the single photodiode, the linearity only occurred for small displacements from the trap center. The signals for large excursions (where the intensity pattern shifts a large amount on the photodiode) were multivalued. Particles far away from the center of the trap could not be tracked.

Two quadrant photodiodes have been used to track two particles in two traps [74] (Section 3.3.5). The traps were created with two orthogonally polarized beams. The image in the back focal plane, a combination of the forward scattered light from both trapped particles, was split by a beam splitter in place of the upper mirror in Figure 3.6, and sent to their respective photodiodes.

3.2.4. Comparison of Tracking Methods

The quadrant photodiode differential voltage is linear with particle position only over a small range of displacements (100 nm). With greater displacements the particle moves out of the beam waist, no longer deflecting the trapping beam. In practice, the limit to the measurable particle displacement depends on the acceptance angle of the imaging objective (Figure 3.6). For a single particle in a dual beam trap, the position may not be recorded as the particle makes transitions between stable points, depending on the particle size, beam separation, and imaging objective NA. The camera tracking system uses the microscope lamp to illuminate the particle anywhere in the objective's field of view. The particle is tracked regardless of the trap position.

In the experiments described in this thesis the potential was tilted by changing the power in one of the beams. A filter in the camera system rejects the reflected laser light

and the image is unaffected. Unless compensated, in a quadrant photodiode system this appears as a periodic shift in z for one beam only.

A camera tracking system marginally achieves the time resolution required by the present experiments. To track the intrawell motions of the particle the sampling rate should be many times the intrawell relaxation rate, in this case ~200 Hz. Meiners and Quake [75] used a quadrant photodiode system running at 50 kHz to measure hydrodynamic interactions (Section 3.3.5). However, to measure the much slower interwell transitions in our experiment the 200 frame per second CCD camera used by McCann et al. [8] is sufficient.

A disadvantage of the CCD camera system is its image storage requirements. A quadrant photodiode at 50 kHz requires 8- to 16-bits per channel, for a data rate on the order of 250 kB per second. A 256 x 256, 8-bit grayscale camera running at 200 frames per second produces more than 10 MB per second (36 GB per hour), requiring extensive computer memory if the images are stored. In this experiment the memory requirements have been reduced by analyzing the image in real time, then discarding the image and storing the position.

The cost to implement a quadrant photodiode tracking system is approximately $1000 for a multichannel analog to digital converter board, $1000 for the computer, and $20 for the photodiode. To determine the particle position the voltages are digitized and converted to position through calibration or calculation. By comparison a high speed camera, a framegrabber, and a computer fast enough to analyze the images in real time cost around $15,000. Specialized software was developed to perform the pattern matching analysis that determines the sphere position from the images.

The camera system requires external illumination in addition to the trapping beam. For higher frame rates, greater illumination intensity is required. These systems are expensive and can have adverse thermal effects on the fluid surrounding the trapped particle. In the photodiode tracking systems, the intense and highly localized trapping laser illuminates the particle.

3.3. Prior Experiments Using Optical Traps

This section describes prior work relevant to this experiment. (For an overview of optical trapping experiments see [76,77].) The shape of the potential was calculated from the fluctuation spectrum, the position distribution, or direct application of an external force. Two types of dual beam trapping experiments dealt with problems similar to this experiment, described in Chapter 4. The problems of creating two beams, tracking a one or two particles, maintaining a constant beam spacing, and introducing beam power modulation have been addressed here.

3.3.1. Measurement of Spring Constants from the Fluctuation Spectrum

Ghislain, et al. [49] measured the spring constants of a particle in an optical trap by measuring the position fluctuation spectrum with the single photodiode setup (Section 3.2.2). These quantities were derived knowing only the corner frequencies and the Stokes damping rate, calculated from the particle size and solution viscosity.

For small displacements from the trap center (Figure 3.7), the potential was assumed to be harmonic so that the overdamped one dimensional equation of motion is

(3.3) $$\gamma\dot{x}(t) = -kx(t) + \xi(t),$$

where k is the spring constant, γ is the Stokes damping coefficient, and $\xi(t)$ is the random driving force. The damping coefficient for a spherical particle in a fluid is given by the Stokes expression $\gamma = 6\pi\eta a$, where η is the viscosity of the surrounding medium and a is the sphere radius. A three dimensional trap with radial symmetry has a radial and an axial spring constant. Divided into separate equations of motion $\gamma\dot{x}(t) = -k_x x(t) + \xi(t)$ and $\gamma\dot{z}(t) = -k_z z(t) + \xi(t)$, Ghislain et al. measured these spring constants simultaneously by measuring displacements projected onto a line in x and z.

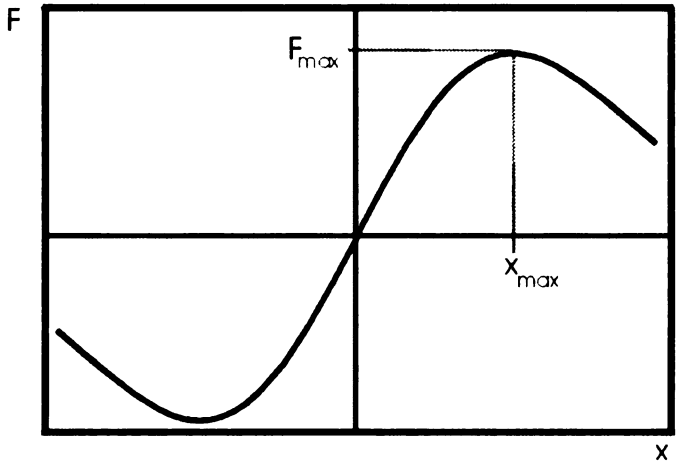

Figure 3.7 Trapping force vs. position in the Rayleigh size regime. For small displacements in x the force F is linear. A maximum trapping force F_{max} is reached when the sphere center is at x_{max}, approximately one sphere radius from the trap center.

Driven by the random force, the particle position fluctuates in three dimensions. The power spectrum of fluctuations in a single dimension is the square of the Fourier transform of the positions, $S_x(f) = |x(f)|^2$, where $x(f) = \int_{-\infty}^{\infty} dt x(t) \exp(2\pi i f t)$ and the Fourier transform of $\dot{x}(t)$ is $-2\pi i f x(f)$.

The power spectrum of a white noise source is $S_{\xi}(f)=4\gamma k_B T$. The Fourier transform of equation (3.3) gives $(k-2\pi i\gamma f)x(f)=\xi(f)$. Squaring both sides gives $4\pi^2\gamma^2(f_c^2+f^2)S_x(f)=S_{\xi}(f)=4\gamma k_B T$, where $f_c=k/2\pi\gamma$. Solving for $S_x(f)$, $S_x(f)=k_B T/\pi^2\gamma(f_c^2+f^2)$. In one dimension the spectrum is a Lorentzian with corner frequency f_c.

The power spectrum of the position fluctuations (and also the voltage fluctuations from the photodiode) produced a spectrum with two corner frequencies, found at 40 Hz and 400 Hz for a 2 μm particle trapped in a 150 mW beam. These corresponded to the axial (z) and radial (x) spring constants $k_z=2\times10^{-5}$ N/m and $k_x=2\times10^{-4}$ N/m, respectively. The axial intensity gradient, created by the beam converging to the beam waist, is an order of magnitude smaller than the radial gradient.

3.3.2. Measurement of Potential Energy from the Position Distribution

A trapped particle in thermal equilibrium has a probability distribution $p(x,y,z)$ related to the potential energy distribution $U(x,y,z)$ by the Boltzmann distribution

$$(3.4)\quad p(x,y,z)=\frac{1}{Z}\exp\left(-\frac{U(x,y,z)}{k_B T}\right),$$

where $k_B T$ is the temperature (in units of energy), and constant A normalizes the total probability to unity. By measuring the probability distribution, the potential energy for every region the particle visits is calculated [8,78-80]. This technique makes no assumptions about the shape of the potential, only that the particle is in thermal equilibrium and the position is measured over times much longer than the slowest time scale. For a single trap the slowest time scale is the axial relaxation time, on the order of

1 ms, while for a single particle in a bistable potential they are the interwell transition times which depend on barrier height.

McCann, et al. [8] obtained the three dimensional potential energy for a particle in a bistable optical potential. They measured the particle position $\vec{r}(t)$ at 5 ms intervals for thousands of interwell transitions using the CCD camera tracking system in described Section 3.2.3. The position data were converted into a three dimensional histogram $P(x,y,z)$ by segmenting the volume into elements of size $\Delta V = \Delta x \Delta y \Delta z$ and counting the number of times the particle was in each volume element.

From this discrete distribution the potential energy $U(x,y,z)$ was calculated at each volume element. From (3.4),

$$U(x,y,z) = -k_B T \ln\left(\frac{P(x,y,z)}{P_0}\right) - k_B T \ln(Z).$$

The probability distribution $p(x,y,z)$ is represented by the ratio of the discrete position distribution $P(x,y,z)$ and the total number of counts P_0. A depends on the shape of the potential, and creates a constant offset in the energy. Figure 3.8 shows a typical result for a particle in a bistable potential. The color scale represents energy in 1 $k_B T$ steps with an arbitrary offset. The red regions contain an average of 1100 counts, while the blue regions contain only one count.

A stable trap holds a particle for an indefinitely long time; by definition, a stably trapped particle can never explore outside of the trap. Therefore the absolute energy is not measured with this method. To measure the potential in the well at greater distances from the minimum, the particle must be tracked over intervals of time that increase exponentially with energy.

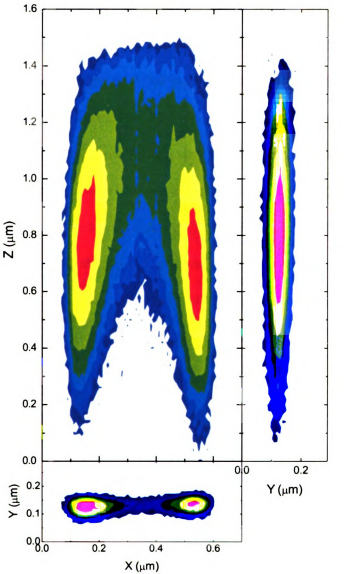

Figure 3.8 Three dimensional potential energy histogram of a particle in a bistable potential. The xz, yz, and xy planes are slices through the minimum potential energy (x = -0.21 μm) The data set (labeled 101403-03) contains 2,000,000 points with more than 16000 transitions between the stable points. The contours represent 7 to 13 $k_B T$ in 1 $k_B T$ steps (with arbitrary offset), corresponding to averages of 500, 180, 67, 25, 9, and 1 counts in the corresponding volume element ΔV.

3.3.3. Measurement of Trapping Force from Stokes Damping

The maximum trapping force and force vs. position relations have been measured using the velocity-dependent Stokes drag to apply external forces to a trapped particle. Figure 3.7 shows a typical trapping force vs. position curve. The force is linear for small displacements from the trap center, then reaches a maximum force F_{max}. Felgner et al. [81] measured this maximum force by flowing water around a trapped sphere with increasing velocity until the particle was pushed out of the trap.

Theoretical trapping force calculations (Appendix A) show that the force varies linearly with beam power. Ashkin [82] grouped the geometrical factors (particle size, beam convergence angle, etc.) into a dimensionless trapping efficiency Q, the ratio of the force on the particle to the total incident photon momentum. $F_{max} = (n_b P/c)Q$, the maximum force F_{max} is proportional to the beam power P and the index of refraction of the surrounding medium n_b. For particles trapped in water (n_b = 1.33), $n_b/c = 4.4\,\mathrm{pN/mW}$.

Felgner et al. translated the cell on a motorized sample stage, flowing the solution around the particle with velocity v. At velocities such that $6\pi\eta a v_{max} \geq (n_b P/c)Q$, the Stokes force exceeded the maximum trapping force and the particle escaped. A camera displayed the image of the particle on a monitor. When the particle escaped it moved away from the trap in the direction of the fluid flow. The procedure was repeated to reduce the uncertainty in v_{max} due to random fluctuations. This method was used to test the predictions of the trapping force calculations [83]. Felgner et al. [81] measured trapping efficiencies of 0.01 in the axial direction and 0.1 in the radial direction for 1.2 μm diameter silica spheres (corresponding to F_{max} = 0.44 pN/mW P).

The force for small displacements (the linear region of Figure 3.7) was measured using a similar technique. The flow velocity v was held below v_{max} and the time-averaged position relative to the trap center measured. From the equation of motion (equation (3.3)) the spring constant in the direction of motion was calculated [49,81,84]. Spring constants were on the order of 2×10^{-4} N/m in the radial direction and 5×10^{-5} N/m in the axial direction for a 1 μm diameter sphere.

Removing the assumption of linearity from equation (3.3), the equation of motion becomes $6\pi\eta a v = F(x) + \xi(t)$. Averaging over long times (such that $\langle\xi(t)\rangle = 0$), the trapping force $F(x)$ was measured from the particle velocity by Simmons et al. [51]. They measured the velocity of a 1 μm diameter silica sphere falling into a trap by first trapping a particle, then displacing the trap by around 500 nm. From the particle's velocity they calculated the force in one dimension for positions beyond x_{max} in Figure 3.7, the region of maximum trapping force.

Sections 3.3.1 through 3.3.3 describe three methods of inferring the shape of the potential from the particle motions. The fluctuation spectrum measurement uses a model potential and the damping rate to calculate the spring constants. The sampling rate must be large enough to observe the changes, greater than the relaxation rate. The Stokes damping force measurement gives the force vs. position curve in a single dimension, from a free particle to the stable point. Calculating the potential energy from the position distribution gives the shape of the potential without a predetermined model potential.

3.3.4. Hydrodynamic Interactions Between Colloidal Particles

In a viscous solution, colloidal particles interact through motions of the solvent (amongst other forces). The motions of two particles in two optical traps are correlated due to these hydrodynamic interactions [74,75]. The position correlation functions parallel and transverse to the beam separation were measured as a function of r.

The optical traps were created using a λ = 1064 nm beam from a single solid state laser. The beams were split by a polarizing beam splitter, creating two orthogonally polarized beams. After passing through beam steering optics, the beams were recombined and focused into the sample cell by a high power microscope objective. A 1 μm diameter sphere was trapped in each beam. Trap separation was measured with a camera.

To track each particle independently, the forward-scattered light was collected by an imaging objective. The beams were split based on polarization orientation by a polarizing beam splitter (replacing the upper mirror in Figure 3.5). Each beam was sent to its own quadrant photodiode, where positions were measured with nm resolution. To prevent crosstalk and interference effects, Meiners and Quake [75] alternately chopped the beams at 100 kHz. (The chopping was too fast for the particle to react. Instead it saw a time averaged potential as described in Section 2.3.1.)

The particle trajectories were recorded for around 10^7 data points. Henderson, et al. discovered that the laser pointing instability caused the traps to move randomly in the focal plane, over distances on the order of 10 nm with time scales of seconds. While these fluctuations were too slow to affect the particle dynamics (the fluctuations were slower than the ~1 kHz relaxation rate), the beam motion changed the voltages measured

at the photodiodes. To reduce this effect, they split the dataset into 20,000 data point blocks that were analyzed then averaged together.

The particle position autocorrelation function showed the expected decay, with a decay rate corresponding to the relaxation rate. The motions of two closely spaced (< 10 sphere radii), trapped particles were anticorrelated. As a particle moves, the surrounding fluid will flow in the opposite direction. If another sphere is close enough, it will be caught in this flow and pushed in the opposite direction [74]. The peak position in the crosscorrelation function depends on the trap strength and the friction on the particles.

3.3.5. Synchronization of Transitions in a Bistable Potential

Simon and Libchaber [30] measured the transitions of a 1 μm diameter particle over the barrier of a bistable potential under tilt modulation. The bistable potential was formed by two overlapping optical traps. An Argon ion laser beam with $\lambda = 488$ nm was split by a nonpolarizing beam splitter. Each beam reflected off a steering mirror to a second beam splitter, where they were recombined then focused into the water filled cell by a 100x objective lens. Each beam passed through a neutral density filter wheel to independently control the beam power.

The particle image was projected onto a camera running at 30 frames per second, then transferred to S-VHS video tape. Analysis was performed directly off the video monitor. The residence time τ (the time between interwell transitions) was recorded, ignoring the crossing time (usually around 70 ms).

Inside the cell the beams were separated by approximately 1 μm. The particle made thermally activated transitions over the barrier. The transition probability was

assumed to be constant in time, therefore the residence time probability distribution $p(\tau)$ was Poissonian (plotted in Figure 3.9), with normalized distribution $p(\tau) = \lambda \exp(-\lambda\tau)$.

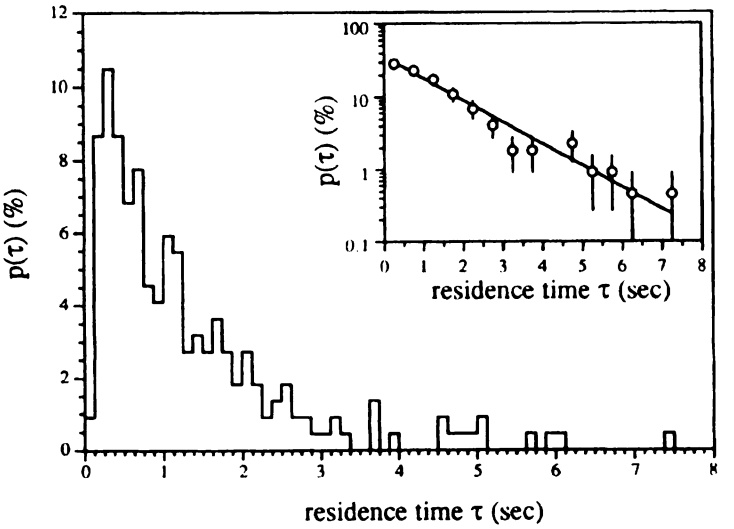

Figure 3.9 Residence time histogram in a static bistable potential [30]. The probability $p(\tau)$ of making a transition is plotted vs. the time since the previous transition. The probability decays exponentially with decay time $\bar{\tau}$ = 1.3 s, with a cutoff for short times. Inset: Logarithmic plot with fit corresponding to transition rate $\lambda = 0.76$ Hz.

Fitting the dwell time histogram for the N = 219 transitions (sampled over 15 minutes) binned at 1/8 second intervals yielded λ = 0.76 ± 0.05 Hz. The mean escape time $\tau_k = 1/\lambda = 1.3 \pm 0.1$ s. The distribution also showed a cutoff at short residence times. The authors concluded that the particle relaxed to the potential minimum before making another transition, with time scales of the relaxation time t_r. The relaxation time was estimated to be $t_r = 0.1 \pm 0.1$ s. From Kramers' theory

$$\frac{1}{\tau_k} = \frac{1}{t_r} \exp\left(-\frac{U}{k_B T}\right),$$

the barrier height was calculated to be 2.6 ± 1.0 $k_B T$.

The potential was modulated by varying the beam power in each beam with the motor controlled neutral density filter wheels. The filter wheels were rotated π out of phase to provide tilt modulation. (The change in the potential is represented in Figure 2.6). Approximating the double well potential as a quartic with a time dependent linear tilt, the particle followed the Langevin equation $\dot{x} = Ax\cos(\Omega t + \theta) + Bx - Cx^3 + \xi(t)$, where A is the tilt amplitude, with frequency Ω and phase shift θ. The static parameters B and C define the double well potential. $\xi(t)$ represents the random force due to Brownian motion. The filter wheel rotation was set so the amplitude was 7% of the total beam power. Comparisons of residence time histograms above to those in the present experiment show that the 7% change in beam power corresponds to approximately 1.5 k_BT change in the height of the 2.6 k_BT barrier.

At modulation rates below the mean static transition rate, the transitions became partially synchronized with the modulation. The particle was more likely to escape when the barrier is low, but because the modulation was so slow there was still a finite probability to escape at any other time. This was seen in the residence time distribution (Figure 3.10a) as a peak at time $\tilde{\tau} \equiv \pi/\Omega$ (half of the modulation period) overlapping with the static exponential distribution.

At modulation rates above the mean static transition rate but below the relaxation rate the particle almost always made a transition when the barrier was low. The potential changed so quickly that if the particle did not make a transition immediately it would wait a full modulation period until the barrier was low again. The dwell time distribution (Figure 3.10b) showed a decaying series of peaks at odd half-integers of the modulation period.

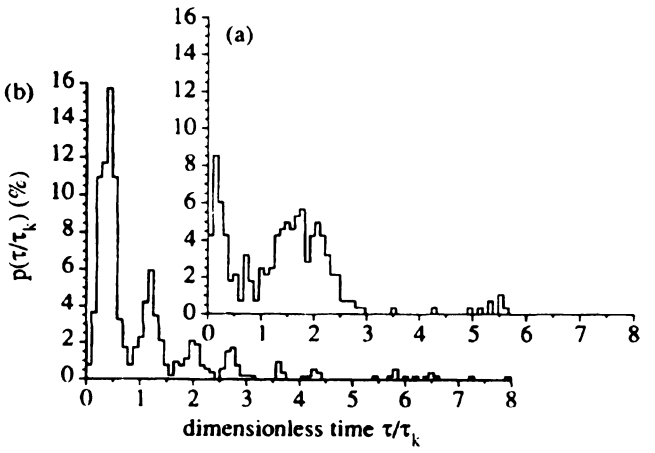

Figure 3.10 Residence time histograms under modulation [30]. The probability $p(\tau)$ for (a) modulation slower than the mean transition rate, $\tilde{\tau}/\tau_k = 1.54$, showing a synchronization peak along with the exponential decay at short times. (b) shows the odd harmonics for faster modulation, $\tilde{\tau}/\tau_k = 0.38$. Plots contain (a) $N = 282$ events and (b) $N = 225$ events with bin width 1/8 s.

When the modulation rate was one half of the mean static transition rate, maximum synchronization occurred. The probability to escape during the first modulation period was a maximum, and higher order harmonics were reduced or eliminated. Simon and Libchaber considered this peak as confirmation of stochastic resonance in their system.

At modulation frequencies higher than the relaxation rate (not studied in their experiment), the particle would no longer have time to respond to the modulation. For $\tilde{\tau} << \tau_k$ the particle would see a time averaged potential with a barrier height equal to the static barrier. The residence time distribution would lose the harmonic structure, reverting back to an exponential decay with a mean transition rate lower than the static rate.

The experiment demonstrated the synchronization of a particle with the tilt modulation of a bistable potential for a small range of frequencies and a single amplitude.

Increasing the modulation amplitude the harmonics in Figure 3.10b should shift towards the first peak. Eventually the barrier disappears for some fraction of the modulation period, during which the particle's motion will be diffusive.

The relaxation rate in their system was 10 Hz, but the largest modulation frequency was 1.2 Hz. The range of frequencies from the mean transition rate to the relaxation rate and beyond was unexplored. Theory predicts a crossover from adiabatic to nonadiabatic dynamics as the modulation frequency approaches t_r^{-1} [45]. This crossover also depends on the amplitude, since the relaxation rate changes as the potential distorts.

A Brownian particle moves in three dimensions, yet only one dimension was considered. Force measurements have shown that the z axis restoring force is an order of magnitude softer than in x or y [49]. The creation of the barrier breaks the symmetry between x and y, creating three relaxation rates. These rates affect the residence time distribution in Figure 3.9, creating the cutoff at short times. Since a single relaxation rate is inferred from this cutoff, it is unknown how each contributes to the dynamics. A better method would be to measure the potential through another means, as described in Sections 3.3.1 to 3.3.3.

3.4. Summary

Three dimensional optical traps are formed by the interaction of transparent particles with a focused laser beam. The particle is drawn to the region of highest field gradient with a force depending on the beam convergence, beam power, and particle size. The present experiment uses two of these traps, positioned roughly one sphere radius

apart, to create a bistable potential with a barrier height that depends on the beam power and trap spacing.

The position of the particle was determined from either the forward scattered light or by traditional video microscopy. In the dual beam system two quadrant photodiodes were used to track two particles simultaneously. However, for a single particle in a bistable potential, it is difficult to determine which beam contains the particle. When making transitions the particle will always leave the linear sensitivity region, obscuring some of the dynamics of the transition. Camera based particle tracking is used in the present experiment to measure the position. Temporal resolution below 5 ms is not advantageous due to the intrawell relaxation rates of approximately 200 Hz.

The three dimensional potential energy was calculated using the position data. This has an advantage over the Stokes damping measurements for large displacements from the trap center or for more complicated (e.g., bistable) potentials. The absolute depth of the potential could not be measured from the position data alone.

Simon and Libchaber [30] performed experiments combining these techniques. They positioned two beams within one sphere diameter to create a bistable potential. They also modulated the beam powers to tilt the potential, synchronizing the transitions between stable points. The residence time distribution showed peaks at the odd half-integer harmonics of the modulation period. The harmonics decayed faster as the frequency approached half of the mean transition rate.

The present experiment improves on this system, increasing stability and flexibility. The potential remains stable over a longer period, increasing the statistics and ensuring changes in the dynamics are due to applied modulation and not drift. The

electro-optic beam power modulation extends the maximum frequency range above the maximum relaxation rate, and can vary the amplitude beyond the bifurcation point. Measurement of the particle position in three dimensions allows calculation of the full three dimensional potential and its time scales. These changes allow the exploration of the frequency and amplitude dependence of transitions in a bistable potential.

Chapter 4 Experimental Methods

To study the dynamics of a Brownian particle in a metastable potential, it is necessary to create a representative model system. The physical embodiment developed here is formed by a single Brownian particle trapped by the partially overlapping laser beams depicted in Figure 4.1.

The system consists of a sub-micron diameter silica sphere suspended in water, trapped by the bistable potential formed by the particle's interaction with the beams. The beams create a potential maximum that separates two minima, or stable points, of the potential. A cross-section is shown in Figure 4.1, although the potential created is actually three dimensional. Thermal fluctuations cause the particle to undergo fluctuations near the bottom of the potential until eventually a large fluctuation causes the particle to overcome the barrier, leading to an interwell transition. The potential barrier height is controlled by the relative beam spacing and the beam powers on the scale of

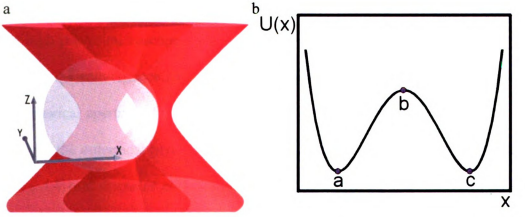

Figure 4.1 Optical trap formed by two focused laser beams. Representation of the (a) two beam optical trap with 0.6 μm sphere and (b) potential energy (U(x)) cross-section. The beams propagate in the z direction and are separated in the x direction. Interaction of the beams and particle create a potential with barrier b and stable points a and c.

zero to 10 k_BT. To measure the transition statistics (and three dimensional potential energy) the particle is imaged on a CCD camera and computer analyzed to obtain the three coordinates of the particle as a function of time $\vec{r}(t)$. The resulting time series is then analyzed to obtain several statistical measures of the transition dynamics, such as instantaneous and average transition rates. Analysis of the time series also leads to an accurate determination of the three dimensional potential surface.

Particles ranging in size from 25 nm to 10 μm diameter have been stably trapped in single beam optical traps [48]. Outside this range the thermal fluctuations overcome the trapping forces. Smaller particles intercept a reduced intensity gradient while larger particles require larger beam powers until the scattering forces overcome the trapping forces. A HeNe laser emitting less than 20 mW, focused by a 100x objective lens can stably trap a silica sphere of around 1 μm diameter in water. Two focal points separated by approximately 0.5 μm create a bistable potential with barrier heights less than 10 k_BT. The transition rate is exponentially sensitive to the distance between beams.

The optical traps are created by focusing two lasers to diffraction limited spots with a high power microscope objective lens. Radial and axial optical trapping forces increase as the convergence angle increases. The Olympus 100x PLAN-APO objective has a numerical aperture of 1.4, corresponding to a full angle beam convergence of 144 degrees for the outermost rays. To take advantage of the larger forces from these outer rays, the 4.8 mm diameter entrance aperture of the objective lens is overfilled by the 4.9 mm diameter beams. Two pairs of lenses expand the beams from the diameter at the laser output (0.98 mm) before they enter the objective lens.

The HeNe lasers with 20 mW output power exceed the minimum trapping threshold of 5 mW (for a 0.6 μm diameter sphere). Exceeding 100 mW risks damaging the microscope optics. Higher beam powers result in a trap with larger curvature and thus higher barriers. For comparable barriers, higher beam powers must have smaller beam separations, amplifying the effect of beam steering instabilities (which are independent of power and position). For this reason the beam power entering the microscope was set around 8 mW.

There are two limitations on the sphere size. At diameters smaller than the wavelength of the illumination (λ = 0.5 μm) the sphere is difficult to resolve. It requires more power to trap and the traps need to be closer together for the desired barrier height. For spheres above 1 μm diameter the beam separation becomes comparable to the sphere diameter. The beams travel through the edges of the sphere, creating a third stable point between the beam waists. The spheres used are 0.6 μm diameter silica (Bangs Laboratories), large enough to resolve with a light microscope and small enough so no third stable point appears at any trap separation.

For 8 mW per beam entering the microscope a 0.6 μm diameter silica sphere will experience a potential barrier of approximately 6 k_BT with 0.5 μm beam separation. These conditions lead to a mean interwell transition rate of 0.2 Hz. The separation between the traps is controlled with a mirror in each beam. The mirrors change the angle at which the collimated beams enter the objective lens, displacing the beams in the focal plane.

The power in each beam is controlled independently by a laser power stabilizer. A single beam is sinusoidally modulated at rates from 0.2 Hz to 2 kHz at amplitudes up

to and beyond the amplitude at which the barrier disappears. This allows us to modulate the barrier of both traps at rates above the largest relaxation rate (500 Hz).

An interwell transition takes between 10 and 25 ms. A camera recording to videotape has been used [30] to measure particle position with 33 ms resolution. The faster photodiode tracking techniques in Section 3.2 are not viable due to the large displacements of the particle from the beam center. The CCD camera used here operates at 200 frames per second, recording the image of the sphere in the objective's focal plane. The images are analyzed by a computer in real time, extracting and storing the x, y, and z positions then discarding the image. This reduces the memory used by a factor of 1000, allowing the particle to be tracked for more than 12 hours. The 5 ms integration time is fast enough to capture interwell transitions.

The CCD camera attached to the side viewport of the microscope images the particle in the objective lens's focal plane. The digitized signal is sent to the data acquisition card in the computer. A pattern matching routine is used to find the x and y positions. The particle's z position is calculated from the integrated brightness of the image, centered on the x and y coordinates. The transparent spherical particle acts like a lens, focusing the background illumination. For a small range of displacements the image brightness changes linearly with z position. A calibration of the sum of the image's pixel values vs. the particle's position relative to the focal plane allows x, y, and z to be measured for every image.

The escape rate changes with the beam spacing and barrier height. For a barrier of 6 k_BT the average rate is approximately 1 Hz. For a static potential, the particle has a constant probability of escape; the escape process is Poissonian. The statistical

uncertainty of a Poissonian process with N events is $\sqrt{N}$. To get an uncertainty below 10%, the potential needs to remain stable for over 100 transitions in each direction or an average of 200 seconds for the 6 k_BT barrier. To study the dynamics under modulation of the barrier, the static barrier height should remain within ± 0.1 k_BT for the entire set of varying frequencies or amplitudes, typically 1 to 2 hours.

This chapter describes the optics used to create and control the dual beam optical trap, including the optics used to expand, position, and modulate the beams, the microscope optics, and the sample cell. Particle tracking with the CCD camera will also be explained. Finally the modifications made to increase the beam power and pointing stability will be discussed.

4.1. Trapping Optics

The optical system (Figure 4.2) is designed to expand the 0.98 mm diameter beams from the two HeNe lasers to slightly overfill the 4.8 mm diameter entrance aperture of the objective lens. Additional optical elements stabilize and modulate the beam powers and provide independent beam steering in the objective lens's focal plane.

The two independently steerable optical traps are created by two 17 mW HeNe lasers emitting at 633 nm. Laser power stabilizers (S1 and S2) filter out intensity fluctuations and control beam power. Each beam travels the same distance before being combined at the polarizing beam splitter, BS1. The lenses L1 through L4 expand the beam from 0.98 mm diameter at the lasers to a 4.9 mm diameter collimated beam at the entrance aperture of the objective. The beams are independently positioned in the objective lens's focal plane with the gimbal mounted mirrors G1 and G2. The 100x oil

immersion objective lens focuses each beam to a diffraction limited spot in a water filled cell mounted on the microscope stage.

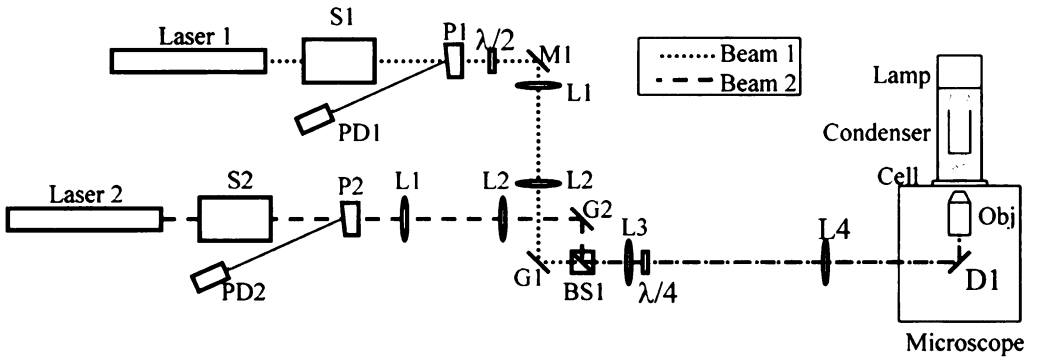

Figure 4.2 Optical system schematic. Lasers 1 and 2 emit beams 1 and 2, respectively. The beams travel through stabilizers S1 and S2, lenses L1 and L2, steering mirrors G1 and G2, are combined at beam splitter BS1, then lenses L3 and L4 before entering the microscope where it reflects off of dichroic mirror D1 and enters the objective lens. The cell is on the microscope stage and illuminated from above by the lamp and condenser. Beam samplers P1 and P2 pick off part of the beam and send it to photodiodes PD1 and PD2. The half-wave retarder ($\lambda/2$) rotates beam 1's polarization before it reflects off mirror M1. Both beams travel through the quarter-wave retarder $\lambda/4$ after L3.

4.1.1. Optical Bench

To damp floor vibrations, the lasers, optics, and microscope are mounted on an optical vibration isolation table. Two 2000 pound optical tables, bolted together in an L shape, are suspended on six air piston supports, damping vibrations above 10 Hz.

The optical system exists entirely on a 5 foot × 10 foot × 12 inch thick Technical Manufacturing Corporation Cleantop II optical table. One end butts against the side of a 4 foot × 14 foot × 12 inch thick table, connected by steel yoke. Two Gimbal Piston air supports are at each end and at the corner of the L. The 3/16 inch thick stainless steel top is epoxied to a steel honeycomb. This provides rigidity without the mass of a solid table. Tapped screw holes in a 1 inch rectangular array allow easy mounting of the optical elements.

4.1.2. Lasers

The two independent optical traps are created by two Research Electro-Optics LHRP-1701 Helium-Neon lasers (labeled Laser 1 and Laser 2 in Figure 1). The laser's output is 17 mW (minimum) at 633 nm (actual powers are greater than 20 mW) with vertical polarization. The beam diameter at the output coupler of the laser is 0.98 mm with a divergence of 0.82 mrad.

The lasers are mounted in Newport ULM-TILT cylindrical laser mounts. The 1.75 inch diameter laser head is clamped to a V-groove with a nylon screw. The V-groove's angular orientation in two axes is controlled by a pair of screw actuators and a ball pivot. The ULM-TILT is mounted to a 10" tall, 1½" diameter hollow stainless steel post. The post's base is clamped to the optical bench with two custom aluminum table clamps. To eliminate the need to change the beam height before entering the microscope, the laser is positioned so the beam is 8.5 inches above the table.

4.1.3. Stabilizers

Each laser is followed by a laser power stabilizer (S1 and S2 in Figure 4.2). Inadvertent laser intensity fluctuations modulate the potential, contributing noise in addition to the spontaneous thermal Brownian motion. The stabilizers reduce these fluctuations by factors of 80 to 200 from DC to 10 kHz, with decreasing attenuation up to 2 MHz. The stabilizer also changes the laser power in response to an external voltage signal. This is used to control the DC power in both beams and to modulate beam 1 at frequencies ranging from 1/5 Hz to 2 kHz and amplitudes from 0.06 to 6 mW.

Labeled S1 in Figure 1, the Cambridge Research & Instrumentation LS-100 stabilizer follows Laser 1. The LS-100 uses a Pockels cell to rotate the polarization of

the linearly polarized incident beam (Figure 4.3). The angle of rotation is directly proportional to the applied voltage. A calcite polarizer removes the horizontally polarized portion, emitting an attenuated beam polarized perpendicular to the optical bench. A beam splitter sends 3% of the transmitted beam to a temperature compensated photodiode. The photodiode voltage is used as a feedback control of the Pockels cell voltage, reducing noise over a 0 to 2 MHz bandwidth.

The LS-100 is mounted on two 2 inch long, ½ inch diameter stainless steel posts. Each post is secured to a 2 inch long, 1 inch OD aluminum post holder, which is screwed into a 3 inch x 2 inch x 3/8 inch aluminum base. Each base is clamped to the table with two custom aluminum table clamps.

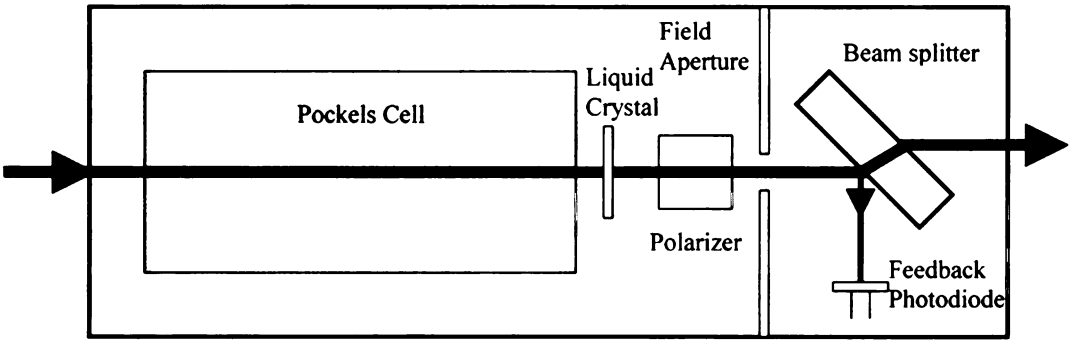

Figure 4.3 LS-100 and LS-PRO schematic. The beam enters the Pockels cell where the polarization is rotated. In the LS-PRO only this is followed by a liquid crystal element which rotates the polarization at frequencies below 10 Hz. The polarizer removes the horizontally polarized component of the beam. Before exiting, the beam passes through the field aperture and the beam splitter, where a small fraction of the beam is sent to the feedback photodiode.

Proper alignment eliminates distortions in the beam profile due to diffraction and maximizes stabilization, especially since the LS-100 entrance aperture diameter is 2 mm, only slightly larger than the beam diameter. The first step in alignment is to remove the cover. The manual recommends using less than 25 mW while aligning the stabilizer, therefore the 20 mW from the HeNe laser does not need to be reduced. Positioning the

front end of the LS-100 aligns the input beam with the entrance aperture. The height and orientation of the rear end are adjusted so the beam passes through the Pockels cell, field aperture, and output aperture. The beam should exit the stabilizer without beam profile distortions. To maximize stabilization, the beam should be centered on the photodiode.

The maximum input power is limited to 25 mW by the photodiode response. For higher power lasers, a neutral density filter should be installed between the beam splitter and photodiode. With the neutral density filter, the stabilizer can accept up to 10 W of laser power with reduced power resolution.

The LS-100 output power is controlled and modulated by the external power supply, which applies from 0 to 250 V across the Pockels cell, causing a greater than 90° rotation to the beam polarization. The laser power knob on the power supply controls the beam power offset over the range set by the feedback gain knob. The feedback gain is set to the maximum of 1000 V/mA. The power supply also accepts a low voltage external signal supplied by a Stanford Research Systems DS345 Synthesized Function Generator to control the DC beam power set point. The amplified external signal directly drives the Pockels cell, allowing modulation of the beam power at frequencies from 0.2 Hz to 2 kHz.

Laser 2 is stabilized and controlled by a CRI LS-PRO stabilizer, labeled S2. Similar to the LS-100, the LS-PRO uses a Pockels cell and polarizer to reduce the beam power fluctuations in the range of 10 Hz to 2 MHz. A liquid crystal variable retarder, in series with the Pockels cell, rotates the incident beam polarization to eliminate fluctuations below 10 Hz (Figure 4.3). With a liquid crystal to set the DC beam power, the voltage across the Pockels cell is greatly reduced, extending its lifetime.

The LS-PRO output power is controlled by an external control circuit. An AC converter supplies the LS-PRO with 18 V DC. The beam power is externally controlled through a 9-pin serial connector on the stabilizer body. A custom-built control circuit allows the user to vary the setpoint with a 10 turn potentiometer or with a 0 to 2 V signal from a second SRS DS345 function generator. Due to the slow response of the liquid crystal element, the maximum modulation rate is 10 Hz.

Since there is no external power supply, the LS-PRO has an ON/OFF button and a MODE button on its chassis. When the LS-PRO is turned on or the MODE button pressed the stabilizer cycles through its dynamic range to optimize the gain of the external voltage to the beam power. The stabilizer is kept on to prevent the gain from changing, invalidating the beam power to voltage calibration. Alignment of the LS-PRO follows the same procedure as the LS-100.

4.1.4. Beam Power Monitoring

The beam power is monitored by measuring a small fraction of the total power, sampled by the beam sampling optics P1 and P2 following the stabilizers. The beam sampler is a 1 inch diameter antireflection coated glass window with a slight wedge shape. It reflects a small portion of the incident beam (up to 10% at 45 degrees) without distorting the transmitted beam. The beam samplers are mounted in 1 inch mirror mounts screwed into ½ inch diameter stainless steel posts, secured in an aluminum post holder mounted on a 3 inch x 2 inch x 3/8 inch aluminum base. The base is clamped to the table with two custom aluminum table clamps. The mirror mount can rotate the beam sampler and reflected beam, but this translates the beam and changes the alignment further down the beam line.

The power in each sampled beam is measured by a Centronic OSD155T silicon photodiode in a shielded box (PD1 and PD2). The photodiode acts in photovoltaic mode (i.e., unbiased) with a 1100 Ω resistor in parallel. Coaxial cables connect each circuit output to the 1 MΩ terminated inputs on the LeCroy 9310AM digital oscilloscope. The beam power vs. photodiode voltage and power vs. function generator offset are calibrated for each beam. Using the math functions on the oscilloscope, the beam powers are displayed vs. time.

The power vs. modulation voltage curves are calibrated for the LS-100 and LS-PRO. A calibration of beam 1 power entering lens L4 (P_1) to the offset voltage of the LS-100 (V_1) has the linear relationship $P_1 = -6.31(\text{mW/V})V_1 + 7.98\,\text{mW}$, and is valid for frequencies from 0 to 2 kHz above which the photodiode PD1 response rolls off. The LS-PRO's power (P_2) to voltage (V_2) calibration is $P_2 = 20.7(\text{mW/V})V_2 - 0.19\,\text{mW}$. These calibrations change when the gain is modified (through the LS-100's power supply or the LS-PRO's automatic gain optimization).

4.1.5. Polarization Optics

To prevent the loss of 50% of the beam power when the beams are combined, the polarizations are adjusted with a half-wave retarder so a polarizing beam splitter can be used. To remove any polarization dependent effects the linearly polarized beams are transformed to circular polarization with a quarter-wave retarder.

In beam 1 the beam sampler is followed by an Edmund Scientific zero-order quartz half-wave (λ/2) retarder mounted in a rotation mount, held by a ½ inch stainless steel post, aluminum post holder, and aluminum base clamped to the table with aluminum table clamps. The half-wave retarder rotates the polarization of beam 1 from vertical to

horizontal. The beams are orthogonally polarized when they are combined at the polarizing beam splitter (BS1) (Newport 10BC16PC.4, 633 nm polarizing beam splitter cube).

The polarizing beam splitter/combiner transmits 90% of a horizontally polarized beam while reflecting 99% of a vertically polarized beam. A non-polarizing beam splitter transmits and reflects 50% of each beam, losing 50% of the power from the 17 mW lasers and severely limiting the dynamic range. The beam splitter is mounted on a prism table held by a ½ inch stainless steel post, aluminum post holder, and aluminum base clamped to the table with two aluminum table clamps. Motions of the beam splitter add extra noise to beam 2 only. To improve stability the prism table is also held from the side opposite beam 2 by a ½ inch stainless steel post in an aluminum post holder. The post holder is screwed into a Newport 340-RC clamp on a 1½ inch stainless steel post, clamped to the table with two aluminum table clamps.

To remove any polarization dependent trapping effects, the beams are circularly polarized with a quarter-wave retarder (Tower Optical zero-order quartz quarter-waveplate) positioned after lens L3. The quarter-wave retarder is mounted the same way as the half-wave retarder. The fast axis is aligned by setting each beam to the same power. A polarizer at any orientation is put in front of a power meter. The power in each beam is measured and the quarter-wave retarder rotated until these powers are equal. At this point the orthogonally polarized beams are rotated by the same amount and must be circularly polarized. The polarizer is rotated to confirm that the power doesn't change for either beam.

4.1.6. Beam Expanding Optics

Theoretical trapping force estimates [82,85-87] show that the trapping force increases with the convergence angle and thus the size of the beam entering the objective lens. The 0.98 mm diameter beam emitted by the REO HeNe lasers is expanded by two pairs of lenses to 4.9 mm, overfilling the 4.8 mm entrance aperture of the Olympus PLAN-APO 100x oil immersion lens.

The propagation of the Gaussian beam produced by the TEM_{00} mode is different from geometrical optics [88]. The Gaussian beam is always either diverging from or converging to a beam waist, the region where the beam diameter is smallest. Due to diffraction, the beam does not collapse to a point. It has a minimum diameter $d_0 = 4\lambda/\pi\theta$, where θ is the full angle beam divergence. The quantity $d_0\theta$ is constant. The beam waist diameter is inversely proportional to the convergence angle.

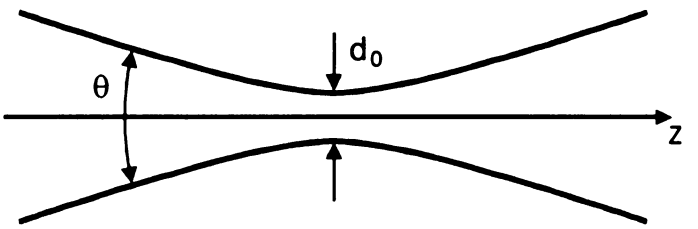

Figure 4.4 Beam waist of a converging Gaussian beam. The beam propagates in the z direction, converging at an angle θ to a beam waist diameter d_0.

At a distance z away from the beam waist the beam diameter is $d^2 = d_0^2 + \theta^2 z^2$. Far away from the beam waist the diameter is approximated by the geometrical optics expression $d = \theta z$. The extent of the beam waist region is characterized with a parameter called the Rayleigh range z_R, defined as the distance from the beam waist to the beam diameter $d = \sqrt{2}d_0$. This distance is $z_R = d_0/\theta$ and the beam diameter becomes $d = d_0\sqrt{1+(z/z_R)^2}$.

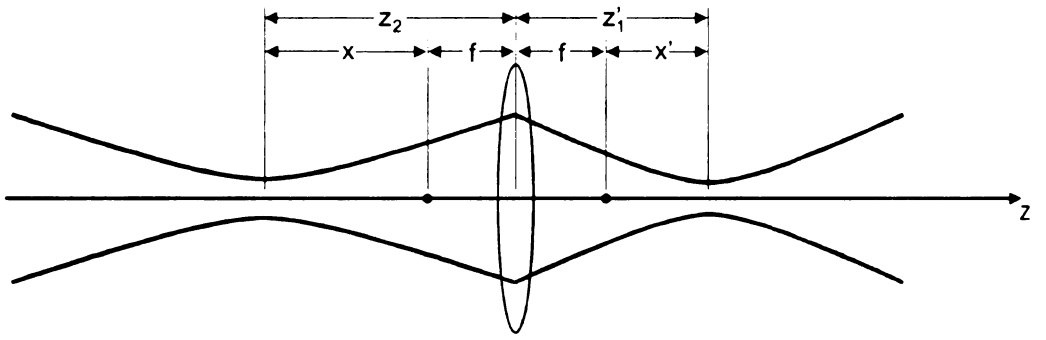

Figure 4.5 Gaussian beam propagation through a lens. The beam, propagating in the z direction, expands from the beam waist a distance z_2 from the lens. The beam is focused to the beam waist at z_1'. f is the focal length, $x=(z_2-f)$ and, $x'=(z_1'-f)$. Primed coordinates indicate distances on the right (rear) side of the lens.

Gaussian beam propagation through a lens is considered in terms of the Newtonian form of the thin lens equation for geometrical optics is $-xx'=f^2$, where f is the focal length of the lens, x is the distance from the front focal point to the object, and x' is the distance from the rear focal point to the image. For Gaussian beams this becomes $(z_2-f)(z_1'-f)=f^2-f_0^2$, where z_2 is the distance from the lens to the front beam waist and z_1' is the distance from the lens to the rear beam waist. (Primed coordinates are on the rear side of the lens.) The diffraction term f_0^2 is defined

$$f_0=\frac{d_0'}{\theta}=\frac{d_0}{\theta'}=\sqrt{z_R z_R'}\,.$$

The beam waist diameters on the left and right side of the lens are related by $d_0'^2(z_2-f)=d_0^2(z_1'-f)$. The relationship between d_0 and d_0' is calculated in terms of $\alpha=|f|/\sqrt{(z_2-f)^2+z_R^2}$, $d_0'=\alpha d_0$, and $\theta'=\theta/\alpha$. The position of the new beam waist is $(z_1'-f)=\alpha^2(z_2-f)$.

A Gaussian beam can never be truly collimated ($\theta = 0$). The beam is considered collimated when the distance to the next beam waist, z_1', is maximized. This occurs when $\alpha = f/\sqrt{2z_R^2}$ and $z_2 = f + z_R$. In this case, $z_1' = f + f^2/2z_R$.

Each beam is expanded by two pairs of lenses. The diverging beam from the laser is doubled in diameter by lenses L1 and L2. After the beams are combined, both are expanded by an additional factor of 2 by lenses L3 and L4. A single pair of lenses could have been used to expand the beam, but the L1-L2 pair is necessary to make independent adjustments to the position and angle of each beam during alignment. The L3-L4 pair is required for beam steering, discussed below.

Table 4.1 Gaussian propagation spreadsheet (from Lenses4.xls). The beam waist diameter d0, Rayleigh range zR and position z1 for each lens are calculated from equations (4.1 to 4.4) in units of mm (angles are in radians). dL1, d12, d2G, dG3, d34, and d4O are the distances between the laser and lens L1, L1 and L2, L2 and the gimbal mounted mirror, the gimbal mirror and L3, L3 and L4, and L4 and the objective lens's entrance aperture, respectively. The lens spacings and focal lengths were adjusted so the beam slightly larger than 4.8 mm at the entrance aperture. The beam expands from 0.98 to 1.28 mm by the time it gets to the first lens. The final beam diameter is 4.91 mm with a divergence angle of 0.3 milliradians. The objective focuses this to a 0.2 μm diameter beam waist with a Rayleigh range of 50 nm inside the cell.

	Laser		L1		L2		L3		L4		Aperture	
d0		0.98		0.07		1.8		0.07		3.599		2E-04
zR		1192		5.34		4018		5.34		16072		5E-05
z1		0		104		3933		195		15330		1.19
distance between		1000		309		400		600		400		
alpha		0.07		27.4		0.04		54.8		5E-05		
size at lens			1.28		2.52		2.4		4.97		4.91	
focal length			100		200		200		400		1.19	

dL1	1000
d12	309
d2G	200
dG3	200
d34	600
d4O	400

Beam diameter at aperture	4.91 mm
Divergence angle at aperture	3e-4 rad

Lens pair L1-L2 is positioned so L1 is 1000 mm from the lasers (Table 4.1). At that distance the beam has expanded from 0.98 mm to 1.27 mm diameter. The lenses have focal lengths f_1 = 100 mm and f_2 = 200 mm, and are spaced 310 mm apart. The output is a nearly collimated beam with diameter 2.41 mm. After being combined at the polarizing beam splitter, the beams are expanded by the L3-L4 pair with focal lengths f_3 = 200 mm and f_4 = 400 mm spaced the sum of their focal lengths (600 mm) apart. The result is a collimated beam with diameter 4.91 mm entering the objective lens 400 mm after lens L4.

4.1.7. Beam Steering

The potential barrier height is controlled by varying the distance between the optical traps. Using a gimbal mounted mirror in each beam (G1 and G2), the beams are independently positioned in the objective's focal plane. The mirrors and lenses L3 and L4 are positioned so that, under rotations of the mirrors, the beam stays centered on the entrance aperture of the objective. The mirrors and entrance aperture are in confocal planes. This prevents clipping of the beam during translation in the focal plane, which would change the trap power and shape based on the trap position.

The general expression [85] for the distance between the gimbal mirror and the first lens d_{G3} in terms of the lens spacing d_{34}, the distance from the fourth lens to the objective entrance aperture d_{4O}, and the focal lengths f_3 and f_4 is

$$d_{G3} = f_3 \frac{f_4 d_{34} - d_{4O}(d_{34} - f_4)}{f_4(d_{34} - f_3) - d_{4O}(d_{34} - f_3 - f_4)}.$$

If the distance between the lenses is equal to the sum of the focal lengths ($d_{34} = f_3 + f_4$) the expression simplifies to

$$d_{G3} = \frac{f_3}{f_4}\left(f_3 + f_4 - \frac{f_3}{f_4} d_{4O}\right).$$

The tilt angle at the entrance aperture is $\theta_O = -2(f_3/f_4)\theta_G$, where θ_G is the gimbal mirror mechanical angle. In the focal plane of the objective, the distance traveled $\Delta x = f_{EFL}\theta_O$, where f_{EFL} is the effective focal length of the objective lens. (f_{EFL} = 1.19 mm for the Olympus PLAN-APO 100x objective.)

For focal lengths f_3 = 200 mm and f_4 = 400 mm and lens spacings $d34$ = 600 mm and $d4O$ = 400 mm, $dG3$ = f_3 = 200 mm. Each beam needs its own gimbal mirror, therefore the mirrors are positioned before the beams are combined at the polarizing beam splitter. To make room for the beam splitter mount, lens L3 was chosen to have a focal length larger than 100 mm. From the selection of lenses including 100 mm, 125 mm, 150 mm, 200 mm, and 250 mm (each with a corresponding lens of twice the focal length for L4), the 200 mm focal length was chosen. This provided a large enough distance between the gimbal mirrors and L3 while keeping the total distance from the gimbal mirror to the microscope 100 mm smaller than the 250 mm – 500 mm combination.

4.1.8. Microscope

The beams are focused to diffraction limited spots in the cell by a 100x microscope objective mounted in the Olympus IX-70 inverted microscope (Figure 4.6). The microscope provides a framework for objective mounting, illumination, and sample translation. The beam enters the microscope below the stage, reflects off of the dichroic mirror (D1 in Figure 1) then enters the objective. The beam is considered "inside" the Olympus IX-70 microscope when it is directly over the first edge of the microscope base,

260 mm from lens L4. The beam travels 80 mm to the dichroic mirror (Chroma Technologies 632DCRB) which reflects the beam up into the entrance aperture of the objective 60 mm away. The dichroic mirror is designed to reflect all polarizations equally, preventing distortions of the circularly polarized beams.

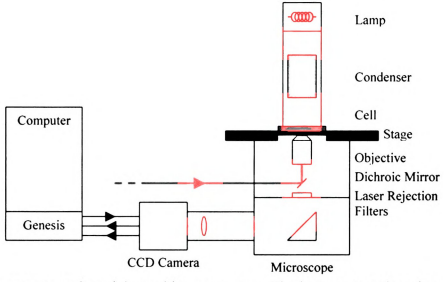

Figure 4.6 Microscope and particle tracking apparatus. The beam enters the microscope below the stage, reflecting off the dichroic mirror into the 100x oil immersion objective lens. The beam is focused to a diffraction limited spot in the water filled cell. The condenser focuses the illumination into the cell. The objective and 5x eyepiece focus the image onto the CCD camera. The dichroic mirror and laser rejection filters remove the backscattered trapping beam. The image is transferred to the computer via the Genesis framegrabber for analysis.

The beams enter the Olympus PLAN-APO 100x oil immersion objective. The objective focuses the beam 0.2 mm past the lens with numerical aperture 1.4. (Numerical aperture is defined in Section 3.1.3.) A layer of index matching oil between the objective and the cell reduces the reflections at the glass interface and increases the numerical aperture. The objective lens is flat field corrected (indicated by the PLAN designation). The focal point remains in the same plane throughout the field of view. An uncorrected lens would focus closer to the lens at the edges of the field of view. The objective is also apochromatic (APO). Due to dispersion, an uncorrected lens would have a focal distance

that changes with wavelength. The apochromatic correction adds triplet lenses to make red, green, and blue wavelengths focus at the same point.

A 0.55 NA condenser focuses the illumination from a 100 W halogen lamp onto the trapped particle in the sample cell. The condenser is aligned for Kohler illumination, which creates a uniform intensity over the field of view. The light captured by the objective lens travels through the dichroic mirror and into the microscope. The light scattering off the particle and the cell's glass/water interface are much brighter than the illumination. A pair of 3 O. D. laser rejection filters (Omega Optical 633-S1E) below the dichroic mirror eliminate the scattered laser light.

The particle image enters the microscope where it is distributed to the viewports. It is magnified by 1.5x before a beam splitter sends 80% of the light to the side viewport where a 5x eyepiece focuses the light on the Dalsa CA-D1 CCD camera. The remaining 20% goes to the trinoc head (not shown in Figure 4.6) where 80% is sent to the Sony DXC-151A color CCD camera and displayed on a Sony PVM-14N2U monitor, while the other 20% goes to the eyepieces.

4.1.9. Optical Alignment Procedure

The trapping efficiency and stability are maximized for a properly aligned system. The alignment of the 18 optical elements pictured in Figure 4.3 is broken down in order of necessity, starting with lasers and mirrors, then stabilizers and beam samplers, and finally lenses. The alignment is checked during each step using the reflections of a piece of glass on the microscope stage. The final alignment is tested by tracking a trapped particle.

The optical system is initially aligned with as few elements as possible. The lasers, mirrors, and beam splitter (equivalent to a mirror for beam 2) are mounted and placed to the proper positions. To simplify alignment, the beams travel in directions parallel to the table's edges. The mirrors are rotated so the beams enter the microscope. In practice, one beam is aligned at a time.

The shape of the beam in the focal plane is used to verify the alignment at every step. A piece of glass is mounted on the stage to provide a surface for reflections. The laser rejection filters are removed so the reflections can be viewed on the Sony monitor. The mirrors are rotated to center the beams in the objective's field of view. At the same time, the mirror positions are adjusted so the reflections are radially symmetric. This assures that the beams are both centered on the objective's entrance aperture and enter vertically.

Next the elements that cause shifts in beam position are added. The beam splitters in the LS-100 and LS-PRO stabilizers translate the beam up 3 mm. The beam sampling elements translate the beams a distance that depends on the angle of the reflected beam. After installation, the beams are realigned with the same procedure. This step usually requires the laser mounts to be lowered.

Finally the lenses are added, starting with L1 in beam 1. The beam is aligned using the reflections from the front and back of the lens. When the lens is properly aligned, both reflections should overlap and travel back into the stabilizer. Due to imperfections in the previous alignment steps, the beam may not be centered in the field of view of the objective. The lens is translated perpendicular to the beam direction until

the reflection is centered and uniform on the Sony monitor. The lens mount is clamped to the table.

This procedure is repeated with lens L2 in beam 1 and lenses L3 and L4 after the beam splitter. With L3 and L4 in place the positions of gimbal mounted mirror G2 and the beam splitter usually need to be adjusted. Once beam 2 is centered and uniform in brightness the remaining lenses in beam 2 are aligned, beginning with L1.

The final step in alignment is tracking a particle in each trap. The three dimensional potential energy will show if the beams are vertical or if one beam is deeper in the focal plane. If the beams are not vertical, lens L2 is moved until the soft axis of the potential energy is aligned with the z axis. If necessary, a trap is translated in z by moving L2 closer to or farther from L1. After each translation the potential is measured and the process repeated until the traps are vertical and in the same focal plane.

4.1.10. Sample Cell

The 0.6 μm diameter silica spheres are dispersed in water and placed in a glass cell sealed with epoxy resin. The cell design allows light from the condenser to pass through to the objective lens without obstruction. To limit convection the cell thickness is less than 200 μm. The buffer solution places a slight negative charge on the spheres and glass surfaces to prevent bonding. The cell is designed to be used with the objective clamp (discussed in section 4.3.1).

Due to the short working distance of the objective, the bottom surface of the cell is #1 cover glass. The 100x oil immersion objective has a working distance (distance from the lens housing to the beam waist) of 0.2 mm. Only #1 cover glass, with a thickness of 0.13 to 0.16 mm, is thin enough to be practical. #1½ cover glass, with

thickness 0.16 to 0.19 mm, allows only 20 to 30 μm of working distance above the glass while the focal plane would be inside a piece of #2 cover glass (thickness 0.19 to 0.25 mm). The objective lens focuses upwards in the Olympus IX-70 inverted microscope, therefore only the bottom surface of the cell needs to be #1 cover glass.

The condenser focuses the illumination from the lamp to a 1 mm diameter spot. The local heating causes convection currents in the cell which increase with cell thickness. To limit this anisotropic force the cell is less than 0.2 mm thick. For thinner cells the proximity of the glass surfaces would change the effective damping of the particle motion. At this thickness the convection current forces are observed to be orders of magnitude smaller than the Brownian forces.

The 0.6 μm silica spheres are dispersed in a 0.0001 M NaOH solution. The hydroxyl groups bond with the surface, producing a net negative charge (0.5 OH/nm^2 at pH = 10) [89]. This prevents the spheres from colliding with and adhering to the glass cell. Normally silica particles in deionized water will not bond, but the epoxy used in cell construction leaches ions into the solution, eventually adhering the spheres to the surface. The buffer solution extends the life of the cell from less than one week to four weeks.

The solution is created by mixing dry 0.6 μm spheres and the NaOH solution. A 22 gauge needle is used to scoop a small amount (enough to coat 1 mm of the needle) into 40 ml of the NaOH solution. The solution is placed in an ultrasonic cleaner for 30 minutes to break up the clumps into single spheres. This solution is diluted 1:150 in NaOH solution and placed in the ultrasonic cleaner for another 30 minutes. Approximately 10 μl is deposited in the cell with a syringe.

The cell is constructed with an 18 mm diameter #1 cover glass on the bottom, attached to a 3 inch x 1 inch, 1.25 mm thick glass slide with epoxy. The gap between is wedge shaped with 100 μm to 200 μm thickness. The glass slide spans a gap in the sample stage so the cell can be translated without the stage colliding with the objective clamp (Section 4.3.2). The 18 mm diameter cover glass was chosen to fit the objective clamp's 28 mm inside diameter. Therefore the objective clamp supports the cell on the flat glass slide rather than the cover glass and epoxy.

The glass pieces are cleaned, assembled, then baked before being filled. The glass is washed in Alconox detergent for 15 minutes in an ultrasonic cleaner. The glass is rinsed with deionized water, then cleaned in acetone for 15 minutes, then methanol for 15 minutes. Devcon 5-Minute Epoxy is applied to ¾ of the circumference of the 18 mm diameter cover glass. The cover glass is placed on the slide with a #1 cover glass shard as a spacer (Figure 4.7a). The capillary action of the epoxy causes the open end to have an approximately 200 μm gap and the closed end a 100 μm gap. The cell is baked at 50 °C for at least 12 hours to fully cure the epoxy.

The cleaned and baked cell is filled with 0.6 μm diameter spheres in the buffered solution. After curing, the spacer is removed and the cell is rinsed in deionized water and blown dry at least four times to remove deposited solvents. A small volume of 0.6 μm sphere solution is drawn into a 3 cc syringe with a 22 gauge needle. The needle is placed in contact with the slide at the open end of the cell. The wedge shape of the gap draws the solution to the closed end of the cell. The cell is filled to within 3 to 5 mm of the top.

The cell is sealed with 5 Minute Epoxy (Figure 4.7b). If the epoxy touches the solution, the cell lifetime is reduced to a few days. To prevent this, a minimum amount

of epoxy is applied. As the epoxy flows into the gap the escaping air forms a 1 mm wide channel to the edge. The channel is filled when the epoxy is so viscous that it no longer flows into the gap (around 3 minutes). If the cell is not airtight more epoxy is mixed and applied to the edge.

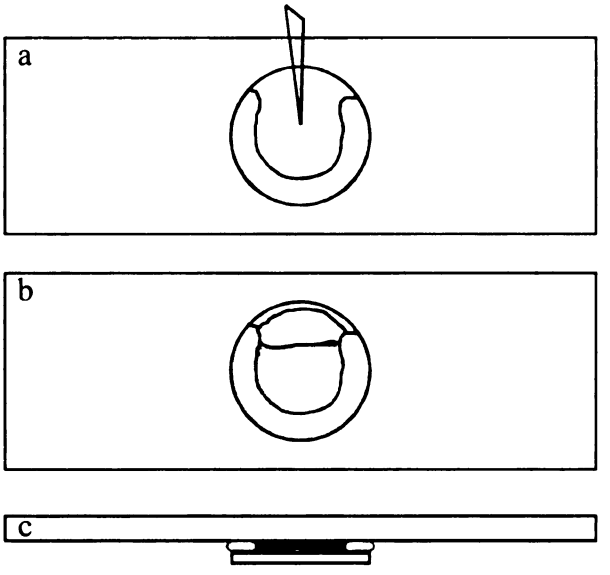

Figure 4.7 Cell construction. (a) The 18 mm diameter cover glass is epoxied on ¾ of its circumference and adhered to the 3 inch x 1 inch glass slide. A #1 cover glass spacer (0.13 mm thick) is placed in the open end to prevent the gap from closing. (b) After curing, the cell is filled with solution (blue) then capped with more epoxy. A 3 to 5 mm air gap is left so the epoxy does not contact the solution. (c) cell side view.

4.2. Particle Tracking

The particle position is the only output of this experiment. The potential energy in three dimensions is calculated from the three dimensional position distribution, and the potential parameters from one dimensional potential profiles. The interwell transition statistics are measured from the x position fluctuations with 5 ms time resolution.

The particle is trapped in the transparent, water filled cell and illuminated from above by the lamp focused by the 0.55 NA condenser (Figure 4.7). The objective lens

sends the image to the CCD camera on the microscope's side viewport. The camera exposes the image for 5 ms then transfers it to the computer for pattern matching analysis. The analysis calculates the center of the particle in x and y, and the integrated image brightness centered on (x, y) is used to calculate z.

The analysis takes less than one exposure time (5 ms), so the double-buffered algorithm calculates the position and discards the image before the next one has finished being transferred. The x, y, and z coordinates are stored in the computer's memory until the run is complete, possibly more than 12 hours.

4.2.1. Camera Interface

The CA-D1 camera is a 256 x 256 pixel, 8-bit CCD image sensor with 16 μm square pixels and 100% fill factor. It receives a synchronization signal from the Genesis framegrabber, triggering the transfer of a single image. The camera transfers data at 15 MB per second, corresponding to a maximum frame rate of 200 frames per second. The particle image is magnified by the 100x objective, a 1.5x magnifier inside the microscope, and the 5x eyepiece before the camera. Calibration with a fixed grating shows that each 16 μm wide pixel is equivalent to 0.071 μm in the focal plane. The camera's fixed pattern noise is 0.5 pixel values.

The camera uses a charge transfer process to read out the image, minimizing the inactive time. The incident photons from the objective's focal plane create a charge in the CCD elements. After a set exposure time (signaled by an RS422 pulse), the charge is shifted from the photosensitive region to an optically masked storage region of the CCD. While this secondary array is transferred the primary array is free to expose the next

image. The parallel design lowers the minimum time between frames to the frame transfer time (5 ms).

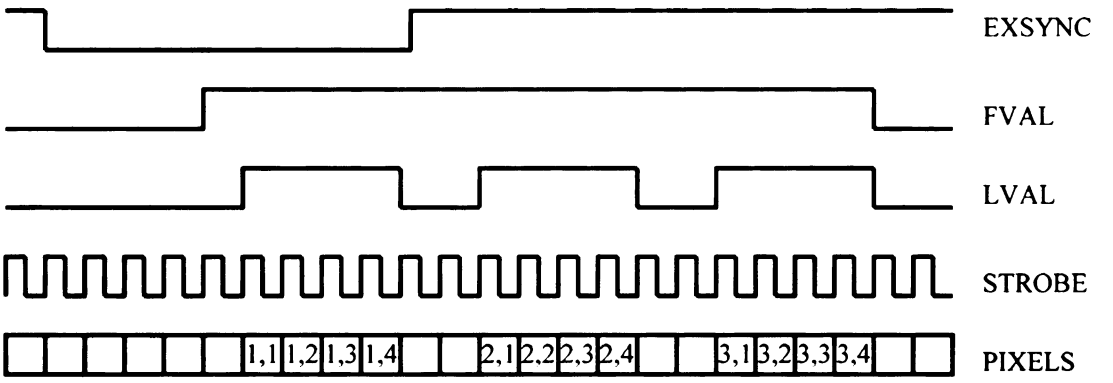

Figure 4.8 Dalsa CA-D1 timing diagram. The EXSYNC pulse triggers frame readout. The frame valid signal, FVAL, is set to high for the duration. The line valid signal, LVAL, is set high during each line readout. A single pixel value is output over 8 single bit channels synchronized with the 15 MHz pixel clock, STROBE. (This timing diagram is for a 3 x 4 pixel CCD array.)

The camera exposure and frame transfer is controlled through the RS422 (2 V differential) external synchronization signal, EXSYNC. The falling edge triggers a frame transfer (Figure 4.8). The primary CCD continues exposure until the next EXSYNC falling edge. If EXSYNC is held low, the camera operates in free-run mode and will transfer at the maximum frame rate. The EXSYNC signal is also used to synchronize the beam power modulation and thus the camera is always operated in triggered mode. A secondary control signal, PRIN, drains the charge from the CCD and can be used as an electronic shutter.

The camera outputs the image along with signals to synchronize reception by the framegrabber. The camera timing is illustrated in Figure 4.8. EXSYNC is sent from the computer and set low for at least 100 nanoseconds to trigger frame readout. The frame valid (FVAL) signal tells the data acquisition system that a frame is being transferred.

The line valid (LVAL) is set high as each line is transferred. Each 8-bit pixel is output over 8 parallel channels, at the same rate as the 15 MHz STROBE signal.

4.2.2. Data Acquisition and Analysis

The Dalsa CA-D1 camera transfers its image to the Matrox Genesis imaging system's framegrabber for analysis. The image is analyzed on the Genesis processor board and the host computer's hardware using a series of C functions from the Matrox Imaging Library (MIL). *WinMil2*, the data acquisition program, uses MIL commands to acquire images and find the x, y, and z position of the particle in real time. After acquisition *WinMil2's* analysis routines are used to calculate three dimensional histograms and the intrawell dwell times (Appendix E).

The Genesis framegrabber and processor each occupy one PCI slot in the dual processor data acquisition computer. Over a SCSI-2 type connector the framegrabber accepts 32 bits at 40 MHz from a camera. This data is transferred to the processor board over a ribbon cable (not through the PCI bus), during which formatting and zooming operations occur. The image is stored in 64 MB of onboard SDRAM. Image analysis can be performed with the TMS320C80 (C80) digital signal processor or the image can be transferred to the computer memory and analyzed with the host CPU. The Pentium Xeon 550 MHz processor outperforms the 50 MHz C80 DSP in pattern matching analysis speed, therefore all images are transferred to the host memory for analysis. The processor board has its own VGA display adapter which controls a second (overlay) monitor.

4.2.3. WinMil2 – Data Acquisition Program

The data acquisition and analysis are performed by the custom Visual C++ program *WinMil2*. The program uses the MIL commands to interface with the Dalsa CA-D1 camera, acquire images at 201 frames per second, and perform pattern matching analyses at the same rate. The program sends instructions to the framegrabber to change the region of interest and contrast of the incoming image, the model image and model parameters are chosen, and the x, y, and z position data is saved in ASCII or binary format.

Matrox Imaging Library

The Matrox Imaging Library is a set of C routines included in the Matrox Genesis imaging system, used to control the camera interface and image acquisition. There are also more than 100 image processing algorithms ranging from image rotation and pixel value modification to Fourier transform, edge detection, and pattern matching. The image processing commands are run on either the host computer CPU or the optimized image processing hardware on the Genesis processor board.

MIL separates the individual hardware components into systems, all under control of the MIL application. The available systems are: (1) the Genesis board for image acquisition, display, and processing; (2) the Host CPU for image processing; and (3) the Host VGA adapter to display the image on the computer monitor. Buffers and displays are allocated on each system and reside in that system's hardware. The systems communicate over the PCI bus.

Camera Interface

To acquire images at the maximum rate without image distortion, the Genesis framegrabber is given the camera timings in Figure 4.8. These values are stored in the digitizer configuration format (dcf) file, CAD10256MSU3.dcf. This file is downloaded to the framegrabber when *WinMil2* is initialized.

The dcf file for the CA-D1 included with the MIL software was modified to achieve the maximum frame rate using Matrox's camera interfacing application, Intellicam. Readout of the horizontal lines is triggered by an EXSYNC pulse. The line transfer begins two STROBE pulses after this, a period called the back porch. 256 pixels are transferred at the 15 MHz STROBE rate, followed by a front porch of 24 STROBE pulses until the next sync pulse. 282 total pulses at 15 MHz give a horizontal frequency of 53.2 kHz. The entire frame contains 256 horizontal readouts for a final rate of 207.8 Hz.

The dcf sets the external synchronization (EXSYNC) pulses sent to the camera from the framegrabber. The time the signal is active (low) or inactive (high) can each be set between 20 μs and 1 second. To achieve the maximum frame rate, the active time is set to 164 horizontal sync pulses, or 3.1 ms, and the inactive time is to 100 sync pulses, or 1.9 ms. Since the frame transfer is triggered by the falling edge of the EXSYNC signal, the actual active and inactive times are arbitrary as long as they sum to 264 pulses. The active and inactive times are controlled by MIL commands in *WinMil2*.

WinMil2 User Interface

The *WinMil2* user interface (Figure 4.9) divides the program functionality into 6 sections. The controls are buttons (push buttons, radio buttons, and check boxes), edit

boxes, and text boxes. The upper right section, marked Area 1, sets the lookup table (LUT) and region of interest (ROI) parameters. Area 2 controls the RunningCOG routine. Area 3 contains the data acquisition controls. Area 4 controls the acquisition of the pattern matching model as well as the model parameters. Areas 5 and 6, discussed in Sections 5.3 and 5.2, respectively, control the intrawell dwell time (switcher) calculation and the 3D potential energy calculations.

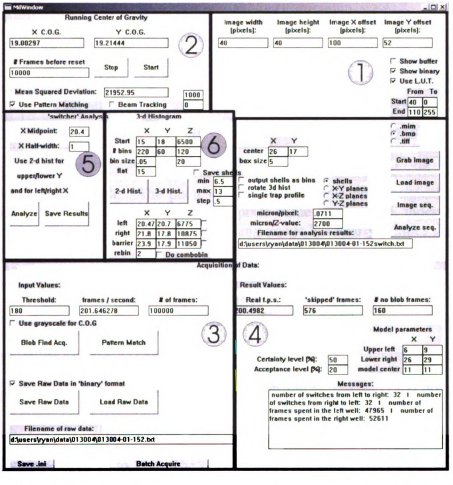

Figure 4.9 WinMil2 user interface. The program functions are roughly divided into six areas. Area 1: LUT and ROI parameters. Area 2: RunningCOG. Area 3: data acquisition and saving routines. Area 4: pattern matching model image parameters. Area 5: intrawell dwell time analysis. Area 6: 3D potential energy analysis.

Lookup Table

To increase contrast in an image with pixel values that do not span the full 0 to 255 range the values over the entire image are changed using a lookup table (LUT). This occurs as the frame is transferred from the framegrabber to the processor board. For each input value in the table there is an output value. The LUT generation function can be a polynomial, trigonometric or logarithmic function, but *WinMil2* uses a linear function.

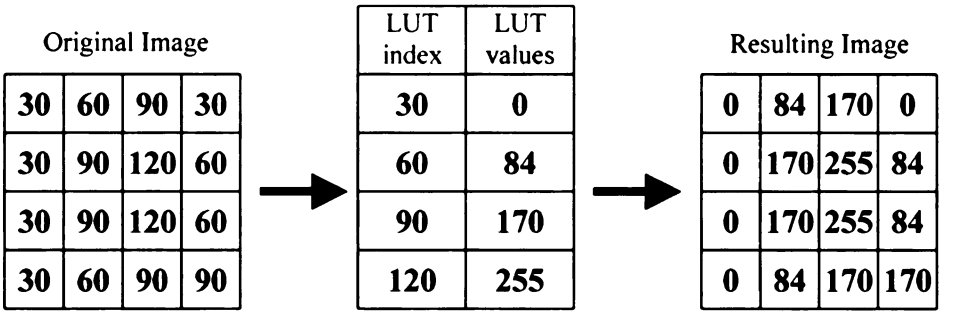

Figure 4.10 Lookup Table. The pixel values in the 4 by 4 pixel original image are transformed by the LUT. For each pixel value in the LUT index there is a corresponding output value. The resulting image has nearly 3 times the dynamic range.

The LUT scales pixel values from the index to the LUT value (Figure 4.10). The LUT is defined in area 1 of the user interface in Figure 4.9. The beginning and ending LUT index values (in the "From" edit boxes) represent the minimum and maximum expected pixel values. The LUT values (in the "To" edit boxes) represent the final pixel value range. Figure 4.10 demonstrates a four value lookup table. The original image's pixel values range from 30 to 120. The LUT expands the range to 0 to 255 to create the resulting image. This increases the contrast and dynamic range, but the fixed pattern camera noise is amplified.

Region of Interest

To increase analysis speed the transferred image is cropped to a region of interest (ROI) around the sphere. The image of the particle is much smaller than the field of view of the CA-D1 camera. Each camera pixel corresponds to 0.071 μm in the objective lens's field of view. A 0.6 μm diameter sphere spans 15 pixels (with diffraction), and the traps are spaced less than 0.5 μm (7 pixels) apart, for a total of 22 pixels in the x direction. Analysis of the image outside of a 40 x 40 pixel ROI is a waste of processing time.

Set in area 1 in Figure 4.9, the ROI parameters are downloaded into the framegrabber before acquisition begins. As the image is acquired, only the pixels within this area are saved to a buffer; the others are discarded. This increases the pattern matching speed by a factor of 4.

Running Center of Gravity

RunningCOG, a modified version of the real time particle tracking routine, is used to display the motion of a trapped sphere. This provides visual feedback when positioning the beams (using the gimbal-mounted mirrors) to achieve the desired transition rate. The particle position is determined with the pattern matching algorithm and the model center is displayed as a white dot on the image. To center the model and eliminate mismatches, the model image and model parameters are changed in the model parameter section (Figure 4.9, area 4). RunningCOG is also used to track two instances of the model image with the beamtracker subroutine, used to track beam positions (Section 4.3).

The RunningCOG routine is controlled in area 2 of Figure 4.9. The start button initializes the buffers. A "grab" buffer on the Genesis system receives the image from

the camera. This is transferred to the overlay buffer for display on the overlay monitor. Two analysis buffers are allocated on the host CPU system, used in the blob analysis or pattern matching analysis below. Three display buffers and two displays are allocated on the host VGA system. The dcf file, LUT and ROI are downloaded to the framegrabber.

RunningCOG grabs an image, displays it on the selected computer monitors, and finds the particle center. A Windows system timer is set to post a message to *WinMil2's* message queue every 5 ms. This message triggers a Grab command, transferring the next available image to a buffer on the Genesis board. This image is copied to the Genesis VGA memory for display on the overlay monitor and to the host CPU system for analysis. If the Show buffer box is checked (Figure 4.9, area 1) the image is displayed on the computer monitor. The x and y positions of the sphere, calculated through either blob analysis or pattern matching analysis, are displayed in a separate window along with a histogram of x positions. The average x and average y positions are displayed in the X COG and Y COG edit boxes. The averages and position window are reset after the number of frames in the "# Frames before reset" edit box.

If the "Use Pattern Matching" checkbox is not checked, the sphere position will be calculated using blob analysis, explained in the next section. The image is binarized using the threshold value entered in area 3 of Figure 4.9. Binarization sets all pixel values above the threshold to 1 (white) and all values below the threshold to 0 (black). Blob analysis finds the largest white region and calculates the center of mass. If the "Show binary" checkbox in area 1 is checked the binarized buffer is displayed. The threshold value is set so the largest possible area of the sphere is white while the

background is black. This maximizes the precision of the x and y positions while preventing false matches to bright areas in the background.

Pattern matching analysis is performed if "Use Pattern Matching" is checked. The model is selected and its parameters set in area 4 of Figure 4.9 before acquisition is begun. If "Show binary" is checked in area 1 the center of the sphere is displayed on top of the image. The model parameters are adjusted to center the model. If the model matches to another region of the image (mismatches), the model image is replaced. This iterative process produces a model valid over a large range of sphere positions with a minimum analysis time.

Checking the "Beam Tracking" checkbox selects the beamtracker subroutine, which tracks two objects displaced in the x direction, used in stability measurements of the beam positions by pattern matching the laser reflections from the cell's glass-water interface (Section 4.3). The image is shifted by the number of pixels entered in the lower edit box, first to the right then to the left. Pattern matching analysis finds a single instance of the model in each shifted image. The sampling period is entered in the top edit box in milliseconds (to a minimum of 10 ms). The x and y positions and the integrated brightness (z position) are stored to the filename in area 3 of Figure 4.9.

Data acquisition

To track the particle over long time periods without filling the computer memory, images are analyzed and discarded in the 5 ms interval between image transfers and only the x, y, and z positions recorded. At 200 frames per second, storing 40 x 40 pixel images at 1 byte per pixel requires more than 300 kB per second, filling the computer's 512 MB of physical memory in less than 30 minutes (or 350,000 frames). Storing the

position as two floating point (8 byte) and one long precision (4 byte) values requires less than 4 kB per second, increasing the upper limit to 37 hours.

The Matrox Imaging Library has two routines for finding an object in an image: blob analysis and pattern matching analysis. Blob analysis finds connected regions of similar pixels in an image, in this case white pixels representing the sphere on a black background. The x and y positions are determined from the center of mass. Pattern matching analysis finds the position of a model in the image. Pattern matching is slower than the blob analysis, but has greater precision. Both routines find the x and y particle center and sum the pixel values in an 11 x 11 box centered on x and y within the 5 ms window, therefore all data acquisition uses pattern matching analysis.

Particle Tracking by Blob Analysis

Blob analysis finds regions of similar pixels in an image and calculates features based on the distribution of pixels. These features range from blob area, perimeter, and position to complicated geometrical features such as roughness, convexity, and moment of inertia.

To find the sphere center, the image is copied to a binary (1 bit) image and the "center of gravity" determined. The 0.6 μm diameter sphere appears as a fuzzy white dot surrounded by a dark ring (Figure 4.11a). Pixel values above a threshold value, input in area 3 of Figure 4.9, are set to 1 and values below are set to 0. The threshold is set just above the average background value, low enough to make the sphere's blob as large as possible but high enough to keep any background blobs smaller than the sphere's blob. Figure 4.11b shows Figure 4.11a binarized with a threshold of 169. The sphere blob is 21 pixels in area with three smaller background blobs visible.

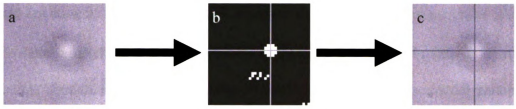

Figure 4.11 Blob analysis. The acquired image (a) is binarized with a threshold of 169 pixel values. The largest blob in the binarized image (b) is found and the center of mass computed (represented by the intersection of the two lines). (c) The original image with center.

The only relevant blob analysis features to particle tracking are the center of gravity in x and y. The values, $\bar{x}$ and $\bar{y}$, are calculated from the first moments,

$$\bar{x} = \frac{\sum_i x_i p_i}{\sum_i p_i} \text{ and } \bar{y} = \frac{\sum_i y_i p_i}{\sum_i p_i},$$

where p_i is the pixel value of the blob at position (x_i, y_i). The center of gravity is calculated from either the binary image (p_i = 0 or 1) or the grayscale image (p_i = 0 to 255). To take advantage of the higher resolution, *WinMil2* uses the grayscale center of gravity. Figures 4.11b and c show the position of the center of the image on the binary and grayscale images. The threshold is adjusted so the largest blob is the sphere, therefore the analysis is always performed on the first (largest) blob in the result list.

Even with the grayscale center of gravity, the resolution of the blob analysis is larger than the pattern matching analysis. The dark diffraction ring around the sphere limits the size of the blob to 5 x 5 pixels, less than ¼ the sphere's area. The estimated resolution of this method is ¼ pixel, compared to less than 1/8 pixels for the pattern matching analysis.

Particle Tracking by Pattern Matching Analysis

Pattern matching analysis finds the instance of a user defined model in an image. The image containing the model is captured from the camera and the model parameters chosen using RunningCOG. Pressing the "Pattern Match" button in the user interface (Figure 4.9, area 3) begins the real time data acquisition function. This routine continues until the number of frames in the "# of frames" edit box are captured, during which the x, y, and z positions are stored in memory. After acquisition these data are written to the hard disk and analyzed.

The Matrox Imaging Library's pattern matching routine scans the model across the image, searching for the region that is most similar. This is quantified by the normalized correlation of the image pixel values I_i and model pixel values M_i over the N overlapping pixels,

$$r = \frac{N\sum_i I_i M_i - \left(\sum_i I_i\right)\sum_i M_i}{\sqrt{\left(N\sum_i I_i^2 - \left(\sum_i I_i\right)^2\right)\left(N\sum_i M_i^2 - \left(\sum_i M_i\right)^2\right)}}.$$

The routine outputs the position of the model where the score, defined as $r^2 \times 100\%$, is maximized. The match center is calculated from the model center, entered by the user. Because the model does not change, the sums $\sum_i M_i$ and $\sum_i M_i^2$ are calculated before the pattern matching analysis begins, reducing the analysis time.

To achieve sub-pixel accuracy, a curve is fit to the values neighboring the position of the maximum score and the exact peak position calculated. The highest accuracy achievable based on the fit algorithm is 0.05 pixels. Noise in the image and the model

increase the uncertainty to around 0.1 pixels in x and y. At 0.071 μm/pixel this corresponds to 7 nm.

To further increase the pattern matching speed, the algorithm performs a hierarchical search. It begins with a lower resolution version of the target image and model to exclude regions of the image without an instance of the model. It continues at higher and higher resolutions, narrowing down the model position. Because the position is already known at lower resolutions, the number of correlation functions that need to be calculated is reduced. A counter-intuitive result of this procedure is that larger models tend to be found faster than smaller ones. Smaller models cannot be sub-sampled as much as larger ones, so the search must start at a higher level. The lowest resolution is chosen by the MIL software during the preprocessing step described below.

The pattern match position is not returned unless the score is greater than a user defined minimum acceptance level. If the score is lower than this level, the model and target image are considered not to match. If multiple objects in the target image have scores above this value, all are returned to the results buffer in order of decreasing score. A user defined certainty level can reduce the time spent finding the mismatched objects. The first time the pattern matching algorithm returns a score higher than the certainty level, the algorithm assumes it has found the object and stops searching for a better one. Due to distortions of the sphere's image during large z excursions, the acceptance level is set around 20 %. Larger levels mean no matches at large z, while smaller levels lead to mismatches at large z. The certainty level is set to 50% to speed analysis when the sphere is in the focal plane.

The model selection is the most important part of the pattern matching analysis. A model that does not match the particle during its full range of motions will cause mismatches or frames with no match. If the model is not centered the measured x and y positions change with z position.

The model is a subset of an image of the sphere while it is in the bistable potential, called the model image. This image is stored as a .mim file (a TIFF 6.0 file with extra information in the comment field). The image is acquired using the "Grab Image" button in area 4 of Figure 4.9, then immediately smoothed. From this image the center of the sphere is chosen. The model is defined by an upper left corner, a lower left corner, and a center measured from the upper left corner.

To make sure the model represents the largest range of possible particle images the model is tested. First the particle is tracked using RunningCOG with the pattern matching checkbox checked. The image on the overlay monitor shows the trapped particle with a white dot over the matched center. The model parameters are adjusted so the center overlaps with the actual particle center. If the model is seen to mismatch or have no match either the acceptance level is changed or, more frequently, a new model image is chosen. Once the model matches by eye, a short (20,000 frame) data acquisition run is performed. The number of no match frames, displayed in the "# no blob frames" edit box in area 4 of Figure 4.9, should be as close to the minimum of 16 as possible. If the number is too large (greater than 50) a new model is chosen. Finally, the xz and yz projections of the potential energy are calculated. A tilt in either distribution shows that the model center is not positioned correctly, probably due to the particle being between

pixels in the model image (e.g., the center is at 10.5 pixels instead of 11.0 pixels) and a new model is chosen.

Real Time Pattern Matching Algorithm

The real time data acquisition and analysis takes place in a single function, OnPatMatch(), called when the "Pattern Match" button is pressed. All buffers are allocated and all parameters set before the time critical loop acquires images and calculates the sphere position. The x, y, and z positions are each stored in a global array until the desired number of frames is acquired. After the loop the arrays are processed to remove skipped frames and the allocated buffers are freed.

The real-time analysis is to the highest priority to avoid being interrupted or delayed by other programs. Visual C++ allows the program to set its priority class in Windows 2000. At the beginning of OnPatMatch() the priority class is set to REALTIME, telling the operating system to execute commands from *WinMil2* before any others. The priority of the current thread is set to TIME_CRITICAL, so commands from this thread will execute before any other thread in *WinMil2*. These commands prevent other applications, such as Windows Explorer or the GPIB temperature monitoring software from causing delays in the analysis.

OnPatMatch() next reads the parameters from the user interface and sets up the MIL buffers. The model image and parameters are loaded, the certainty and acceptance levels are set, and the LUT and ROI values are downloaded to the digitizer. The data arrays are allocated, with double precision for the x and y position and long integer precision for the z position. Two additional arrays are created to keep track of both mismatched or no match frames. The MIL buffers are allocated on the Genesis board and

the Host CPU. An additional buffer and display is allocated on the VGA system if the "Show buffer" checkbox in area 1 of Figure 4.9 is checked, but the system resources required to draw the image reduce the frame rate to around 27 frames per second.

The method by which the MIL application interacts with *WinMil2* during image transfer affects the maximum frame rate. The image is acquired with the MdigGrab() command. The framegrabber waits for the current frame transfer to finish then grabs the next image. The application can respond to this command in three ways, depending on the grab mode. If the grab mode is set to M_SYNCHRONOUS, the application will be synchronized with the end of each frame transfer. It will wait until the frame has been transferred before executing any more commands.

If the grab mode is set to M_ASYNCHRONOUS, the application is not synchronized; it will continue executing commands while the frame is transferred. To take advantage of this, two buffers on the Genesis system are allocated to receive the incoming image. Buffer 1 receives the frame from the camera while the program completes the pattern matching analysis on buffer 2. When the frame transfer is finished, analysis of buffer 1 begins and a new image is transferred to buffer 2. In asynchronous mode the program will wait if another MdigGrab() command appears before the previous one has finished. (The camera cannot transfer two images at once.) This double buffering technique reduces the time between analyses to zero.

When the grab mode is set to M_ASYNCHRONOUS_QUEUED, the program does not stop at the next MdigGrab(). It adds another grab to the framegrabber's queue and continues with the program. If the analysis speed is greater than the frame rate, a

single image could be analyzed multiple times. The uncertainty introduced is not worth the possible slight speed increase.

The pattern matching parameters are set to maximize position resolution and analysis speed. The accuracy is set to the maximum level, with error ±1/8 pixel. The hierarchical search is hard coded so the final search level is at the resolution of the image. The model is preprocessed with a typical image (transferred from the camera). This command determines the analysis shortcuts that can safely be used without affecting resolution, speeding up subsequent analysis.

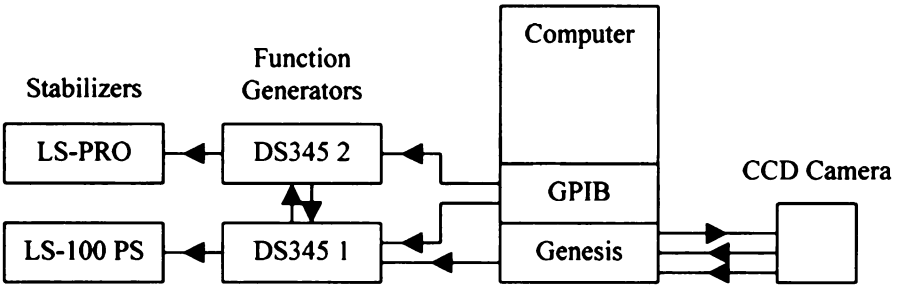

Figure 4.12 Electronic component diagram. The Genesis framegrabber sends the EXSYNC signal to the camera and function generator DS345 1, triggering an integer number of modulation periods. DS345 1 triggers DS345 2. Both function generators use the DS345 2 10 MHz pixel clock. The output is sent to the laser power stabilizers to modulate the beam power. The function generator offset voltage, modulation amplitude, and frequency are set via the general purpose interface bus (GPIB) during batch acquisition (4.2.3.10).

For an unknown reason, the framegrabber produces a single white frame after around 50 images are transferred. To remove this and any other startup effects, 200 frames (approximately 1 second) are transferred before analysis begins.

The Stanford Research Systems DS345 function generators used to modulate the beam power are triggered by the EXSYNC signal from the Genesis framegrabber (Figure 4.12). The function generators execute a burst modulation, sending an integer number of modulation periods beginning on the EXSYNC rising edge. Since the framegrabber is

always sending EXSYNC pulses to the camera (even while not receiving frames), the relative phase of the modulation and data is unknown.

The modulation is synchronized by turning on the EXSYNC pulse a known amount of time before data acquisition begins. The exposure signal active time (Section 4.2.1) is set to the maximum of one second. Five consecutive grabs are performed, allowing previous modulation cycles of 1 Hz or higher frequency to finish. The function generators are reset, waiting for the next EXSYNC signal. The exact phase of the modulation at frequencies below 1 Hz is unknown but equal to $2\pi nf$, where f is the frequency and n is an integer, $0 \le n < 1/f$. After five frames the exposure signal active time is set to the default value in the dcf file.

Camera output	1	2	3	4	5	6	7
Frame analyzed	zero	1		2	4	5	6
Frame transferred	1	2	none	4	5	6	7

Figure 4.13 Origin of skipped frames during data acquisition. The rows represent the camera output (unaffected by the analysis time), the frame number being analyzed, and the frame being transferred. As frame 1 is transferred, the program analyzes the previous frame (frame zero). After transfer the analysis begins as the program transfers frame 2. If the analysis takes too long, the command to transfer frame 3 will be skipped. The Genesis board will ignore the camera signal. After frame 1's analysis is complete, analysis of frame 2 begins. The next frame transfer will be frame 4, but the program labels it frame 3 and mislabels all subsequent frames. The skipped frame number (3) is stored in an array along with the total analysis time (in case multiple frames are skipped).

The real-time analysis sometimes requires more than 5 ms, leading to skipped frames and changing the timing. The time critical loop begins with an MdigGrab() command, transferring the image to be analyzed in the next iteration of the loop. The initial iteration analyzes the previous image. The amount of time required for this analysis is recorded with the MIL timer function. If this time is longer than 1.2 times the

frame period (6 ms) the next frame is flagged as a skipped frame. Figure 4.13 illustrates the timing involved. After frame 1 is transferred, analysis begins and frame 2 begins transfer to the second buffer. If frame 1's analysis takes too long, the program does not get to the MdigGrab() command before the camera begins transferring frame 3. After the analysis finally ends, the program begins analyzing frame 2 while waiting for frame 4's transfer to begin. Even though frame 1's analysis is too long, it is frame 3 that was skipped. To keep track of these skipped frames, two arrays record the frame number and the delay time, just in case the analysis causes multiple frames to be skipped. After data acquisition is complete these frames are reintegrated into the data arrays with zeros for the positions of the skipped frames.

After the newly acquired image is transferred to the Host CPU the command MpatFindModel() performs the pattern matching analysis, returning the x and y position and score of the match. In the case of multiple matches the list is sorted by descending score. The x and y positions are extracted from the first result and saved to the data arrays. The z position is inferred from the integrated pixel values over a 13 x 13 pixel array centered on x and y. If there are zero matches, the positions are set to zero. The image is copied to the Genesis VGA memory for display on the overlay monitor.

The brightness of the sphere's image is linear with z displacement over the range of z positions the trapped particle explores. As the sphere moves in and out of the focal plane it acts like a lens, focusing the microscope illumination. An 11 x 11 pixel box was shown to have the largest dynamic range of integrated pixel values (pixelsum) vs. particle position relative to the focal plane for a 0.6 μm diameter sphere. (Due to diffraction, the image of the sphere can extend outside of this 11 x 11 pixel (0.78 μm square) box.) If the

center of the sphere moves from one integer to another (e.g., from x = 19.99 pixels to x = 20.01 pixels) the center of the 11 x 11 array will jump by one pixel, leading to discontinuities in the z position.

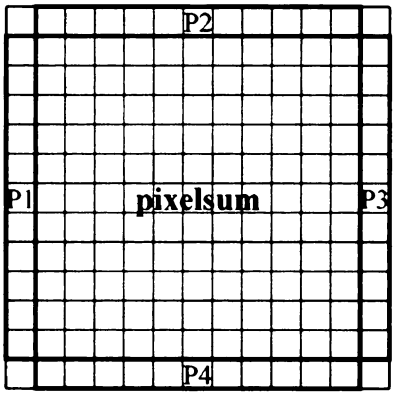

Figure 4.14 13 x 13 pixel array used in the z position calculation. The integrated pixel value equals the sum over pixel values in the 11 x 11 pixelsum array, centered on the particle's x and y position. To reduce the effect of discrete steps in array center, the next outer row is included in the sum, weighted by the fraction of a pixel particle center.

The solution is to sum over the 11 x 11 pixel box (pixelsum in Figure 4.14), then sum the next set of rows (represented by P1 through P4) and weight them based on particle position. For example, if the particle is centered at (x, y) = (19.9, 20.2),

$$\text{pixelsum} = \sum_{11\times11}\text{image} + (1-\text{xr})\sum_{P1}\text{image} + \text{xr}\sum_{P3}\text{image} + (1-\text{yr})\sum_{P2}\text{image} + \text{yr}\sum_{P4}\text{image},$$

where xr = 0.9 and yr = 0.2.

After the time critical acquisition loop, the skipped frames are filled into the data arrays with zeros for the positions. The measured frame rate is written to the "Real fps" edit box in area 4 of Figure 4.9, and the number of skipped frames and no match frames are written to "'skipped' frames" and "# no blob frames", respectively. The MIL buffers allocated at the beginning of the function are freed. The three data arrays were declared globally, and thus exist after OnPatMatch() finishes. They are either analyzed to

calculate the intrawell dwell times and three dimensional potential energy or saved to a file for later analysis.

The data is saved in either ASCII or binary format. The ASCII format writes the double precision x and y positions as 6 digit numbers and the long integer precision z position as 5 digit numbers, for a total of 17 ASCII characters (including decimal points, commas and carriage returns) or 17 bytes. The binary format reduces each value to 24 bits. The x and y positions are multiplied by 100,000, then converted to binary. The z position, ranging in value from 0 to 30,000, is directly converted to binary. These values are written to the file without commas or endline characters, reducing the required disk space to 9 bytes. For a 1,000,000 frame data set (1 hour, 23 minutes), this reduces the file size from over 16 MB to less than 9 MB. Both files are written with a header containing the model parameters and image file, the LUT and ROI, the type of analysis (blob or pattern matching), the file type, and the number of skipped or missing frame with the frame number and time arrays.

Z Position Calibration

The z position is calculated from a calibration of the integrated brightness vs. z position. As the sphere moves in the z direction, focusing of the microscope illumination causes the image to change brightness. For a small range of positions, which include the trapped particle motions, this relationship is linear. The calibration depends on background intensity, and must be performed every time the illumination is changed.

The z calibration is performed with either a sphere stuck to the surface of the cell or with a trapped sphere brought into contact with the surface. The stuck sphere will not move, allowing a calibration over the full range of possible particle positions relative to

the focal plane. However, the stuck sphere may not be the same size or shape as a subsequently trapped sphere. The trapped sphere calibration can be performed on any sphere, but only for z displacements above the focal plane.

The z position of the particle is changed by moving the cell relative to the objective lens using the microscope's focusing knob, driven by a z translation stage for increased resolution. The minimum step size of the focusing knob is approximately 0.3 μm, or ½ of the sphere diameter. To reduce the step size a Line Tool z translation stage is placed in contact with the focus knob. The focus knob travels 22.3 μm per inch of translation. The micrometer has a resolution of less than 0.001 inches, corresponding to 22 nm. Step sizes were usually 0.005 to 0.01 inches, or 0.1 to 0.2 μm.

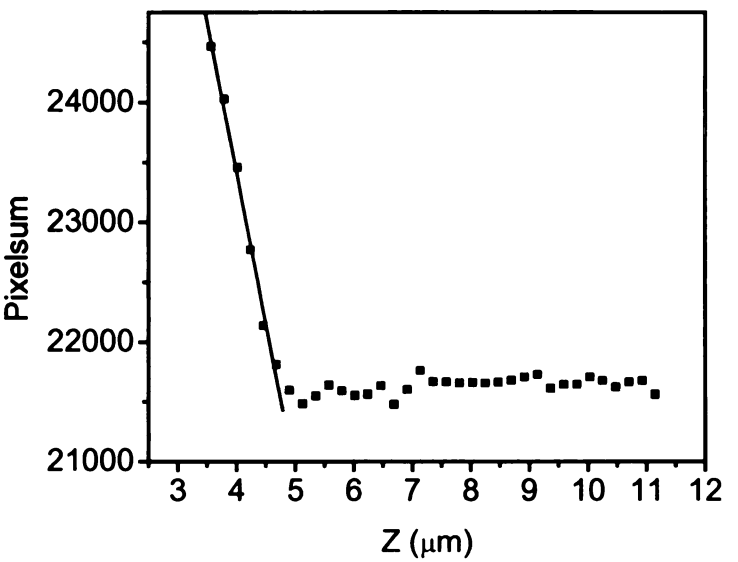

Figure 4.15 Z calibration. A trapped particle was lowered to the cell bottom using the microscope's focusing knob. The sphere contacts the cell around z = 5 μm. The integrated pixel value (pixelsum) increases linearly with position with a slope of 2500 ± 200 pixelsum/μm (solid line). Decreasing focus position corresponds to the sphere moving higher in the trap.

RunningCOG's beamtracker subroutine is used to measure the x, y, and z position over at least 50 frames at around 100 frames per second. For calibration of a trapped sphere this integrates over the sphere's motions. The RunningCOG model is chosen the same way as the pattern matching model, therefore the z position range over which the model still matched would be the same. The average integrated pixel sum is plotted vs. z position (Figure 4.15). A trapped sphere was lowered to the bottom of the cell (z = 5 μm) where the brightness increased until the model no longer matched. The slope of the linear regression fit was 2500 pixelsum/μm.

Beam Power Modulation and Synchronization

The barrier height is modulated by changing the left beam power. The LS-100 stabilizer used to modulate beam power is controlled by the signal from the Stanford Research Systems DS345 synthetic function generator (Figure 4.12). The function generator is triggered by the framegrabber's EXSYNC output and synchronized to the beginning of the acquisition.

Since the camera and function generator have their own internal clocks the camera's frame rate relative to the function generator was measured. One period (measured in frames) is the camera frame rate divided by the modulation frequency. The EXSYNC signal rate was measured relative to DS345 2, controlling the LS-PRO stabilizer. DS345 1, controlling the LS-100, is synchronized to the DS345 2 10 MHz clock. The LeCroy 9310AM oscilloscope was set to trigger off of the falling edge of the EXSYNC signal in channel 1, while the function generator sent a 200 Hz square wave to channel 2. The function generator frequency was adjusted until channel 2 was stationary with respect to channel 1. The oscilloscope sweep rate was increased until the maximum

precision of the DS345 was reached. The frame rate is 201.646278 ± 0.000005 Hz, with an uncertainty corresponding to one part in 40,000,000. Therefore, for a typical run of 100,000 frames, the phase is expected to slip by 0.0025 frames.

The phase shift is set to a constant, integer number of frames by triggering the function generators with the framegrabber's EXSYNC signal, eliminating all phase slip. The EXSYNC output from the framegrabber is sent via BNC cable to the DS345 2 function generator where it triggers the Burst modulation feature. Burst modulation sends an integer number of periods of user defined frequency, amplitude, offset and phase shift. After these periods are sent, the function generator returns to the offset voltage as it waits for the next trigger. During the modulation period all triggers are ignored.

To reduce the amount of time the function generator signal is constant (i.e., the time it is waiting for a trigger), the modulation frequency is set so one period ends just before the next EXSYNC pulse arrives. Ideally, the correct frequency is the frame rate (measured above) divided by the number of frames per period. The Burst modulation requires a finite amount of time to reset, less than 200 nanoseconds. This time is not constant with frequency, so the function generator frequency was measured for each desired modulation frequency (Table 4.2)

The EXSYNC and function generator time traces were sent to the LeCroy 9310AM oscilloscope. The sweep was triggered by the falling edge of the function generator's sine output. At the end of the burst, the function generator output went to a constant DC offset until the next EXSYNC pulse. The modulation frequency was reduced until the constant voltage disappeared. The modulation frequency was measured

to within 0.000001 Hz, or a constant voltage interval of $\leq$ 1 μs. Table 4.2 lists the approximate frequency, the period in number of frames, and the function generator setting from 0.2 Hz to 2 kHz. At modulation frequencies above 10 Hz the burst count (number of periods output by the burst modulation) is set to 10. This allows minimum modulation periods of 0.1 frames.

The modulation, while synchronized with the images themselves, was not synchronized with the beginning of the data acquisition. The framegrabber is continually producing the EXSYNC signal and triggering modulation periods, even when the frame is not transferred. To synchronize the modulation with the first recorded frame the trigger signal is interrupted just before the time critical loop. Using the MIL commands, the EXSYNC active time is set to the maximum of 1 second. Five single images are acquired, producing 5 triggers at one second intervals. The EXSYNC active time is then reset to the default value in the dcf and the data acquisition begins.

The phase was calibrated by directly measuring the beam power with the real time pattern matching analysis routine. Due to the difference in index of refraction, the beam reflects off the glass-water interface at the bottom of the cell. The laser rejection filters below the dichroic mirror filter out this reflection before it reaches the camera. These filters were removed, and a 4 O.D. neutral density filter mounted after lens L4. The beam reflection was a dim dot on the camera, requiring amplification of around 8 times by the lookup table. The beam power was modulated by the LS-100 stabilizer with 3 mW peak to peak amplitude, controlled by the function generator signal. The integrated pixel sum measurement, used to find the z position of the particle, measured the beam power as a function of time. The 10,000 data points were fit to the function

Table 4.2 Function generator settings to minimize burst modulation errors. The approximate frequency is calculated from the approximate frame rate (200 frames per second) divided by the number of frames. At 10 Hz and above there are 10 periods per burst, allowing periods of less than one frame.

Approx. Frequency	Number of Frames	DS345 Setting	Approx. Frequency	Number of Frames	DS345 Setting	Approx. Frequency	Number of Frames	DS345 Setting	Approx. Frequency	Number of Frames	DS345 Setting
			1.111111	180	1.120272	11.11111	18	11.202254	111.1111	1.8	112.029442
			1.25	160	1.26025	12.5	16	12.602723	125	1.6	126.027916
			1.333333	150	1.344286	13.33333	15	13.443171	133.3333	1.5	134.431414
			1.428571	140	1.440355	14.28571	14	14.403383	142.8571	1.4	144.033589
			1.666667	120	1.680334	16.66667	12	16.803585	166.6667	1.2	168.037221
0.2	1000	0.201649	2	100	2.016486	20	10	20.164757	200	1	201.653051
0.25	800	0.252061	2.5	80	2.520655	25	8	25.205377	250	0.8	252.071715
0.285714	700	0.28807	2.857143	70	2.880710	28.57143	7	28.806013	333.3333	0.6	336.077971
0.333333	600	0.336081	3.333333	60	3.360843	33.33333	6	33.60839	400	0.5	403.309152
0.4	500	0.403298	4	50	4.032877	40	5	40.329513	666.6667	0.3	672.201123
0.444444	450	0.448095	4.444444	45	4.480967	44.44444	4.5	44.811777	1000	0.2	1008.305921
0.5	400	0.50415	5	40	5.041309	50	4	50.410754	2000	0.1	2016.84062
0.526316	380	0.530641	5.263158	38	5.306538	52.63158	3.8	53.063805			
0.555556	360	0.560136	5.555556	36	5.601118	55.55556	3.6	56.014721			
0.588235	340	0.593092	5.882353	34	5.930600	58.82353	3.4	59.306969			
0.606061	330	0.611032	6.060606	33	6.110633	60.60606	3.3	61.103546			
0.625	320	0.630133	6.25	32	6.301362	62.5	3.2	63.013611			
0.666667	300	0.672162	6.666667	30	6.721586	66.66667	3	67.21678			
0.714286	280	0.720178	7.142857	28	7.201526	71.42857	2.8	72.015952			
0.740741	270	0.746824	7.407407	27	7.468322	74.07407	2.7	74.686295			
0.769231	260	0.775566	7.692308	26	7.755799	76.92308	2.6	77.555453			
0.8	250	0.806561	8	25	8.065903	80	2.5	80.657765			
0.833333	240	0.840197	8.333333	24	8.401931	83.33333	2.4	84.018611			
0.909091	220	0.916548	9.090909	22	9.165950	90.90909	2.2	91.655984			
1	200	1.008243	10	20	10.082379	100	2	100.822333			

$I = A\sin(2\pi f(t - t_0)) + y_0$ with a non linear least squares fit in Origin 7.0. The phase shift t_0 is 3.0 ± 0.3 frames over frequencies from 1 to 50 Hz.

Below 1 Hz, the absolute phase shift is not known exactly. By spacing the EXSYNC triggers 1 second apart, the phase becomes an integer multiple of $2\pi f$, up to 2π. For example, 0.2 Hz modulation can be triggered by any of the five pulses, depending on when the previous period ends. The phase shift is 0, 0.4π, 0.8π, 1.2π, or 1.6π. In units of frames, the phase shift is 0, 200, 400, 600, or 800 frames.

Batch Data Acquisition

After the sphere is trapped, the gimbal mounted mirrors adjusted, the model chosen, and the cell clamp set, data acquisition requires very little input from the operator. At the end of each run, typically 100,000 frames (500 seconds or 8.3 minutes), the data are saved, the modulation frequency and/or amplitude are changed, and the next analysis begun. This process is automated in *WinMil2* using a batch acquisition system.

The function generator settings are controlled by a text file. When the "Batch Acquire" button in area 3 of Figure 4.9 is pressed, *WinMil2* loads the batch file specified in the "Filename for analysis results" in area 4. Table 4.3 shows a typical batch file. The first number in this file is the number of individual data sets. This is followed by six columns of numbers representing the function generator frequency setting (from Table 4.2), the DS345 2 (beam 2) and DS345 1 (beam 1) DC offset, the DS345 2 and DS345 1 modulation amplitude (in V_{pp}), and the number of frames. These values are stored in 6 global arrays. *WinMil2* begins a loop, iterating through each setup. The batch file in Table 4.3 acquired 152 datasets over 18 hours.

Table 4.3 Typical batch acquisition file. The first number (152) is the number of data sets to be recorded. *WinMil2* performs one acquisition per row. Columns represent the frequency, LS-PRO voltage offset (V), LS-100 voltage offset, LS-PRO voltage amplitude (V_{pp}), LS-100 voltage amplitude, and the number of frames. (The table is truncated after dataset number 32).

152					
1.008243	0.360	0.125	0	0	100000
1.008243	0.360	0.105	0	0	100000
1.008243	0.360	0.085	0	0	100000
1.008243	0.360	0.145	0	0	100000
1.008243	0.360	0.165	0	0	100000
1.008243	0.360	0.125	0	0	100000
1.008243	0.360	0.125	0	0.05	100000
1.008243	0.360	0.125	0	0.1	100000
1.008243	0.360	0.125	0	0.15	100000
1.008243	0.360	0.125	0	0.2	100000
1.008243	0.360	0.125	0	0.25	50000
1.008243	0.360	0.125	0	0.3	50000
1.008243	0.360	0.125	0	0.35	50000
1.008243	0.360	0.125	0	0.4	50000
2.016486	0.360	0.125	0	0	100000
2.016486	0.360	0.125	0	0.05	100000
2.016486	0.360	0.125	0	0.1	100000
2.016486	0.360	0.125	0	0.15	100000
2.016486	0.360	0.125	0	0.2	100000
2.016486	0.360	0.125	0	0.25	50000
2.016486	0.360	0.125	0	0.3	50000
2.016486	0.360	0.125	0	0.35	50000
2.016486	0.360	0.125	0	0.4	50000
2.520655	0.360	0.125	0	0	100000
2.520655	0.360	0.125	0	0.05	100000
2.520655	0.360	0.125	0	0.1	100000
2.520655	0.360	0.125	0	0.15	100000
2.520655	0.360	0.125	0	0.2	100000
2.520655	0.360	0.125	0	0.25	50000
2.520655	0.360	0.125	0	0.3	50000
2.520655	0.360	0.125	0	0.35	50000
2.520655	0.360	0.125	0	0.4	50000

The frequency, offset, amplitude, and burst counts are adjusted via the GPIB interface with the DS345 function generator before every data set. Next the OnPatMatch() function is called; data acquisition is performed as explained above. After the set number of frames are acquired, the interwell dwell times are calculated using the

OnAnalysis() function, explained in Appendix E. The position and dwell time data are saved to separate files and the next iteration begins.

4.3. Optical Stability

To measure the effect of modulation on the transition rate, the uncertainty in the static potential is minimized through mechanical stabilization and thermal control. Slow changes in the trap positions in x, y, and z, caused by thermal expansion and mechanical relaxation, are reduced by temperature controlling the optical mounts and fixing the objective lens to cell separation. Faster fluctuations due to air motions are eliminated by baffling the optics and microscope. The z position motions are almost eliminated, while the x and y motions are reduced by a factor of 4.

4.3.1. Laser Power Stability

The intensity of the HeNe lasers fluctuates due to input power noise and thermal fluctuations, changing the barrier height and creating a non-white noise source. The stabilizers positioned after the beams reduce this driving by at least a factor of four.

The beam power fluctuation amplitude was calculated from the power spectrum. The power spectrum of fluctuations was measured using a Centronic OSD155T silicon photodiode sampling the beam using the beam sampling optics (Section 4.1.4). A Glan laser calcite polarizer (Newport product number10GL08AR.14) attenuated the beam to 0.6 mW total power, preventing saturation of the photodiode. The beam diameter (0.98 mm) was smaller than the photodiode active area. The photodiode integrated over beam profile and was insensitive to beam pointing fluctuations. The photodiode signal was sent via coaxial cable to the HP3561A spectrum analyzer.

The HP3561A Dynamic Signal Analyzer performs a discrete Fourier transform over user defined frequency ranges from 0.01 Hz to 100 kHz. The dynamic range is ≥80 dBV below the input range, which was set to -15 dBV (177 V_{rms}). Below 80 dBV distortions and aliasing occur. (The HP3561A defines dBV = 20 log (*V*), where V is in volts.)

The HP3561A output is the magnitude of the discrete fast Fourier transform (FFT) normalized to the bandwidth $|F(\nu)|$, in units of dBV/√Hz. The photodiode power spectral density is defined $S(\nu)=|F(\nu)|^2$.

The power over a certain bandwidth is calculated from the power spectral density by integrating the square over that bandwidth $P=\int_{bandwidth} S(\nu)d\nu$. The FFT is discrete, so instead the power is the sum $P=\sum_{bandwidth} S(\nu)\Delta\nu$. The power measured over the entire frequency range is equal to the total power $P_T=\sum_{\nu=0}^{\infty} S(\nu)\Delta\nu$ The optical power is the intensity of the beam incident on the photodiode, and is linearly proportional to the photodiode voltage (recorded by the HP3561A). The total power $P_T=V^2/2$, therefore the total optical power P_{opt} is proportional to $\sqrt{P_T}$, with conversion factor from a beam power vs. photodiode voltage calibration.

The bandwidth depends on the input window. For a flat top window the bandwidth 0.00955 × frequency range. To resolve narrow peaks or low frequency features, the spectral density was recorded over many spans.

A C++ program *HP3561A.cpp* was written to send a series of frequency ranges and numbers of rms averaging steps to the HP3561A via the general purpose interface

bus (GPIB). The program serial polls the device until the average is complete, then copies $|F(\nu)|$ to a file and begins the next average with the next frequency span and number of averages.

$|F(\nu)|$ was measured over four frequency spans: 0 – 100 Hz, 0 – 1000 Hz, 0 - 10 kHz, and 0 – 100 kHz. The ranges were combined by taking 0 – 100 Hz from the 0 – 100 Hz range, 100 – 1000 Hz from the 0 – 1000 Hz range, 1 – 10 kHz from the 0 - 10 kHz range, and 10 – 100 kHz from the 0 – 100 kHz range.

The power was measured over the entire range then over the DC and AC portions of the spectrum. (Here DC is defined as all frequencies below one bandwidth of the input window, in this case $\leq$ 1 Hz.) Table 4.4 shows the total optical power, the DC power, and the AC power for HeNe laser 1 and laser 2. Using the voltage to beam power conversion, laser 1's power fluctuations (above 1 Hz) contained 0.0018 mW out of 0.60 mW, or 0.3%. Laser 2's power fluctuations were 0.4% of the DC power.

From the static tilt measurements in Section 5.2 the beam power fluctuations were converted into change of barrier height ΔU_{AC}. The slope of the linear term in the quartic approximation vs. beam power was 240 k_BT/μm V (Figure 5.14), or 7.6 k_BT/mW. 0.3% of the approximately 7 mW input power is 0.021 mW, or $\Delta U_{AC} = 0.16\ k_BT$.

Measured after the LS-100 and LS-PRO beam power stabilizers the fluctuation spectrum amplitude was below the dynamic range of the HP3561A spectrum analyzer. Assuming the AC power was equal to –95 dBV/√Hz (input range of –15 dBV/√Hz and -80 dBV/√Hz dynamic range), the AC optical power was 0.5 μW, corresponding to 0.04 k_BT barrier height fluctuations.

Table 4.4 Beam power fluctuation amplitude.

	Total P_{opt} (mW)	DC P_{opt} (mW)	AC P_{opt} (mW)	ΔU_{AC} (k_BT)
Laser 1	0.60	0.60	0.0018	0.16
Laser 2	0.50	0.50	0.0018	0.19
Stabilized laser	0.60	0.60	≤ 0.0005	≤ 0.04

The laser power stabilizers remove at least ¼ of the beam power fluctuations, with the measurement limited by the sensitivity of the spectrum analyzer. The expected noise reduction is greater than 80:1 up to 100 kHz.

4.3.2. Focal Plane Position

The barrier height depends strongly on the distance between the focal plane in the cell bottom. Simulations by Fallman and Axner [90] show that the axial trapping efficiency (the ratio of the trapping force to the input power) falls by 50% over a distance of 2 sphere radii. A measurement of transition rates vs. height in this system showed a 40% change in rate over 3 μm. The distance changes were eliminated by securing the sample to a clamp around the objective.

Objective Clamp

In the first design, the cell rested on the stage with the objective viewing from below. The cell was constructed from two 22 mm #1 cover glass pieces. They were cleaned, sealed on three sides, then baked for 6-24 hours, similar to the process described in section 4.1.10. A temporary glass spacer left a 100 μm gap between the cover glass. The gap was filled with 0.6 μm diameter spheres in 0.0001 M NaOH solution. An air gap of 3 to 5 mm was left at the top and the final side sealed with epoxy.

After setting the focus height with the focus knob on the microscope, the height changed by 10s of μm in a few hours. This effect was independent of temperature and was attributed to the mechanical drift of the objective turret relative to the stage.

To remove this drift, the cell was mounted on a clamp which fit around the objective lens (Figure 4.16). It was thus independent of the microscope stage. The clamp was a hollow stainless steel cylinder with a slit along the length. A screw on the side tightened the clamp, allowing the height (i.e., vertical position along the objective) to be adjusted. The cell rested on the top of the clamp, held a fixed distance from the lens.

To take advantage of the clamp, a new stage was built and the cell redesigned (see section 4.1.10). The top surface of the cell is a 3 x 1 inch glass slide. An 18 mm diameter #1 cover glass piece is epoxied on ¾ of its circumference and attached to the center of the slide. A temporary #1 glass spacer is used to keep the cell open. After baking for 6 – 24 hours, the spacer is removed and the cell filled with the 0.6 μm sphere/0.0001 M NaOH solution. The slight wedge shape created by the capillary action of the epoxy causes the solution to wick away from the open end of the cell. The cell is capped with epoxy, leaving a 3 – 5 mm air gap, and allowed to set for 6 hours.

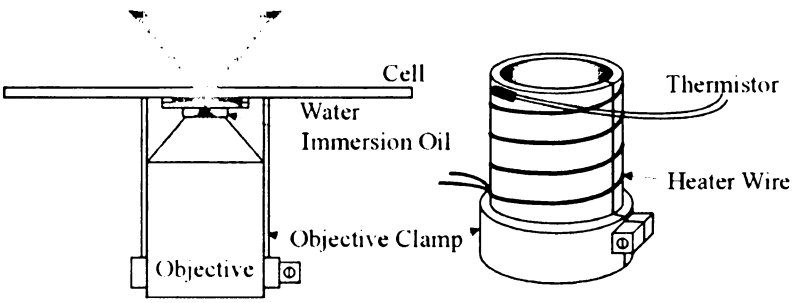

Figure 4.16 The objective clamp. The clamp fits around the objective lens. It is tightened with a screw at the bottom. The cell rests on the clamp, keeping it a fixed distance from the objective lens. Nichrome heater wire was wrapped around it and a thermistor attached at the top.

The redesigned stage has a 2.5" square opening to prevent collisions with the objective clamp. The cell spans the opening, its ends resting in a machined groove. This allows the cell to be moved using the stage. When a particle is trapped, the objective clamp is raised until the cell clears the groove and rests on the clamp alone.

To prevent the cell from sliding sideways a 200 gram weight is placed on top of the cell. The weight is a 1.5 inch diameter, ½ inch tall cylinder with a ¾ inch hole through the center for illumination to pass through. The weight was positioned directly above the walls of the objective clamp.

Despite the above modifications, the focal plane continued to move over long time scales. Plots of z position vs. room temperature showed a direct correlation. The external temperature changes caused thermal expansion of the objective/objective clamp system, changing the focal plane height by tens of μm/°C.

The objective clamp temperature was controlled with a heater and feedback circuit. A 3 foot length of 30 Ω per foot resistance wire was wrapped around the objective clamp. A thermistor mounted near the top of the clamp measured the temperature. A feedback circuit, capable of supplying 2 W to the resistance heater, maintained the temperature to within 50 mK, even when the microscope was exposed to air currents. When the microscope was baffled with cardboard (and later insulating foam), the temperature fluctuations on the scale of seconds disappeared. The thermal control circuit performance improved, keeping the objective clamp temperature constant to within 10 mK.

Nonetheless, the focus height continued to change with room temperature shifts. To make sure that the objective/objective clamp system was capable of compensating for

changes of this magnitude, the heater wire was driven with a 0 – 4 V square wave at 1 mHz to evaluate the time-temperature response. This caused a 0.4 °C change in the temperature measured by the thermistor. The focal plane height was inferred from the integrated brightness of the beam reflections off of the cell's glass-water interface. Over less than 10 μm the focal plane height was monotonic with measured brightness.

It was found that, rather than the objective moving closer to the cell as it heats, the cell first moves away (2900 seconds in Figure 4.17a). After 30 seconds the cell-objective distance reaches a maximum and reverses direction. The distance decays exponentially with a time constant of approximately 200 seconds.

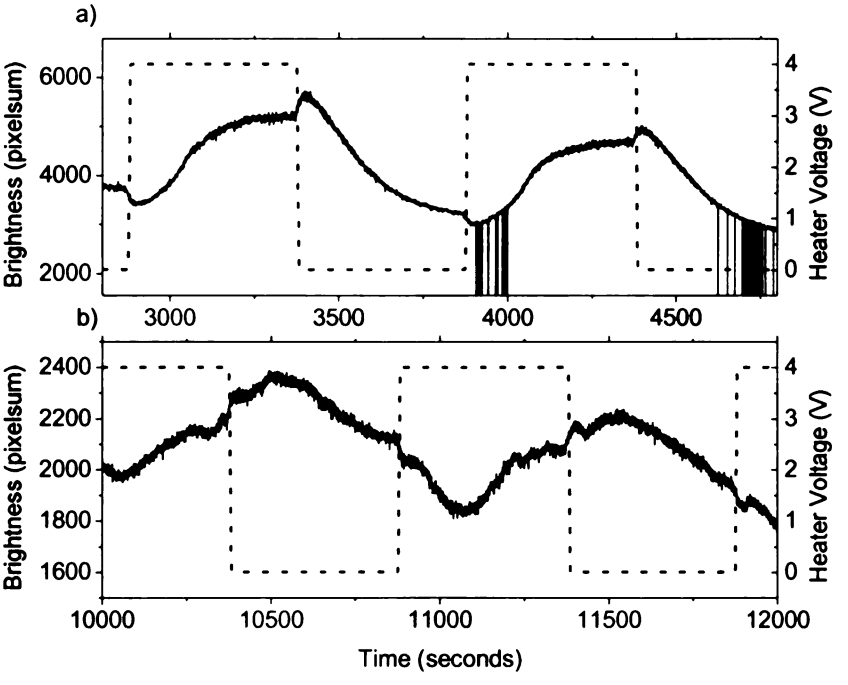

Figure 4.17 Objective to cell distance changes with objective clamp heating. The brightness of the beam reflection from the glass water interface (solid lines) decreases with increasing separation. Dashed lines indicate heater voltage, from 0 to 4 V. (a) with weight and (b) without weight on the cell. Vertical lines in (a) are mismatches in the pattern matching analysis.

The effect was due to differential heating between the clamp and objective. At the beginning of the heating cycle, the objective clamp heated up first because the wire was in direct contact. It expanded, moving the cell away from the objective. After 30 seconds the objective began to expand while the clamp's expansion rate decreased, decreasing the separation. On the cooling cycle there was a similar effect. The objective clamp was exposed to the air, cooling more quickly. The cell moved towards the objective. As the objective cooled, it moved away from the cell.

The weight on the cell affected this process. Figure 4.17b shows that when the weight was removed the distance increased for 30 seconds, then began to decrease. After 60 seconds, the distance began to increase again. 90 seconds later the distance decreased.

This was caused by thermal flexing of the cell itself. Upon heating, the bottom of the cell expanded faster than the top. This caused the center of the cell to move away from the objective. After approximately 150 seconds the temperature equilibrated across the 1.25 mm thick glass slide and the cell relaxed again. The remaining distance change came from the objective lens expansion. The weight either prevented the cell from flexing or kept it in better thermal contact with the clamp. In the latter case the cell would still flex, but it would happen at the same time as the differential expansion of the objective and objective clamp.

To increase the thermal contact a new objective clamp was built (Figure 4.18). The cell rests on a ½ inch wide "shelf", increasing the contact area by a factor of 10. The objective clamp was wrapped in 80 Ω of Nichrome resistance wire and heated with a 0 - 4 V, 1 mHz square wave. The feedback thermistor is attached to the bottom of the clamp.

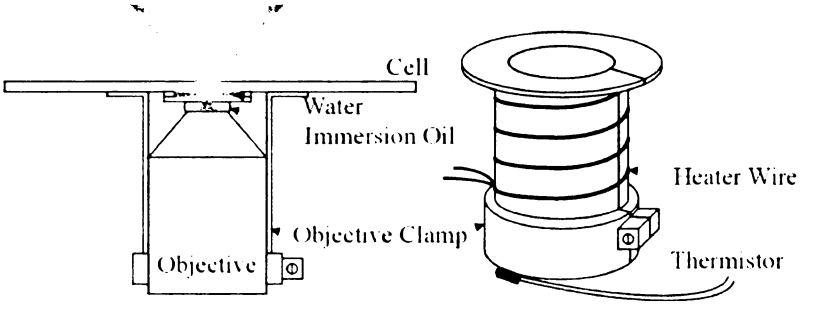

Figure 4.18 The objective clamp with wide shelf. The shelf provides much larger thermal contact area with the cell. The clamp is wrapped in 80 Ω of Nichrome heater wire.

Without the weight on the cell, the focal plane height change due to cell flexing does not appear (Figure 4.19a). The cell-objective distance increased at the beginning of the heating cycle, then leveled off after 140 seconds. The objective clamp expanded, but the extra thermal mass made the expansion slower than the previous clamp. It took 150 seconds for heat to propagate through the cell (Figure 4.17b). Therefore if the cell was flexing, its effects were obscured by the differential expansion.

With the weight, the time scale of the motion was reduced further. At the beginning of the heating cycle the cell moved away from the objective for 40 seconds, then the distance closed for the remainder of the cycle. The amplitude of this motion was smaller than any focal plane height changes previously recorded. (The focal plane height was measured as a function of the brightness of beam reflections off cell's the glass-water interface. The relationship is monotonic but not linear, so direct comparisons between datasets are difficult.)

These results show that there is a change in focal plane height because temperature fluctuations were changing the cell-objective separation. The change is minimized when there is large thermal contact between the objective clamp and the cell.

The thermal contact is increased with the addition of a weight to hold the cell down. A feedback control circuit isolates the objective from room temperature variations.

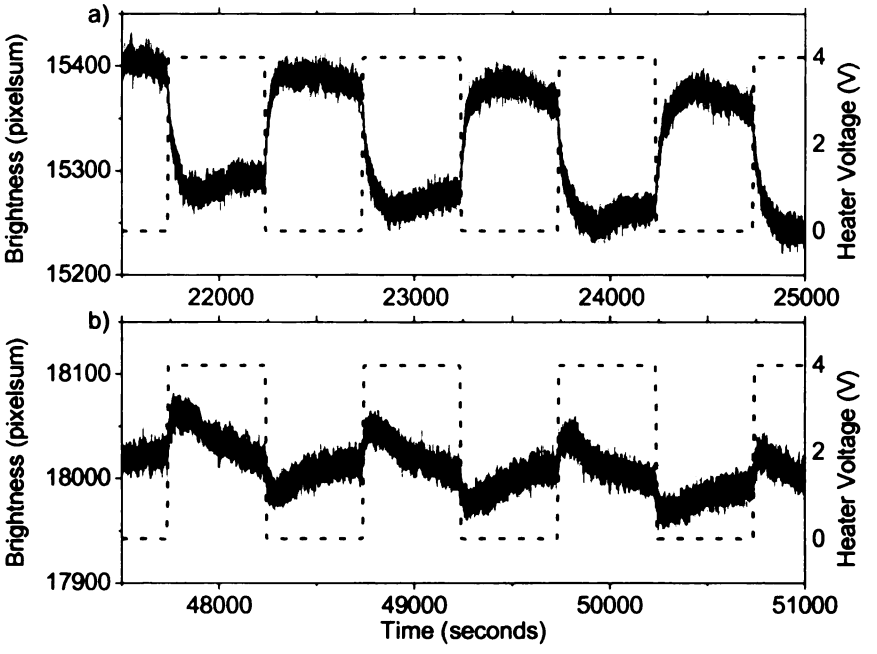

Figure 4.19 Objective to Cell distance changes with redesigned objective clamp. The brightness of the beam reflection from the glass water interface (solid lines) decreases with (a) increasing separation and (b) decreasing separation. Dashed lines indicate heater voltage, from 0 to 4 V. (a) without weight and (b) with weight on the cell.

Cell Clamp

The height of the focal plane continued to change, but on much longer time scales. These motions correspond to relaxation of the objective-cell distance by 2 to 8 μm over more than 10 hours. The constant force of the weight is not large enough to relax the stresses out on a short enough time scale.

A cell clamp was built to replace the weight. The cell clamp is made of three pieces. The top piece is a 2 inch diameter, ¼ inch thick brass cylinder with a 1 inch hole

for the illumination. Screws at the perimeter travel down past the objective clamp shelf to two 2 inch long, ¼ inch square aluminum bars. The aluminum bars contact the underside of the shelf, clamping the cell to the objective clamp (Figure 4.20).

The application of the cell clamp caused the focal plane to move > 100 μm into the cell. This caused the trap to become unstable and the particle escaped. The clamp was most likely distorting the objective clamp shelf, moving the cell closer to the objective.

To prevent distortions, a series of washers was used as spacers to set a maximum distortion of the objective clamp. The focal plane only moved 20-30 μm when the cell clamp was tightened. Over 12 hours, the cell clamp relaxed and the focal plane moved down by approximately 20 μm. The screws had loosened slightly, causing the force on the cell to change.

The cell clamp was modified to hold two ball nose spring plungers, which have constant force for a small range of distances. The spring plungers have a maximum force of five pounds before the ball is entirely recessed into the plunger. Two pieces of 1 inch long, ½ inch wide, 1/16 inch thick stainless steel under the plungers distribute the point load over a larger area of the cell (Figure 4.20).

The cell was clamped and the spring plunders set to just under 5 pounds of force each. Over 14 hours, the focus height drifted by less than 2 μm.

The cell clamp with spring plungers performs better than the simple cell clamp or the weight. The spring plungers provide a constant force over 100 μm (compared to the cell clamp without spring plungers). If the screws holding the clamp relax there is still a total of 10 pounds on the cell.

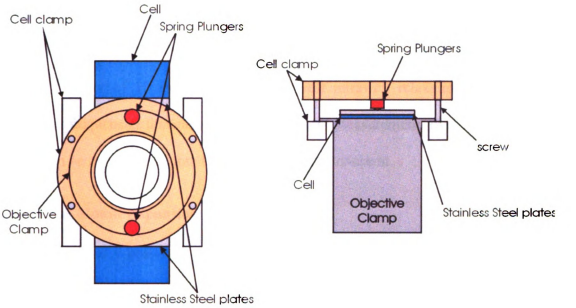

Figure 4.20 Cell Clamp. The ball nose spring plungers press on two stainless steel plates, distributing the force across the cell as it is held against the objective clamp. The brass ring is kept in place with two aluminum bars that fit below the shelf of the objective clamp.

The cell resting on the stage introduced drifts due to mechanical relaxation of the microscope and temperature changes. The cell mounted on the objective clamp removes the microscope relaxation. Thermal control of the objective removes most of the thermal changes. Clamping the cell to the objective clamp reduces the relaxation of the objective-cell distance to less than 2 μm in 14 hours. This corresponds to an estimated 25% change in the transition rate or 1 k_BT in the barrier height. If the data acquisition is limited to 2 hours (1.4 million frames) the barrier height changes would be 0.15 k_BT or less, depending on the size of the room temperature variations.

Measurement of the transition rate dependence on modulation frequency or amplitude requires an unchanged potential over multiple data sets. The use of ten 100,000 frame (500 s) sets limit the minimum transition rate W_0 , which limits the minimum modulation frequency f ($f > W_0$). For 10% uncertainty in W_0 the number of

transitions $N = 100$ in each direction, for a mean transition rate of 0.4 Hz. (The number of transitions increases with the modulation amplitude, reducing the uncertainty.) This value is a factor of 10 smaller than the slowest intrawell relaxation time, allowing modulation frequencies that can explore this region. Measurements over times exceeding 2 hours can be made if the room temperature remains constant.

4.3.3. Lens Mount Expansion

The x and y positions of the traps changed with temperature over many hours. Both beams moved in the same direction during these changes. Since the objective was temperature controlled, the problem was coming from one of the other optics.

To find the individual optics most susceptible to change, the positions of the laser reflections off the glass-water interface of the cell were measured as the mounts were heated. Around 80 Ω of Nichrome wire was wrapped around the mounts (Figure 4.21). A thermistor mounted on the post mount measured the temperature change.

Heating of the laser mount and the mirror mounts by 0.5 °C had no observable effect on the beam position. Heating the lens mounts caused a large displacement in the beam position. A linear fit of the x position vs. temperature had a slope of 20 nm/°C. (Due to the camera orientation, x position changes correspond to lens motions perpendicular to the table.)

The beam deflection occurs when the lens mount expands, moving the lens up relative to the beam. The mount is made of aluminum and stainless steel, which have coefficients of thermal expansion of 2.3×10^{-5} per °C and 1.8×10^{-5} per °C, respectively. A 1 °C change in the 225 mm tall mounts corresponds to an approximately 4.5 μm change in lens height.

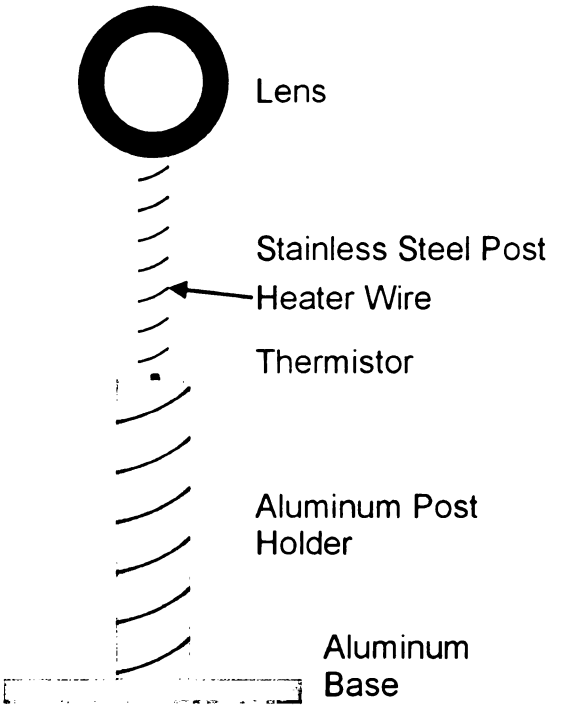

Figure 4.21 Lens mount heater. Nichrome wire is wrapped around the post and postholder and attached to a DC power supply. The thermistor placed at the top of the postholder is used to measure the temperature.

The deflection of a beam travelling through the displaced lens was calculated using geometrical optics. A ray travelling along the lens's optic axis will not be deflected by the lens. A ray that is off axis by a distance h will be deflected at an angle $\theta = \tan^{-1}(h/f)$ by a lens with focal length f (Figure 4.22). For a 1 μm displacement of a 100 mm focal length lens, $\theta = 1\times10^{-5}$ rad. The beam will travel through the focal point of the lens, which has been translated by h.

The optical system contains five lenses in each beam; the pairs L1-L2 and L3-L4 to resize the beam and the objective lens to focus the beam to a diffraction limited spot. If all of the lenses move up the same amount, the beam will be displaced by $h_f = \frac{f_4}{f_3} h_i = \frac{f_4}{f_3}\frac{f_2}{f_1} h$ entering the objective. If the expansion is not uniform, (Figure

4.23), the beam angle changes as well. When the beam enters the objective with an angle φ_f, the focal point is displaced by $\Delta x = f_{\mathrm{EFL}} \tan\varphi_f$, where f_{EFL} is the effective focal length of the objective lens.

Using a spreadsheet in Lenses4.xls (Table 4.1) to propagate the effects of lens displacement on trap positions, a 1 μm relative displacement of any lens results in a 3 nm shift in the beam position. This is nearly 1% of the typical beam spacing of 400 nm. A full 1 °C change in a single lens mount would cause a 13.5 nm (more than 3%) displacement of a single beam.

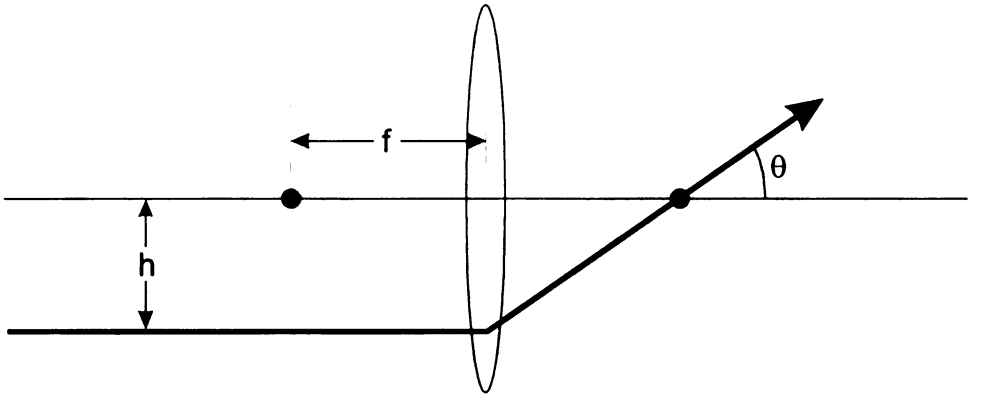

Figure 4.22 Deflection of a beam through a single lens. The beam has moved upwards a distance *h* relative to the beam. The beam travels through the focal point at an angle θ.

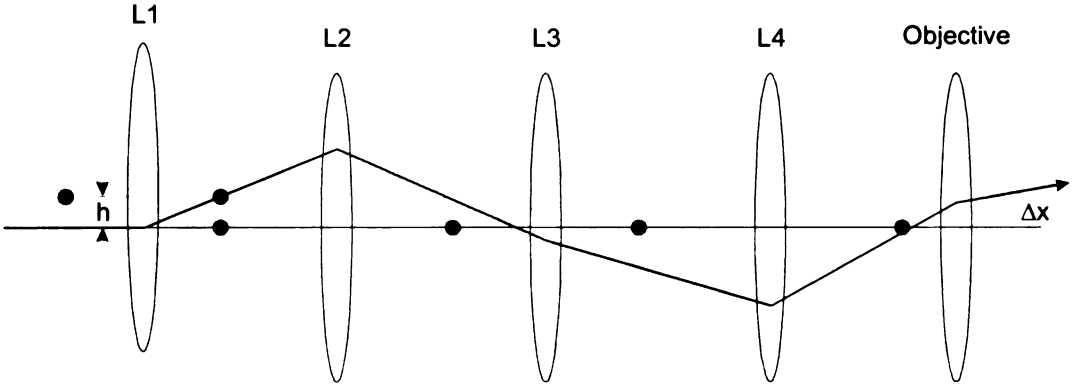

Figure 4.23 Diagram of the beam deflection as it propagates through the optical system. A displacement of lens L1 by *h* will cause the beam entering the objective lens to be deflected. The trap position moves a distance Δx.

To test these predictions, 100 Ω of Nichrome wire were wrapped around individual lens mounts. The wire was heated with a 0 – 10 V, 1 mHz square wave. The temperature was measured with a calibrated thermistor mounted at the top of the postholder, about ½ of the total height (Figure 4.21).

The mount for lens L3 was heated by 1.25 °C, producing an x displacement of each beam of 20 nm. (Due to the Dalsa CA-D1 camera orientation, a vertical motion of the beam on the optical bench corresponds to an *x* displacement on the camera.) The x position vs. temperature data (Figure 4.24a) are roughly linear with a slope of 17 nm/°C for both beams. The direction of the motion corresponded to the predictions of the beam propagation calculations.

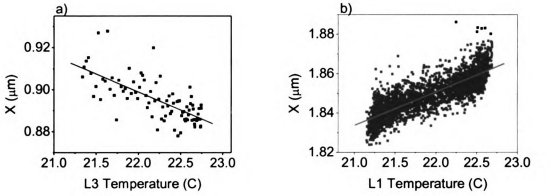

Figure 4.24 X position vs. lens mount temperature. Plot (a) shows the beam position deflection due to heating of lens L3's mount. Plot (b) shows the deflection due to heating beam 2's lens L1's mount. The lines are the linear fits. Both have a slope of 17 nm/°C.

The mount for lens L1 in beam 2 was heated to 1.4 °C. As expected, beam 2 moved 25 nm while beam 1 remained stationary. A fit to beam 2's *x* position vs. temperature gives a slope of 17 nm/°C (Figure 4.24b).

The calculations show that the beam position change due to the motion of any single lens should have the same magnitude, 14 nm/°C. The experiments show 17 nm/°C. This is explained by poor thermal contact between the thermistor and post. If the thermistor were reading a temperature too low the slope of the x vs. temperature plot would be artificially increased.

Room temperature variations of 0.1 °C, resulting in 2 nm beam displacements, are common. Relative temperature changes across the table fluctuate by more than 0.2 °C over hours. A thermal control system was designed to eliminate these slow temperature variations.

Using the same setup as for the lens mount heating experiments, Nichrome wire was wrapped around each of the remaining lens mounts. Two wires were needed for L4's cantilever mount. 10 kΩ thermistors were mounted to the top of the post holder on each mount. A resistance bridge measures the thermistor resistance. An integrating amplifier uses this signal to control the current across the heater wire via a power transistor, dissipating a maximum of 2 W.

The feedback circuits keep the temperature constant to within 25 mK, corresponding to beam displacements of 0.4 nm. The feedback circuits filter out room temperature fluctuations of up to 0.1 °C/hour.

Thermal variations have been shown to move the beam in the focal plane of the objective. Calculations and measurements show that the motions due to lens mount expansion are around 17 nm/°C, or 4% of the beam spacing. The thermal feedback system controls the temperature of the lens mounts to 25 mK for room temperature fluctuations of 0.1 °C/hour.

4.3.4. Pointing Fluctuations Caused by Air Motion

Moving air creates vibrations of optical mounts and induces index of refraction changes in optical elements. The effect of air motion on the beam positions became apparent during a set of coherence length measurements (Appendix C). The interference fringes would undergo rapid motions on the order of 10 – 500 Hz when the laboratory HEPA filter fans were set to maximum. Turning off the fans eliminated the fast fluctuations but temperature changes caused a slow (<1 Hz) drift of the fringe position.

A Plexiglas box was constructed to protect the optics from air motion. An aluminum frame holds 0.090" thick Plexiglas panels. The frame is 8 feet long, 3.5 feet wide and 16 inches tall at its tallest point. The panels are removable and allow easy access to the optics. A 1 inch diameter hole was cut to allow the beam to exit the box and enter the microscope.

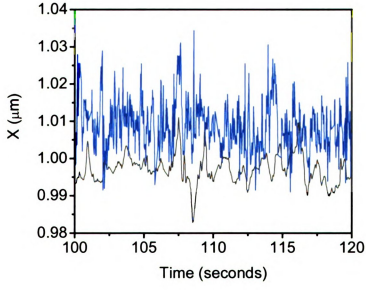

Figure 4.25 X beam positions with Plexiglas box. The position fluctuates on the order of 0.1 Hz with the Plexiglas box closed (black) and 5 Hz with the box open (blue).

The position of the beams in the field of view was measured with the Plexiglas panels on and off (Figure 4.25 black and blue lines, respectively). With the box open, the beams move at frequencies above 5 Hz over distances of 10 nm. With the box closed, the high frequency motions disappeared and slower, 0.1 Hz motions were visible. The sizes of these fluctuations were 5 nm in the x direction and 12 nm in the y direction. Motions in the x direction in the field of view correspond to motions perpendicular to the table.

The increased air vibration with the open box reduced size of the y fluctuations. The turbulent air caused changes in the index of refraction along the beam path. A 1% pressure variation across the 1 mm diameter beam over 10 cm causes deflections on the order of 10 microradians. Amplified by the lenses, this causes the beam to move ~70 nm.

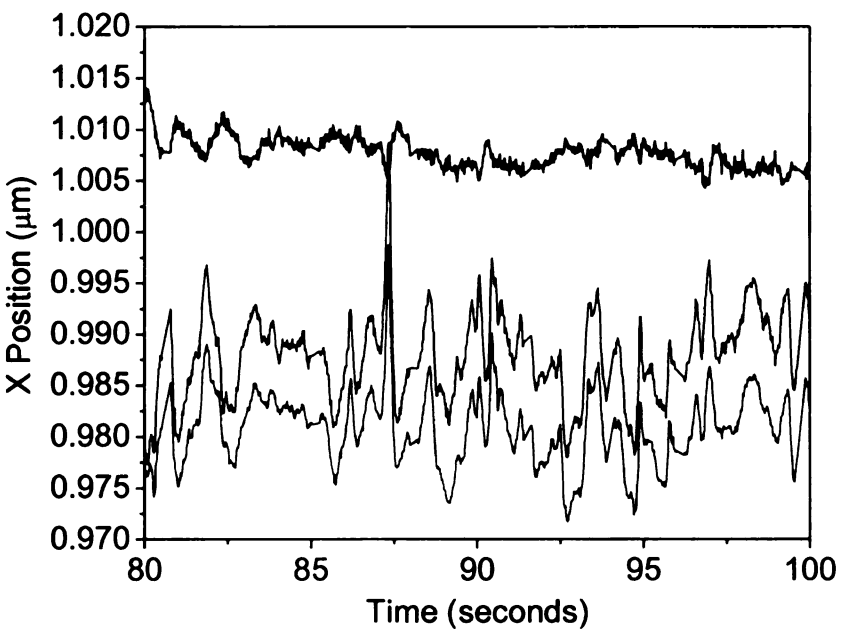

Figure 4.26 Beam separation vs. time. The dashed and dotted curves show the slow 10 nm position fluctuations of beams 1 (black) and 2 (blue). The green curve shows the beam separation with amplitude 2 nm.

With the Plexiglas box closed, the fast air motions are eliminated, but the cause of the slower beam motions is uncertain. The REO HeNe laser rms beam steering fluctuations are less than 50 μrad. These fluctuations, propagated through the optical system, could account for the beam motions. However, the anisotropy suggests that the motions of the lenses in the plane of the table are a contributing factor.

The beams exhibit correlated motion when the box is closed (Figure 4.26). The distribution of beam separation has a width of only 2 nm in x and 3 nm in y. The potential is much more sensitive to the change in the beam separation than the beam positions, especially if the position fluctuations are slower than the relaxation rate of the potential (3 Hz). Therefore the correlated motions with the box closed are preferred over the uncorrelated motions when the box is open.

The Olympus microscope is 10 inches outside the Plexiglas box. To reduce the air vibrations and temperature fluctuations at the microscope the region directly underneath its stage was baffled. Two aluminum plates, layered with foam insulation, were fit to both sides of the objective lens turret. A ¾ inch diameter hole cut into one plate allows the beam to enter. The stage has a 2.5 inch square hole, so the region just above the stage was baffled with cardboard. This baffle fits around the condenser and is lined with foam insulation. For further protection, the entire microscope except the lamp housing is sealed with a plastic cover. One side of this cover connects to the Plexiglas box, isolating the small volume where the beam leaves the box.

The microscope baffles reduced the beam position fluctuations, indicating that some part of the microscope was moving. The cell was clamped to the objective, so there should have been no high frequency motion. The other optical element, the dichroic

mirror, was held in a modified fluorescence beam splitter turret. This turret was designed to allow light from a UV lamp in the rear of the microscope to be reflected up, into the objective. Olympus produced a modified version that allows light to enter from the side.

Designed for easy switching of optical elements, the turret was weakly spring clamped, and it was found that a small pressure on the microscope housing caused the beams to move by tens of nanometers. Therefore, a fixed mount was built to hold the dichroic mirror. The mount was designed to be interchangeable with the turret, using the slide to mount it to the microscope and the original dichroic mirror holder.

However, measurements of the beam positions over an hour taken before and after installing the dichroic mount showed no improvement. Beam position fluctuations due to the beam splitter turret were either smaller than those observed or on a time scale longer than one hour.

Apparent collective beam motions might originate in motions of the Dalsa camera. The camera is attached to the microscope by a 6 inch long camera tube that contains the 5x eyepiece. If the camera or tube should shift the position of the beams on the CCD array would change.

To eliminate possible motion the camera was clamped to the optical table. Aluminum plates of varying thickness were used as a base. A ¼ inch thick Teflon block was used to make contact to the camera. The Teflon deforms slightly under pressure, giving a more uniform clamping force than aluminum. The camera was clamped from the top by an aluminum bar held in two ½ inch stainless steel posts. A second piece of Teflon made contact to the top of the camera.

The camera clamping reduced the y beam position fluctuations by 13%. Thus, motion of the camera parallel to the table was partially responsible for the beam displacements. The beam position fluctuations in the x direction were unchanged. While the camera was probably also moving perpendicular to the table, the other fluctuation sources were much larger, washing out any improvement.

The long term stability of the potential was increased using electrooptic, mechanical, and thermal controls. The beam power fluctuations were reduced by at least a factor of 4 using the LS-100 and LS-PRO laser power stabilizers. The depth of the focal plane in the cell was held constant with the thermally controlled objective clamp and cell clamp. Integral feedback heaters controlled the lens mount temperatures, reducing in plane beam position changes to less than 1 nm for slow room temperature variations. Baffling the optics and microscope eliminated the high frequency beam position changes due to air motions.

4.4. Summary

This chapter described the apparatus used to create the bistable potential, record the particle positions, and isolate the system from external sources of noise. The 0.6 μm diameter sphere is trapped by two focused laser beams positioned 0.4 μm apart. The particle makes transitions between stable points over a barrier of between 0 and 10 k_BT, controlled with the trap separation. Gimbal mounted mirrors are used to change the angles at which the beams enter the objective lens, changing the positions of the traps. The beam power is modulated electro-optically in a single beam only, tilting the potential.

The particle position is recorded in three dimensions at 200 Hz. The sphere's image is projected onto the CCD camera and transferred to the analysis computer. The x and y center of the particle is found to ±10 nm and the z position determined from the image brightness to ±40 nm. Image analysis takes less than 5 ms so the image is not saved, reducing memory usage by a factor of 160.

Changes in the potential due to beam power and position fluctuations and changes in the depth of the focal plane in the cell were reduced using electro-optic, mechanical, and thermal stabilization. The beam power fluctuations were reduced by at least a factor of 4 using beam power stabilizers, corresponding to barrier height changes of less than 0.04 k_BT above 1 Hz. The beam positions were stabilized by thermally controlling the lens mounts and eliminating air motions. Thermal control results in an estimated 0.4 nm position fluctuation, or 17 nm/°C if the room temperature changes by more than 0.1 °C/hour. The Plexiglas box surrounding the optics removed the high frequency beam fluctuations (> 1 Hz), leaving mean x changes of 5 nm and mean y changes of 12 nm. The relative beam spacing fluctuations are only 2 nm in x and 3 nm in y. Additional apparent beam motions due to motion of the camera itself were eliminated, reducing measured y fluctuations by an additional 13%. Long term variations in the objective/cell separation due to mechanical and thermal drift were reduced using a thermally controlled objective clamp and a cell clamp (Figure 4.18). The motion was reduced to 2 μm over 14 hours, corresponding to 25% change in the transition rate or 1 k_BT in the barrier height. This limits the window of stability to approximately 2 hours, during which the barrier changes by 0.15 k_BT or less, depending on the size of the room temperature variations.

In the next chapter the particle position $\vec{r}(t)$ is analyzed to extract the potential energy and the transition statistics. The three dimensional potential energy surface is calculated from the position distribution. The transition rate is determined from the x position as the particle crosses the barrier. Using these results the distribution of paths leading to a transition is measured for a static potential. The transition rate in a driven system is measured as a function of modulation amplitude and frequency, verifying the expected power law dependence of the activation energy on the amplitude near critical driving.

Chapter 5 Experimental Results

This chapter describes the analysis of the Brownian particle dynamics and measurements of transition rates in a bistable potential. To introduce the methods for obtaining a quantitative measure of the trapping potential, the static single beam trap is first considered. Introduction of a second beam creates a bistable potential, which depends not only on beam power but also on beam spacing. By modulating one or both of the beams a time-dependent potential barrier is created.

The calculation of the potential is described in Section 5.2. The particle position time series $\vec{r}(t)$ is transformed into a three-dimensional probability distribution from which the potential energy $U(\vec{r})$ is calculated. The gradients of the potential near its extrema (i.e., at its two minima and its single saddle point) are calculated. The behavior of the potential under modulation is obtained from direct measurement as well as from parametric representation using experimentally measured coefficients.

Analysis of over-barrier transition rates is described for static and periodically modulated potentials. Spatial and temporal distribution functions are calculated from the time series. The distribution of particle trajectories resulting from over-barrier transitions is analyzed. Consideration of the conditional probability for escape leads to visualization of the so-called prehistory distribution. This represents a measure of the "optimal path", the set of trajectories by which a particle is most likely to escape from a deep potential minimum.

When periodic modulation of the potential occurs, the transition rates are a function of modulation amplitude and frequency. The asymptotic dependence of the escape rate

as the modulation amplitude, the control parameter, approaches a critical value is measured. Using a recent theory which predicts a power law singularity as a function of the control parameter [44], we extract best estimates of critical exponents under two conditions: the slow modulation regime, where the particle can follow the potential adiabatically, and under nonadiabatic modulation.

5.1. Measurement of Particle Dynamics in Single and Two Beam Traps

The particle position $\vec{r}(t)$ is used to calculate the potential energy and transition statistics in the optical trap. Prior experiments with a particle in a single beam trap were discussed in Section 3.3. The potential energy surface for a single beam trap in this system was mapped using the method in Section 5.2. In a two beam trap the particle makes transitions over the barrier between the two stable points. The rate of transitions is calculated from the particle's x position.

The following symbols are used in this and later sections.

Symbol	Definition	Equation
x	Direction connecting stable points	
y	Direction with largest t_r^{-1}	
z	Direction of beam propagation, smallest t_r^{-1}.	
$t_{r,x}^{-1}$	Relaxation rate in the x direction (Hz)	$t_{r,x}^{-1} = \omega^2/2\pi\Gamma$
Γ	Viscous damping rate (Stokes damping)	$\Gamma = 6\pi\eta a/m$
W	Mean transition rate (Hz)	$1/\langle\tau\rangle$
$\langle\tau\rangle$	Mean dwell time (s)	$\langle\tau\rangle = \int_0^\infty \tau p(\tau) d\tau$

The data in Sections 5.1 through 5.3 as the result of closely spaced measurements conducted over a four-day period. The single beam potential is calculated from data labeled 022804-01. The double well potential labeled 101403-03 is used to show the three dimensional potential energy, transition rates, and the optimal path in Section 5.3.

It is the longest run (with little drift), containing 2×10^6 points. Data denoted as 012304-01 are used for the tilted potentials in Section 5.2. The large amplitude static tilts in Section 5.2 are labeled 021703-01. Table 5.1 lists the mean static barrier height ΔU, transition rate W_0 for the left and right wells, the x, y, and z components of the relaxation time t_r in, and the overall acquisition time per data set.

Table 5.1 Static potential parameters for data used in Sections 5.1, 5.2, and 5.3. Units: energies ΔU (k_BT), rates W_0 (Hz), relaxation times t_r (s).

Dataset Label	ΔU_{left}	ΔU_{right}	W_0 left	W_0 right	$t_{r,x}$	$t_{r,y}$	$t_{r,z}$	Time
022804-01	-	-	-	-	0.002	0.002	0.2	500 s
101403-03	3.4	2.8	2.5	4.4	0.007	0.002	0.3	2.8 hr
012304-01	5.2	5.7	0.7	0.5	0.005	0.002	0.3	500 s
021703-01	3.3	3.3	1.5	1.4	0.010	0.004	0.5	1500 s

5.1.1. Single Beam Trap

The x, y, and z positions vs. time for a particle trapped in a single beam trap are plotted in Figure 5.1. The particle center (solid lines) fluctuates in a 50 nm x 50 nm x 1μm volume around its equilibrium position (dashed lines). The position is recorded every 5 ms, or 200 times in the 1 second interval shown.

The time scale of z fluctuations is much slower than the x and y fluctuations, with larger amplitude. Prior experiments have shown the axial trapping forces (along the direction of beam propagation, z) to be more than an order of magnitude smaller than the radial (x and y) forces [49].

Figure 5.1 (right) shows the position distributions. In a harmonic potential the position distribution $P(x)$ is Gaussian with

$$P(x) = C\exp\left[-\frac{B}{2}(x-x_0)^2\right],$$

where B is the spring constant and A is a normalization constant. A least squares fit to the distributions (solid lines) agrees well with expectations. A small deviation is noted for z fluctuations in the tails of the distributions.

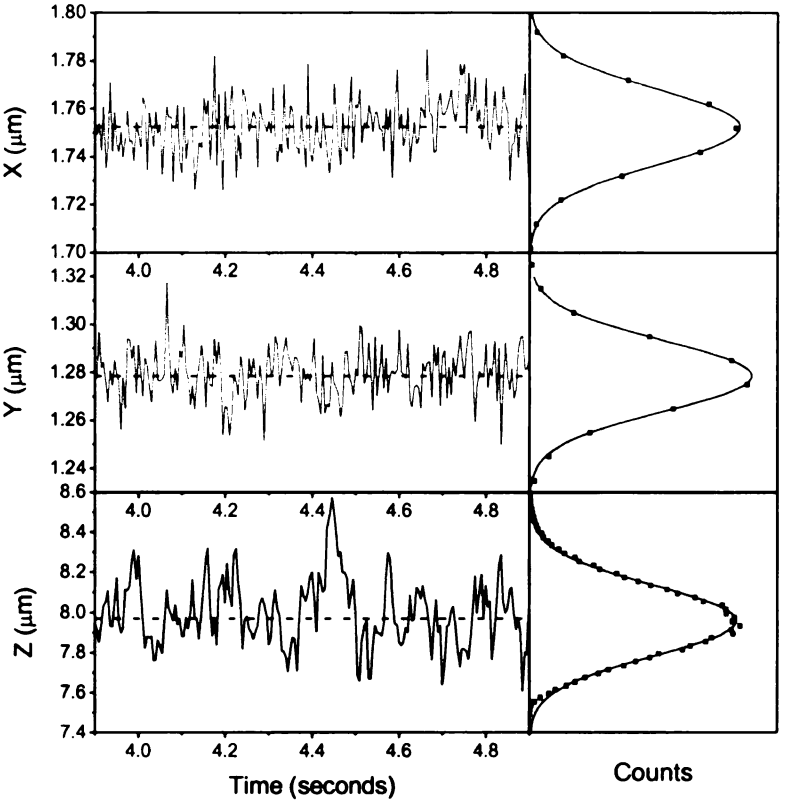

Figure 5.1 Time series and position distributions for a single-beam trap. The x, y, and z position data are plotted as a function of time at 5 ms intervals for 1 second. The plot ranges are 100 nm for x and y and 1.2 μm for z, with arbitrary position offset. The dashed lines indicate the position of the trap center. The position distributions from the full 500 second data set are plotted to the right of the time series. Gaussian fits to each distribution show deviation from the harmonic approximation. (Data labeled 022804-01, 100,000 frames. Standard deviations of Gaussian fits σ_x = 16 nm, σ_y = 15 nm, σ_z = 175 nm.)

The potential energy $U(\bar{r})$ is calculated from the position distribution (Section 5.2). Energy contours, corresponding to a cross-section (slice) through the stable point of the single beam trap are plotted in Figure 5.2. The potential is nearly ellipsoidal, with its

major axis along the axial (z) direction. The potential is also skewed in the direction of beam propagation. This is the result of the scattering force (F_{scat} in Section 3.1.2), which decreases as the particle moves away from the beam waist, breaking the z symmetry.

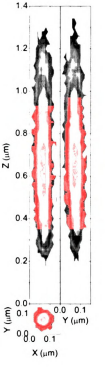

Figure 5.2 Single beam potential energy slices. The potential energy of each volume element is plotted for the xz, yz, and xy planes running through the trap center. Contours indicate energy steps of 1 k_BT. The beam propagates in the +z direction. (Data labeled 022804-01, 100,000 frames, histogram bin size = 0.01 μm in x and y, 0.02 μm in z.)

The curvature near the minimum is obtained from a least squares fit of a quadratic function (solid line in Figure 5.3) to the one dimensional profiles extracted from the three dimensional potential energy (see Section 5.2). (The energy offsets are arbitrary normalization.) The curvatures ω are listed in Table 5.2. For a harmonic oscillator, the spring constant $k = m\omega^2$. The spring constants for a 0.6 μm diameter silica sphere

($m = 2.3\times10^{-16}$ kg) are listed in Table 5.2. The radial spring constants in this experiment are an order of magnitude smaller than those measured by Ghislain [49] owing to lower beam power (7 mW here vs. 150 mW), different sphere diameters ($2a$ = 0.6 μm vs. 1 μm), and different optics. The axial spring constant is 100 times weaker than the radial spring constant. The relaxation rate of the overdamped particle near the potential minimum is given by $t_r^{-1} = \omega^2/2\pi\Gamma$, where $\Gamma = 6\pi\eta a/m = 2.5\times10^7\,\mathrm{s}^{-1}$ in water with viscosity η = 0.001 kg/m s.

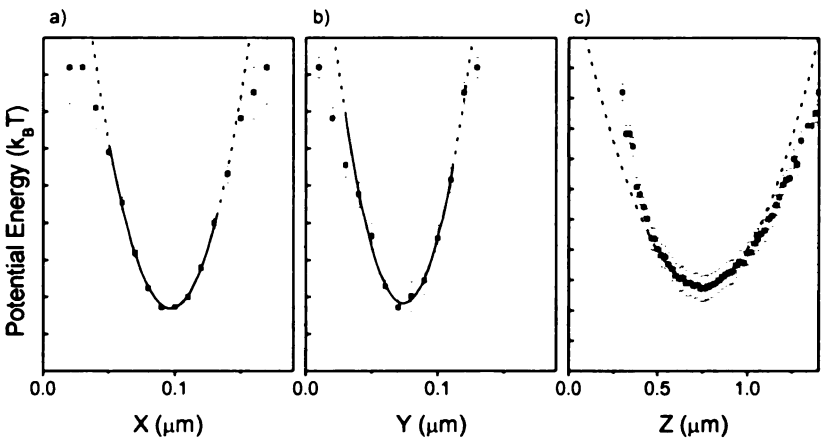

Figure 5.3 One dimensional potential energy profiles of a single beam trap. The (a) x, (b) y, and (c) z profiles centered on the potential minimum are plotted vs. position. Quadratic fits at the minimum (solid lines) are extrapolations (dashed lines). The potential energy tick marks: 1 k_BT steps. The harmonic approximation is valid to 3 k_BT from the minimum. (Data labeled 022804-01, 100,000 frames. Fit function $U(q) = U_0 + B_q/2(q-q_0)^2$ (q = x, y, z) with B_x = 4100 k_BT/μm^2, B_y = 4400 k_BT/μm^2, B_z = 42 k_BT/μm^2.)

Table 5.2 Single beam oscillation frequencies and damping rates.

i	ω_i (s^{-1})	$t_{r,i}^{-1}$ (Hz)	k_i (N/m)
X	270000	470	1.7×10^{-5}
Y	280000	490	1.8×10^{-5}
Z	27000	4.7	1.7×10^{-7}

5.1.2. Two Beam Trap

The introduction of a second beam breaks radial symmetry, softening the trap along the line separating beam centers (defined as the x direction). For 0.5 μm spacing and about 10 mW in each beam, the system is bistable with a barrier height that depends on beam separation and relative power. Figure 5.4 shows the x profile as the power in the left beam P_l varies from 5.5 mW to 7.0 mW with the right beam at 7.3 mW. As a

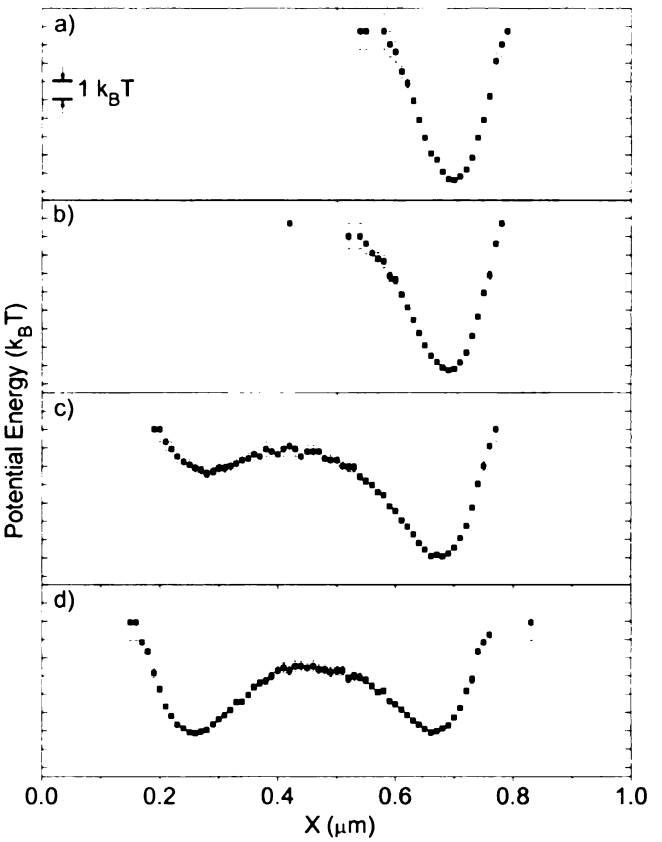

Figure 5.4 X profile with varying beam power for a two beam trap. (a) for low left beam power the particle is confined to the right beam. (b) as power increases the right well curvature decreases and tilts towards the left beam. A second stable point forms with a small barrier in (c). The potential nears symmetry about x = 0.46 μm (d). (Data labeled 022804-03, right beam power 7.3 mW, left beam powers (a) 5.5 mW, (b) 6.1 mW, (c) 6.7 mW, (d) 7.0 mW.)

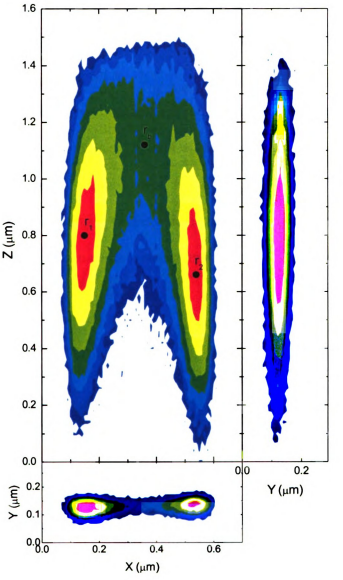

Figure 5.5 Three dimensional potential energy slices for a two-beam trap. The potential energy of the volume elements are plotted for the xz (y = 0.13 μm), yz (x = 0.16 μm), and xy (z = 0.78 μm) planes through the left stable point. The contours represent 1 k_BT energy steps with local minima at the stable points. The particle fluctuates around the stable point r_1. As it moves in x to make a transition it also moves up, in the direction of beam propagation +z through r_b to the stable point r_2. (Data labeled 101403-03, 2,000,000 frames, 16280 transitions.)

second stable point forms, the curvature of the right stable point decreases. At P_1 = 7.0 mW the potential is symmetric about the line connecting the two minima. (The beam powers for a symmetric potential may be slightly different owing to small differences in the optical alignment.)

Three dimensional energy contours for slices through two stable points are plotted in Figure 5.5. The two stable points r_1 and r_2 define the direction x. The top of the barrier is the saddle point r_b; unstable in x, but stable in y and z. The scattering force breaks the z symmetry, creating a single saddle point displaced from the focal plane in the +z direction. Therefore the particle makes transitions it moves out of the objective's focal plane in addition to moving along x.

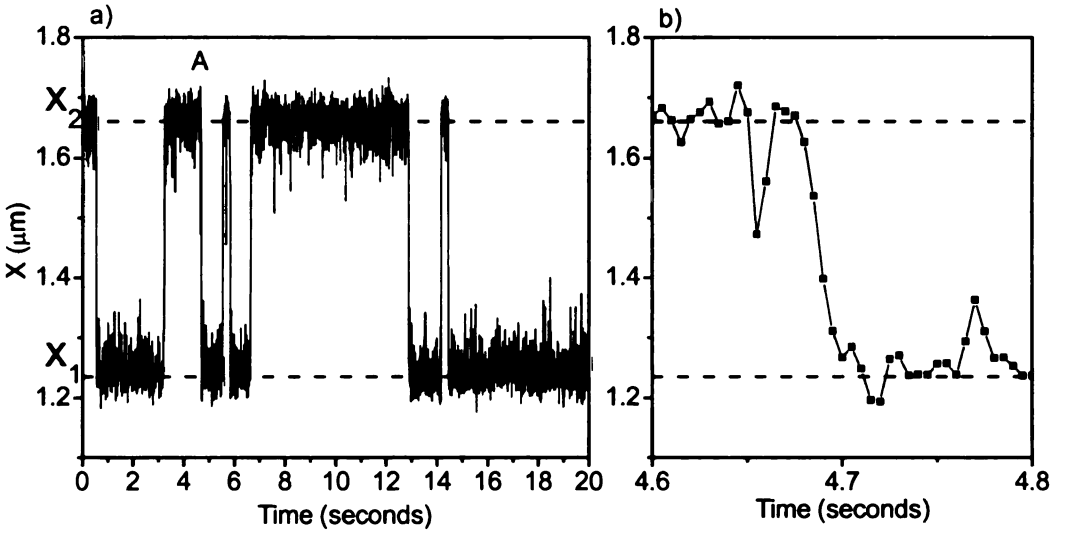

Figure 5.6 Dynamics of over-barrier transitions in a bistable potential. The particle undergoes small fluctuations near a stable point (dashed lines) x_1 and x_2; occationally a large fluctuation pushes it over the barrier. (a) shows the particle's position as it makes multiple transitions. (b) shows the x positions during the transition marked A, where the symbols represent the positions measured at 5 ms intervals. (Data 012304-01-01, 100,000 frames. Mean transition rate W = 0.5 Hz.)

The time trace in Figure 5.6 shows the x coordinate as the particle makes transitions between the stable points in a symmetric potential. The particle fluctuates about a stable point until a large fluctuation drives it over the barrier. The transition duration is 5 to 15 ms.

5.1.3. Determination of Transition Rates

Transition Criteria

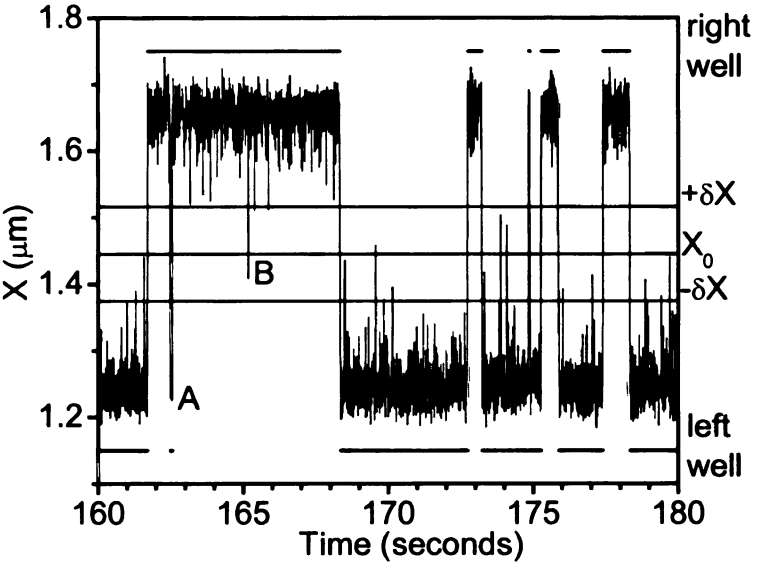

Figure 5.7 Determination of transition events. The x position vs. time is plotted, with lines indicating the barrier top (X_0) and the half-widths ($\pm\delta X$). The "current" well is indicated by the line above and below the data, with length equal to the dwell time τ. The particle makes a transition when it crosses the midpoint then the half-width on the other side (event labeled A). A particle crossing only the midpoint is not counted as a transition (event labeled B). (Data labeled 012304-01-01)

A transition is herein identified as an event in which the particle crosses the saddle point by a distance δX (Figure 5.7). The reason for incorporating δX into the definition is the following. At the saddle point the force exerted by the potential vanishes and the particle undergoes free diffusion in x. It is possible that the particle could cross

the midpoint several times without entering the region of attraction of either stable point. Since these diffusive transitions should not be counted, the constraint that the particle must pass a line on the other side of the barrier (half-width) before a transition is recorded.

The midpoint is taken at the top of the barrier. The half-width δX is set to one pixel (0.071 μm), around 40% of the distance from the midpoint to the stable point, close to the inflection point of the potential along x. To assess the sensitivity to δX, Figure 5.8a shows that the transition rate (calculated below) changes by less than 5% for δX between 0.071 μm and 0.2 μm. If the choice of midpoint is displaced by 0.02 μm (two histogram bins) in either direction (Figure 5.8b) the rate changes by less than 2%. The same half-width and midpoint positions are used for all data recorded in the same set.

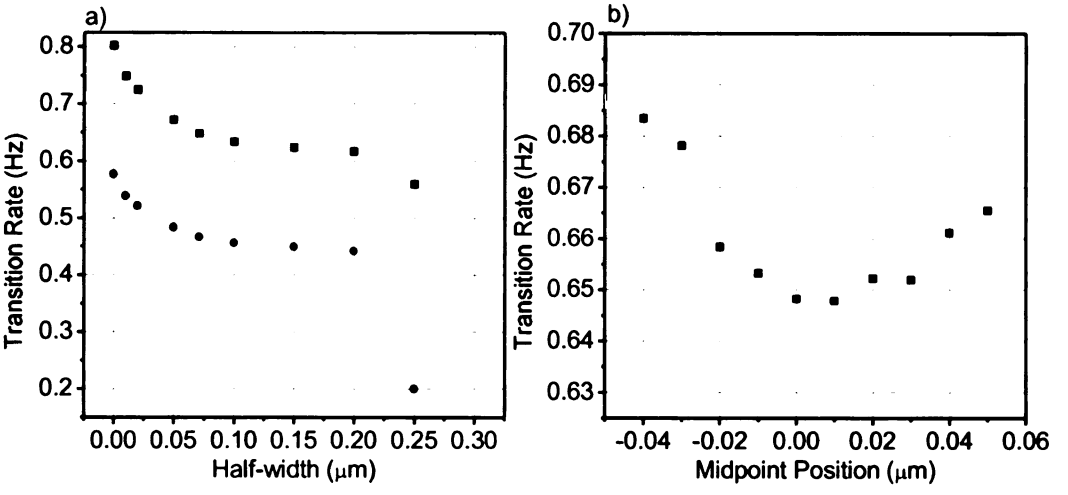

Figure 5.8 Sensitivity of transition rate to changes in half-width δX and midpoint X_0. (a) transition rate (W = (number of transitions)/(total dwell time)) for differed half-widths. The region between 0.071 μm and 0.20 μm is insensitive to δX, changing by less than 5%. In (b) the transition rate varies by 2% for changes in midpoint position of ±0.02 μm from the saddle point. (Data labeled 012304-01-01, 5.5 k_BT barrier, saddle point to stable point spacing = 0.21 μm.)

Transition Rate in the Bistable Potential

The left well dwell time is defined as the time interval between a particle crossing the line at -δX from the right to the time it crosses +δX. The transition analysis calculates the dwell time τ for left-to-right and right-to-left transitions. The mean transition rate is calculated from the normalized dwell time probability distribution $p(\tau)$. In equilibrium, it is assumed that the particle has equal probability to escape at any time, so that $p(\tau) = \lambda \exp(-\lambda\tau)$, with mean transition rate λ. The dwell time distribution (Figure 5.9) for the potential in Figure 5.5 shows that this is not necessarily the case. The first 10 ms wide bin shows a dip, which corresponds to the finite x relaxation time (150 Hz). (This was also seen in earlier experiments [30].) This occurs because the particle must relax to the bottom of the well at a rate $t_{r,x}^{-1}$ before making another transition. The data also indicates deviation from the exponential behavior at times below 0.1 s. This may appear in deviation from a white noise spectrum at frequencies from 10 to 100 Hz. At long dwell times, the distribution decays exponentially, shown by the solid line in Figure 5.9.

The mean dwell time is defined by $\langle\tau\rangle = \int_0^\infty \tau p(\tau) d\tau$. For the discrete distribution of dwell times t_i the mean dwell time is calculated by computing the average value $\langle\tau\rangle = \frac{\sum \tau_i}{N} = W^{-1}$, where W is the mean transition rate. The dwell times for the left and right wells are recorded separately, leading to W_L and W_R, the left-to-right transition rate and right-to-left transition rates.

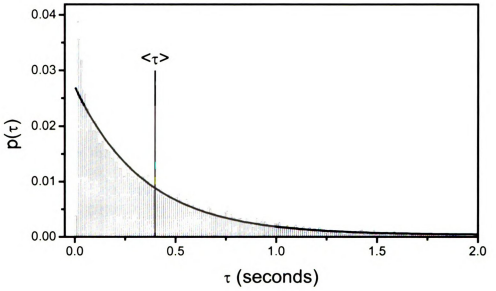

Figure 5.9 Dwell time distribution for a static potential. The solid line is an exponential fit to the dwell times. The vertical line represents the value of the mean dwell time. Inverse dwell time $1/\langle\tau\rangle$ = 2.48 Hz, exponential decay rate λ = 2.89 Hz. (Data labeled 101403-03, 2,000,000 frames, 16280 transitions, Bin size 2 frames (10 ms).)

5.2. Double-well Potential Calculation

The following symbols are used in this section.

Symbol	Definition	Equation
$P(x,y,z)$	Particle position distribution. A discrete 3D histogram of particle positions	
$U(x,y,z)$	Potential energy distribution, calculated from $P(x,y,z)$.	$U(x,y,z) = -k_B T \ln\left(\frac{P(x,y,z)}{P_0}\right)$
x_i	x position of left stable point (i = 1), right stable point (i = 2), or saddle point (i = b), measured from local fits.	
U_i	Potential energy at left stable point (i = 1), right stable point (i = 2), or saddle point (i = b), measured from local fits.	
ΔU	Barrier height	$\Delta U = U_b - U_{1,2}$
ω	Eigenfrequency (curvature) of $U(x,y,z)$	

Symbol	Definition	Equation
A_0	Potential Tilt. Linear term in quartic approximation of x potential energy.	
A_b	Bifurcation amplitude. Tilt A_0 at which the stable and unstable states merge, calculated from the quartic approx.	$A_b = \frac{2\lvert B\rvert^{3/2}}{3\sqrt{3C}}$

5.2.1. Extraction of the Potential and Potential Surfaces

A particle in thermal equilibrium, measured on time scales longer than the mean interwell transition time, has a Boltzmann position distribution. The distribution is inverted to create a discrete map of the potential energy in three dimensions. The position probability distribution is given by

$$\frac{P(x,y,z)}{P_0} = \frac{1}{Z}\exp\left[\frac{-U(x,y,z)}{k_B T}\right],$$

where P_0 is the total number of positions in the data set and Z is a normalization constant. The three dimensional position distribution $P(x,y,z)$ is computed from the position data. The coordinate space is separated into discrete volume elements $\Delta V = \Delta x \Delta y \Delta z$. $P(x,y,z)$ is the number of positions in each volume element

$$P(x,y,z) = \sum_{\text{frames}} \begin{cases} 1 & (x < x(t) < x + \Delta x), (y < y(t) < y + \Delta y), (z < z(t) < z + \Delta z) \\ 0 & \text{otherwise} \end{cases}.$$

The potential energy $U(x,y,z)$ is

$$U(x,y,z) = -k_B T \ln\left(\frac{P(x,y,z)}{P_0}\right) + k_B T \ln(Z).$$

The normalization constant Z is ignored, creating an energy offset that changes depending on the shape of the potential. Figure 5.5 shows slices through $U(x,y,z)$, centered on the left stable point.

The one dimensional potential profiles are extracted from $P(x,y,z)$. The x profile is extracted for the entire width of the potential. The maximum $P(x,y,z)$ (corresponding to the minimum $U(x,y,z)$) in each yz plane is found. The diamonds in Figure 5.10 follow the path of maximum $P(x,y,z)$ through the xz plane shown in Figure 5.5. The potential is

$$U(x) = -k_B T \ln\left(\frac{\max[P(x,y,z)]}{P_0}\right).$$

The y and z profiles are calculated at the stable and saddle points only. The y profile is calculated for constant x_s and z_s, the x and z positions of the stable or saddle point. $U(z)$ is calculated for constant x_s and y_s (squares in Figure 5.10),

$$U(y) = -k_B T \ln\left(\frac{P(x_s,y,z_s)}{P_0}\right) \text{ and } U(z) = -k_B T \ln\left(\frac{P(x_s,y_s,z)}{P_0}\right).$$

If the saddle point is sparsely populated (due to low mean transition rate or short acquisition time) the potential is also spatially averaged. This increases the size of the volume elements without changing the spacing. In the *Profiles* data analysis program (Appendix E) this is controlled with the *rebin* number. If rebin = 0 there is no averaging. For nonzero rebin the position distribution is summed over an area perpendicular to the profile direction. For example, when averaging in the x profile calculation the path of minimum energy is found from the maximum sum, where

$$P_s(x) = \max\left[\sum_{n=-\text{rebin}}^{n=\text{rebin}} \sum_{m=-\text{rebin}}^{m=\text{rebin}} P(x, y+n\Delta y, z+m\Delta z)\right].$$

The potential energy is calculated from P_s,

$$U_{\text{ave}}(x) = -k_B T \ln\left(\frac{P_x(x)}{P_0 \times (2 \times \text{rebin} + 1)^2}\right).$$

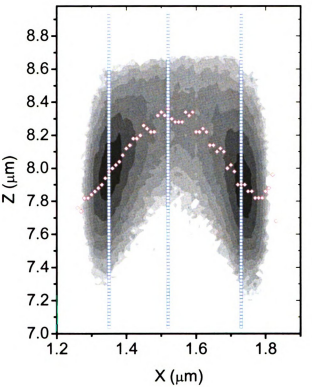

Figure 5.10 Calculation of one dimensional profiles from the three dimensional histogram. Contours represent potential energy in a single xz plane, where darker areas have lower energy. The diamonds follow the path for calculation of the x profile. The squares follow the paths for calculation of the stable point and saddle point z profiles. The x and z axes begin with an arbitrary offset. (Data labeled 101403-03, 2,000,000 points, x bin size = 0.01 μm, z bin size = 0.02 μm.)

5.2.2. Parameterization of the Potential

Local and global approximations to the one dimensional profiles are used to parameterize the full three dimensional potential. The curvature of the potential is estimated for small displacements from the stable points and saddle point and the x barrier height calculated. The tilt A_0 of the potential due to changing beam power is

estimated from the full x profile for multiple static, tilted systems. This process was adopted since direct measurement of the potential for very large tilts takes prohibitively long times.

Quadratic Fits to Stable Points and Saddle Point

Each one dimensional profile is plotted with error bars (Figure 5.11) using OriginLab's Origin 7.0 graphing and analysis software (with three plots of the x profile). The quadratic function

$$(5.1) \quad U(q) = C_1 + \frac{C_2}{2}(q - q_0)^2 ,$$

is fit to the stable points and saddle point, with coordinate $q = x$, y, or z. C_1 equals the potential offset U_0, q_0 is the position of the minimum, and $C_2 = m\omega^2$ in the harmonic approximation. The fit is weighted by $1/\sigma^2$ (instrumental weighting), where $\sigma = \delta U$. The uncertainty δU is calculated from the number of counts in the volume element, assuming Poisson statistics in the number of counts P ($\delta P = \sqrt{P}$).

$$\delta U = \delta\left(\ln\left(\frac{P}{P_0}\right)\right) = \frac{P_0}{P}\frac{\delta P}{P_0} = \frac{\delta P}{P} = \frac{1}{\sqrt{P}}$$

The number of points fit with (5.1) varies depending on the potential and the size of the volume elements. Typically 9 points are fit in the y profiles, 9 points at the stable points of the x profile, 20 points in the z profiles, and 25 points at the barrier in the x profile. The fit range is centered at the minimum. Figure 5.11 shows the results of these fits (solid lines), plotted with the profiles. The dashed lines represent the extrapolations of the fits, showing the deviation from the harmonic approximation.

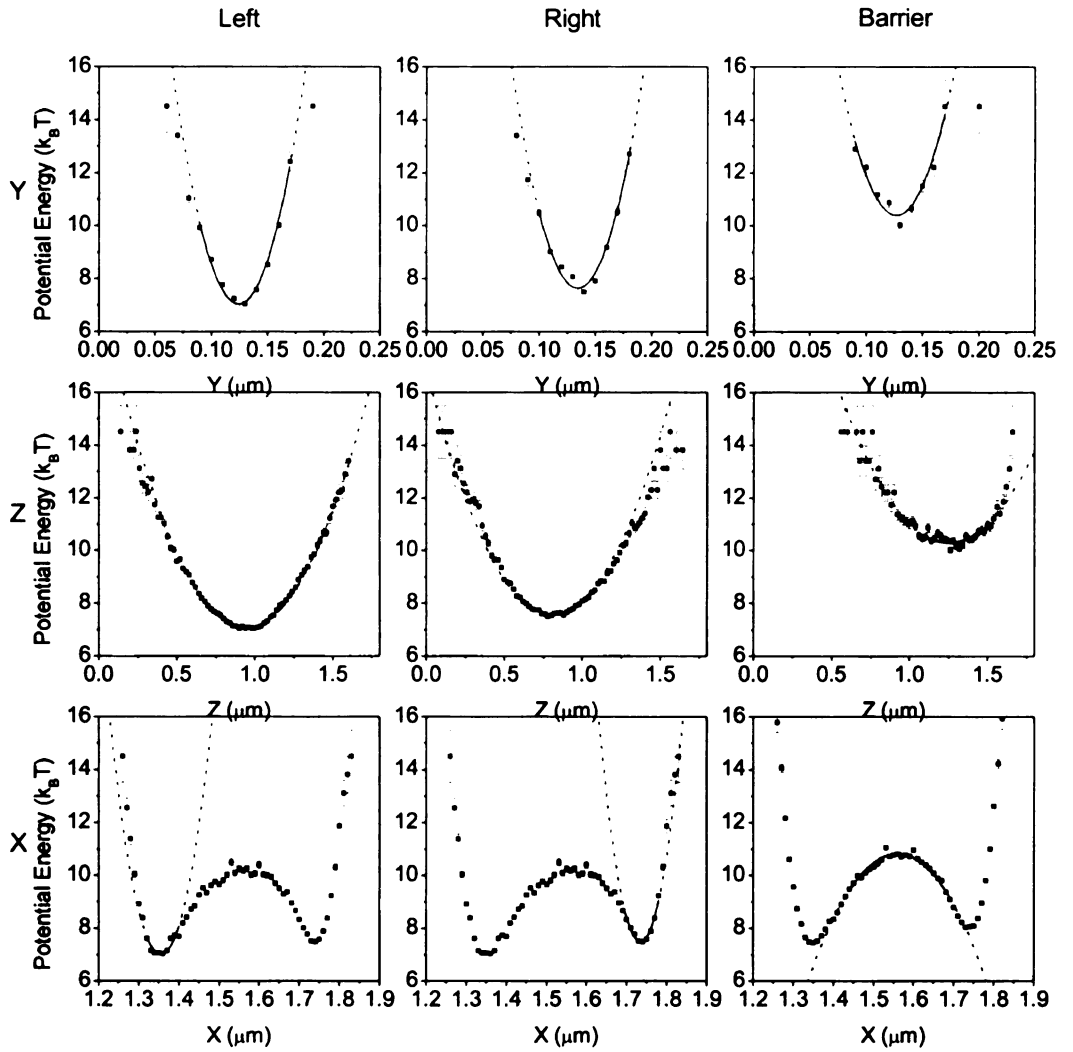

Figure 5.11 One dimensional profiles with quadratic fits. The y, z, and x profiles (rows) for the left well, right well, and barrier (columns) are plotted with error bars $1/\sqrt{\text{counts}}$. The results of the quadratic fits (solid lines) are extrapolated to the extents of each plot (dotted lines). (Data labeled 101403-03, 2,000,000 points, x and y bin size = 0.01 μm, z bin size = 0.02 μm, rebin = 0 except for x barrier where rebin = 2.)

Results of the fits in Figure 5.11 are displayed in Table 5.3. The conversion factor between fit parameter C_2 (units $k_BT/\mu m^2$) and the curvature (s^{-1}) is $\omega^2 = 1.77\times10^7 C_2$ at room temperature (293 K) for a 0.6 μm diameter silica particle with mass $m = 2.3\times10^{-16}$ kg. The $t_{r,z}^{-1}$ (3 – 4 Hz) is 40 times smaller than $t_{r,x}^{-1}$ (100 – 150 Hz),

and more than 100 times smaller than $t_{r,y}^{-1}$ (500 Hz). The y and z relaxation rates differ by about 20% between the stable points and saddle point.

Table 5.3 Double-well parameters from quadratic fits to one dimensional profiles.

	ω (s^{-1})	t_r^{-1} (Hz)	U_0 (k_BT)	x_0 (μm)
X left well	140000	125	7.0	1.36
X right well	160000	175	7.5	1.74
X barrier	59000	-22	10.8	1.56
Y left well	300000	570	7.0	0.125
Y right well	290000	540	7.6	0.125
Y barrier	270000	460	10.4	0.127
Z left well	23000	3.4	7.1	0.947
Z right well	22000	3.1	7.6	0.810
Z barrier	20000	2.5	10.3	1.26

The barrier height $\Delta U_{L,R}$ is calculated from differences in potential offset U_0 for the x barrier and stable point fits. Averaging the position distribution (nonzero rebin value) changes the constant C_1 in equation (5.1). Therefore only the U_0 values for the same rebin number are used. Table 5.4 shows the measured potential offset and calculated ΔU for rebin 0 (no averaging), 1, and 2. The barrier height varies by 3% for the different averages. Since the barrier often has very few points, the U_0 value for rebin = 2 is used. For the data in Figure 5.11 the barrier heights are $\Delta U_{left} = 3.39\ k_BT$ and $\Delta U_{right} = 2.78\ k_BT$.

Table 5.4 Barrier height measurement results with spatial averaging.

	rebin = 0	rebin = 1	rebin = 2
U_0 barrier	10.25	10.58	10.82
U_0 left	7.00	7.18	7.43
ΔU left	**3.25**	**3.40**	**3.39**
U_0 right	7.49	7.76	8.04
ΔU right	**2.76**	**2.82**	**2.78**

Estimation of Potential Changes Under Modulation

Instead of measuring the changes in each volume element for each beam power, the tilt is described by a single parameter A_0. The full three dimensional potential is approximated to fourth power in x,

$$U_{3D}(x,y,z) = A_0 x + \frac{B_x}{2}x^2 + \frac{C}{4}x^4 + \frac{B_y}{2}y^2 + \frac{B_z}{2}z^2 + C_{xz}x^2 z\,.$$

The y and z curvatures B_y and B_z depend on the overall beam power. The 10% power changes used in tilt experiments cause only small changes in curvature B_y and B_z compared to B_x. The cross term C_{xz} depends on the positions of the stable points and thus changes only with beam separation. Therefore the tilt A_0 is calculated from the x profile only, using

$$(5.2)\quad U(x,y,z) = A_0(x-x_0) + \frac{B}{2}(x-x_0)^2 + \frac{C}{4}(x-x_0)^4 + U_0$$

The coefficients A_0, B, C, x_0, and U_0 in equation (5.2) are calculated using a three point fit to the x potential profile. Figure 5.12 shows the results of two methods of parameterizing the potential. The solid lines are created from matching $U(x)$ and $\partial U/\partial x\big|_{x=x_i} = 0$ to the local fit results. This ensures that the quartic potential follows the positions of the barrier and stable point as they merge at large tilts. The dashed lines are the results of least squares fits with instrumental weighting. The weighting causes the fit to match the shape of the lowest energy points and overestimates the barrier by more than 2 k_BT in Figure 5.12c. The transition rate dependence at large modulation amplitudes depends on the potential when the barrier is low, therefore the three point fit is used.

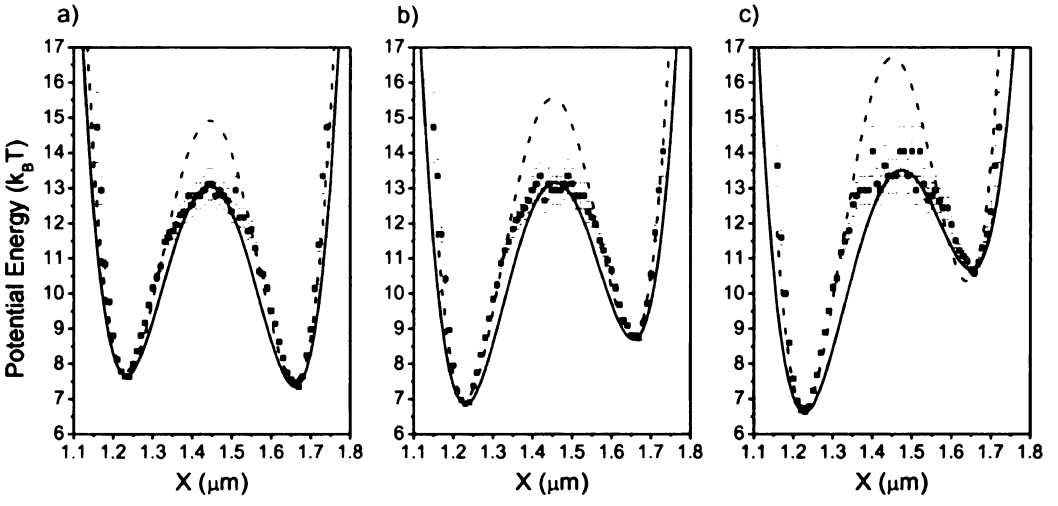

Figure 5.12 Quartic fits to tilted x profiles. The x profiles for increasing beam power (squares) are approximated using three point fits (solid lines) or a least squares fit to the entire potential (dashed lines). (Data labeled (a) 012304-01-01, (b) 012304-01-02, (c) 012304-01-03, 100,000 points. Static tilt amplitudes (a) –0.9 k_BT/μm, (b) 4.3 k_BT/μm, and (c) 9.6 k_BT/μm.)

The quartic parameters are calculated from the system of equations

$$U(x_1)=U_1,\quad U(x_2)=U_2,\quad U(x_b)=U_b,\quad \frac{\partial U}{\partial x}(x_1)=0,\quad \frac{\partial U}{\partial x}(x_2)=0,$$

using $U(x)$ in equation (5.2). The positions of the left well x_1, the right well x_2, and the barrier x_b, and the potential energy at the left well U_1, right well U_2, and barrier U_b are obtained with local quadratic fits. The quartic is constrained to have potential energy U_b at the point x_b but has an unconstrained spatial derivative, allowing freedom in the position of the barrier top. Solving for the parameters,

$$C=\frac{4\left(U_b(x_1-x_2)^3-U_1(3x_1-x_2-2x_b)(x_2-x_b)^2-U_2(x_1-x_b)^2(x_1-3x_2+2x_b)^2\right)}{(x_1-x_2)^3(x_1-x_b)^2(x_2-x_b)^2},$$

$$x_0=\frac{4U_1-4U_2+C(x_1-x_2)^3(x_1+x_2)}{2C(x_1-x_2)^3},$$

$$B = \frac{4U_1 - 4U_2 - C(x_1 - x_2)^2\left(6x_0^2 + x_1^2 + 2x_1x_2 + 3x_2^2 - 4x_0(x_1 + 2x_2)\right)}{2(x_1 - x_2)^2},$$

$$A_0 = \frac{4U_1 - 4U_2 + (2x_0 - x_1 - x_2)(x_1 - x_2)\left(2B + C\left(2x_0^2 + x_1^2 + x_2^2 - 2x_0(x_1 + x_2)\right)\right)}{4(x_1 - x_2)}, \text{ and}$$

$$U_0 = U_1 - A_0(x_1 - x_0) - \frac{B}{2}(x_1 - x_0)^2 - \frac{C}{4}(x_1 - x_0)^4.$$

The results from the static tilt measurements in Figure 5.12 are listed in Table 5.5. The uncertainties are estimated by varying the positions and potentials from the local fits by the fit error (δx = 2 nm, δU = 0.1 k_BT) and calculating the change in the parameters.

Table 5.5 Results of 3 point quartic fit to static tilt potentials in Figure 5.12. B and C are weakly dependent on the tilt amplitude A_0.

	A_0 (k_BT/μm)	B (k_BT/μm^2)	C (k_BT/μm^4)	x_0 (μm)	U_0 (k_BT)
Figure 5.12a	-0.9 ± 0.5	-490 ± 20	10700 ± 500	1.446 ± 0.002	13.0 ± 0.1
Figure 5.12b	4.3 ± 0.5	-480 ± 20	10600 ± 500	1.446 ± 0.002	13.2 ± 0.1
Figure 5.12c	9.6 ± 0.5	-430 ± 20	9700 ± 500	1.446 ± 0.002	13.5 ± 0.1

For increasing tilts the stable and unstable points approach, eventually merging when A_0 equals the bifurcation amplitude A_b. The extrema are the positions that satisfy $\partial U(x)/\partial x = 0$. Solving equation (5.2) for A_0 when $x_b = x_i$ yields $A_b = 2|B|^{3/2}/3\sqrt{3C}$. For the values in row 1 of Table 5.5, A_b = 38 ± 3 k_BT/μm.

A_0 vs. Beam Power Calibration, Large Two Beam Tilts

The relationship between beam power and A_0 is found from several static potentials with differing nonzero tilts. The powers in both beams were changed with equal magnitudes but opposite direction using the SRS DS345 function generator's offset voltage V. The positions and potential energies of the extrema were obtained using local

fits and the quartic parameters calculated. The resulting calibration, A_0 vs. offset voltage, is plotted in Figure 5.13a, along with potential well parameters dependent on tilt.

These two-beam measurements were made with the modified trapping system (see Appendix C). The LS-100 beam power stabilizer was replaced with another LS-PRO, controlled using the offset voltage from the DS345 function generator. The power vs. offset voltage calibration was linear, but with slope and intercept different from the calibrations for the other experiments in this chapter. The beam power was 7.5 mW. The potential was tilted by changing power in both beams in opposite directions, as opposed to the single beam modulation in Section 5.4.

Figure 5.13a shows that A_0 is linear with beam power from the three point fit for tilts up 17 k_BT/μm. The bifurcation amplitude calculated from parameters B and C obtained for $A_0 = 0$ is $A_b = 21 \pm 2$ k_BT/μm. (This potential has a lower barrier than the potentials listed in Table 5.5, requiring a smaller A_b to make the barrier disappear.) A_0 changes linearly with offset voltage up to 80% of A_b. $A_0 = a_1V + b_1$ (and $A_0 = a_2P + b_2$) where a_1 = -580 ± 20 k_BT/μm V and b_1 = 280 ± 4 k_BT/μm. The $A_0 = 0$ voltage was 0.470 V and $A = A_b$ when V changes by 0.036 V.

Figure 5.13b shows the positions x_1, x_2, and x_b obtained from the local quadratic fits. These show qualitatively that the stable and unstable points approach at large A_0. Poor statistics in the shallow stable point cause large uncertainties in both the stable point and barrier positions, preventing a quantitative examination of $x_1(A_0)$ and $x_b(A_0)$.

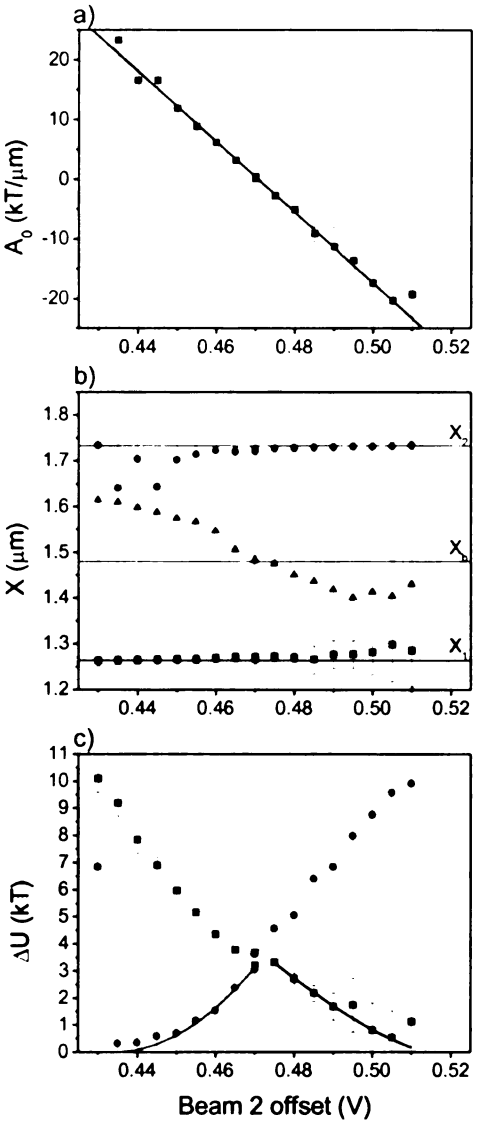

Figure 5.13 Measurement of tilted potential up to $A = A_b$. (a) the tilt parameter A_0 varies linearly with offset voltage (and beam power) up to ± 17 $k_BT/\mu m$ (A_b = 21 $k_BT/\mu m$), with slope m = -590 ± 10 $k_BT/\mu m$ V. (b) the positions of the left well (squares) and right well (circle) approach the barrier position (triangles) for large tilt amplitudes. At large amplitude the barrier height decreases, reducing the statistics and leading to poor local fits. (c) the barrier height vs. voltage for the left well (squares) and right well (circles). A power law fit to the right barrier height gives an exponent 1.9 ± 0.2 for A_b set to 0.435 V and the left barrier gives 1.4 ± 0.3 for A_b = 0.515 V. (Data labeled 021703-01-, 100,000 to 300,000 points.)

For a metastable potential near the bifurcation point the barrier height varies as $(A_b - A)^{3/2}$ [91]. The barrier height obtained from the quadratic fits at the stable point and minimum are plotted in Figure 5.13c. The barrier height $\Delta U(A_0) = U(x_b(A_0)) - U(x_2(A_0))$ was fit with $\Delta U(V) = \varepsilon(V_b - V)^{\nu}$ for $\Delta U < 3\ k_B T$ (solid lines). For the left barrier (squares) the bifurcation offset voltage V_b was set V_b = 0.515 V, fitting for ε and ν. The exponent $\nu = 1.4 \pm 0.3$ agreeing with the prediction. The right barrier (circles), with V_b = 0.435 V returned $\nu = 1.9 \pm 0.2$, two standard deviations from the expected ν = 1.5. Since the uncertainty is greater near the bifurcation point the fit puts greater weight on the higher barrier points, on the edge of the range of validity in the 3/2 power law approximation.

At large A_0 the particle spends less time in the shallow well. The only way to reduce the uncertainty in the potential energy is to record for longer periods. The 20 data sets in Figure 5.13 were collected over 5 hours, beyond the expected interval of stability of the system (The stability was checked by returning to V = 0.470 V and measuring the potential. The values of A_0, x_i, and U_i in Figure 5.13 changed by < 10%.) Since A_0 is linear with beam power, the calibration for potentials with small tilts is extrapolated to $A = A_b$.

A_0 vs. Beam Power Calibration, Small Single Beam Tilts

With the system in the configuration described in Chapter 4, the potential was tilted over a small range ($A_0 < A_b/4$) and the A_0 vs. V extrapolated to $A = A_b$. The beam power in a single beam only was changed by a small amount, corresponding to a change of 0.5 – 1 $k_B T$ in barrier height. The beam power was controlled by the DS345 function

generator offset voltage sent to the LS-100 stabilizer, (see Section 4.1). The beam power P is linear with offset voltage V, $A_0 = a_1 V + b_1$.

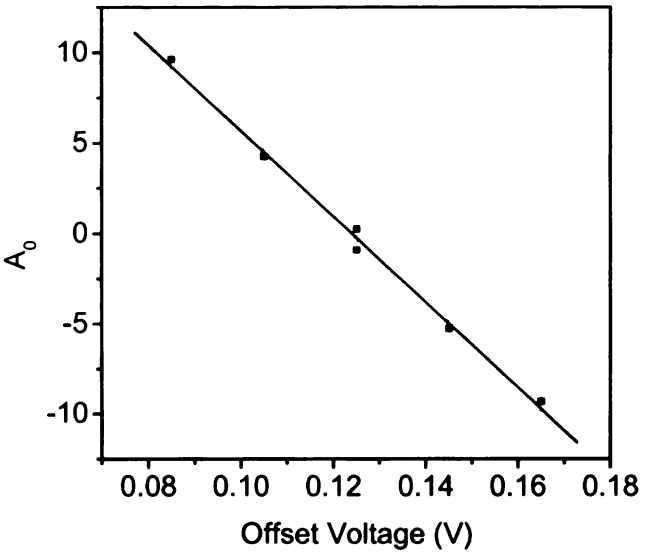

Figure 5.14 A_0 vs. offset voltage. Tilt A_0 is calculated from the 3 point quartic fit for varying beam power (in terms of offset voltage), with linear regression fit. Slope is –240 ± 10 k_BT/μm V, with offset 29 ± 1 k_BT/μm. (Data labeled 012304-01-01 through 012304-01-06, 100,000 points each.)

The slope shown in Figure 5.14 was recorded using beam powers of 7.63 mW in beam 1 and 7.26 mW in beam 2. Beam 1 power was adjusted in 0.125 mW steps over five points (two points above $A_0 = 0$, two below). The potentials were parameterized and the slope of the tilt vs. offset voltage curve is -240 ± 10 k_BT/μm V. The bifurcation amplitude is A_b = 38 k_BT/μm. This corresponds to a tilt modulation of 2 mW peak-to-peak in each beam, or an amplitude that is 13% of the DC power.

These results suggest that the x profile of the three dimensional potential changes with a variation in beam power as the quartic expression (5.2) does to a change in the linear coefficient A_0. The results in Figure 5.13 are for an antisymmetric tilt as both beam

powers were changed in opposite directions. In the modulation experiments studied in Section 5.4 only one beam is modulated.

However, it is argued that, if the potential is deep enough (relative to an untrapped, freely diffusing particle) a change in the depth of a single well is equivalent to an antisymmetric change in both wells i.e., the potential barrier is a perturbation of the overall potential well. For example, if the stable points have energy $-20\ k_BT$ relative to a free particle, the potential with an additional $2\ k_BT$ in the left well will have approximately the same shape as a potential with $+\alpha\ k_BT$ in the left well and $-\alpha\ k_BT$ in the right (where α is less than 1).

To estimate the depth of the potential, we note that a single particle is typically trapped for days or weeks. Assuming the mean rate is 1 escape/day (1×10^{-5} Hz) and comparing to the interwell escape rate of 0.2 Hz for $\Delta U = 6\ k_BT$, the "potential depth"

$$U_{\text{pot}} = \Delta U + k_BT \ln\left(\frac{0.2}{1\times10^{-5}}\right) = 16\ k_BT.$$

5.3. *Determination of Optimal Particle Trajectories*

In this section, consideration is given to analysis of the actual trajectories followed by a particle in an over-barrier transition. The most probable particle trajectory during a transition is calculated from the prehistory distribution. The particle spends most of the time near one of the stable points. Eventually a large fluctuation will drive the particle over the barrier into the other well. These fluctuations are rare, and the probability of making a transition sharply peaked around the most probable fluctuation that moves the particle to a point on the other side of the barrier. The corresponding particle trajectory is called the *optimal path* [2]. The optimal path is measured from $\vec{r}(t)$

by considering all of the trajectories starting in one well that end up in a certain region on the other side of the barrier.

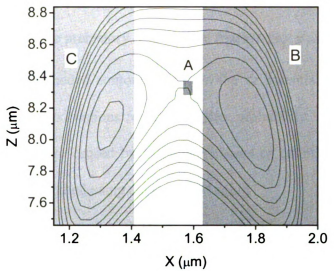

Figure 5.15 Constraints for prehistory calculation. The rules for selecting paths are shown superimposed on a schematic of the potential (contours represent 2 k_BT steps). The paths must be in region A at time t = 0. None of the previous 20 frames can be in the right well, region B. At least one of the previous 20 frames must be in the left well, region C.

The left-to-right transition paths are extracted from the position data using the *Optpath* program. An area around the point (x_f, z_f) is chosen on the right side of the barrier (Figure 5.15 region A). Since the relaxation rate in y is faster than the sampling rate and y is independent of x, no useful information could be extracted from y motions. All y positions are collapsed to increase the statistics. The program steps through the recorded positions until it finds one in this area. The particle positions prior to reaching (x_f, z_f) are recorded. The prehistory distribution $P(x, z, t_i; x_f, z_f, 0)$ is created from all positions (x, z) at time t_i that arrive at (x_f, z_f) at time $t = 0$, where $t_i < 0$. The paths are separated into bins of width 15 nm in x, 40 nm in z, and 5 ms (1 frame) in time.

Two constraints limit the paths to left-to-right transitions only. Paths are eliminated if the particle is in the right well (inside the shaded region B in Figure 5.15) for any of the frames stored in the prehistory distribution. Also, the path must have at least one point in the left well (region C in Figure 5.15).

Figure 5.16 shows the prehistory distribution $P(x,z,t_i;x_f,z_f,0)$ for times leading up to the transition. (The shaded contours are from the xz potential slice in Figure 5.5 with 2 k_BT steps.) Darker red regions represent higher probability. The fluctuations in the distribution amplitude are caused by the low numbers of counts in each histogram bin. The distribution is smoothed using adjacent averaging.

For large times prior to t = 0 (t_i = -85 ms in Figure 5.16) the prehistory distribution is the static distribution $P(x,z) \propto \exp(-U(x,z)/k_BT)$ for a particle in a single well. At t_i = -25 ms the prehistory distribution begins to move in the +z direction. At t_i = -15 ms it distorts in the x direction, moving towards the saddle point. By t_i = -5 ms the particle positions are distributed near the saddle point, arriving in the region around (x_f, z_f) at t_i = 0. After the transition, the distribution continues moving in the x direction (t_i = +5 ms) before settling down into the right well.

The symbols in the t_i = 0 graph represent the peak in the probability distribution from t_i = -25 ms to t_i = 0, then to t_i = +25 ms as the particle moves into the right well, literally the most probable escape path. Due to poor statistics the maximum may not represent the peak of the distribution. A weighted average

$$\bar{x}(t_i) = \frac{\sum_x \sum_z xP(x,z,t_i;x_f,z_f,0)}{\sum_x \sum_z P(x,z,t_i;x_f,z_f,0)}$$

over a 7 x 7 bin box centered on the maximum gives the mean values $\bar{x}$ (and through a similar expression, $\bar{z}$) for each time step. The x and z components are plotted vs. time in Figure 5.17 for t_i = -25 ms to t_i = +25 ms.

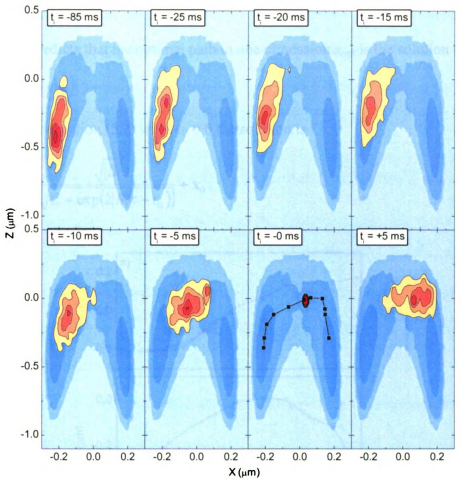

Figure 5.16 Prehistory distribution and optimal path. The distribution of x and z positions is given for a long time before the transition (t_i = -85 ms), the frames leading up to the transition (t_i = -25 ms to t_i = 0 ms), and one frame after the transition (t_i = +5 ms). The shaded contours are the xz potential energy slice from Figure 5.5 with 2 k_BT steps. The symbols in the t_i = 0 ms distribution shows the average position from t_i = -25 ms to t_i = +25 ms. The particle begins near the left stable point (x = -0.21 μm) and ends up within 30 nm in x and 70 nm in z of the point (x_f, z_f) = (0.03, 0), 30 nm to the right of the barrier top. (Data labeled 101403-03, 709 transitions tracked.)

There are two separate stages of motion before the particle makes a transition. The particle begins moving in the +z direction only at t_i = -25 ms. When it is in the same z plane the particle begins moving in x, increasing velocity as it climbs the barrier. After the transition the particle moves in x for 10 ms before settling down into the right stable point.

Theory predicts that the optimal path in one dimension x_{opt} is the solution to [2]

$$\dot{x}_{opt} = U'(x_{opt}). \tag{5.3}$$

For the quartic in equation (5.2) with $A_0 = 0$ the solution is

$$x_{opt}(t) = \frac{\sqrt{|B|}}{\sqrt{C + \exp(2|B|(t - t_0))}} + x_0 . \tag{5.4}$$

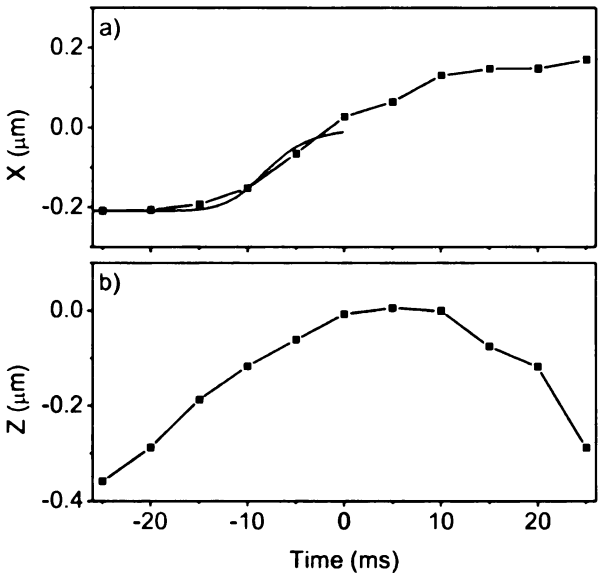

Figure 5.17 X and z components of the optimal path vs. time. The symbols represent the (a) $\bar{x}$ vs. t and (b) $\bar{z}$ vs. t shown in Figure 5.16, t_i = 0 graph. The least squares fit to equation (5.4) (solid line in (a)) shows that the transition is not as sharp as expected. During a transition the particle first moves in the z direction for at least 10 ms. When z is within 0.2 μm of z_f the particle begins moving in x, making a transition over the barrier at x = 0 in 10 to 15 ms. The particle continues moving in x for 10 ms before moving down into the right stable point.

The curve in Figure 5.17a shows the shape of equation (5.4) with the x optimal path. The transition takes longer than expected, due to the motions in the z direction. Equation (5.3) shows that the optimal path asymptotically approaches the barrier ($x = 0$), while the actual particle makes a transition in finite time.

The two dimensional optimal path shows that this three dimensional potential can not simply be projected onto a one dimensional bistable potential. As seen in the next Section, both the time scales in the bistable direction (x) and an orthogonal, universally stable direction (z) must be considered.

5.4. Transition Rate Dependence on Modulation Amplitude and Frequency

Periodic modulation of the potential at frequency f synchronizes the particle transitions to the modulation, increasing the transition rate W (for systems with a static rate $W_0 < 2f$). Under slow modulation the particle follows the potential adiabatically. With increasing frequency the particle lags behind the modulation and ultimately the response falls off, analogous to a damped harmonic oscillator driven above the relaxation frequency. A necessary condition for adiabaticity is $ft_r << 1$, or the modulation period is much less than the intrawell relaxation time t_r.

Modulation with amplitude $A \to A_c^{\mathrm{ad}}$, the potential curvature $\partial^2 U/\partial x^2 \to 0$ so that $t_r \to \infty$. Thus, the adiabatic condition is violated at some value of $A \approx A_c^{\mathrm{ad}}$ and the system becomes nonadiabatic. In addition, adiabaticity may be broken for weak (and slow) driving if $|\partial t_r/\partial t| \approx 1$ [45], i.e., the rate of change of the relaxation time is large.

The activation energy δR is predicted to have power law dependence on the distance from A_c^{ad}, $\delta R \propto \left|A_c^{\mathrm{ad}} - A\right|^{\mu}$. In the adiabatic regime the critical exponent

$\mu = 3/2$. In the weakly nonadiabatic regime (where only $|\partial t_r/\partial t| << 1$ is broken) the critical amplitude is the "slow driving" bifurcation point A_c^{sl} depends on modulation frequency, $A_c^{sl} = A_c^{ad} + 2\pi\gamma f/\beta$ and $\mu = 2$.

The potential in the current experiment is three dimensional, bistable in the x direction and stable in y and z, introducing additional time scales. The relaxation times in the static potential (calculated in Section 5.2) are always ordered $t_{r,z} > t_{r,x} > t_{r,y}$. The condition for adiabaticity applied to x, becomes $ft_{r,x} << 1$, and $|\partial t_{r,x}/\partial t| << 1$. However, the optimal path measurements show that the particle moves in both x and z when making a transition. Thus it is likely that, in addition to the conditions on $t_{r,x}$, there is the condition $ft_{r,z} << 1$. Since the y coordinate is not affected by perturbations in x or z and $t_{r,x} > t_{r,y}$ the condition $ft_{r,y} << 1$ always holds in the present experiments.

The following symbols are used in this section.

Symbol	Definition	Equation
A	Modulation Amplitude (k_BT/μm)	$A_0 = A\cos(2\pi ft)$
f	Modulation Frequency (Hz)	
ΔU_0	Static barrier height ($A = 0$)	
ΔU_{min}	Minimum barrier height during one modulation period.	
W_0	Transition rate in the static potential	
$\overline{W}$	Period averaged transition rate	$\overline{W} = f\int_0^{1/f} dtW$
$\overline{p}$	Escape probability per period	$\overline{p} = \int_0^{1/f} p(\tau)d\tau$
A_c	Critical amplitude in power-law fits	$\ln(W/W_0) = C\lvert A_c - A\rvert^{\mu} + y_0$
μ	Critical exponent in power-law fits.	
A_c^{ad}	Adiabatic critical amplitude (from theory)	
A_c^{sl}	Nonadiabatic critical amplitude under slow driving (from theory)	$A_c^{sl} = A_c^{ad} + (2\pi\gamma/\beta)f$

The data in this section are taken from stable runs over a three day period. The W vs. f data in Figure 5.21 are labeled 110303-03. The low frequency W vs. A data (frequency group A) in Figures 5.23 and 5.24 are labeled 012904-01. The higher frequency W vs. A data (frequency group B) in Figures 5.25 and 5.26 are labeled 012404-01. Table 5.6 lists the mean static barrier height ΔU_0, transition rate W_0 for the left and right wells, the relaxation time t_r in x, y, and z, and acquisition time per data point for these data sets.

Table 5.6 Static potential parameters for data used in Section 5.4. Units: energies ΔU ($k_B T$), rates W_0 (Hz), relaxation times t_r (s).

Dataset Label	ΔU_{left}	ΔU_{right}	W_0 left	W_0 right	$t_{r,x}$	$t_{r,y}$	$t_{r,z}$	Time
110303-03	4.4	4.9	1.5	0.98	0.006	0.002	0.28	500 s
012404-01	5.2	4.7	0.62	0.85	0.005	0.002	0.26	500 s
012904-01	6.4	5.9	0.26	0.36	0.004	0.002	0.29	500 s

5.4.1. Transition Rate in a Periodically Modulated Potential

Periodic modulation causes a periodic change in the tilt A_0 in equation (5.2). $A_0 = A\cos(2\pi ft)$, with modulation amplitude A and frequency f. The barrier height changes as $\Delta U(t) = \Delta U_0 \pm \delta U(t)$, (+ for the left well, - for the right well) where ΔU_0 is the static barrier and $\delta U(t)$ is a periodic function. The probability to escape is increased when the barrier is lowest, synchronizing the transitions with the driving field; this leads to synchronous pulses in escape probability.

Figure 5.18a shows $x(t)$ (solid line) for a particle in the bistable potential. The particle is most likely to hop out of the left well when the left barrier height (dashed line) is low. The return transition tends to occur when the right barrier is low (and ΔU_{left} is high), an odd half-integer number of modulation periods later. Figure 5.18b shows the probability of escape vs. modulation period. The escapes occur during 1/2 of the period.

Thus, if the particle does not escape during a half-cycle, it tends to wait an integer number of full periods before escaping.

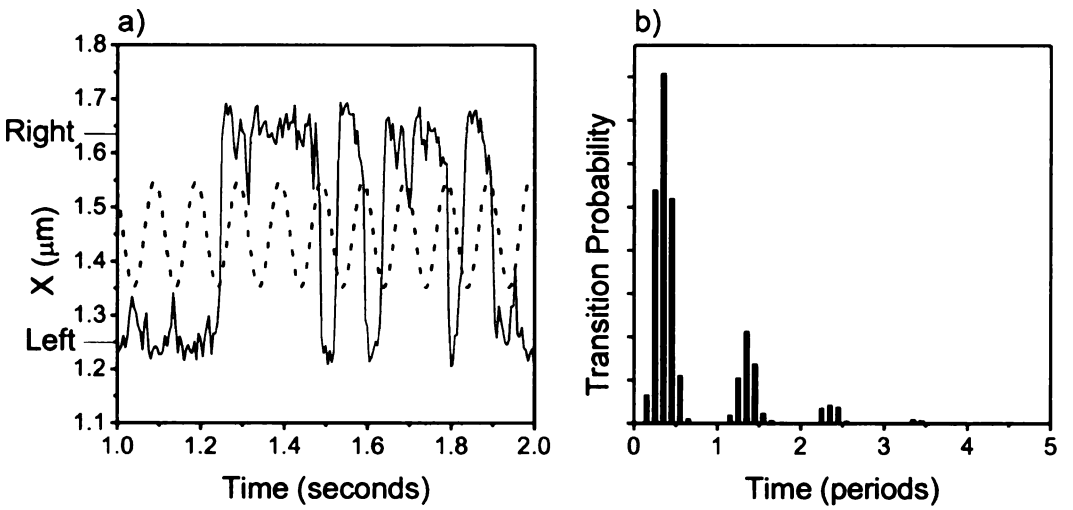

Figure 5.18 Interwell transitions under periodic modulation. (a) the particle makes transitions from the left well (x = 1.25 μm), over the barrier (x = 1.44 μm), and into the right well (x = 1.63 μm). The dashed line represents the left barrier height due to periodic modulation. (b) the transition probability vs. time. Peaks indicate that the particle generally makes transitions during the portion of the period when the barrier is lower. (Data labeled 012404-01-93, 10 Hz, 4.9 k_BT modulation of 5.2 k_BT barrier, 1366 transitions.)

The period averaged transition rate $\overline{W}$ is calculated from the dwell time distribution $p(\tau)$, the probability of the particle leaving the well a time τ after entering. Figure 5.19 shows $p(\tau)$ with f = 1 Hz for two values of A. In the adiabatic regime and for small A the distribution is $p(\tau) = P_0 \exp[-\lambda\tau + A\cos(2\pi f\tau)]$ (solid lines), having a decaying exponential envelope with $\lambda = \overline{W} = 2\overline{p}f$ where $\overline{p} = \int_0^{1/f} p(\tau)d\tau$ is the escape probability per period.

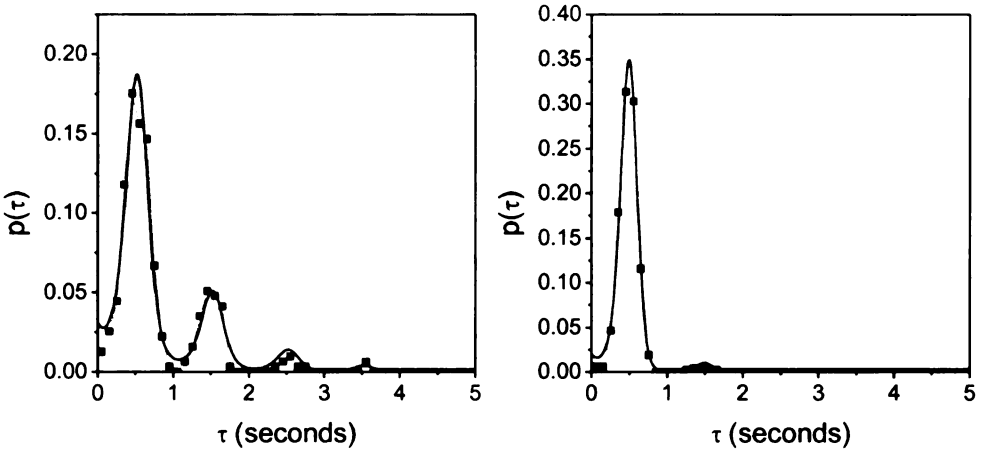

Figure 5.19 Transition rate measurement from fit to decaying peaks. The dwell time distribution (squares) is plotted vs. dwell time for 1 Hz modulation with minimum barrier (a) 3.2 k_BT and (b) 1.5 k_BT. The superimposed least squares fit (solid lines) gives transition rate $\overline{W}_f$ of (a) 1.36 Hz and (b) 3.3 Hz. The lack of higher harmonics in (b) produces a worse fit, adversely affecting the measured decay rate. (Data labeled 012904-01-83 and 012904-01-87, ΔU_0 = 6.4 k_BT, 314 and 476 total transitions, respectively.)

There are several methods to extract $\overline{W}$ from data of the type shown in Figure 5.19. Ideally, each method should produce the same transition rate (using $\overline{W} = 2\overline{p}_p f$).

- Calculate $W_f = \lambda$ from a least squares fit using $p(\tau) = C\exp[-\lambda\tau + A\cos(2\pi f\tau)]$.
- Integrate the probability under the first peak, equal to the period averaged transition probability. $\overline{p}_p = \frac{N_1}{N}$ where N_1 is the number of transitions with dwell time $\tau < 1/f$.
- Calculate the mean transition rate $W = \frac{1}{\langle\tau\rangle} = \frac{N}{\sum\tau_i}$

Since the probability to escape in the first cycle approaches 1 as $A \to A_b$, the uncertainty is dominated by the number of transitions that do <u>not</u> occur in the first period. The rate measurement needs to be sensitive to small changes in the second peak.

The least squares fit is preferred when there are multiple peaks. As higher order peaks disappear the fit overestimates the decay rate λ, fitting poorly when the second peak has fewer than 20 counts (Figure 5.19b).

The first peak area is the number of transitions with $\tau < 1/f$, normalized by the total number of transitions. The probability $\bar{p}_p$ approaches unity as $A \to A_b$. The uncertainty is the uncertainty in both N_1 and (N - N_1), i.e., it depends on the number of dwell times in the second peak as well. $\delta\bar{p}_p = \sqrt{\frac{1}{N_1} + \frac{1}{N - N_1}}$ for $\delta N_1 = \sqrt{N_1}$. $\delta\bar{p}_p$ is large for high frequencies or small modulation (where N_1 is small) and large modulation (where (N - N_1) is small).

The mean transition rate $W = 1/\langle\tau\rangle$, at complete total synchronization $W = 2f$, and the first probability peak is centered at $\tau = W^{-1}$. A small second peak causes W to increase with the number of points under the peak. This measure is also valid for small modulation and in the static case. The transition rate vs. modulation amplitude measurements use either $\bar{p}_p$ or W as noted.

5.4.2. Locating the Adiabatic and Nonadiabatic Regimes

The regions of adiabatic and nonadiabatic dynamics have been identified through measurements of the transition rate in a modulated bistable system. Figure 5.20 shows the regions in the frequency-amplitude plane where adiabatic and nonadiabatic characteristics have been observed. For modulation frequencies below 0.5 Hz the transition probability is independent of frequency, implying that the particle follows the potential, i.e., is adiabatic. For frequencies above 0.5 Hz the system enters a crossover

region. In the range 3.3 Hz to 20 Hz, a power-law behavior is found with critical exponent $\mu \approx 2$, consistent with theoretical predictions for the weakly nonadiabatic regime. The critical amplitude is linearly dependent on frequency, extending above the adiabatic bifurcation amplitude A_b. For frequencies near the relaxation rate, the particle falls strongly out of equilibrium with the driving field and the mean transition rate decreases.

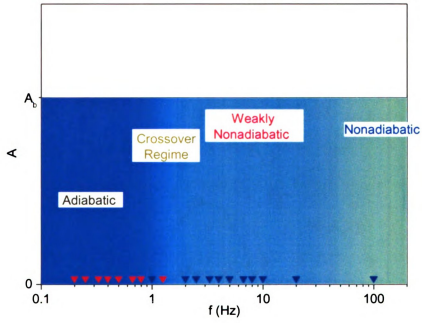

Figure 5.20 Phase diagram of experimentally observed modulation regimes. The arrows represent frequencies for which $\ln(W)$ vs. A was measured. Frequency group A = red, frequency group B = blue. Below 0.5 Hz the modulation is adiabatic (blue). Between 0.5 Hz and 3.3 Hz is a crossover regime. From 3.3 to 20 Hz the modulation is weakly nonadiabatic (cyan), with critical exponent $\mu \approx 2$. The nonadiabatic critical amplitude extends beyond the adiabatic critical amplitude calculated in Section 5.2.2. Above 80 Hz both adiabatic approximations fail (green).

Transition Rate vs. Frequency Measurements

Figure 5.21 shows the mean transition rate W vs. modulation frequency f for several modulation amplitudes. Note that frequency is plotted on a log scale. By inspection, there are three regimes with different frequency dependence of the transition rate. At low frequencies the transition rate increases linearly with frequency and is weakly dependent on amplitude. Above 2 – 3 Hz the rate saturates, i.e. reaches a maximum of $W = 2f$ at a characteristic frequency that increases with amplitude. Another characteristic frequency scale appears near 30 Hz where W falls until it levels off near $W = W_0$, the static transition rate.

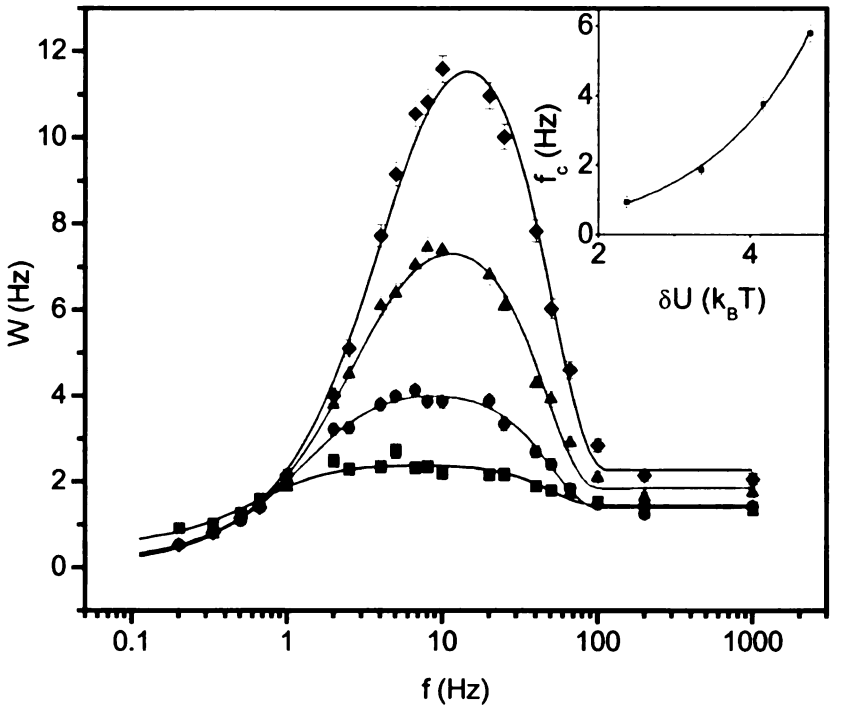

Figure 5.21 Mean transition rate vs. frequency for several modulation amplitudes. Transition rates are plotted for 2.4 k_BT (squares), 3.3 k_BT (circles), 4.2 k_BT (triangles), and 4.8 k_BT (diamonds) modulation of the barrier height. Solid curves are fits to equation (5.5) with parameters listed in Table 5.7. Inset: fit of exponential equation (5.6) to corner frequency f_c. (Data labeled 110303-03, static barrier height = 4.4 k_BT.)

The particle is most likely to make a transition when the barrier is low. The instantaneous barrier height $\Delta U(t) = \Delta U_0 + \delta U(t)$, where $\delta U(t) \approx \Lambda \cos(2\pi f t)$ and $\Lambda \propto A$ for small tilt amplitude A. (I.e., the stable and unstable points do not move much and $U(x_b) - U(x_1) = \Delta U_0 + A\cos(2\pi f t)(x_b - x_1)$.) The transition probability depends exponentially on the change in the barrier height Λ, and a maximum instantaneous transition rate is defined by $W_A = W_0 \exp(\Lambda / k_B T)$. If the modulation is slow enough ($f < W_A$) the transition probability per period approaches unity. The transitions are totally synchronized and the rate $W = 2f$.

At higher frequencies ($f > W_A$) the transition probability per period decreases. The barrier is not low for a long enough time for the particle to escape every period, producing multiple peaks in the dwell time distribution (as shown in Figure 5.18b). The transition probability is proportional to the time the barrier is low ($1/f$), and the total number of transitions is proportional to the number of periods f. The transition rate is independent of frequency.

At higher frequencies the particle cannot respond fast enough to the changes in the potential. The effective minimum barrier height becomes $\Delta \overline{U}_{\min} = \Delta U_0 - \delta \overline{U}(f)$, where $\delta \overline{U}(f) \leq \Lambda$. This occurs when the modulation frequency approaches the intrawell relaxation rate.

To quantitatively model W in the low and intermediate frequency regimes an analogy is made to the driven, overdamped harmonic oscillator. The harmonic oscillator has a characteristic time scale, the relaxation rate, which defines the rate at which the particle returns to the stable point. For driving above this frequency the response decreases. In this system the analogous time scale is W_A, the maximum rate at which the

particle makes a transition. Using a functional form similar to the harmonic oscillator amplitude, $W \propto f/\sqrt{f^2+\beta^2 W_A^2}$, with constant β. This has the correct asymptotic behavior, $W \propto f$ for $f << \beta W_A$ and W independent of f for $f >> \beta W_A$.

In the nonadiabatic regime the barrier height is averaged over some time t_{ave},

$$\Delta\bar{U}(t)=\frac{1}{t_{ave}}\int_{t-t_{ave}/2}^{t+t_{ave}/2}\Delta U(\tau)d\tau \approx \Delta U_0+\left[\frac{\Lambda}{\pi f t_{ave}}\sin(\pi f t_{ave})\right]\cos(2\pi f t),$$

with the integration interval limited to one period) The mean transition rate is found by averaging the rates for a single period

$$W = W_0 f\int_0^{1/f}\exp\left[\frac{\Lambda}{k_B T}\frac{\sin(\pi f t_{ave})}{\pi f t_{ave}}\cos(2\pi f t)\right]dt = W_0 I_0\left(\frac{\Lambda}{k_B T}\frac{\sin(\pi f t_{ave})}{\pi f t_{ave}}\right),$$

where the zero order modified Bessel function of the first kind I_0 is defined

$$I_0(x)=\frac{1}{\pi}\int_0^{\pi}\exp[x\cos(t)]dt\,.$$

Combining the frequency regimes, the transition rate vs. frequency is fit with instrumental weighting ($1/\delta W^2$, where δW = uncertainty in W) using

$$(5.5)\quad W = B\frac{f}{\sqrt{f^2+f_c^2}}I_0\left(\frac{\Lambda}{k_B T}\frac{\sin(\gamma)}{\gamma}\right)+y_0, \text{ where } \gamma=\begin{cases}\pi f t_{ave} & f t_{ave}\le 1\\ \pi & f t_{ave}>1\end{cases}$$

Table 5.7 Results of fits of equation (5.7) to W vs. f data.

A (k_BT/μm)	δU (k_BT)	Λ (k_BT)	B (Hz)	f_c (Hz)	t_{ave} (s)	y_0 (Hz)
12.5	2.4	1.8 ± 0.2	1.0 ± 0.2	1.0 ± 0.2	9.8 ± 1.3	0.4 ± 0.2
18.7	3.4	2.44 ± 0.09	1.3 ± 0.1	1.9 ± 0.2	9.6 ± 0.5	0.08 ± 0.08
25.0	4.2	2.90 ± 0.07	1.8 ± 0.1	3.8 ± 0.2	9.8 ± 0.3	0.06 ± 0.06
31.2	4.8	3.22 ± 0.06	2.3 ± 0.1	5.8 ± 0.3	8.7 ± 0.2	0.00 ± 0.05

for the W vs. f data in Figure 5.20. The fit parameters are Λ, B, f_c, t_{ave}, and y_0. Table 5.7 displays the results. The averaging times t_{ave} are close to the x relaxation time obtained for the static potential (9 ms).

The fit parameter $f_c = \beta W_A$. f_c was measured at four amplitudes and plotted vs. the change in the barrier height δU, extrapolated from the 3 point quartic fit (Section 5.3). The values of f_c in Table 5.7 are fit with

(5.6) $$f_c = \sigma \exp(-\lambda\, \delta U/k_B T) + y_0$$

(inset Figure 5.20). $\lambda = 0.77 \pm 0.18$, indicating that the assumption $f_c \propto \exp(\delta U/k_B T)$ is not correct.

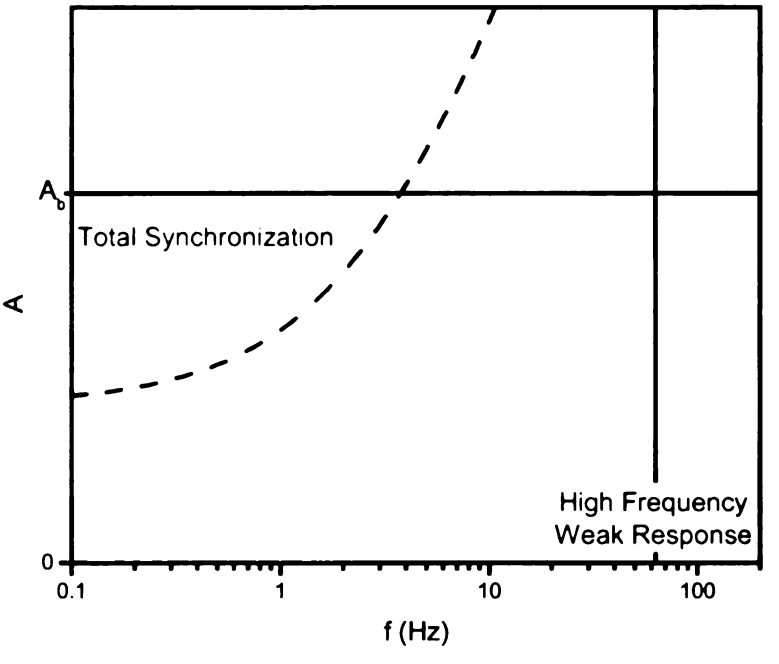

Figure 5.22 Phase diagram derived from W vs. f measurements. Above the dashed line the transitions are totally synchronized with the modulation; transition rates are constant in A. The boundary line is given by the corner frequency f_c. In this region no information about amplitude dependence near the bifurcation point is available. Above 50 Hz the potential becomes averaged, and the transition rate falls until $W = W_0$. The remaining area is explored using W vs. A measurements.

Based on these experimental results only the (f, A) plane is split into three regions (Figure 5.22). The dashed line is the total synchronization boundary, representing the path of f_c in (f, A) space. Above this boundary the transition rate is $W = 2f$. All transitions are synchronized, and the second peak in the dwell time distribution disappears (Figure 5.19). This limits the frequency range over which there is a measurable signal near $A = A_b$. When the relaxation time becomes a large fraction of the modulation period ($t_r \approx \tau_F$) the particle sees a time averaged potential and the synchronization disappears. The modulation regime in the region between boundaries is explored by measuring the transition rate dependence on A.

Identification of the Adiabatic Regime in Frequency Group A

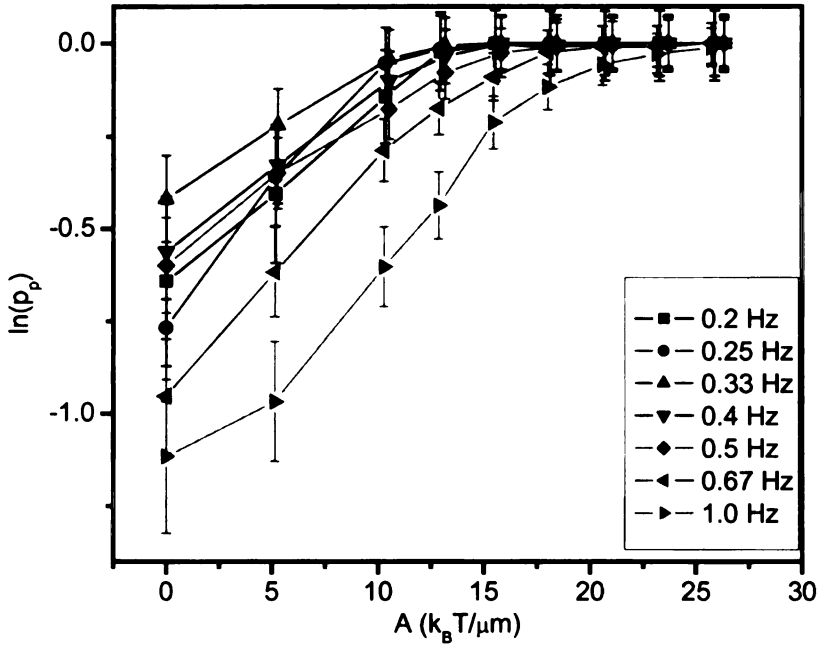

Figure 5.23 Transition probability vs. modulation amplitude for low frequency modulation. The overlapping data (up to f = 0.5 Hz) exhibit frequency independence, a characteristic of adiabaticity. (Data labeled 012904-01, left-to-right transitions, $A_b = 40 \pm 4\ k_BT/\mu m$.)

In the adiabatic regime the particle follows the instantaneous potential. A consequence is that the transition probability per period is independent of frequency, changing only with modulation amplitude. $\ln(\bar{p}_p)$ is plotted as a function of A in Figure 5.23 for modulation frequencies from 0.2 Hz to 1 Hz. Within statistical uncertainties the transition probability is independent of frequency for $f \leq 0.5$ Hz. Above 0.5 Hz the transition probability decreases suggesting the presence of a crossover occurs near $f = 0.5$ Hz.

To examine the power law behavior in the low frequency regime, $\ln(W)$ vs. A is plotted and fit in Figure 5.24 for the 0.5 Hz data set. Near the bifurcation point the activation energy is predicted to have power-law dependence on the distance from a critical amplitude A_c [44], $\ln(W) = C\left|A_c^{\mathrm{ad}} - A\right|^{\mu} + y_0$, where μ is a critical exponent and C and y_0 are constants. For critical exponents greater than one, $\ln(W)$ approaches y_0 as $A \to A_c^{\mathrm{ad}}$ with slope zero. To properly fit this to the data the function is modified,

$$\ln(W) = \begin{cases} C(A_c - A)^{\mu} + y_0 & A \leq A_c \\ y_0 & A > A_c \end{cases} \tag{5.7}$$

and fit with free parameters A_c, μ, C, and y_0. The fit is applied to amplitudes above 10 $k_B T$/μm only. The weighting is instrumental (inversely proportional to the uncertainty squared).

The fit parameters are listed in the caption of Figure 5.24. The critical exponent is $\mu = 1.5 \pm 1.9$, consistent with the predicted $\mu = 3/2$ but with uncertainty too large to draw a conclusion. However, as noted blow, there is good reason to believe the asymptotic power law is not valid when $W \sim f$.

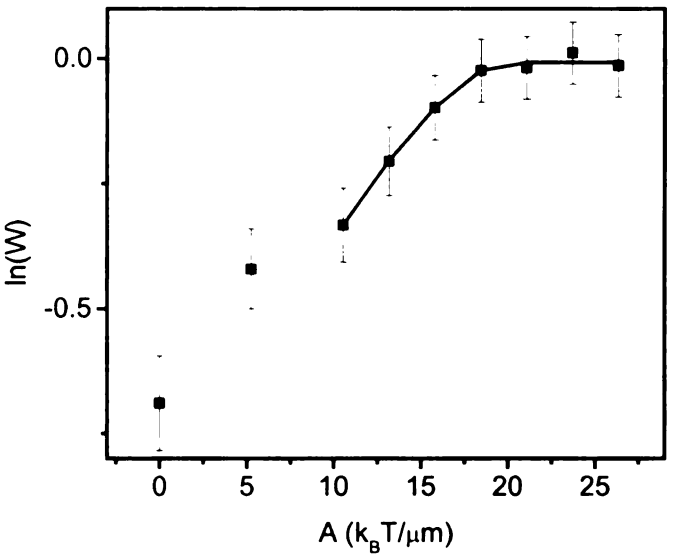

Figure 5.24 $\ln(W)$ vs. A in the adiabatic regime. Modulation frequency: 0.5 Hz. The solid line is a fit to equation (5.7), with parameters A_c = 19 ± 7 k_BT/μm, C = -13 ± 65, μ = 1.5 ± 1.9, and y_0 = -0.008 ± 0.036. The error bars are calculated from statistical uncertainty in the number of transitions. (Data labeled 012904-01, left-to-right transitions, calculated A_b = 40 ± 4 k_BT/μm.)

The error bars are calculated from the statistical uncertainty in the number of transitions N. $\delta W = \sqrt{N}/T$ and $\delta \ln(W) = \delta W/W = 1/\sqrt{N}$. For f = 0.5 Hz measured over 500 seconds the number of transitions under total synchronization is 250 so $\sqrt{N} = 16$. This uncertainty propagates through the least squares fit.

The bifurcation amplitude calculated from the quartic tilt approximation is A_b = 40 ± 4 k_BT/μm, twice A_c. Measurements closer to the bifurcation point are not experimentally possible; since small changes in transition rates near complete synchronization are masked by statistical fluctuations. To increase the precision the synchronization boundary (Figure 5.22) would need to be shifted by changing the corner frequency. Since $f_c \propto W_0$, increasing the static barrier height would move the boundary

to the left. For $f_c < 0.5$ Hz at $A = A_b$, the static transition rate would need to be decreased by a factor of 10 (from 0.2 Hz to 0.02 Hz).

Identification of the Nonadiabatic Regime in Frequency Group B

Figure 5.25 shows $\ln(W)$ vs. A for 6 data sets in frequency group B, ranging from 3.3 Hz to 20 Hz. The solid lines represent least squares fits with the power law in equation (5.9). As $A \rightarrow A_c$ the transitions are totally synchronized so that $W = 2f$, i.e., y_0 can be treated as a known parameter. This reduces the number of fitting parameters

The total number of transitions N is the same for both wells. The sum of the total dwell times $T_1 + T_2 = T$, the total acquisition time. When the transitions are totally synchronized,

$$\frac{T}{N} = \frac{1}{f} = \frac{T_1 + T_2}{N} = \frac{1}{W_1} + \frac{1}{W_2}.$$

The mean transition rates for the left (W_L) and right (W_R) wells are not independent. In a symmetric potential $W_R = W_L = 2f$, but in an asymmetric potential W_L may be greater than $2f$. The difference in mean transition rates W_L - W_R nonetheless decreases as A increases. Therefore y_0 is set equal to $\ln(2f)$.

The values of μ in Table 5.8 yield a typical value of 2.3± 0.3 over this frequency range. This agrees with the predicted exponent 2 in the nonadiabatic regime. At 20 Hz, the maximum modulation amplitude is smaller than the critical value A_c.

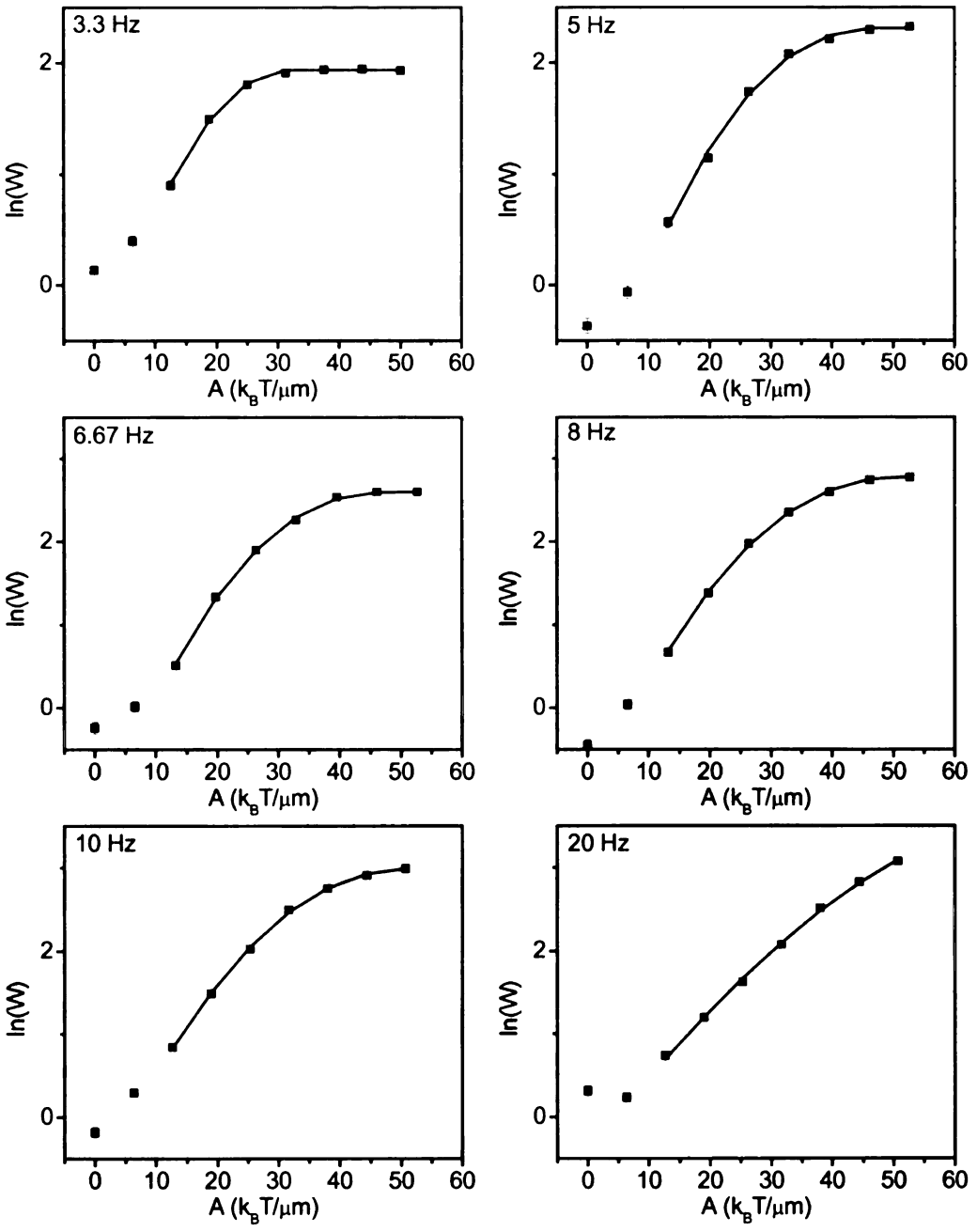

Figure 5.25 $\ln(W)$ vs. A in the nonadiabatic regime. Solid lines are fits to equation (5.9), with parameters listed in Table 5.8. (Data labeled 012404-01, left-to-right transitions, $A_b = 36 \pm 4\ k_BT/\mu m$.)

Table 5.8 Power law fit results for the nonadiabatic regime.

f(Hz)	A_c (k_BT/μm)	C	μ	y_0
3.3	34 ± 6	-0.7 ± 2.3	2.4 ± 0.9	1.93
5	48 ± 4	-0.6 ± 1.0	2.3 ± 0.4	2.31
6.7	48 ± 3	-0.6 ± 0.8	2.3 ± 0.3	2.60
8	52 ± 3	-0.4 ± 0.5	2.3 ± 0.3	2.76
10	54 ± 3	-0.5 ± 0.5	2.2 ± 0.2	3.00
20	81 ± 5	-0.1 ± 0.1	2.4 ± 0.3	3.70

The critical amplitude A_c derived from these fits increases with frequency. To examine only the frequency dependence the data in Figure 5.25 were fit again (Table 5.9). A_c is plotted to the same function in Figure 5.26 and fit by $A_c = c + df$. The slope d = 2.13 ± 0.04 k_BT/μm Hz and c = 30.1 ± 0.5 k_BT/μm.

Table 5.9 Power law fit results for the nonadiabatic regime, with $\mu = 2$ and $y_0 = \ln(2f)$.

f(Hz)	A_c (k_BT/μm)	C	μ	y_0
3.3	31 ± 1	-2.8 ± 2.3	2	1.93
5	45 ± 0.8	-1.8 ± 1.0	2	2.31
6.7	45 ± 0.7	-2.0 ± 0.8	2	2.60
8	49 ± 0.7	-1.66 ± 0.08	2	2.76
10	51 ± 0.6	-1.47 ± 0.06	2	3.00
20	73 ± 0.6	-0.80 ± 0.01	2	3.70

The change in the critical amplitude is predicted to be linear in frequency [45], with $A_c^{sl} = A_c^{ad} + 2\pi\gamma f/\beta$ (see Section 2.3.3). For a quartic potential in the x direction (see equation (5.2)), the coefficients γ and β are

$$\beta = \frac{1}{m\Gamma} \text{ and } \gamma^2 = \frac{A_c^{ad}}{6Cx_s} = \frac{2B^{3/2}/3\sqrt{3C}}{6C\sqrt{B/3C}} = \frac{1}{9}\frac{B}{C}.$$

Using the values in the first row of Table 5.5, the slope of the fit parameter A_c vs. f is

$$\frac{2\pi\gamma}{\beta} = 2\pi m\Gamma\sqrt{\frac{B}{9C}} = \frac{2\pi 2.5\times10^7\,\text{s}^{-1}}{1.77\times10^7\,\mu\text{m}\,\text{s}^{-2}(k_BT)^{-1}}\sqrt{\frac{490\,k_BT/\mu\text{m}^2}{9\times10700\,k_BT/\mu\text{m}^4}} = 0.63\,k_BT\text{s}/\mu\text{m}.$$

Therefore $A_c^{sl} = A_c^{ad} + 0.63f$ for A in units of k_BT/μm.

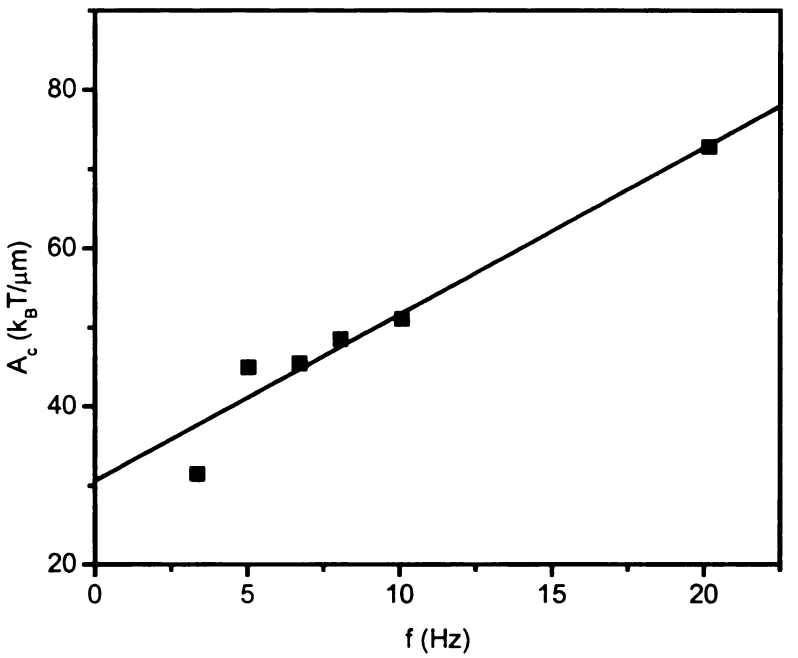

Figure 5.26 Frequency dependence of the critical amplitude. A_c from least squares fits in the nonadiabatic regimes is linearly proportional to the modulation frequency. Slope $d = 2.11 \pm 0.05\ k_BT/\mu m$ Hz and offset $c = 30.6 \pm 0.6\ k_BT/\mu m$. (Data labeled 012403-04, left-to-right transitions, $A_b = 36 \pm 4\ k_BT/\mu m$.)

The experimentally determined slope d in Figure 5.25 is four times larger than the value of $2\pi\gamma/\beta$, calculated from the parameter representation of the potential However, the theoretical model is an expansion of the potential about the bifurcation point, trat than about the equilibrium ($A = 0$) potential. This calculation assumes that the potential does not deviate from the quartic approximation at large A. The ratio B/C from the large amplitude tilts in Section 5.2.2 (Figure 5.13) is constant to $0.8\ A_c^{ad}$.

Details of the Experimental Procedure

The mean transition rate was calculated for consecutive data sets with constant modulation frequency and increasing amplitude using the batch data acquisition function

of *WinMil2* (Section 4.2.3). The traps were positioned approximately 0.45 μm apart for a barrier height of greater than 6 k_BT and mean transition rate from 0.1 to 0.2 Hz for frequency group A and ΔU = 5 k_BT and W = 0.5 Hz for frequency group B. A sample batch progression is shown in Table 4.3. A data acquisition begins with a series of static tilts from which the potential parameters and estimated adiabatic critical amplitude are calculated. The next 9 data sets send a constant frequency (1.008243 Hz) and increasing modulation amplitude (in units of V_{pp}) to the SRS DS345 function generators controlling the LS-100 beam power stabilizer. The frequency is incremented for the next run and the amplitude progression repeated.

Even with the optical stability improvements in Section 4.3 there is a drift due to temperature variations, with time scales on the order of hours. To minimize this effect on the individual amplitude progressions the data sets are as short as possible. With an unmodulated transition rate of 0.2 Hz there are 50 ± 7 transitions in each direction during a 100,000 frame (500 second) data set (assuming Poisson statistics). With increasing modulation amplitude the transitions become synchronized and the maximum mean transition rate is twice the modulation frequency. The relative uncertainty decreases and thus the data set length is decreased, as shown in Table 4.3. If the system drifts the static tilt measurements in Section 5.2.2 are no longer valid. After every three or four amplitude progressions another static tilt measurement is made.

To determine if the system drifted during an amplitude progression the static potentials measured before and after are compared. The barrier heights and stable point positions are calculated from the x profile. Assuming the barrier varies linearly with the beam positions (for a small range of displacements), a 5 nm change creates a 0.07 k_BT

change in a 6 k_BT barrier (1%). Since the transition rate depends exponentially on the barrier height the rate changes by 7 %. A "stable" amplitude progression has < 5 nm beam position change, < 0.1 k_BT barrier height change, and transition rate changes within the statistical uncertainty for the static potentials before and after the progression.

5.5. Summary

The particle dynamics and the energy surfaces in the bistable potential have been calculated from the position $\vec{r}(t)$, recorded at 5 ms intervals for 500 seconds (typically). The overdamped particle is in thermal equilibrium, and the Boltzmann relation is used to calculate the potential energy in the volume the particle explores. From this three dimensional map the time scales of the system are estimated. At the stable points there are three orthogonal relaxation rates: the slow z rate (3 Hz), the intermediate x rate (150 Hz) and the fast y rate (500 Hz). The transition rate depends on the barrier height and is usually 0.1 Hz to 2 Hz.

The transitions rates are measured from $x(t)$. The mean transition rate was calculated from the mean dwell time in each well. The optimal path is calculated by computing the condition probability of the particle occupying the well escaping at time t_i later. The results indicate a process that involves two distinct steps: a preparative step in which the particle moves in the +z direction, then an over the barrier along x in a time $t_{r,x}$.

The adiabatic and nonadiabatic regimes of the periodically modulated bistable potential were identified through measurements of transition rate vs. modulation amplitude and frequency. The existence of the adiabatic region was inferred from the frequency independence of the transition probability per period. Above f = 0.5 Hz the probability decreased with increasing amplitude, indicating that the particle was not

following the potential. A comparison to the predicted power law dependence on amplitude could not be performed (with reasonable uncertainties) due to limits on the system's long term stability. The nonadiabatic region 3.3 Hz $\leq f \leq$ 20 Hz was modulated beyond $A = A_c^{ad}$ and the function $\ln(W) = C|A_c - A|^{\mu} + y_0$ fit with known y_0. The critical exponents agreed with the predicted $\mu = 2$, and the critical amplitude A_c^{sl} was linearly dependent on frequency. The next chapter compares these results with the theoretical predictions [44-46].

Chapter 6 Discussion

6.1. Theoretical Predictions of Adiabatic Criteria

In the previous section, adiabatic and nonadiabatic regimes were tentatively identified by examination of the $\ln(W)$ vs. A data with some guidance from recent theory [45]. Since the relevant relaxation times are available from knowledge of the modulated potential, we are now able to check for internal consistency in our assignment of adiabatic and nonadiabatic regimes.

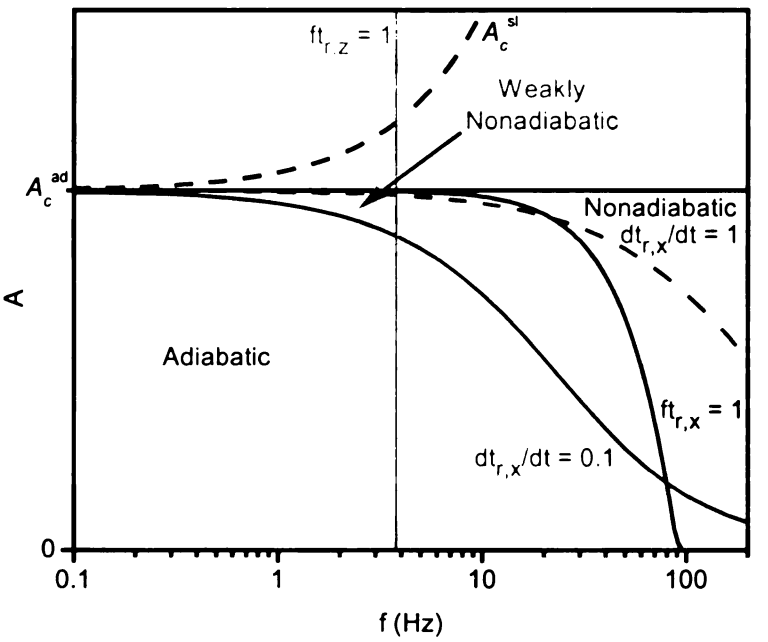

Figure 6.1 Boundaries of adiabatic and nonadiabatic regimes in the (f, A) plane. Black lines are the adiabatic critical amplitude A_c^{ad} (solid) and A_c^{sl} (dashed). Red lines are the weakly nonadiabatic crossover, $|\partial t_{r,x}/\partial t| = 0.1$ (solid) and $|\partial t_{r,x}/\partial t| = 1$ (dashed). The blue line is the strongly nonadiabatic crossover, $ft_{r,x} = 1$, and the cyan line is $ft_{r,z} = 1$, the crossover due to $t_{r,z}$. The modulation frequency is plotted on a $\log_{10}$ scale.

In a periodically modulated one-dimensional potential recent theoretical work has identified an adiabatic regime and two nonadiabatic regimes [45]. The regions are characterized by relationships between the modulation frequency f and the intrawell relaxation time. At low modulation frequency and amplitude the particle follows the field; the motion is adiabatic. As frequency increases the condition $\left|\partial t_{r,x}/\partial t\right| << 1$ first is violated, leading to a weakly nonadiabatic regime. During part of the modulation period the relaxation time $t_{r,x}$ changes too quickly and the particle lags behind the modulation. The solid and dashed red lines in Figure 6.1 represent $\left|\partial t_{r,x}/\partial t\right| = 0.1$ and $\left|\partial t_{r,x}/\partial t\right| = 1$, respectively. At yet higher frequency $ft_{r,x} \approx 1$ and the particle falls out of equilibrium through the entire modulation period. Above the blue $ft_{r,x} = 1$ line in Figure 6.1 the system is highly nonadiabatic.

The distortion of the stable and unstable states causes the bifurcation amplitude (the amplitude at which the states merge) to increase with frequency. For relatively slow driving, theory predicts $A_c^{\mathrm{sl}} = A_c^{\mathrm{ad}} + 2\pi\gamma f/\beta$. This boundary is plotted in Figure 6.1 as the dashed black line.

For multi-dimensional system additional adiabatic criteria may appear that depend on the relaxation times in other directions. In the present system it is known that, since $t_{r,z} > t_{r,x}$, the condition $ft_{r,z} << 1$ must also be satisfied to obtain adiabaticity. The cyan curve in Figure 6.1 represents $ft_{r,z} = 1$. ($t_{r,z}$ is assumed to be independent of the modulation amplitude.) This condition adds two new regions to the (f, A) plane. The region where $ft_{r,z} << 1$ is violated but $\left|\partial t_{r,x}/\partial t\right| << 1$ holds is not expected to be adiabatic

but also not weakly nonadiabatic. When both conditions are violated it is unknown if the system is weakly nonadiabatic or enters some other frequency regime.

6.2. *Comparison to Experimentally Determined Frequency Regimes*

The regions where the adiabatic approximations are violated are compared to the results in Section 5.4 (Figure 6.2). Below f = 0.5 Hz the transition probabilities are insensitive to frequency and thus adiabatic. From f = 3.3 Hz to 20 Hz the power-law exponents obtained from fits to $\ln(W) = C\left|A_c^{sl} - A\right|^{\mu} + y_0$ are consistent with $\mu = 2$ and the bifurcation amplitude scales linearly with frequency. f = 1 Hz to 3.3 Hz is a crossover region between adiabatic and weakly nonadiabatic.

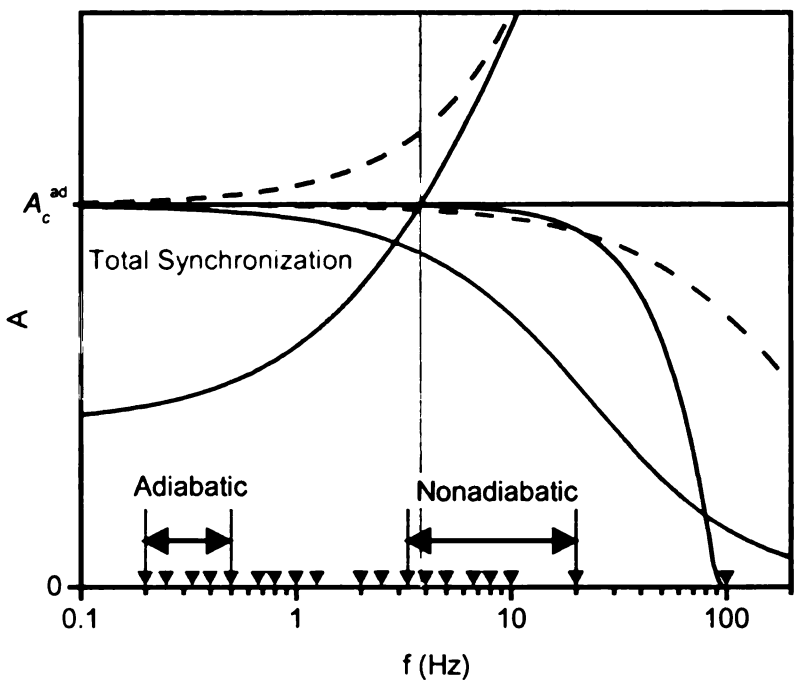

Figure 6.2 Comparison of experimental data with theoretical frequency regimes. The red and blue arrows represent the frequencies of the $\ln(W)$ vs. A measurements in frequency group A and frequency group B, respectively. The experimentally identified adiabatic region and nonadiabatic (power-law exponent μ = 2) regions are marked. The green line is the total synchronization boundary from Figure 5.22. (The other curves are labeled in Figure 6.1.)

The boundaries are estimated from our measurements as follows. The x relaxation time is $t_{r,x} = 2\pi\Gamma/\omega^2$, where $m\omega^2 = U''(x_s) = B + Cx_s^2$ using the quartic approximation $U(x) = A_0 x + Bx^2/2 + Cx^4/4$ and x_s is the position of the stable point. Γ is the Stokes damping rate 2.5×10^7 s^{-1} and the conversion from k_BT/μm to s^{-2} is $\omega^2 = 1.77\times10^7 U''$. The position of the minimum x_s is found by solving $U'(x_s) = 0$,

$$x_s(A_0) = \frac{3A_b}{2B}\frac{1+\left(\sqrt{A_0^2/A_b^2+1}-A_0/A_b\right)^{2/3}}{\left(\sqrt{A_0^2/A_b^2+1}-A_0/A_b\right)^{1/3}},$$

with bifurcation amplitude $A_b = 2|B|^{3/2}/3\sqrt{3C}$.

Under modulation, $A_0 = A\cos(2\pi ft)$ and x_s and t_r are time dependent. The adiabatic conditions are applied to the period maximum $t_{r,x}$ and $|\partial t_{r,x}/\partial t|$. Solving numerically, the boundary $ft_{r,x} = 1$ is shown in Figure 6.2 (blue line). At low frequencies the boundary is close to $A = A_b$. At $f = 10$ Hz it begins falling, reaching $A = 0.9A_b$ at $f = 27$ Hz. All modulation violates this condition at $f = 90$ Hz.

$|\partial t_{r,x}/\partial t|$ is calculated and the amplitude A found such that $\max|\partial t_{r,x}/\partial t| = 0.1$ (solid red curve in Figure 6.2) and $\max|\partial t_{r,x}/\partial t| = 1$ (dashed red curve). The solid curve leaves the area around $A = A_b$ at $f = 0.3$ Hz and reaches $A = 0.9A_b$ at $f = 3$ Hz.

The adiabatic condition from the z relaxation time is calculated using $t_{r,z} = 0.26$ s, measured from the local quadratic fits. $ft_{r,z} = 1$ for $f = 3.8$ Hz.

The $f \leq 0.5$ Hz data satisfy all of the adiabatic criteria, as expected by the frequency independent transition probability per period. Above 0.5 Hz the transition

probability decreases, possibly due to violation of $ft_{r,z} << 1$. This occurs when $ft_{r,z} \approx 0.1$, lending some justification to the assumption that $\max\left|\partial t_{r,x}/\partial t\right| = 0.1$ (solid red line in Figure 6.2) represents the onset of the weakly nonadiabatic regime.

Alternatively, if nonadiabatic z motions do not affect the transition probability the breakdown would have to come from violation of $\left|\partial t_{r,x}/\partial t\right| << 1$ or $ft_{r,x} << 1$. Since the transitions become totally synchronized and the transition probability reaches unity for $A \approx A_c^{\mathrm{ad}}/2$ (i.e., the amplitude dependent nonadiabatic crossover is far away), this means that the assumptions are violated for frequencies two orders of magnitude below $\max\left|\partial t_{r,x}/\partial t\right| = 1$ and $ft_{r,x} = 1$. If this were true, the fully nonadiabatic regime would extend to very low frequencies and the observed weakly nonadiabatic behavior would not be seen. Since this is not the case, adiabaticity in the z direction must be considered.

The measured nonadiabatic region from 3.3 Hz to 20 Hz falls below $\max\left|\partial t_{r,x}/\partial t\right| = 0.1$ for the majority of the modulation amplitudes. This contradicts the critical exponent μ = 2 obtained from the power-law fits and the frequency dependent bifurcation amplitudes.

The three dimensional potential energy surfaces (Figure 5.5) show that the stable point to saddle point distance is 200 nm in z. If the stable point and saddle point approach as $A \rightarrow A_c^{\mathrm{ad}}$ then there must be motion in the z direction, and another adiabatic condition $\left|\partial t_{r,z}/\partial t\right| << 1$ appears. Assuming the potential is a quartic of the form

$$U_{2D}(x,z) = A\cos(2\pi ft) + \frac{Bx^2}{2} + \frac{Cx^4}{4} + \frac{B_z z^2}{2} + C_{xz}x^2 z$$

the path of the stable point in x and z can be estimated. The coefficients B and C are calculated in Section 5.2. The B_z and C_{xz} coefficients are estimated by the curvature in z and the (x, z) positions of the stable and saddle point when A = 0, respectively. The stable and saddle point positions under adiabatic modulation near A_c^{ad} are shown in Figure 6.3. (The model does not exactly represent the potential in z, underestimating the saddle point to stable point distance.) The red and blue curves show that the stable points travel large distances in z as they move towards the saddle point.

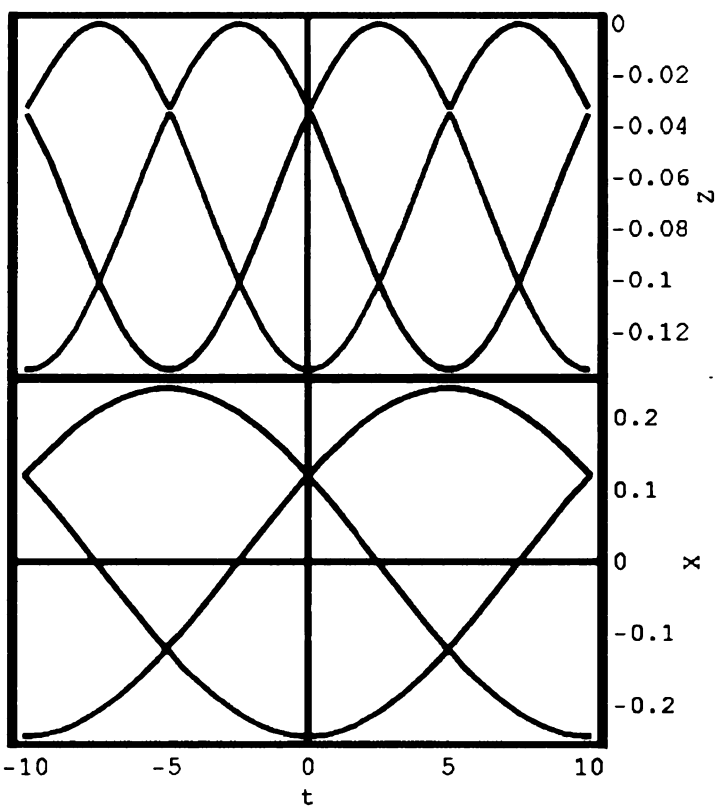

Figure 6.3 Positions of stable and saddle points in a modulated bistable potential. The z and x positions of the stable points (red and blue) and the saddle point (green) approach and recede once per period. In the static potential the stable points are (x, z) = (±0.2 μm, 0.05 μm) and saddle point (x, z) = (0, 0). The stable and saddle points meet at (±0.120 μm, 0.017 μm) and the other stable point is at (0.240 μm, 0.066 μm).

Since it does not appear in the model, the z relaxation time changes are estimated from experimental parameters. The experimental potential is tilted by changing the laser

power, changing the gradient force in all three dimensions. The change in relaxation time $\Delta t_{r,z}$ is inversely proportional to the change in power ΔP, $(\Delta t_{r,z})^{-1} \propto \Delta\omega^2 \propto \Delta F \propto \Delta P$. The power is modulated $P = P_0(1 + \delta P \cos(2\pi f t))$, with $\delta P \approx 0.15$ when $A = A_c^{\mathrm{ad}}$. The maximum $\partial t_{r,z}/\partial t$ over one period is

$$\max\left|\partial t_{r,z}/\partial t\right| = \delta P t_{r,z}(2\pi f)\max\left|\sin(2\pi f t)\right| = \delta P t_{r,z}(2\pi f).$$

The amplitude at which $\left|\partial t_{r,z}/\partial t\right| = 0.1$ is

$$\frac{A}{A_c^{\mathrm{ad}}} = \frac{0.1}{2\pi(0.15) f t_{r,z}}.$$

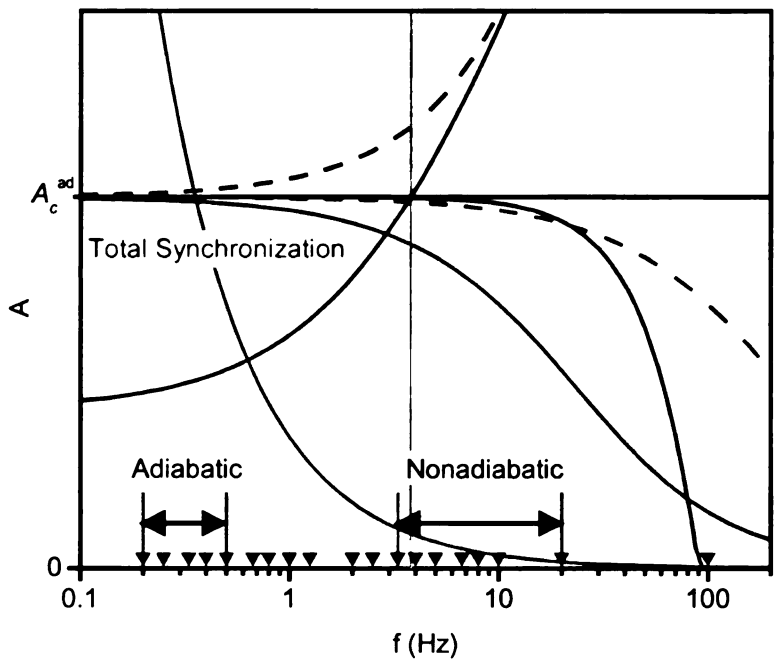

Figure 6.4 Comparison of experimental data with adiabatic criteria on the x and z relaxation rates. The magenta line represents $\left|\partial t_{r,z}/\partial t\right| = 0.1$. The data with $\mu = 2$ are fully contained in the z weakly nonadiabatic regime while the adiabatic data are outside.

The $|\partial t_{r,z}/\partial t| = 0.1$ condition (magenta line in Figure 6.4) falls between the adiabatic and nonadiabatic data. $|\partial t_{r,z}/\partial t| = 0.1$ predicts that modulation below $f = 0.35$ Hz is adiabatic very close to $A = A_b$ and $f = 3.3$ Hz is weakly nonadiabatic above $A = 0.1A_b$, agreeing with observations.

As promising as this explanation appears, it conflicts with approximations made in the theory [45]. The transitions are assumed to take place only when $t = 0$, A is closest to A_b, $t_{r,x}$ is a maximum, and $\max|\partial t_{r,x}/\partial t|$ occurs. Equivalent assumptions are $W << f$ or $\Delta U_0 >> k_B T$; transitions are rare until the barrier height is substantially reduced during modulation. In the z direction, $\max|\partial t_{r,z}/\partial t|$ occurs when $t = 1/2f$ (when $P = P_0$). At $t = 0$, $|\partial t_{r,z}/\partial t| = 0$ and the condition $|\partial t_{r,z}/\partial t| << 1$ is always true.

The assumption $\Delta U_0 >> k_B T$ is not satisfied in the experimental system. The static barrier height $\Delta U_0 = 6\ k_B T$. The transition probability histogram (Figure 5.18b) shows that the transitions are distributed over approximately half of the period (including the time $|\partial t_{r,z}/\partial t|$ is near the maximum) with a peak at $t = 0$. The mean transition rate $W \approx 0.2$ Hz, with modulation frequency $f = 3.3$ Hz. The total synchronization effect is a direct consequence of the low barrier. Even small modulation amplitudes ($A < A_c^{\mathrm{ad}}/2$ in Figure 6.4) can increase the instantaneous escape rate W_A enough so the particle makes a transition every period. Under the $\Delta U_0 >> k_B T$ assumption this only occurs very close to the bifurcation amplitude.

It is possible that the power-law frequency scaling does not even apply under the experimental conditions. More likely, the power-law relation $\ln(W) \propto |A_c^{\mathrm{sl}} - A|^{\mu}$ has a

combination of the adiabatic $\ln(W) \propto \left|A_c^{ad} - A\right|^{3/2}$ and the weakly nonadiabatic $\ln(W) \propto \left|A_c^{sl} - A\right|^{2}$, depending on when the particle escapes. If the transition occurs when $\left|\partial t_{r,x}/\partial t\right| \approx 1$ (close to $t = 0$) then $\mu = 2$. If $\left|\partial t_{r,x}/\partial t\right| << 1$, then $\mu = 3/2$. The difference between these effects is too small to see with the current uncertainties in W.

Finally, there is the $ft_{r,z} << 1$ condition that is violated for $f \approx 3.8$ Hz, and should obscure any weakly nonadiabatic effects due to the z relaxation time. If the particle can not respond to changes in the z potential, it will not respond to changes in the rate of change of the potential. In other words, the particle cannot lag behind the modulation (weakly nonadiabatic) if it can not follow the modulation at all (nonadiabatic).

However, there is definitely some weakly nonadiabatic behavior observed at modulation frequencies between 3.3 Hz and 20 Hz. Estimations of the x weakly nonadiabatic boundary show that, for the lower end of the frequency range, the modulation amplitude is too low to leave the adiabatic (in x) regime (below the red curves in Figure 6.4). Therefore there must be some weakly nonadiabatic effect in z. Why it is not concealed by the nonadiabatic behavior is unknown.

6.3. Summary and Conclusions

The following phenomena have been observed and measured in the periodically modulated bistable potential.

Adiabatic regime

- The adiabatic regime exists for frequencies which satisfy $|\partial t_{r,x}/\partial t| << 1$, $ft_{r,x} << 1$, $|\partial t_{r,z}/\partial t| << 1$, and $ft_{r,z} << 1$. Slow modulation with respect to x alone is not sufficient for complete adiabaticity.
- The transitions may become totally synchronized for A well below A_b, obscuring asymptotic behavior for experiments with poor sensitivity.
- The $\ln(W)$ vs. A power law fit finds μ = 1.5 ± 1.9, consistent with the predicted μ = 3/2 [45].
- The modulation frequencies required are so slow that the uncertainty in the mean transition rate is very large. To increase the number of transitions recorded the measurements at a single amplitude and frequency requires system stability improvement by 1 to 2 orders of magnitude.

Nonadiabatic regime

- The region of total synchronization moves above A_b.
- The critical exponent is μ = 2.3 ± 0.3, agreeing with the predicted μ = 2 for the weakly nonadiabatic regime [45]. This represents the first measurement of a new critical exponent for nonadiabatic critical behavior.
- The critical amplitude A_c is linearly dependent on the modulation frequency. This confirms a new prediction of the theory for nonadiabatic modulation. The slope is larger than predicted in [45] due to uncertainties in the quartic approximation parameters near $A = A_b$.

- The nonadiabatic regime appears to result from violation of $|\partial t_{r,z}/\partial t| << 1$, not $|\partial t_{r,x}/\partial t| << 1$. Thus we find that, in the three dimensional systems, $t_{r,z} > t_{r,x}$ and the relaxation in the z direction can not be neglected.
- Theory and simulations cannot yet go beyond one dimension: thus experiments should stimulate more sophisticated theory and large-scale simulation.

6.4. Suggestions for Further Work

It would be advantageous to decrease the statistical uncertainty in the measurement of the critical exponents near the bifurcation point. There is a lower limit on the mean transition rate uncertainty, proportional to $1/\sqrt{N}$. The uncertainty is reduced by increasing the data acquisition time, but at some point the optical system drifts and systematic errors appear. The interval of stability can be extended by removing temperature fluctuations from the lab, through a heating or cooling unit separate from the building controls. This would reduce differential thermal expansion as a source of drift. The beam positions could be controlled using an active beam steering system. The gimbal mirrors in the system could be replaced with 1- or 2-axis, servo controlled mirrors. A position sensitive detector in a plane confocal with the objective's focal plane would measure the change in beam position and feedback control electronics would change the mirror angle, correcting for the motion. This would eliminate the small beam motions observed in Section 4.3.4 and larger, long term pointing changes.

With long term stability measured over days instead of hours. W_0 could be reduced by an order of magnitude, moving the total saturation boundary in Figure 6.1 to the left. The power law dependence in the adiabatic regime could then be measured for

longer times to reduce uncertainty. The amplitude dependent crossover from adiabatic to nonadiabatic could be mapped, taking many small amplitude steps near $A = A_b$. The frequency regimes based on the z relaxation time could be explored to determine the effects of nonadiabaticity in a universally stable potential ($U'' > 0$) that is orthogonal yet coupled to the bistable direction.

The two-beam optical trap is limited to a small range of potentials, based on the beam powers, beam separation, convergence angle, and particle size. A spatial light modulator (SLM) could be used to create a potential of arbitrary shape. The SLM modifies the phase profile of an incident laser beam. Focused by the objective lens, the Fourier transform of the image appears in the focal plane. The shape and size of the desired intensity gradient would be controlled through the SLM phase profile. This also has the advantage of constant trap separation, since the intensity distribution is set by the phase profile and not individual optical elements. Interesting avenues of study would be transitions in spatially extended systems and modification of the relaxation time in the y and z directions.

Appendix A Quantitative Theory of Optical Trapping

The two laser-induced forces in optical trapping are the force of the radiation scattering off of the dielectric sphere and the forces due to the intensity gradient. The scattering force pushes the sphere in the direction of the beam propagation (axial direction), and the gradient force acts towards the region of highest field gradient. In a stable three dimensional trap the gradient force in the axial direction exceeds the scattering force to prevent the particle from being pushed out of the focal point.

Theoretical calculations of these forces are simplified in two regimes. In the Rayleigh regime, where the particle is much smaller than the wavelength of the laser, the particle is approximated as a dipole induced by the trapping field. In the ray optics or Mie regime, where the particle is much larger than the wavelength and the beam waist, the principles of geometrical optics are used to calculate the deflection of the individual rays.

A.1 Rayleigh regime

A Rayleigh particle is much smaller than the wavelength of the trapping beam ($a << \lambda$), and the time varying electric field is approximated as uniform over the volume of the particle and, for a TEM_{00} beam, Gaussian over the beam waist.

A dielectric particle in an electric field will have an induced dipole moment of $\mathbf{p} = \alpha\mathbf{E}$, where α is the polarizability. In an anisotropic electric field, the force on the particle is

$$\text{(A.1)} \quad \mathbf{F} = (\mathbf{p}\cdot\nabla)\mathbf{E} = \alpha(\mathbf{E}\cdot\nabla)\mathbf{E} = \frac{1}{2}\alpha\nabla|E|^2 - \mathbf{E}\times\nabla\times\mathbf{E} = \frac{1}{2}\alpha\nabla|E|^2$$

The force on the dielectric particle is directed towards the region of highest electric field gradient, independent of the direction of the field. This phenomenon is called dielectrophoresis.

A dipole in an oscillating electric field scatters waves in all directions, changing the magnitude and direction of the electric field. The momentum transferred to the particle pushes it in the direction of the beam with a magnitude proportional to the square of the dipole moment.

The polarizability of a spherical Rayleigh particle in a uniform electric field is calculated from Maxwell's equations [55]. In terms of the effective index of refraction m, the ratio of the indices of refraction of the particle (n_s) and the surrounding medium (n_b) and the particle radius a, $\alpha = a^3\left(\frac{m^2-1}{m^2+2}\right)$. The intensity of the focused Gaussian beam at a point (x,y,z) measured from the center of the beam waist is

$$\text{(A.2)}\quad I(x,y,z) = \left(\frac{2P}{\pi w_0^2}\right)\frac{1}{1+\left(2z/kw_0^2\right)^2}\exp\left[-\frac{2\left(x^2+y^2\right)/w_0^2}{1+\left(2z/kw_0^2\right)^2}\right]$$

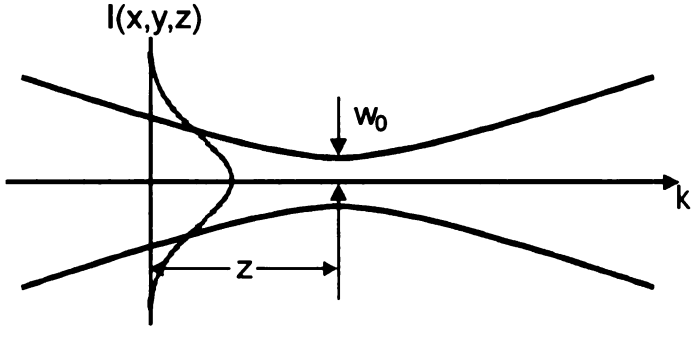

Figure A.1 Gaussian beam intensity profile near a beam waist.

where P is the total power, w_0 is the beam waist radius, and k is the wave number. The beam propagates in the z direction (Figure A.1). The intensity is proportional to the square of the electric field $I(x,y,z)=\frac{n_b\varepsilon_0 c}{2}|E(x,y,z)|^2$.

The scattering force [55] is proportional to the square of the volume and the intensity.

$$\mathbf{F}_{\text{scat}}(x,y,z)=\frac{128\pi^5 a^6 n_b}{\lambda^4 c}\left(\frac{m^2-1}{m^2+2}\right)^2\left(\frac{2P}{\pi w_0^2}\right)\frac{1}{1+2z/kw_0^2}\exp\left[-\frac{2(x^2+y^2)/w_0^2}{1+2z/kw_0^2}\right]\hat{z}$$

$$=\frac{128\pi^5 a^6 n_b}{\lambda^4 c}\left(\frac{m^2-1}{m^2+2}\right)^2 I(x,y,z)\hat{z}$$

From equations (A.1), the gradient force [86]

$$\mathbf{F}_{\text{grad}}(x,y,z)=\frac{2\pi a^3 n_b}{c}\left(\frac{m^2-1}{m^2+2}\right)\nabla I(x,y,z)$$

is cylindrically symmetric. The radial component $\mathbf{F}_{\text{grad},r}$ $\left(r=\sqrt{x^2+y^2}\right)$ and axial component $\mathbf{F}_{\text{grad},z}$ are

$$\mathbf{F}_{\text{grad},r}(x,y,z)=-\frac{2\pi a^3 n_b}{c}\left(\frac{m^2-1}{m^2+2}\right)\frac{4r/w_0^2}{1+(2z/kw_0^2)^2}I(x,y,z)\hat{r}$$

$$\mathbf{F}_{\text{grad},z}(x,y,z)=-\frac{2\pi a^3 n_b}{c}\left(\frac{m^2-1}{m^2+2}\right)\frac{8r/(kw_0^2)^2}{1+(2z/kw_0^2)^2}\left(1-\frac{2r^2}{1+(2z/kw_0^2)^2}\right)I(x,y,z)\hat{z}.$$

The maximum magnitude of $\mathbf{F}_{\text{grad},r}$ occurs at $r=w_0/2$, $z=0$ and for $\mathbf{F}_{\text{grad},z}$, $r=0$, $z=\pm kw_0^2/2\sqrt{3}$. For the trap to be stable in three dimensions, the gradient force must be larger than the scattering force, or

$$\text{(A.3)}\quad R = \frac{F_{\text{grad},z}}{F_{\text{scat}}} = \frac{\sqrt{3}\lambda^5}{128\pi^5 a^3 w_0^2}\left(\frac{m^2-1}{m^2+2}\right)^{-1} \geq 1,$$

where $\mathbf{F}_{\text{grad},z}$ is computed at its maximum.

For a silica sphere in water, $m = 1.46/1.33 = 1.1$. A helium-neon laser focused to a diffraction limited spot will have a beam waist diameter $2w_0 \approx \lambda = 633\text{nm}$. The condition (A.3) is satisfied for sphere diameter $2a \leq 0.5$ μm. (Particles this size are no longer Rayleigh particles.)

For a total power of 100 mW, the maximum forces on a 0.1 μm diameter sphere are

$$\mathbf{F}_{\text{grad},r}(x,y,z) = 6.4\times10^{-13}\ \text{N}$$

$$\mathbf{F}_{\text{grad},z}(x,y,z) = 2.2\times10^{-13}\ \text{N}$$

$$\mathbf{F}_{\text{scat}}(x,y,z) = 2.1\times10^{-14}\ \text{N}$$

A.2 Ray optics regime

For particle diameters much larger than the wavelength ($a >> \lambda$), the wavelength is assumed to be zero, the beam is decomposed into rays and treated with geometrical optics. Rays reflect and refract at surfaces and diffraction is ignored. An off axis ray enters the particle and is refracted towards the particle center. The ray is refracted again as it exits. The photon momentum change at each point creates a force on the particle proportional to the intensity.

In Figure A.2, a single ray with momentum $n_b P/c$ is incident on the sphere at an angle θ. The ray is reflected or transmitted with probabilities R and T, the Fresnel

reflection and transmission coefficients. The transmitted beam travels in a straight line until it reaches the other side of the sphere, where it will again be reflected or transmitted. Incident on the n^{th} interface the ray will have decreasing power PTR^{n-2}.

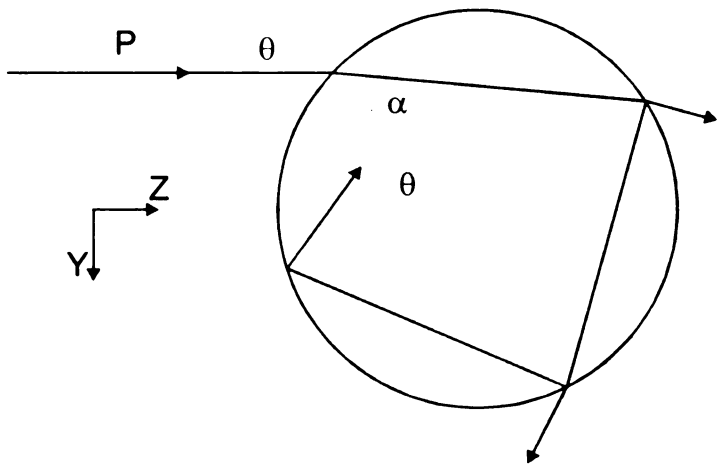

Figure A.2 A single ray incident on the sphere at angle θ is partially transmitted with an angle or refraction α. The beam is either transmitted or reflected at the next surface.

The force in the direction of the initial beam, the scattering force, is

$$F_z \equiv F_s = \frac{n_b P}{c}\left(1 + R\cos 2\theta - \frac{T^2[\cos(2\theta - 2\alpha) + R\cos 2\theta]}{1 + R^2 + 2R\cos 2\alpha}\right),$$

where α is the angle of refraction $n_b \sin\theta = n_s \sin\alpha$. The force in the y direction is the gradient force.

$$F_y \equiv F_g = \frac{n_b P}{c}\left(R\sin 2\theta - \frac{T^2[\cos(2\theta - 2\alpha) + R\cos 2\theta]}{1 + R^2 + 2R\cos 2\alpha}\right).$$

The total force is calculated by integrating over all incident rays in the tightly focused trapping beam. For a particle displaced a distance S in the z direction (Figure A.3), the ray converges to the focal point with angle ϕ. The incident angle θ is calculated from $a\sin\phi = S\sin\theta$. Unlike the Rayleigh regime, the force does not depend on the size of the particle.

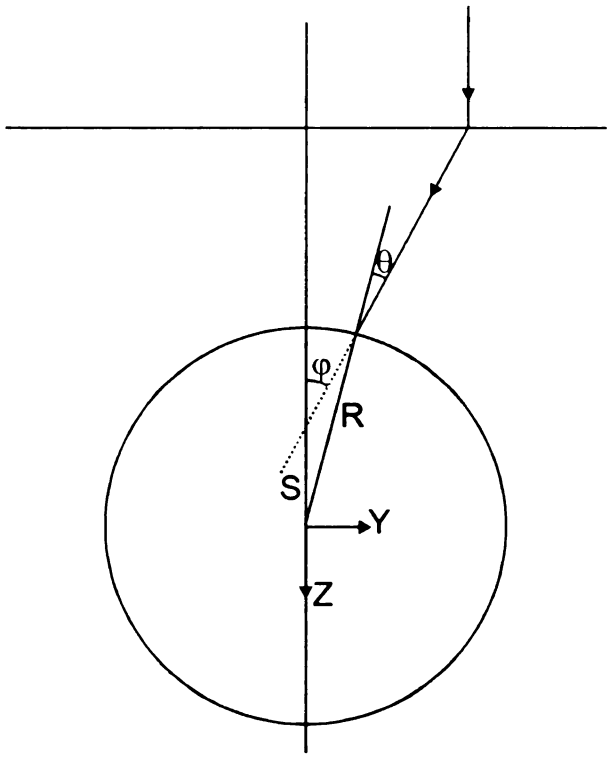

Figure A.3 Calculation of force from a single focused ray. The ray converges with angle ϕ to a point S away from the particle center. Momentum transfer causes a force in the negative z direction.

The force is integrated numerically [82]. It is advantageous to write the force in terms of the efficiency Q that depends on the particle displacement, $F = n_b PQ/c$. The maximum value of Q = 2, corresponding to total backwards reflection. With increasing convergence angle, the efficiency rises until it reaches a maximum near 80°. The outermost rays contribute most to the trapping force.

Due to cylindrical symmetry, the force in the transverse direction F_g will be zero. The axial efficiency increases with displacement from the focal point. It reaches a maximum $Q \approx 0.4$ when the particle is one sphere radius from the focal point. At this point the outermost rays are closest to the angle of maximum efficiency.

For a displacement S' in the transverse direction, the force is again computed from the integral over individual rays. The incident angle θ is $a\sin\phi = S'\sin\theta$. The

integration is more involved because the cylindrical symmetry is broken. The trapping efficiency increases with particle position until it reaches a maximum of 0.3 at displacements of one sphere radius.

The magnitude of these forces is estimated from $F = n_b PQ/c$. For a particle in water (n_b = 1.33) trapped by 1 mW total power, the force at the maximum z displacement (Q = 0.4) is 1.8×10^{-12} N ≈ 1.8 pN. The force depends on the convergence angle and the particle position, but not the particle size.

A.3 Intermediate Regime

In the intermediate size regime, the beam waist diameter and wavelength of the trapping beam are on the order of the size of the particle. Neither of the prior approximations is valid. Near the beam waist the Gaussian intensity profile in equation (A.2) no longer satisfies Maxwell's equations and the forces calculated from the electromagnetic field interactions are no longer accurate. The accuracy is improved [87,92-95] by introducing a higher order correction to the Gaussian beam in terms of $s = \frac{1}{kw_0} = \frac{1}{2\pi}\frac{\lambda}{w_0}$. Barton and Alexander [87] provide a fifth-order correction to the Gaussian beam. The correction becomes less accurate as s approaches one. For s = 0.2 ($w_0 \approx 0.8\lambda$), the percent error is 1.2%. However, for the 0.6 μm diameter sphere used in this experiment there is no analytical formulation of the potential.

Appendix B Dependence of Trapping Forces on Optical System

The experiments in this thesis measure the dynamics of an overdamped particle in a potential with a small range of possible curvatures. These parameters can be modified by changing the optics, particle size, laser wavelength, and surrounding medium. To reach the underdamped regime the damping rate Γ can be decreased by using a larger particle or a lower viscosity. The Kramers crossover [12] from $\Gamma/\omega >> 1$ to $\Gamma/\omega << 1$ can be explored by changing the surrounding medium, thus increasing the trap curvature ω and decreasing Γ. This appendix estimates the effect of changing certain optical parameters on the trapping force, calculated in the Rayleigh regime.

The trapping force is calculated from the induced dipole moment, resulting in equation (3.2) (Section 3.1.2),

$$\text{(B.1)} \quad F_{\text{grad}} = -\frac{n_b^3 a^3}{2}\left(\frac{m^2-1}{m^2+2}\right)\nabla|\mathbf{E}|^2,$$

where a is the particle diameter, n_b is the index of refraction of the surrounding medium, and m is the effective index (n_s/n_b). The damping rate is given by the Stokes damping rate $\Gamma = \frac{6\pi\eta a}{m} = \frac{9\eta}{2\rho a^2}$, for a sphere where η is the viscosity and ρ is the density.

The electric field is related to the intensity of the focused beam. In cgs units $I(r,z) = \frac{n_b c}{8\pi}|\mathbf{E}(r,z)|^2$. The TEM_{00} laser has intensity profile $I(r) = I_0 \exp\left(-r^2/r_1^2\right)$. For

a focused Gaussian beam propagating in the z direction with a focal point at $z = 0$ the width $r_1 = r_0\sqrt{1+z^2/z_R^2}$ (Section 4.1.6) and

$$\text{(B.2)}\quad I(r,z) = \frac{P}{\pi r_0^2\left(1+z^2/z_R^2\right)}\exp\left(\frac{-r^2}{r_0^2\left(1+z^2/z_R^2\right)}\right)$$

for a beam with total power P. The beam waist radius r_0 and Rayleigh range z_R are functions of wavelength λ and convergence angle θ, $r_0 = 2\lambda/\pi\theta$. and $z_R = 4\lambda/\pi\theta^2$.

Substituting (B.2) into (B.1),

$$F_{\text{grad}} = \frac{4\pi n_b^2 a^3}{c}\left(\frac{m^2-1}{m^2+2}\right)\nabla I$$
$$= \frac{4n_b^2 a^3 P}{c}\left(\frac{m^2-1}{m^2+2}\right)\nabla\left[\frac{1}{r_0^2\left(1+z^2/z_R^2\right)}\exp\left(\frac{-r^2}{r_0^2\left(1+z^2/z_R^2\right)}\right)\right]$$

In cylindrical coordinates, $\nabla = \hat{r}\frac{\partial}{\partial r} + \hat{\theta}\frac{1}{r}\frac{\partial}{\partial\theta} + \hat{z}\frac{\partial}{\partial z}$. The radial and axial force components are

$$\text{(B.3)}\quad F_{\text{grad,r}} = -\frac{4n_b^2 a^3 P}{c}\left(\frac{m^2-1}{m^2+2}\right)\frac{2r}{r_0^4\left(1+z^2/z_R^2\right)^2}\exp\left(\frac{-r^2}{r_0^2\left(1+z^2/z_R^2\right)}\right), \text{ and}$$

$$\text{(B.4)}\quad F_{\text{grad,z}} = -\frac{8n_b^2 a^3 Pz}{cr_0^2 z_R^2\left(1+z^2/z_R^2\right)^2}\left(\frac{m^2-1}{m^2+2}\right)\left(1-\frac{2r^2}{r_0^2\left(1+z^2/z_R^2\right)}\right)\exp\left(\frac{-r^2}{r_0^2\left(1+z^2/z_R^2\right)}\right).$$

The potential curvature is calculated from the spring constant (the spatial derivative of the force) near the trap center. The curvatures are

$$\omega_r^2 \propto \left.\frac{\partial F_{\text{grad,r}}}{\partial \text{r}}\right|_{z=0} \propto \frac{n_b^2 a^3 P}{r_0^4}\left(\frac{m^2-1}{m^2+2}\right)$$

$$\omega_z^2 \propto \left.\frac{\partial F_{\text{grad,z}}}{\partial z}\right|_{r=0} \propto \frac{n_b^2 a^3 P}{r_0^2 z_R^2\left(1+z^2/z_R^2\right)^2}\left(\frac{m^2-1}{m^2+2}\right)$$

The adjustable parameters in the optical system are beam power, sphere size, index of refraction of the medium, laser wavelength, and objective lens numerical aperture. The force depends linearly on the beam power. The sphere size affects the trapping force and the damping rate. $F_a \propto a^3$, and $\Gamma_a \propto a^{-2}$, therefore $\Gamma_a/\omega_a \propto a^{-3.5}$. Part of the index of refraction dependence is hidden in m in (B.3) and (B.4), $F_n \propto n_b^2\left(\frac{m^2-1}{m^2+2}\right)$.

The wavelength and convergence angle θ (where $\theta = \sin^{-1}(NA/n_m)$ and n_m is the index of the imaging medium) are implicitly included via the beam waist radius and Rayleigh range. For small displacements from the beam waist, $F_{\text{grad,r}} \propto r/r_0^4$ and $F_{\text{grad,z}} \propto z/r_0^2 z_R^2$. The wavelength dependence is the same for both directions, $F_\lambda \propto \lambda^{-4}$. The convergence angle dependence is stronger for the axial force, $F_{\theta,\text{r}} \propto \theta^4$ and $F_{\theta,\text{z}} \propto \theta^6$.

Table B.1 compares the forces for multiple trapping systems, based on the curvatures measured for the system in this experiment. The force is $\mathbf{F} = m\omega^2\mathbf{r}$, where the maximum radial force is calculated at (r, z) = $\left(r_0/\sqrt{2},0\right)$ and the maximum axial force at $\left(0, z_R/\sqrt{3}\right)$. The damping rate is calculated for a silica sphere (ρ = 2200 kg/m^3). The relaxation rate t_r^{-1} is calculated from the curvature and damping rate. Force units are N and frequency units are s^{-1} or Hz.

The first row has the forces for the current experimental setup. The curvatures are estimated ω_r = 200,000 s^{-1} and ω_z = 20,000 s^{-1}. The first two rows are the forces using

different objectives, 100x dry with NA 0.9 and 60x with NA 0.8. The next two rows use the original objective but change the particle size to a = 1 μm and a = 0.1 μm. The next three rows change laser wavelength from 633 nm to 488 nm, 532 nm, and 1064 nm. The final rows change the medium from water to air, with larger particles. The final row shows the reduction of the damping rate at reduced pressure (with $\eta = 0.01\,\eta_{atm}$).

Table B.1 Trapping forces for various trapping parameters.

	F_r max (N)	F_z max (N)	ω_r (s^{-1})	ω_z (s^{-1})	$t_{r,r}^{-1}$ (Hz)	$t_{r,z}^{-1}$ (Hz)	Γ (s^{-1})
original	2.2×10^{-12}	1.5×10^{-14}	200000	20000	250	2.5	2.50×10^{7}
100x dry	1.9×10^{-12}	1.2×10^{-14}	180000	1700	210	1.9	2.50×10^{7}
60x dry	1.1×10^{-12}	5.9×10^{-15}	120000	9800	100	0.6	2.50×10^{7}
a = 1 μm	8.1×10^{-11}	5.6×10^{-13}	200000	20000	2800	28	2.3×10^{6}
a = 0.1 μm	8.1×10^{-14}	5.6×10^{-16}	200000	20000	28	0.28	2.3×10^{8}
λ = 488 nm	3.7×10^{-12}	2.6×10^{-14}	340000	34000	720	7.2	2.50×10^{7}
λ = 532 nm	4.8×10^{-12}	3.3×10^{-14}	280000	28000	510	5.1	2.50×10^{7}
λ = 1064 nm	4.6×10^{-13}	3.2×10^{-15}	71000	7100	32	0.32	2.50×10^{7}
Air, 2 μm	6.4×10^{-10}	3.5×10^{-12}	180000	14000	47000	290	1.04×10^{5}
Air, 3 μm	2.1×10^{-9}	1.2×10^{-11}	180000	14000	110000	660	4.60×10^{4}
Air, 5 μm	9.9×10^{-9}	5.4×10^{-11}	180000	14000	300000	1800	1.7×10^{4}
Vacuum	9.9×10^{-9}	5.4×10^{-11}	180000	14000	3.0×10^{7}	180000	1.7×10^{2}

The current experiment is in the overdamped regime (Γ/ω = 125). To reach the underdamped regime a larger particle should be trapped in air. Removing the air with a vacuum pump reduces the damping further.

Appendix C Coherence Measurements of the Millennia Laser

To increase the flexibility in the optical system the Spectra-Physics Millennia laser was installed. It emits 5W at 532 nm, for a maximum of 2.5 W per beam in the current experiment. By comparison, the HeNe lasers are limited to a maximum of 12 mW entering the microscope (see Section 4.1). The greater power allows novel trapping systems, such as multiple traps or scanning beam traps.

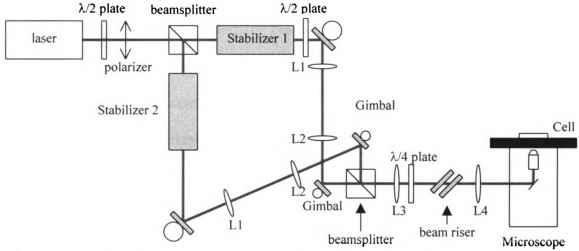

Figure C.1 Single laser optical trapping apparatus. The single beam was split into two equal intensity beams with the first beam splitter. Each beam was stabilized, expanded by lenses L1 and L2, and positioned with the gimbal mounted mirrors before being recombined at the second, polarizing beam splitter. Beam 1's polarization was rotated by 90° by a half-wave retarder. The beams were expanded again by lenses L3 and L4 and elevated by the beam riser before entering the microscope. A half-wave retarder and Glan calcite polarizer were used to attenuate the beam after it exited the laser.

The single laser beam was split into two arms, each with a beam power stabilizer and beam steering optics. The beams were recombined before entering the microscope (Figure C.1), essentially creating a Mach-Zender interferometer. To prevent interference one arm was made 15 cm longer, multiple times the expected coherence length of 3 cm.

Subsequent observations showed that this did not prevent interference. The actual coherence length was predicted to be many meters.

To create two independently steerable optical traps the single laser was split into two beams by a nonpolarizing beam splitter (Figure C.1). A half-wave retarder and polarizer were positioned before the beam splitter for coarse power control. Each beam went through a LS-PRO stabilizer and the beam expanding lens pair L1-L2. Beam 1's polarization was rotated by 90° by a half-wave retarder. Gimbal mounted mirrors were used to change the angle of the beams entering the objective lens (Section 4.1.7). The beams were recombined at a polarizing beam splitter. The beam, emitted from the laser head at a height of 4.5 inches, was elevated to 8.5 inches with a beam riser (i.e., a periscope). A quarter-wave plate transformed the orthogonal linear polarizations into orthogonal circular polarizations. The other elements in Figure C.1 are described in Section 4.1.

The orthogonally polarized and supposedly uncorrelated beams interfered in the focal plane of the objective. The reflections of the beams from the cell's glass/water interface were visible on the Sony monitor (Section 4.1.8). As expected, a circular diffraction pattern was present for a single beam. An interference pattern appeared when both beams were viewed, changing shape with changing beam separation. This occurred for orthogonally polarized beams with optical path lengths differing by more than 5 coherence lengths.

Finite coherence length is derived from the spectral properties of a laser [96]. A laser with delta function spectral output (i.e., all photons emitted have the exact same wavelength) has an infinite coherence length. If split and recombined in an

interferometer the beams always interfere with maximum fringe visibility. A laser with finite width spectral output emits multiple wavelengths. The phase between the photons increases as the beam propagates. In an interferometer, if the optical path length difference is large enough the phases become uncorrelated. The beams no longer interfere and are considered incoherent.

Assuming a Gaussian spectral density with width $\Delta\nu$ the coherence length $l_c = c/\Delta\nu$. For gas lasers the width ranges from more than 10 GHz (l_c = 3 cm) to less than 5 MHz (l_c = 60 m). The quoted spectral line width of the Millennia laser is 15 GHz, for l_c = 2 cm. With the 15 cm path length difference in Figure C.1 there should have been no visible fringes.

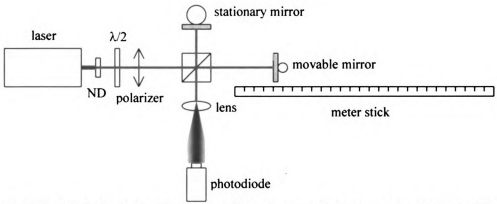

Figure C.2 Michelson interferometer for coherence length measurements. The laser is attenuated using a neutral density filter (ND) and the half-wave retarder/polarizer combination. The beams, split by the beam splitter, are sent to two mirrors. The mirror position was changed to vary the path length, using a meter stick to measure position. The combined beams were expanded by the 25 mm focal length lens and the interference pattern sampled by the photodiode.

To measure the actual coherence length the Michelson interferometer in Figure C.2 was constructed. The beam was split by the beam splitter and sent to two mirrors. The path length was adjusted by moving one of the mirrors in the direction of beam propagation, with a meter stick used to measure position. The path length change was

twice the change in mirror position. The beams were recombined at the beam splitter, expanded by a 25 mm focal length lens, and measured by a photodiode (Centronic OSD155T silicon photodiode). The distance between fringes was 5-10 times the width of the active area of the photodiode to reduce spatial averaging.

The coherence length appears as a reduction of visibility $V = (I_{max} - I_{min})/(I_{max} + I_{min})$, defined in terms of the maximum and minimum fringe intensity. The maximum visibility V = 1, for minimum intensity I_{min} = 0. The photodiode output was recorded on a LeCroy 9310AM digital oscilloscope as the static mirror was moved by hand. Typically 5 fringes were cycled, corresponding to 1 μm motion of the mirror. The minimum and maximum photodiode voltages were measured using the cursor functions on the oscilloscope.

Figure C.3 shows the visibility vs. path length difference over nearly 1 meter. The visibility falls rapidly for small path length differences, as expected by the quoted 2 cm coherence length. After 10 cm the visibility *increases*, coming to a peak near 20 cm. The peak structure repeats with period 22 cm and varying amplitude. Repeated measurements show that the peak structure changes over time.

The quoted 15 GHz line width is actually the width of the gain profile. The gain profile determines which longitudinal cavity modes are sustained. The large gain profile was designed to reduce power fluctuations due to mode hopping by including more than 300 modes. Thus the line width of the individual modes is much smaller, on the order of 5 MHz. The output spectrum is a comb structure, with lines spaced approximately 100 MHz apart. The visibility of such a spectrum would be a series of peaks with spacing corresponding to the spectral line spacing, as shown in Figure C.3.

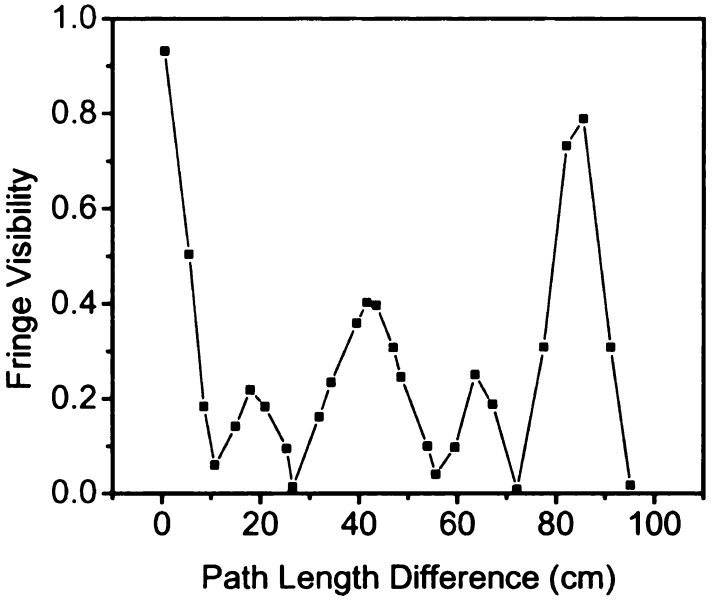

Figure C.3 Visibility vs. path length difference for the Millennia laser. The visibility falls initially, corresponding to the expected 2 cm coherence length. At larger path length differences a periodic structure appears.

In a dual beam system the potential, proportional to the intensity gradient, gains an additional interference induced periodic structure. Figure C.4a shows a typical one dimensional potential in x (solid line) with the intensity distribution (dotted line). Figure C.4b introduces interference effects into the intensity, with resulting potential. The interference pattern is very sensitive to motion of the optical mounts. A position change of 0.1 μm causes a π change in phase, reversing the interference pattern and changing the calculated barrier height by ~20 %. The particle averages over the spatial changes, reducing but not eliminating the effective barrier height changes.

The Millennia diode pumped solid state laser has many advantages over two HeNe lasers, especially in beam power and stability. However, the changes in the potential due to interference and the driving created by interference fluctuations introduce extra noise. Considering these effects, the HeNe lasers are more stable.

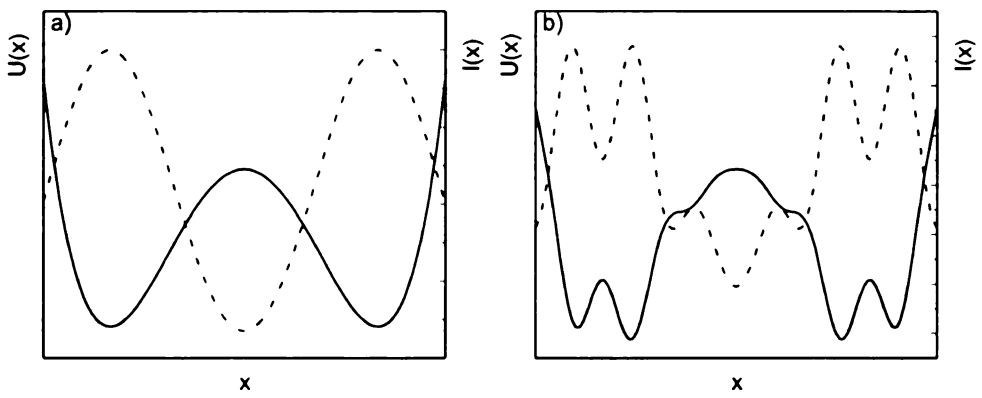

Figure C.4 Change in the potential due to interference. (a) the potential $U(x)$ (solid line) and intensity distribution $I(x)$ (dotted line) for the unperturbed system. (b) interference (visibility = 0.3) added to the intensity distribution, with resulting potential.

Appendix D Trapping in Air and Vacuum

Kramers solved the Fokker-Planck equation in the overdamped and underdamped regimes (with some constraints) [1]. In the intermediate regime the prefactor in equation (2.2) changes with damping, with a peak centered around $\Gamma/\omega \approx 10$ (where Γ is the damping rate and ω is the potential curvature) [12,13]. To explore this range a system for trapping μm diameter silica spheres in air was created, drawing from the prior work of Ashkin and Dziedzic [52-54,97,98] and others [99-101].

The dual beam optical trapping system shown in Figure C.1 was used to trap 2.3 μm to 10 μm diameter silica spheres in air and vacuum. The particles were lifted off the surface using ultrasonic vibration of the substrate and trapped in a single beam. The pressure in the cell was lowered from atmosphere (760 torr) to 250 mtorr using a vacuum pump, crossing from the overdamped to the underdamped regime.

Attempting to create a bistable trap similar to the one made in water, two beams were focused approximately one sphere radius apart by an objective lens. In air (and vacuum) the particle was only confined in the focal plane for a small range of powers. Larger powers "ejected" the particle into an upper stable point, where the laser scattering forces were opposed by gravity instead of the gradient force (see Section 3.1.1). In addition to those at the centers of the beams there were also stable points of unknown origin in the focal plane. (These effects were also observed in a HeNe trapping system, ruling out the Millennia interference (Appendix C) as a cause.)

The particle was stably trapped in a single beam for extended periods. The potential curvature was measured as a function of pressure. The crossover from

overdamped to underdamped was observed in the position fluctuation spectrum, measured as described in Section 3.2.2 [49]. With decreasing pressure the Lorentzian spectrum created by the overdamped particle transformed into a series of peaks, corresponding to the natural frequencies of the potential.

D.1 Apparatus

The dual beam optical trapping system is shown in Figure C.1. The 5 W Millennia laser was used so the beam power could be varied by a factor of 10, or a factor of 3 in potential curvature. The beam was focused by a 40x dry objective lens into the vacuum cell, constructed from a piezoelectric cylinder. The spheres were deposited on the bottom surface and lifted off by 70 – 80 kHz vibration. The cell was moved using the microscope sample stage until a particle was drawn into the trap and the vibration turned off. A mechanical pump slowly removed the air from the cell, to pressures below 100 mtorr.

D.1.1. Trapping Optics

The dual beam optical trap was created by the Spectra-Physics Millennia 5js laser, split into two arms with a beam splitter. Each beam was stabilized and power controlled using an LS-PRO beam power stabilizer. The beams were recombined with a polarizing beam splitter and sent into the microscope. A 40x objective lens (NA = 0.75) with a working distance of 1 mm focused the beams into the cell.

The particle position was tracked using the system outlined in Section 4.2. The 0.071 μm/pixel conversion for a 100x objective becomes 0.27 μm/pixel for a 40x objective after the microscope's internal 1.5x magnifier was removed. Typically the

particles trapped were 4.87 μm (18 pixels) in diameter. The z position determination integrated over a 15 x 15 pixel box with dithered edges (Figure 4.14). The power and angle of illumination from the condenser changed with the stage position due to masking by the cell. Therefore a universal calibration of particle z position vs. integrated brightness was could not be used.

D.1.2. Trapping Cell and Particles

The cell was constructed from a hollow piezoelectric cylinder 20 mm tall, 16 mm inner diameter and 19 mm outer diameter (APC International, product number 42-1020) (Figure D.1). The bottom surface was a 22 mm square piece of #2 cover glass attached with Stycast 1266 epoxy resin. Under vacuum the 0.25 mm thick #2 cover glass flexed 10 μm in the center, compared to the 90 μm for the thinner #1 cover glass needed for the 100x oil immersion objective lens. The top surface was a 1" x 3" glass slide with an o-ring fixture attached with Stycast epoxy. The fixture consisted of two aluminum rings which fit the inner and outer diameters of the cylinder. Between was a 1/8" thick o-ring, sealing to the top of the cylinder. The position of the condenser lens for proper illumination (Section 4.1.8) restricted the height of the cell to 25 mm. A 16 gauge stainless steel pumping line (OD 0.065 inches, ID 0.047 inches) entered through a hole in the side, secured with Huntington's PVC Vacuum epoxy.

The piezoelectric cylinder's vibration was controlled through electrodes coating the inner and outer walls. The inner wall was placed in electrical contact with the stainless steel pumping tube using silver paint. The outer surface was connected to a 24 gauge copper wire, held in place by an o-ring. The cylinder was driven by a SRS DS345

function generator amplified by the HP 463A Precision AC Amplifier, supplying a maximum square wave amplitude of 40 V_{pp} at 100 kHz.

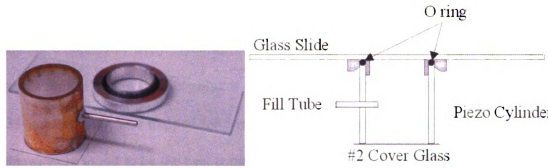

Figure D.1 Vacuum cell photograph and schematic. The cell was constructed from a piezoelectric cylinder with a #2 cover glass epoxied to the bottom. The removable top was a 1 inch by 3 inch glass slide, sealed with an o-ring held in place by two aluminum rings. The air was pumped out through a stainless steel tube entering through a hole in the side.

The trapped particles were 4.87 μm diameter silica spheres (Bangs Labs SS04N/4745). The particles were deposited on the bottom surface of the cell with a spatula. Few enough particles were introduced so regions of the bottom surface were empty. After a sphere was trapped it was moved to an empty region to prevent additional distortion of the beam profile by the other particles.

The piezoelectric cylinder was driven with a 2 V_{pp} square wave at ~76 kHz, near its resonance frequency. A small fraction of the spheres stuck to the surface overcame the electrostatic attraction and lifted off the surface. The moving spheres fell into two categories: "bouncers" and "floaters". The bouncers immediately flew out of the field of view of the microscope. Floaters levitated 10 to 20 μm above the surface at the vibrational nodes of the cell bottom. The cell was moved with the sample stage until a single particle was trapped in a single beam and the vibration shut off.

Larger spheres were easier to dislodge but required more beam power to trap. Also, they were more likely to move to the trap's higher stable points. Smaller spheres were more difficult to remove from the surface and required a smaller trapping power (making a shallower trap). Adding 10 μm spheres to a cell containing smaller spheres created more floating smaller spheres through collisions. The smallest sphere captured, 2.35 μm diameter, was trapped for 5 minutes before escaping. The 3.5 μm and 4.87 μm spheres were found to be the best compromise. However, no bistable potential with both stable points in the objective's focal plane was created.

D.1.3. Trapping in a Vacuum

The cell was evacuated using a mechanical pump, connected to the cell through Tygon and copper tubing. The cell's 16 gauge pumping line was connected to 6 inches of 1/16 inch inner diameter Tygon tubing. The tubing ended at a 16 gauge tube hard soldered to a ¼ inch copper adapter and connected to a compression fit tee. The other ends of the tee led to the pressure measurement devices and the pump (Figure D.2).

The pressure was measured using a 1 atmosphere gauge and a 1 torr capacitance manometer (MKS Baritron 220). The gauges were connected to the tee with 40 feet of ¼ inch copper tubing, matching the flow impedance of the 1/16 inch ID Tygon tubing. The pumping end of the tee was connected to a roughing valve and a needle valve in parallel, both mounted to the optical bench. The Franklin Electric mechanical pump was sitting on the floor, connected to the valves through a 4 inch diameter, 16 inch long helix of ¼ inch copper tubing. The helix helped prevent pump vibrations from reaching the optical bench.

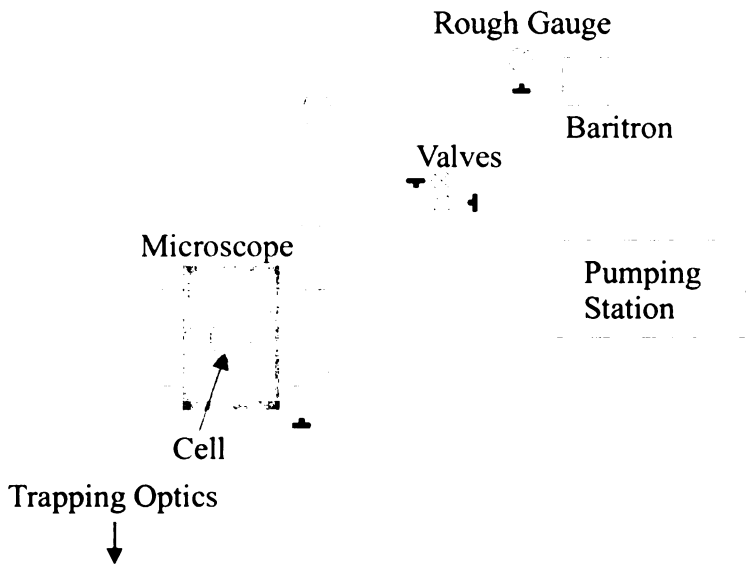

Figure D.2 Schematic of the pumping system. (top view) The cell, positioned on the microscope stage, was connected to the pumping line and pressure measurement line with Tygon tubing. The pumping line was separated from the cell by a roughing valve and a needle valve for fine control of the pumping rate. The pressure in the cell was measured at the end of 40 feet of copper tubing, with flow impedance equivalent to the 6 inches of Tygon tubing. The pressure was measured by a 0 to 1 atmosphere gauge and a capacitance manometer (Baritron). The trapping optics were below the microscope (not pictured).

The particle was trapped before the cell was pumped down. Immediately after spheres were added to the cell the top was replaced. After trapping a sphere the vibration was turned off and the needle valve was opened slowly until the pressure began to drop, typically limited to 20 torr/second. Constant pressure was achieved by limiting the flow with the needle valve.

D.2 Results

The position fluctuation spectrum was measured for a 4.87 μm diameter sphere in a single beam trap as a function of pressure and beam power. At approximately 10 torr peaks appeared in the overdamped Lorentzian spectrum, representing the natural oscillation frequencies. The peak frequencies increased with increasing beam power.

In a related experiment the potential curvature was calculated from the position distribution as a function of pressure. The curvature relative to $k_B T$ increased due to the reduction in damping.

D.2.1. Spectrum vs. Power and Pressure

The fluctuation spectrum was measured from the forward scattered trapping beam using the technique described in [49]. A Centronic OSD155T silicon photodiode was mounted above the condenser lens. The photodiode was moved roughly one photodiode radius from the beam center in the x direction (see Section 3.2.2). Due to space constraints the axial position was not optimized. The photodiode operated in photovoltaic mode with a 10 kΩ resistor in parallel. Coaxial cable connected it to the HP3561A Dynamic Signal Analyzer (see Section 4.3.1), used to record the amplitude of intercepted power fluctuations from 10 Hz to 4 kHz. The amplitude was measured in arbitrary logarithmic units (proportional to dBV) that were consistent between data sets.

Figure D.3 shows the fluctuation spectrum as a function of pressure. A 4.87 μm diameter silica sphere was trapped at atmospheric pressure. The spectrum was measured with the pressure held constant using the needle valve. Above 1.3 torr the pressure was measured using the 1 atmosphere gauge. The pressure was lowered until the sphere escaped from the trap at 278 mtorr. The spectrum was averaged over 1000 sweeps using the HP3561A's rms averaging function. The data were transferred over the general purpose interface bus (GPIB) to the computer.

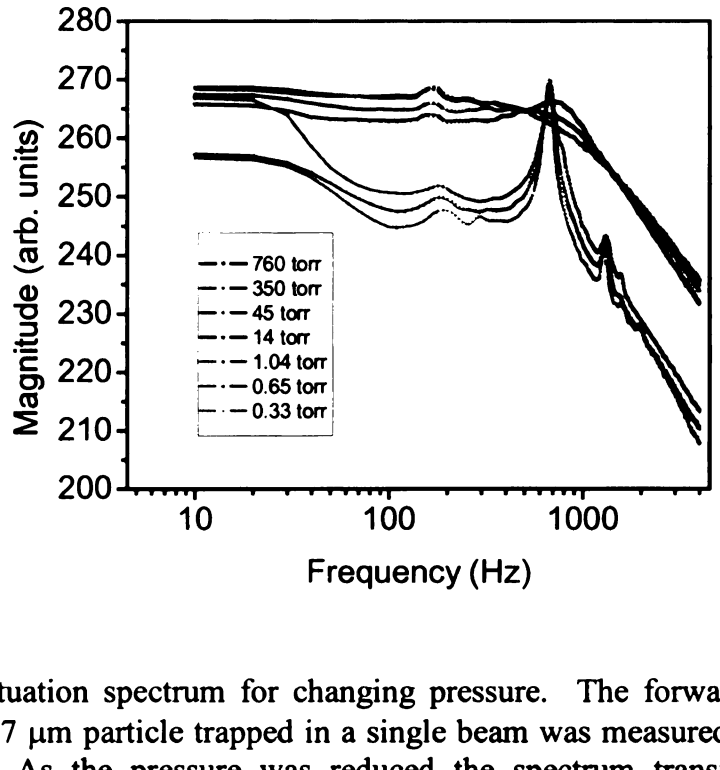

Figure D.3 Fluctuation spectrum for changing pressure. The forward scattered light from a 4.87 μm particle trapped in a single beam was measured with a spectrum analyzer. As the pressure was reduced the spectrum transformed from the overdamped Lorentzian to a series of peaks representing the natural oscillation frequencies in the underdamped system. The z frequency appeared at 190 Hz. The x frequency appeared at 670 Hz. The frequency independent region of the Lorentzian decreaseed in magnitude with decreasing pressure. The peak at 170 □□□Ĥ□-□÷□И□□□□□□□□□□□□□□□Ũ□□□□□□□□□□□□□□□Ā□Ĥ□d 110902, 5.6 mW beam power.)

At 760 torr and 350 torr the spectra show the expected Lorentzian shape. As the pressure was lowered a peak formed near 1 kHz (14 torr). Somewhere between 14 torr and 1 torr the system made the transition from overdamped to underdamped. A peak due to the z potential curvature arose at 190 Hz. (This is different from the 170 Hz peak in the $P \geq 14$ torr curves, caused by a measurement artifact.) The peak at 670 Hz represents the x curvature, with a peak near 1300 Hz representing y fluctuations (frequency doubled due to photodiode position). As the pressure was reduced the peaks narrowed and the background in the 50 Hz to 500 Hz range fell.

The fluctuation spectrum was measured vs. power with pressure held constant at 1.14 torr (Figure D.4). The beam power was changed from 6.3 mW to 3.98 mW using

the LS-PRO laser power stabilizer. At higher powers the particle was ejected to the upper stable point. The power was reduced until the particle escaped. The x and y curvature peaks moved to lower frequency with decreasing beam power. The positions of the second and third peaks are plotted vs. beam power in Figure D.5. The third peak positions were multiplied by 0.53, so the second and third peaks overlapped for 3.98 mW. The positions of the peaks overlap for the entire range. The expected dependence of trap curvature on beam power is $\omega \propto \sqrt{P}$ (see Appendix B), but Figure D.5 indicates a linear relationship.

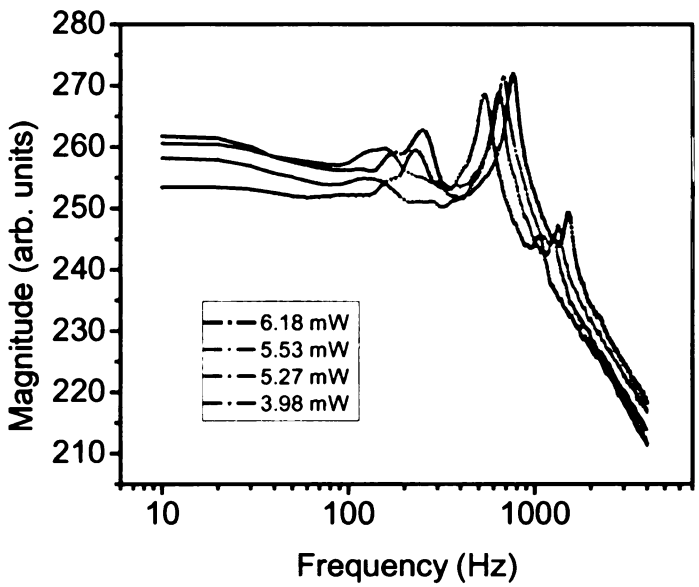

Figure D.4 Fluctuation spectrum of the underdamped particle with changing beam power. The x peak position (near 700 Hz) decreased with decreasing beam power, as did the harmonic (near 1500 Hz). The z peak should occur near 200 Hz and have similar power dependence. (Data labeled 110902, pressure = 1.14 torr.)

These measurements show that the system moved from overdamped to underdamped at a pressure near 10 torr. The particle motions changed from pure relaxation with a rate ω^2/Γ to oscillations about the trap center with frequency ω. The

oscillation frequency can be adjusted using the beam power, within limits. If the power is too large the particle will be ejected into the upper stable point (or out of the trap altogether). If the power is too small the particle will escape.

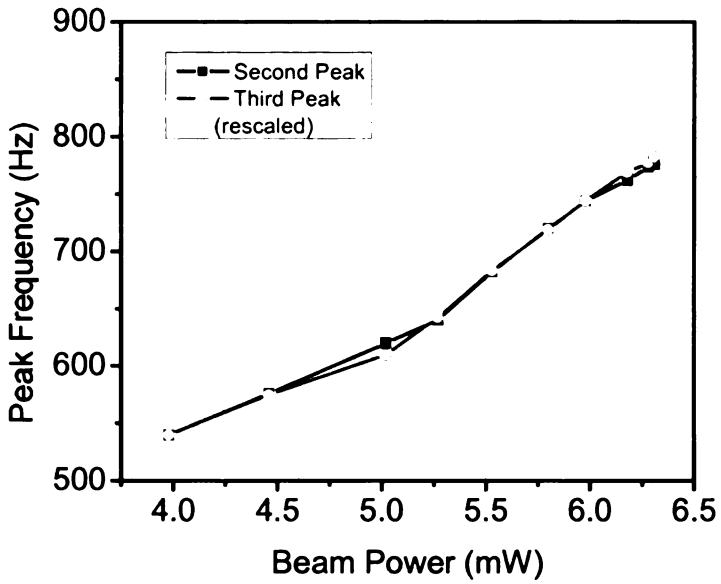

Figure D.5 Position of the second and third spectral peaks vs. beam power. The second and third peaks in Figure D.4 increased frequency with increasing beam power. The third peak position was multiplied by 560/1050, the ratio of the second peak position to third peak position for P = 3.98 mW. (Data labeled 110902, pressure = 1.14 torr.)

D.2.2. Curvature vs. Pressure

The position of the trapped particle was also measured, using the system described in Section 4.2. The three dimensional potential energy was calculated and the one dimensional profiles extracted (see Section 5.2). The z calibration changed with the position of the trap in the cell, therefore the z curvatures could not be accurately determined from the z profiles.

Figure D.6 shows the one dimensional potential energy profiles in the x direction as the pressure was reduced. The increase in the curvature was due to the change in the

damping. The Fluctuation-Dissipation theorem states that the amplitude of the noise (in this case Brownian motion) is proportional to the damping. These changes are not considered when calculating the potential energy.

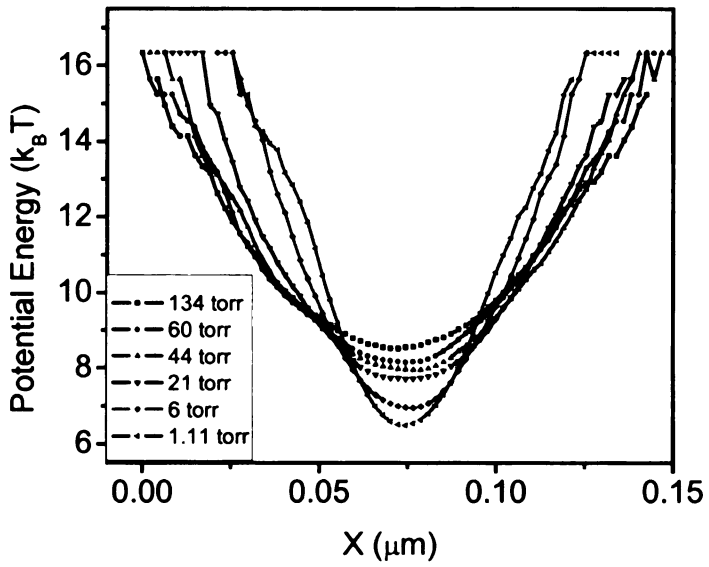

Figure D.6 X potential energy profiles with changing pressure. The curvature increases as the pressure decreases due to the change in the noise intensity. (Data labeled 111202, beam power 5.6 mW.)

The change in the x and y curvatures vs. pressure are plotted in Figure D.7. The curvatures decreased with increasing pressures up to 100 torr. Since the system was overdamped above 10 torr it is unknown whether the peak in the fluctuation spectrum changed.

These measurements show that the overdamped to underdamped crossover in the Kramers rate could be measured if a bistable potential could be formed. In the water system particles larger than the beam waist have an additional stable point between the beams. The smallest particle trapped in air (2.35 μm with 0.6 mW) was twice the size of the beam waist (1.2 μm). If a 1.2 μm diameter sphere could be trapped it is possible that

it would be localized in the focal plane with a bistable potential as seen in Figure 5.5. Techniques for lifting smaller particles and keeping them stably trapped need to be developed.

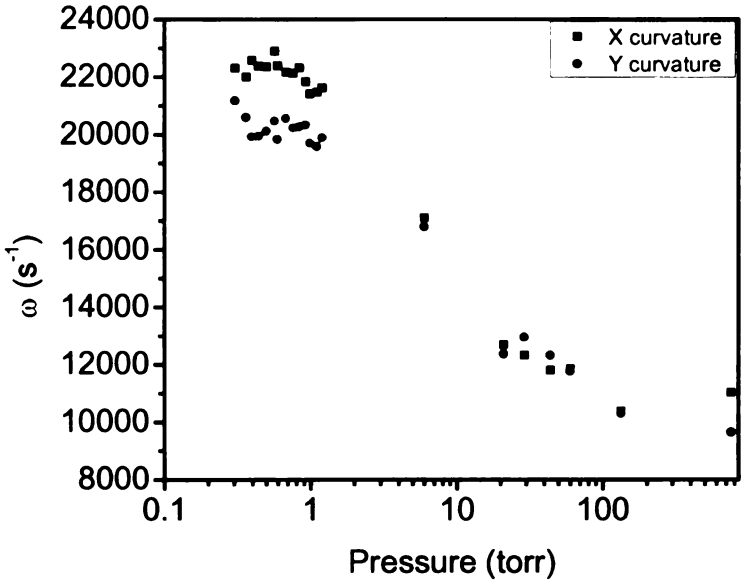

Figure D.7 X and y potential curvatures vs. pressure. The curvature decreases with increasing pressure due to the change in the damping rate. The damping does not change above 100 Hz. (Data labeled 111202, beam power 5.6 mW.)

D.3 Summary

An attempt was made to measure the Kramers rate in the crossover regime. A silica sphere was trapped in an air filled cell, then the air was removed using a vacuum pump. Trapped in a single beam, the particle position fluctuations indicated a transition from overdamped to underdamped with decreasing pressure. The peaks in the fluctuation spectrum decreased in frequency with decreasing beam power. The power was limited to a small range (from 6.3 mW to 3.98 mW for a 4.87 μm sphere) outside of which the particle was either lifted to a higher stable point (gravitationally opposed levitation) or

the particle escaped from the trap. The pressure was also limited to 250 torr, below which the particle was more likely to escape.

The system would be sufficient to study the crossover if a bistable potential could be created. The scattering forces of two overlapping beams tend to move one or both of the stable points out of the focal plane. Additional stable points of unknown origin also appear. These effects may disappear if a small enough particle can be lifted from the cell's bottom and trapped, with a beam convergence angle large enough so the axial gradient force always offsets the scattering forces of the combined beams.

Appendix E Calculation of the Potential Energy and Transition Statistics Using *Profiles*

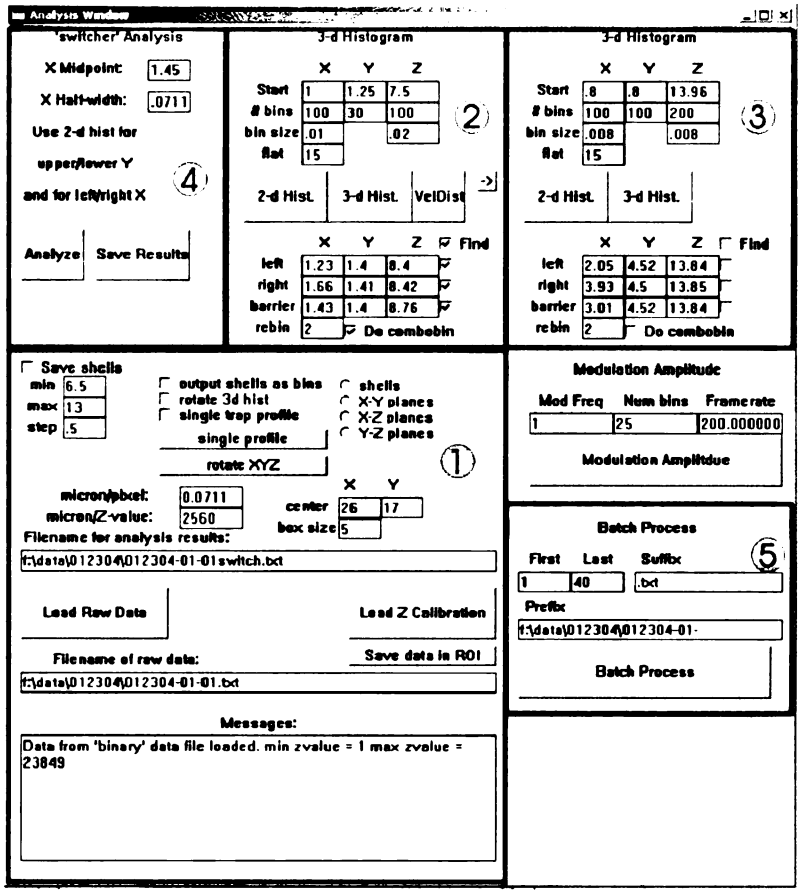

Figure E.1 *Profiles* user interface. *Profiles* was created from *WinMil2*'s analysis sections, areas 5 and 6 in Figure 4.8. Area 1 controls the data input, length calibration, and analysis output. Areas 2 and 3 create the three dimensional potential energy histogram and extract the one dimensional profiles. Area 4 controls the transition analysis. Area 5 is used to analyze multiple files with the same filename prefix.

Calculation of the potential energy occurs in the Visual C++ program *Profiles*. The Matrox Imaging Libraries (MIL) hardware copy protection prevents *WinMil2* from running on another computer. *Profiles* was created from the analysis portion of *WinMil2* (see Section 4.2) with some additional code. Figure E.1 shows the *Profiles* user interface,

separated into 5 subsections of functionality, numbered in the order in which they are typically used. The data file is loaded in area 1, applying the length scale conversion. Results of analysis performed on the data are output to the analysis file. Area 2 controls the three dimensional potential energy and one dimensional profile analysis. Area 3 performs the same function as area 2, and is used for comparisons between histogram parameters. The transition analysis is controlled in area 4. Area 5 allows the user to automate the analysis of multiple, consecutive files with the same suffix and prefix, for use with the batch data acquisition routine in *WinMil2*

E.1 Three dimensional potential energy surface

The position data are loaded from a file in area 1 of Figure E.1. The x and y values are converted from pixels to μm using the conversion 0.071 μm/pixel, and the z values are converted from the integrated particle intensity using the most recent calibration (see Section 4.2.3.8), modified in the "micron/Z-value" edit box.

The histogram parameters set the total analysis volume and bin sizes Δx, Δy, and Δz. These parameters are input into the top half of area 2 in Figure E.1. The three parameters in each direction are *Start*, *# bins*, and *binsize* (x and y use the same bin size). The i^{th} axis has length $L_i = \#bins_i \times binsize_i$ and extends from $Start_i$ to $Start_i+L_i$. To verify that the parameters contain the desired range of particle motions, a series of two dimensional projections of the three dimensional histogram (with given parameters) are displayed using the "2-d Hist" button (Figure E.2). The histogram parameters are modified to create 10 values in the y direction at the stable points (for the local fits in Section 5.2.2), with a typical xy bin size of 0.1 μm. The z bin size is set to 0.2 μm.

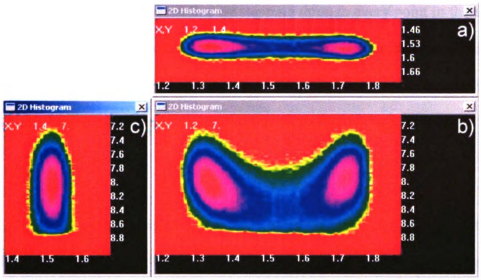

Figure E.2 Two dimensional potential energy projections. The "2-d Hist" button creates the (a) xy projection, (b) xz projection, and (c) yz projection. The numbers on the perimeter indicate the length scale (in μm), with positive z pointing down. The numbers in the upper left of each window are the position of a single pixel in the window, chosen by a left mouse click and used for estimating the stable point and barrier positions. (Data labeled 101403-03, 2,000,000 points, xy bin size = 0.01 μm, z bin size = 0.02 μm.)

Pressing the "3-d Hist" button in area 2 of Figure E.1 calls the OnHist3d() function, which creates the three dimensional and one dimensional potentials. The discrete position distribution is calculated and stored in a global array named Hist[][][]. The histogram parameters define the number of bins and the size of each bin. This array is passed to the functions that extract the one dimensional profiles.

OnHist3d() begins by reading the user inputs for the position distribution and the estimated stable point and barrier positions. The Hist array is initialized to zero. If the "rotate 3d hist" button is checked, the data are rotated in three dimensions until the line connecting the left and right points is parallel to the x axis. (Typically the traps are positioned so this is unnecessary.)

The position distribution is filled by stepping through every point in the data set. If the position is inside the box defined by the histogram parameters, the Hist array element corresponding to the position's volume element is incremented. The array index for each dimension is calculated

$$\text{Xbin} = \text{floor}\left(\frac{x_i - x_0}{binsize}\right),$$

where x_i is the current position, x_0 is the Start value (Figure E.1). The floor function rounds the fraction to the next lower integer. The total number of points is incremented each time a Hist element is incremented.

The equation (5.2) is used to calculate the potential energy in each volume element,

$$\text{PE} = -\ln\left(\frac{\text{Hist}[x][y][z]}{\text{total}}\right),$$

in units of k_BT. Volume elements with zero counts are set to 20 k_BT. This value is used only for file output or comparisons; it is not saved. Recalculating PE has little effect on processing time and conserves memory.

The position distribution is averaged over $(2 \times \text{rebin} + 1)^2$ volume elements, where the rebin number is set in area 2 of Figure E.1. The direction of averaging depends on the calculation. For the one dimensional potential energy profiles, the averaging is perpendicular to the direction of the profile. For example, in calculating the x profile,

$$\text{sum} = \sum_{\delta y=-\text{rebin}}^{\delta y=\text{rebin}} \sum_{\delta z=-\text{rebin}}^{\delta z=\text{rebin}} \text{Hist}[x][y+\delta y][z+\delta z]$$

and the potential energy is

$$(5.2) \quad PE = -\ln\left(\frac{sum}{total \times (2 \times rebin + 1)^2}\right).$$

The OnHist3d() function calculates the one dimensional potential energy profiles, from which the barrier height and potential curvatures are measured. After a header describing the histogram parameters, the first data saved to the analysis output file are the one dimensional profile in the x direction.

OnHist3d() calls a subroutine named StepPlanes() to step along a given direction and find the minimum energy. If rebin is greater than zero the Hist array is averaged in y and z before calculating potential energy. Figure 5.10 shows a single xz plane at the center of the potential. Darker regions represent lower energy. The diamonds show the path of minimum energy calculated by StepPlanes() with rebin = 2.

E.2 One dimensional potential energy profiles

Extraction of the y and z one dimensional profiles from the three dimensional potential energy takes as input the three dimensional coordinates of the stable points and saddle point. These values are either input into the left, right, and barrier edit boxes in area 2 of Figure E.1, or, if the "Find" box is checked, are found from the x profile. When input by hand the values are estimated from the two dimensional projections (Figure E.2). First the x and y positions are estimated from the x-y projection, then the z positions from the x-z projection.

To use the program to find the saddle and stable point positions the potential is split at the x position in the "X Midpoint" edit box. After finishing the StepPlanes() function for x, OnHist3d() steps through the volume elements with x less than the midpoint value and determines the coordinates with the largest number of counts (or

average number of counts if rebin is nonzero). This process repeats for the volume elements on the other side of the midpoint. The barrier is a saddle point, a local minimum for y and z but a local maximum for x. To find the barrier position the x range is limited to the midpoint ± 2% of the x bins. For example, for Figure E.1's values of 100 x bins and midpoint = 1.45 the x range is 1.43 to 1.47 μm. The position with minimum energy in this volume is considered the barrier position. The x, y, and z values for all three extrema are written to the edit boxes.

Originally the StepPlanes() function was repeated for y and z. This either missed one of the stable points, or caused the position of the minimum to jump between stable points while stepping in y or z. A new subroutine was written to correct this problem, Profiles(), which outputs the potential energy for lines in y and z running through the stable points and barrier. The squares in Figure 5.10 represent the z profile paths.

Profiles() is called once for each extremum with a checked box, outputting the profiles in the x and z directions. The minimum energy at the saddle point is found within a 7 x 7 bin area in y and z (but not x, for which the barrier is a local maximum). If rebin is nonzero, the position distribution is averaged over a *volume* of $(2 \times \text{rebin} + 1)^3$ bins. For the stable points the minimum energy is found within a 7 x 7 x 7 bin volume, averaging over the area $(2 \times \text{rebin} + 1)^2$. The potential for the y profile then the z profile is output to the analysis results file.

The output of StepPlanes() and Profiles() contains five columns: the position of the volume element in x, y, and z, the potential energy calculated from equation (5.2), and the number of counts for that element. The final column is used to estimate uncertainties. After the y and z profiles are output the file is closed and OnHist3d() ends.

E.3 Dwell time and transition time

The dwell times are calculated in the OnAnalyze() function in *Profiles* when the "Analyze" button is pressed. The function steps through the particle positions, counting the amount of time spent in each well. When the particle makes a transition (when it crosses the half-width) the counter is reset and the dwell time and frame number are stored.

If there is a mismatched frame the measured position may be on the other side of the midpoint and half-width. If a frame is missing the position is automatically set zero. To prevent these events from being counted as transitions, a bounding box is created using the three dimensional histogram parameters in area 2 of Figure E.1. If a frame has a position outside of this box the counter is incremented and the particle is defined to be in the same well in as the previous frame. Since mismatched and missing frames tend to occur for large z excursions from the stable points, careful choice of the model image limits these events to when the particle is low in the traps (-z) and unlikely to make a transition, reducing the possibility of missing an actual transition.

The "Save Results" button saves the dwell times and transition times (in units of frames) for each well to the analysis results file. This file is opened in Origin and a histogram of dwell times created (Figure 5.9).

After acquisition the data are transferred to Komodo.pa.msu.edu for analysis with the *Profiles* program. A batch analysis routine, controlled in area 5 of Figure 5.8, outputs the dwell time and transition time results and the one dimensional profiles for the sequentially numbered data files. These files are imported into Origin to calculate the mean dwell time (Section 5.1) and the fits to the static potentials (Section 5.2). The

quartic fits to the static tilt data sets are used to estimate the adiabatic critical amplitude A_c^{ad}. The potential energy calculated for modulated data sets does not represent the static potential so the one dimensional profiles fits are not performed.

REFERENCES

1. Kramers, H. A. Brownian motion in a field of force and the diffusion model of chemical reactions. *Physica* **7**, 284 (1940).

2. Dykman, M. I., McClintock, P. V. E., Smelyanski, V. N., Stein, N. D. & Stocks, N. G. Optimal Paths and the Prehistory Problem for Large Fluctuations in Noise-Driven Systems. *Physical Review Letters* **68**, 2718-2721 (1992).

3. Halliday, D., Resnick, R. & Krane, K. *Physics* (John Wiley & Sons, Inc., New York, 1992).

4. Gittes, F. & Schmidt, C. F. in *Methods in Cell Biology, Vol 55* 129-156 (1998).

5. Risken, H. *The Fokker-Planck Equation, Methods of Solution and Application* (ed. Haken, H.) (Springer-Verlag, Berlin, 1984).

6. Gardiner, C. W. *Handbook of Stochastic Methods for Physics, Chemistry and the Natural Sciences* (ed. Haken, H.) (Springer-Verlag, Berlin, 1983).

7. Kampen, N. G. v. *Stochastic Processes in Physics and Chemistry* (North-Holland Publishing Company, New York, 1981).

8. McCann, L. I., Dykman, M. & Golding, B. Thermally activated transitions in a bistable three-dimensional optical trap. *Nature* **402**, 785-787 (1999).

9. Melnikov, V. I. The Kramers Problem - 50 Years of Development. *Physics Reports-Review Section of Physics Letters* **209**, 1-71 (1991).

10. Hanggi, P., Talkner, P. & Borkovec, M. Reaction-Rate Theory - 50 Years after Kramers. *Reviews of Modern Physics* **62**, 251-341 (1990).

11. Dykman, M. I. Large Fluctuations and Fluctuational Transitions in Systems Driven by Colored Gaussian-Noise - a High-Frequency Noise. *Physical Review A* **42**, 2020-2029 (1990).

12. Melnikov, V. I. Activated Decay-Rate - Finite-Barrier Corrections. *Physical Review E* **48**, 3271-3284 (1993).

13. Linkwitz, S., Grabert, H., Turlot, E., Esteve, D. & Devoret, M. H. Escape Rates in the Region between the Kramers Limits. *Physical Review A* **45**, R3369-R3372 (1992).

14. Shneidman, V. A. Transient solution of the Kramers problem in the weak noise limit. *Physical Review E* **56**, 5257-5264 (1997).

15. Arrayas, M., Kaufman, I. K., Luchinsky, D. G., McClintock, P. V. E. & Soskin, S. M. Kramers problem for a multiwell potential. *Physical Review Letters* **84**, 2556-2559 (2000).

16. Soskin, S. M., Sheka, V. I., Linnik, T. L. & Mannella, R. Short time scales in the Kramers problem: A stepwise growth of the escape flux. *Physical Review Letters* **86**, 1665-1669 (2001).

17. Soskin, S. M. et al. Noise-induced escape on time scales preceding quasistationarity: New developments in the Kramers problem. *Chaos* **11**, 595-604 (2001).

18. Devoret, M. H., Esteve, D., Martinis, J. M., Cleland, A. & Clarke, J. Resonant Activation of a Brownian Particle out of a Potential Well - Microwave-Enhanced Escape from the Zero-Voltage State of a Josephson Junction. *Physical Review B* **36**, 58-73 (1987).

19. Dykman, M. I. et al. Activated escape of periodically driven systems. *Chaos* **11**, 587-594 (2001).

20. Smelyanskiy, V. N. & Dykman, M. I. Optimal control of large fluctuations. *Physical Review E* **55**, 2516-2521 (1997).

21. McNamara, B. & Wiesenfeld, K. Theory of Stochastic Resonance. *Physical Review A* **39**, 4854-4869 (1989).

22. Wiesenfeld, K. & Jaramillo, F. Minireview of stochastic resonance. *Chaos* **8**, 539-548 (1998).

23. Benzi, R., Parisi, G., Sutera, A. & Vulpiani, A. A Theory of Stochastic Resonance in Climatic-Change. *Siam Journal on Applied Mathematics* **43**, 565-578 (1983).

24. Dykman, M. I. et al. Stochastic Resonance in Perspective. *Nuovo Cimento Della Societa Italiana Di Fisica D-Condensed Matter Atomic Molecular and Chemical Physics Fluids Plasmas Biophysics* **17**, 661-683 (1995).

25. Gammaitoni, L., Hanggi, P., Jung, P. & Marchesoni, F. Stochastic Resonance. *Reviews of Modern Physics* **70**, 224-283 (1998).

26. Dykman, M. I., Mannella, R., McClintock, P. V. E. & Stocks, N. G. Phase-Shifts in Stochastic Resonance. *Physical Review Letters* **68**, 2985-2988 (1992).

27. Callen, H. B. & Welton, T. A. Irreversibility and Generalized Noise. *Physical Review* **83**, 34-40 (1951).

28. Callen, H. B. & Greene, R. F. On a Theorem of Irreversible Thermodynamics. *Physical Review* **86**, 702-710 (1952).

29. McNamara, B., Wiesenfeld, K. & Roy, R. Observation of Stochastic Resonance in a Ring Laser. *Physical Review Letters* **60**, 2626-2629 (1988).

30. Simon, A. & Libchaber, A. Escape and Synchronization of a Brownian Particle. *Physical Review Letters* **68**, 3375-3378 (1992).

31. Julicher, F., Ajdari, A. & Prost, J. Modeling molecular motors. *Reviews of Modern Physics* **69**, 1269-1281 (1997).

32. Bier, M. Brownian ratchets in physics and biology. *Contemporary Physics* **38**, 371-379 (1997).

33. Magnasco, M. O. Forced Thermal Ratchets. *Physical Review Letters* **71**, 1477-1481 (1993).

34. Faucheux, L. P., Bourdieu, L. S., Kaplan, P. D. & Libchaber, A. J. Optical Thermal Ratchet. *Physical Review Letters* **74**, 1504-1507 (1995).

35. Ajdari, A., Mukamel, D., Peliti, L. & Prost, J. Rectified Motion-Induced by Ac Forces in Periodic Structures. *Journal De Physique I* **4**, 1551-1561 (1994).

36. Mahato, M. C. & Jayannavar, A. M. Synchronized First-Passages in a Double-Well System Driven by an Asymmetric Periodic Field. *Physics Letters A* **209**, 21-25 (1995).

37. Chialvo, D. R. & Millonas, M. M. Asymmetric Unbiased Fluctuations Are Sufficient for the Operation of a Correlation Ratchet. *Physics Letters A* **209**, 26-30 (1995).

38. Dykman, M. I., Rabitz, H., Smelyanskiy, V. N. & Vugmeister, B. E. Resonant directed diffusion in nonadiabatically driven systems. *Physical Review Letters* **79**, 1178-1181 (1997).

39. Smelyanskiy, V. N., Dykman, M. I., Rabitz, H. & Vugmeister, B. E. Fluctuations, escape, and nucleation in driven systems: Logarithmic susceptibility. *Physical Review Letters* **79**, 3113-3116 (1997).

40. Smelyanskiy, V. N. et al. Nucleation in periodically driven electrochemical systems. *Journal of Chemical Physics* **110**, 11488-11504 (1999).

41. Luchinsky, D. G., Mannella, R., McClintock, P. V. E., Dykman, M. I. & Smelyanskiy, V. N. Thermally activated escape of driven systems: the activation energy. *Journal of Physics a-Mathematical and General* **32**, L321-L327 (1999).

42. Turlot, E. et al. High frequency satellites in resonant activation. *Chemical Physics* **235**, 47-50 (1998).

43. Smelyanskiy, V. N., Dykman, M. I. & Golding, B. Time oscillations of escape rates in periodically driven systems. *Physical Review Letters* **82**, 3193-3197 (1999).

44. Dykman, M. I., Golding, B., Kruse, J. R., McCann, L. I. & Ryvkine, D. in *Unsolved Problems in Noise and Fluctuations* (ed. Bezrukov, S. M.) (AIP Publishing, Washington, DC, 2002).

45. Dykman, M. I., Golding, B. & Ryvkine, D. Critical exponent crossovers in escape near a bifurcation point. *Physical Review Letters* **92** (2004).

46. Ryvkine, D., Dykman, M. & Golding, B. Scaling and crossovers in activated escape near a bifurcation point. *cond-mat/0312169* (2003).

47. Ashkin, A. Acceleration and Trapping of Particles by Radiation Pressure. *Physical Review Letters* **24**, 156-& (1970).

48. Ashkin, A., Dziedzic, J. M., Bjorkholm, J. E. & Chu, S. Observation of a Single-Beam Gradient Force Optical Trap for Dielectric Particles. *Optics Letters* **11**, 288-290 (1986).

49. Ghislain, L. P., Switz, N. A. & Webb, W. W. Measurement of Small Forces Using an Optical Trap. *Review of Scientific Instruments* **65**, 2762-2768 (1994).

50. Gittes, F. & Schmidt, C. F. Interference model for back-focal-plane displacement detection in optical tweezers. *Optics Letters* **23**, 7-9 (1998).

51. Simmons, R. M., Finer, J. T., Chu, S. & Spudich, J. A. Quantitative measurements of force and displacement using an optical trap. *Biophysical Journal* **70**, 1813-1822 (1996).

52. Ashkin, A. & Dziedzic, J. M. Optical Levitation by Radiation Pressure. *Applied Physics Letters* **19**, 283-& (1971).

53. Ashkin, A. & Dziedzic, J. M. Optical Levitation of Liquid Drops by Radiation Pressure. *Science* **187**, 1073-1075 (1975).

54. Ashkin, A. & Dziedzic, J. M. Optical Levitation in High-Vacuum. *Applied Physics Letters* **28**, 333-335 (1976).

55. Kerker, M. *The Scattering of Light and other electromagnetic radiation* (ed. Loebl, E. M.) (Academic Press, New York, 1969).

56. Sato, S., Ishigure, M. & Inaba, H. Optical Trapping and Rotational Manipulation of Microscopic Particles and Biological Cells Using Higher-Order Mode Nd-Yag Laser-Beams. *Electronics Letters* **27**, 1831-1832 (1991).

57. Lyons, E. R. & Sonek, G. J. Confinement and Bistability in a Tapered Hemispherically Lensed Optical-Fiber Trap. *Applied Physics Letters* **66**, 1584-1586 (1995).

58. Renn, M. J. & Pastel, R. Particle manipulation and surface patterning by laser guidance. *Journal of Vacuum Science & Technology B* **16**, 3859-3863 (1998).

59. Constable, A., Kim, J., Mervis, J., Zarinetchi, F. & Prentiss, M. Demonstration of a Fiberoptic Light-Force Trap. *Optics Letters* **18**, 1867-1869 (1993).

60. Collins, S. D., Baskin, R. J. & Howitt, D. G. Microinstrument gradient-force optical trap. *Applied Optics* **38**, 6068-6074 (1999).

61. Zemanek, P., Jonas, A., Sramek, L. & Liska, M. Optical trapping of Rayleigh particles using a Gaussian standing wave. *Optics Communications* **151**, 273-285 (1998).

62. Zemanek, P., Jonas, A., Sramek, L. & Liska, M. Optical trapping of nanoparticles and microparticles by a Gaussian standing wave. *Optics Letters* **24**, 1448-1450 (1999).

63. Afzal, R. S. & Treacy, E. B. Optical Tweezers Using a Diode-Laser. *Review of Scientific Instruments* **63**, 2157-2163 (1992).

64. Ogura, Y., Kagawa, K. & Tanida, J. Optical manipulation of microscopic objects by means of vertical-cavity surface-emitting laser array sources. *Applied Optics* **40**, 5430-5435 (2001).

65. Visscher, K., Brakenhoff, G. J. & Krol, J. J. Micromanipulation by Multiple Optical Traps Created by a Single Fast Scanning Trap Integrated with the Bilateral Confocal Scanning Laser Microscope. *Cytometry* **14**, 105-114 (1993).

66. Visscher, K., Gross, S. P. & Block, S. M. Construction of multiple-beam optical traps with nanometer-resolution position sensing. *Ieee Journal of Selected Topics in Quantum Electronics* **2**, 1066-1076 (1996).

67. Mio, C., Gong, T., Terray, A. & Marr, D. W. M. Design of a scanning laser optical trap for multiparticle manipulation. *Review of Scientific Instruments* **71**, 2196-2200 (2000).

68. Dufresne, E. R., Squires, T. M., Brenner, M. P. & Grier, D. G. Hydrodynamic coupling of two Brownian spheres to a planar surface. *Physical Review Letters* **85**, 3317-3320 (2000).

69. Dufresne, E. R. & Grier, D. G. Optical tweezer arrays and optical substrates created with diffractive optics. *Review of Scientific Instruments* **69**, 1974-1977 (1998).

70. Reicherter, M., Haist, T., Wagemann, E. U. & Tiziani, H. J. Optical particle trapping with computer-generated holograms written on a liquid-crystal display. *Optics Letters* **24**, 608-610 (1999).

71. Dufresne, E. R., Spalding, G. C., Dearing, M. T., Sheets, S. A. & Grier, D. G. Computer-generated holographic optical tweezer arrays. *Review of Scientific Instruments* **72**, 1810-1816 (2001).

72. Mogensen, P. C. & Gluckstad, J. Dynamic away generation and pattern formation for optical tweezers. *Optics Communications* **175**, 75-81 (2000).

73. Simon, A. & Libchaber, A. Escape and Synchronization of a Brownian Particle. *Journal of Statistical Physics* **70**, 423-423 (1993).

74. Henderson, S., Mitchell, S. & Bartlett, P. Direct measurements of colloidal friction coefficients. *Physical Review E* **6406** (2001).

75. Meiners, J. C. & Quake, S. R. Direct measurement of hydrodynamic cross correlations between two particles in an external potential. *Physical Review Letters* **82**, 2211-2214 (1999).

76. Ashkin, A. History of optical trapping and manipulation of small-neutral particle, atoms, and molecules. *Ieee Journal of Selected Topics in Quantum Electronics* **6**, 841-856 (2000).

77. Grier, D. G. A revolution in optical manipulation. *Nature* **424**, 810-816 (2003).

78. Prieve, D. C. & Alexander, B. M. Hydrodynamic Measurement of Double-Layer Repulsion between Colloidal Particle and Flat-Plate. *Science* **231**, 1269-1270 (1986).

79. Alexander, B. M. & Prieve, D. C. A Hydrodynamic Technique for Measurement of Colloidal Forces. *Langmuir* **3**, 788-795 (1987).

80. Bartlett, P. & Henderson, S. Three-dimensional force calibration of a single-beam optical gradient trap. *Journal of Physics-Condensed Matter* **14**, 7757-7768 (2002).

81. Felgner, H., Muller, O. & Schliwa, M. Calibration of Light Forces in Optical Tweezers. *Applied Optics* **34**, 977-982 (1995).

82. Ashkin, A. Forces of a Single-Beam Gradient Laser Trap on a Dielectric Sphere in the Ray Optics Regime. *Biophysical Journal* **61**, 569-582 (1992).

83. Wright, W. H., Sonek, G. J. & Berns, M. W. Radiation Trapping Forces on Microspheres with Optical Tweezers. *Applied Physics Letters* **63**, 715-717 (1993).

84. Wright, W. H., Sonek, G. J., Tadir, Y. & Berns, M. W. Laser Trapping in Cell Biology. *Ieee Journal of Quantum Electronics* **26**, 2148-2157 (1990).

85. Fallman, E. & Axner, O. Design for fully steerable dual-trap optical tweezers. *Applied Optics* **36**, 2107-2113 (1997).

86. Harada, Y. & Asakura, T. Radiation forces on a dielectric sphere in the Rayleigh scattering regime. *Optics Communications* **124**, 529-541 (1996).

87. Barton, J. P. & Alexander, D. R. 5th-Order Corrected Electromagnetic-Field Components for a Fundamental Gaussian-Beam. *Journal of Applied Physics* **66**, 2800-2802 (1989).

88. O'Shea, D. C. *Elements of Modern Optical Design* (ed. Goodman, J. W.) (John Wiley & Sons, New York, 1985).

89. Iler, R. K. *The Chemistry of Silica* (John Wiley & Sons, 1979).

90. Fallman, E. & Axner, O. Influence of a glass-water interface on the on-axis trapping of micrometer-sized spherical objects by optical tweezers. *Applied Optics* **42**, 3915-3926 (2003).

91. Dykman, M. I. & Krivoglaz, M. A. Fluctuations in Non-Linear Systems near Bifurcations Corresponding to the Appearance of New Stable States. *Physica A* **104**, 480-494 (1980).

92. Barton, J. P., Alexander, D. R. & Schaub, S. A. Theoretical Determination of Net-Radiation Force and Torque for a Spherical-Particle Illuminated by a Focused Laser-Beam. *Journal of Applied Physics* **66**, 4594-4602 (1989).

93. Rohrbach, A. & Stelzer, E. H. K. Trapping forces, force constants and potential depths for dielectric spheres in the presence of spherical aberrations. *Biophysical Journal* **80**, 163A-163A (2001).

94. Rohrbach, A. & Stelzer, E. H. K. Optical trapping of dielectric particles in arbitrary fields. *Journal of the Optical Society of America a-Optics Image Science and Vision* **18**, 839-853 (2001).

95. Tlusty, T., Meller, A. & Bar-Ziv, R. Optical gradient forces of strongly localized fields. *Physical Review Letters* **81**, 1738-1741 (1998).

96. Hecht, E. *Optics* (Addison-Wesley, 1998).

97. Ashkin, A. & Dziedzic, J. M. Feedback Stabilization of Optically Levitated Particles. *Applied Physics Letters* **30**, 202-204 (1977).

98. Ashkin, A. & Dziedzic, J. M. Observation of Light-Scattering from Nonspherical Particles Using Optical Levitation. *Applied Optics* **19**, 660-668 (1980).

99. Omori, R., Kobayashi, T. & Suzuki, A. Observation of a single-beam gradient-force optical trap for dielectric particles in air. *Optics Letters* **22**, 816-818 (1997).

100. Omori, R., Shima, K. & Suzuki, A. Rotation of optically trapped particles in air. *Japanese Journal of Applied Physics Part 2-Letters* **38**, L743-L745 (1999).

101. Kaiser, T., Roll, G. & Schweiger, G. Enhancement of the Raman-Spectrum of Optically Levitated Microspheres by Seeded Nanoparticles. *Journal of the Optical Society of America B-Optical Physics* **12**, 281-286 (1995).